APPLIED COMPUTATIONAL ELECTROMAGNETICS SOCIETY JOURNAL

AUGUST 2019 REVIEWERS: REGULAR PAPERS

Pradeep A. S.
Mahmood Abbasi Layegh
Mohammad Abdolrazzaghi
Ghulam Ahmad
Kiran Ajetrao
Giovanni Angiulli
Jaume Anguera
Sami Barmada
Hsi-Tseng Chou
Theofilos Chrysikos
John Daniel
Ian Flintoft
Alfredo Gomes Neto
Michael Johnson
Fadil Kuyucuoglu
Kang Lan
Raja Mchaalia
Zahéra Mekkioui

César Méndez Ruiz
Pejman Mohammadi
Andrew Peterson
Camelia Petrescu
Mohammd Pourbagher
Rashid Saleem
Vitawat Sittakul
Chalasani Subba Rao
Sheng Sun
Stelios Tsitsos
Sanjay Velamparambil
Guoan Wang
Wei-Chung Weng
Traianos Yioultsis
Xingqiu Yuan
Lei Zhao
Shouzheng Zhu

AUGUST 2019 REVIEWERS: EXPRESS PAPERS

Saad Alhossin
Reza K. Amineh
Yang Bao
John Daniel
Changjiang Deng
Amin Gorji
Niamat Hussain
Zi-Liang Liu

Peyman Mahouti
Mahdi Naghshvarian Jahromi
MuhibUr Rahman
Rajni Rajni
Pavel Roy Paladhi
Kapil Sharma
Jiangong Wei
Shaoyong Zheng

THE APPLIED COMPUTATIONAL ELECTROMAGNETICS SOCIETY JOURNAL

Vol. 34 No. 8   August 2019

TABLE OF CONTENTS – REGULAR PAPERS

TABLE OF CONTENTS – EXPRESS PAPERS

EMC Simulation Based on FDTD Analysis Considering Uncertain Inputs with Arbitrary Probability Density

Jinjun Bai [1], Gang Zhang [2], and Lixin Wang [2]

[1] College of Marine Electrical Engineering
Dalian Maritime University, Dalian, 116026, China
baijinjun@dlmu.edu.cn

[2] School of Electrical Engineering and Automation
Harbin Institute of Technology, Harbin, 150001, China
zhang_hit@hit.edu.cn, wlx@hit.edu.cn

Abstract ─ Stochastic Galerkin Method, a prevailing uncertainty analysis method, has been successfully used in today's EMC simulation, in order to consider non-ideality and unpredictability in actual circumstance. In this case, the inputs of the simulation are no longer certain values, but random variables with corresponding probability density distribution. This paper focuses on the arbitrary probability density cases at inputs. Two constructing orthogonal basis methods, the Wiener Haar expansion and the Stieltjes procedure, are generalized into the Stochastic Galerkin Method which is combined with the Finite Difference Time Domain analysis. With the help of the Feature Selective Validation, the quantitative precision comparison of the proposed methods in different cases (the probability density function is continuous or discontinuous) can be presented in detail.

Index Terms ─ Arbitrary probability density, EMC simulation, FDTD analysis, stochastic Galerkin method, uncertainty analysis.

I. INTRODUCTION

Recent years, the Electromagnetic Compatibility (EMC) community usually takes uncertainty factors of input parameters into account, in order to improve the reliability of calculation results. The uncertainty factors may come from the lack of knowledge, manufacturing tolerance and so forth. For example, the uncertainty into material or excitation source is always considered, thanks to the complexity of the electromagnetic environment. Meanwhile, Finite Difference Time Domain (FDTD) analysis is a powerful tool in EMC simulation [1, 2]. In order to analyze this uncertainty in EMC simulation, many uncertainty analysis methods have been generalized into the FDTD analysis in recent studies [3-6].

Among the existing references, the Monte Carlo Method (MCM) is conventionally widely adopted [3, 4].

In MCM, the uncertain inputs are sampled in terms of their distributions. At each sampling point, a certain simulation will be performed. The final uncertainty analysis result should be the statistical characteristic of the results in every point. As confirmed by [3] and [4], MCM has been proved accurate, though its computational efficiency presents quite low [4]. Anyway, thanks to its high accuracy, the results given by the MCM are always treated as the reference data to evaluate the precision of other uncertainty analysis methods in the theoretical research.

Other uncertainty analysis methods have been also successfully used in EMC simulation based on the FDTD analysis, such as Stochastic Collocation Method (SCM) [5], Method of Moments (MOM) [6] and Stochastic Galerkin Method (SGM) [7]. The SCM is based on the multidimensional Lagrange Interpolation theorem, and the interpolation errors might be brought in the results. Thus, the SCM can hardly guarantee high accuracy when the output results are not smoothness enough [5]. In MOM, the first order Taylor series expansion is applied to calculate the expectation and the standard deviation of the outputs. However, the precision of MOM tends to be very poor when the magnitude is large in inputs or outputs [6].

The SGM is rooted in the generalized Polynomial Chaos (gPC) expansion theory, and it has been attached much attention to in recent research thanks to its high accuracy, though the realization of it is quite complex comparing with the SCM and the MOM [7, 8]. In reference [7] and reference [8], the SGM is generalized into the FDTD analysis to solve the stochastic Maxwell's equations, the shielding effectiveness analysis with uncertain materials and 3D sphere scattering calculation with uncertain geometric parameters are presented. It is proved that the accuracy of the SGM is highly consistent with that of the MCM in these calculation examples.

In using the SGM, the uncertain inputs must be

modeled by the random variables with corresponding probability density distributions. However, in previous studies [7, 8], the distributions of the uncertain inputs are all supposed the common distributions, like the Uniform distributions or the Gaussian distributions. Little attempts in considering the arbitrary probability density distributions have been made, which greatly limits the application of the SGM.

In this paper, the Stieltjes procedure [9, 10] and the Wiener Haar expansion [11] are proposed to construct the orthogonal basis of the SGM when considering the uncertain inputs with arbitrary probability density distributions. A published example in reference [12] is brought in, and the uncertain inputs are assumed the stochastic excitation source with arbitrary probability density distributions. The uncertainty analysis results given by the MCM are regarded as the reference data, in order to evaluate the accuracy of two proposed methods in different cases.

The structure of the paper is as follows: Section II gives a brief introduction of the SGM mechanism combined with FDTD analysis. Stieltjes procedure and Wiener Haar expansion in constructing orthogonal basis of the SGM are presented respectively in Section III. The accuracy comparison by using FSV is demonstrated in Section IV. Section V provides the conclusion part of this paper.

II. THE STOCHASTIC GALERKIN METHOD MECHANISM

In the real electromagnetism environment, lack of knowledge or manufacturing tolerance may cause the uncertainty in material parameters or geometric parameters in EMC simulation model, and they can be called random events. Conventional deterministic FDTD analysis are not capable of dealing with this uncertainty, since that some input parameters are no longer certain values.

The random variables can be used to model the random events, and they are expressed as:

$$\xi(\theta) = \{\xi_1(\theta),\ \xi_2(\theta),\ \cdots,\ \xi_M(\theta)\}, \tag{1}$$

where θ represents the random events. $\xi_i(\theta)$ is a random variable with its own distribution depending on the random events. $\xi(\theta)$ is the random variable vector, and M is the number of the random variables in the vector.

The one-dimensional Maxwell's equations in discrete version by using Finite Difference Time Domain Method are given as:

$$H_y^{n+1/2}(i+1/2) = H_y^{n-1/2}(i+1/2) + \gamma\left(E_z^n(i+1) - E_z^n(i)\right), \tag{2}$$

and

$$E_z^{n+1}(i) = \alpha E_z^n(i) + \beta\left(H_y^{n+1/2}(i+1/2) - H_y^{n+1/2}(i-1/2)\right). \tag{3}$$

The direction of propagation is along the x axis. H_y

stands for the magnetic field intensity in y axis, and E_z is the electric field intensity in z axis. Where n presents the Discrete-time, and i stands for the Discrete-space. α, β and γ are the constant values which are calculated by material parameters, time interval and space interval.

Suppose the position of the excitation source is $i = ks$, equation (3) can be arranged as:

$$E_z^{n+1}(ks) = \alpha E_z^n(ks) + \beta\left(H_y^{n+1/2}(ks+1/2) - H_y^{n+1/2}(ks-1/2)\right). \tag{4}$$

If the excitation source is uncertain, the random variable vector ξ would be introduced into the Maxwell's equations and (4) can be re-written as:

$$E_z^{n+1}(ks,\xi) = \alpha E_z^n(ks,\xi) + \beta\left(H_y^{n+1/2}(ks+1/2,\xi) - H_y^{n+1/2}(ks-1/2,\xi)\right), \tag{5}$$

where $E_z^{n+1}(ks,\xi)$ and $E_z^n(ks,\xi)$ are the excitation source, and they are uncertain inputs. Obviously, the output parameters $H_y^{n+1/2}(ks+1/2,\xi)$ and $H_y^{n+1/2}(ks-1/2,\xi)$ would be influenced by the uncertain inputs.

In Stochastic Galerkin Method (SGM), the uncertainty analysis results, namely the uncertain output parameters, should be expressed as the form of the polynomial of the random variables at first. It can be expressed as:

$$H_y^{n+1/2}(ks+1/2,\xi) = h_0(ks+1/2)\varphi_0(\xi) + h_1(ks+1/2)\varphi_1(\xi) + h_2(ks+1/2)\varphi_2(\xi), \tag{6}$$

and

$$H_y^{n+1/2}(ks-1/2,\xi) = h_0(ks-1/2)\varphi_0(\xi) + h_1(ks-1/2)\varphi_1(\xi) + h_2(ks-1/2)\varphi_2(\xi), \tag{7}$$

where $\varphi_i(\xi)$ is the Chaos polynomial (or named orthogonal basis), and it is depended on the distribution of the random variable in (1). $h_i(ks+1/2)$ and $h_i(ks-1/2)$ are the coefficients to be determined later. When these coefficients are calculated, equation (6) and equation (7) are the final uncertainty analysis results what we want.

The polynomials given in (6) and (7) are orthogonal to each other, and their relationship can be presented as:

$$\langle\varphi_i,\ \varphi_j\rangle = \langle\varphi_i^2\rangle\delta_{ij}, \tag{8}$$

where δ_{ij} represents the Kronecker function and satisfies:

$$\delta_{ij} = \begin{cases} 1 & (i = j) \\ 0 & (i \neq j) \end{cases}. \tag{9}$$

The inner product calculation $\langle.\ ,\ .\rangle$ is defined as:

$$\langle\varphi_i,\ \varphi_j\rangle = \int\varphi_i(\xi)\varphi_j(\xi)w(\xi)d\xi, \tag{10}$$

where $w(\xi)$ is the weight function which can be obtained by calculating the joint probability density of the random variables in (1).

By substituting equation (6) and (7) into equation (5), it can be rearranged to obtain:

$$\begin{aligned} E_z^{n+1}(ks,\xi) &= \alpha E_z^n(ks,\xi) \\ &+\beta\left(h_0(ks+1/2)-h_0(ks+1/2)\right)\varphi_0(\xi) \\ &+\beta\left(h_1(ks+1/2)-h_1(ks+1/2)\right)\varphi_1(\xi) \\ &+\beta\left(h_2(ks+1/2)-h_2(ks+1/2)\right)\varphi_2(\xi). \end{aligned} \tag{11}$$

The inner product calculation $\langle\varphi_0(\xi)\,,\,.\rangle$ is performed on the both sides of equation (11), and we can get:

$$\begin{aligned} \langle E_z^{n+1}(ks,\xi),\varphi_0(\xi)\rangle &= \alpha\langle E_z^n(ks,\xi),\varphi_0(\xi)\rangle+ \\ \beta\left(h_0(ks+1/2)-h_0(ks+1/2)\right)&\langle\varphi_0(\xi),\varphi_0(\xi)\rangle+ \\ \beta\left(h_1(ks+1/2)-h_1(ks+1/2)\right)&\langle\varphi_1(\xi),\varphi_0(\xi)\rangle+ \\ \beta\left(h_2(ks+1/2)-h_2(ks+1/2)\right)&\langle\varphi_2(\xi),\varphi_0(\xi)\rangle. \end{aligned} \tag{12}$$

According to the relationship in (8), (13) can be translated into:

$$\begin{aligned} \langle E_z^{n+1}(ks,\xi),\varphi_1(\xi)\rangle &= \alpha\langle E_z^n(ks,\xi),\varphi_1(\xi)\rangle \\ &+\beta\left(h_1(ks+1/2)-h_1(ks+1/2)\right), \end{aligned} \tag{13}$$

where $\langle E_z^{n+1}(ks,\xi),\varphi_0(\xi)\rangle$ and $\langle E_z^n(ks,\xi),\varphi_0(\xi)\rangle$ are the constants that can be calculated by (10):

$$\begin{aligned} \langle E_z^{n+1}(ks,\xi),\varphi_1(\xi)\rangle &= \alpha\langle E_z^n(ks,\xi),\varphi_1(\xi)\rangle \\ &+\beta\left(h_1(ks+1/2)-h_1(ks+1/2)\right), \end{aligned} \tag{14}$$

and

$$\begin{aligned} \langle E_z^{n+1}(ks,\xi),\varphi_2(\xi)\rangle &= \alpha\langle E_z^n(ks,\xi),\varphi_2(\xi)\rangle \\ &+\beta\left(h_2(ks+1/2)-h_2(ks+1/2)\right). \end{aligned} \tag{15}$$

The process of SGM mechanism is shown from equation (11) to equation (15). Obviously, the uncertain equation (5) is translated into three certain equations, namely equation (13), equation (14) and equation (15). Admittedly, conventional Finite Difference Time Domain Method can be carried out in these three equations, and the coefficients $h_i(ks+1/2)$ and $h_i(ks-1/2)$ in (6) and (7) will be obtained. Sampling the random variables in (6) and (7) in terms of their distributions, the statistical property of the results can be easily got. For example, expectation, variance, the worst case value, the probability density curve and so forth. These statistical properties can stand for the uncertainty analysis outputs.

III. STIELTJES PROCEDURE AND WIENER HAAR EXPANSION

This section shows the schemes in constructing orthogonal basis $\varphi_i(\xi)$ in (6) or (7). It is usually the first step of the SGM. It is worth noting that the random variables in this paper are all in arbitrary probability density form.

A. Stieltjes procedure

The Stieltjes Procedure is firstly applied into the

uncertainty analysis of the Computational Fluid Mechanics in reference [9]. For simplicity, only the construction of one-dimensional orthogonal basis is presented, since that the high-dimensional basis can be obtained by performing the tensor products calculation. The three-term recurrence relation in the Stieltjes Procedure is presented as:

$$\begin{aligned} \varphi_{i+1}(\xi) &= (\xi-a_i)\varphi_i(\xi)-b_i\varphi_{i-1}(\xi), \quad i=0,1,\ldots, \\ \varphi_0(\xi) &= 1, \quad \varphi_{-1}(\xi)=0, \end{aligned} \tag{16}$$

where a_i and b_i are recurrence coefficients, which can be calculated by:

$$a_i = \frac{\langle\xi\varphi_i(\xi),\varphi_i(\xi)\rangle}{\langle\varphi_i(\xi),\varphi_i(\xi)\rangle}, \tag{17}$$

and

$$b_0 = \langle\varphi_0(\xi),\varphi_0(\xi)\rangle, \quad b_i = \frac{\langle\varphi_i(\xi),\varphi_i(\xi)\rangle}{\langle\phi_{i-1}(\xi),\varphi_{i-1}(\xi)\rangle}. \tag{18}$$

The inner product calculation is same as the equation (10). The orthogonal basis in the Stieltjes Procedure is in form of polynomial, and it satisfies the relationship in (8).

If the order of the polynomial is higher, the results will be more accurate, but the simulation time will be longer. Furthermore, it is worth mentioned that the number of high-dimensional orthogonal basis is exponential times of that of one-dimensional orthogonal basis. Thus, although the Stieltjes Procedure can be performed infinitely, the order is usually less than 10.

B. Wiener Haar expansion

The Wiener Haar Expansion is another orthogonal basis constructing method. Similarly, the high-dimensional basis is tensor products of one-dimensional basis, so only one-dimensional case is presented.

Considering the one-dimensional random variable ξ, the relationship between probability density function $pdf(\xi)$ and distribution function $p(\xi)$ are shown as:

$$pdf(\xi) = \begin{cases} \dfrac{dp(\xi)}{d\xi} > 0 & \forall\xi\in(A,B) \\ 0 & \forall\xi\notin(A,B) \end{cases}, \tag{19}$$

where A and B are the boundary of random variable.

The distribution function $p(\xi)$ satisfies the character as:

$$y = p(\xi)\in[0,1]\to\xi = p^{-1}(y)\in[A,B]. \tag{20}$$

It indicates that the distribution function value is one-to-one correspondence with the interval [0, 1].

The Haar wavelet function can implement the orthogonal decomposition in the interval [0, 1]. Using this particular character, the orthogonal basis can be obtained as:

$$X(\xi\in[A,B]) = X_0\chi_{0,0}(p(\xi))+\sum_{j=0}^{\infty}\sum_{k=0}^{2^j-1}X_{j,k}\psi_{j,k}(p(\xi)), \tag{21}$$

where $X(\xi\in[A,B])$ represents the output parameters

under solved, like $H_y^{n+1/2}(ks+1/2,\xi)$ in (5). $\chi_{0,0}(p(\xi))$ is the orthogonal basis which is structured by Haar Father Wavelet, and $\psi_{j,k}(p(\xi))$ is the orthogonal basis given by Haar Mother Wavelet. X_0 and $X_{j,k}$ are coefficients like $h_i(ks+1/2)$ in (6), and they can be calculated by

$$X_0 = \int_0^1 X(\xi)\chi_{0,0}(p(\xi))dp(\xi)$$
$$= \int_{[A,B]} X(\xi)pdf(\xi)d\xi, \qquad (22)$$

and

$$X_{j,k} = \int_0^1 X(\xi)\psi_{j,k}(p(\xi))dp(\xi)$$
$$= \int_{[A,B]} X(\xi)\psi_{j,k}(p(\xi))pdf(\xi)d\xi. \qquad (23)$$

It is obviously seen that the orthogonal basis of the Wiener Haar Expansion is in the form of Haar Wavelet function. Thus, the convergence rate of the Wiener Haar Expansion must be different from that of the Stieltjes Procedure in different cases. For example, if the PDF function of the random variable is smooth enough, and the Stieltjes Procedure will perform better due to its polynomial decomposition. On the contrary, the Wiener Haar Expansion is more suitable for the PDF function with some transient peaks or some gaps, thanks to the nature of the Haar Wavelet function.

In next section, the performance of Stieltjes Procedure and Wiener Haar Expansion using in SGM is presented, taking the MCM results as the reference data.

IV. ACCURACY COMPARISON BY USING FEATURE SELECTIVE VALIDATION

In this example, a Gaussian pulse with uncertain parameters is introduced into a one dimensional problem space. The example comes from a calculation model in reference [12], and it is electromagnetic wave propagation problem.

Only one dielectric slab is contained in the model, and Fig. 1 represents the geometry construction of this model. The length of the space is 1m, and the location of the slab is from $x=0.1\text{m}$ to $x=0.2\text{m}$. The relative permittivity of the slab is supposed $\varepsilon_r=4$, and other spaces are supposed full of vacuum. The output result is the absolute value of the frequency response of the electric field component, which is recorded at $x=0.5\text{m}$. A Gaussian pulse is simulated from the point $x=0.7\text{m}$ in the space, and it is a probably 1 V/m uncertain input excitation. The input excitation should be

$$E_z(x=0.7,t) = E_0(\xi)\exp(\frac{-(t_0-t)^2}{2\beta^2}), \qquad (24)$$

where $E_0(\xi)$ is the maximum amplitude of the pulse, and it is an uncertain input parameter which is modeled by the random variable ξ. t_0 stands for the onset time

delay of the pulse, t represents the time and β is the width of the pulse at half its maximum height.
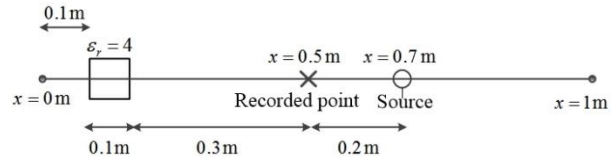
Fig. 1. The model of one dimensional problem space [12].

In this simulation, the Finite Difference Time Domain (FDTD) method is proposed to calculate the outputs. The FDTD cell size is $\Delta x=0.005\text{m}$, and the FDTD time step is supposed $\Delta t=8.33\text{ps}$. Meanwhile, $t_0=40\Delta t$ and the duration is $\beta=5\sqrt{2}\Delta t$. This excitation is a broad Gaussian pulse, and it guarantees that the electric field can be calculated over a broad frequency range. The time response of the electric field is recorded from 0 to 41.67ns.

The uncertain input $E_0(\xi)$ satisfies:
$$E_0(\xi) = (0.5+0.5\xi)\times E_m, \qquad (25)$$
where E_m is the electric field intensity, $E_m=1\text{V/m}$. ξ is the random variable with arbitrary probability density, which will be given in different cases in the following texts.

A. Continuous probability density case

In this case, the continuous PDF of the random variable is given as:
$$PDF_c(\xi) = \begin{cases} \frac{1}{2}\sin(\frac{3\pi}{2}\xi)+(1-\frac{1}{3\pi}), & 0\leq\xi\leq1 \\ 0, & \text{others} \end{cases}. \qquad (26)$$
We call it continuous thanks to the values are concentrated near only one place, 0.5. Figure 2 presents this continuous PDF curve.

Stochastic Galerkin Method with Stieltjes procedure (SP-SGM), Stochastic Galerkin Method with Wiener Haar expansion (WHE-SGM) and Monte Carlo Method (MCM) are proposed to perform the uncertainty analysis. The results given by MCM are regarded as the reference data to test the precision of the other two methods. 20000 times samplings of MCM have been done in order to make sure that the MCM has reached the convergence.

Figure 3 shows the expectation of uncertainty analysis results, and Fig. 4 gives the standard deviation information.

Feature Selective Validation (FSV) has proved its successful applications in credibility evaluation of CEM results [13, 14]. By using FSV, the difference between the simulation results under evaluated and the reference data can be quantified. Total-GDM, a key value in FSV,

reflects the quantitative description of validity evaluation. Total-GDM value is lower, and it means that the simulation results perform better. Table 1 presents a one-to-one correspondence between Total-GDM and the qualitative description. More details about the FSV can be found in [14].
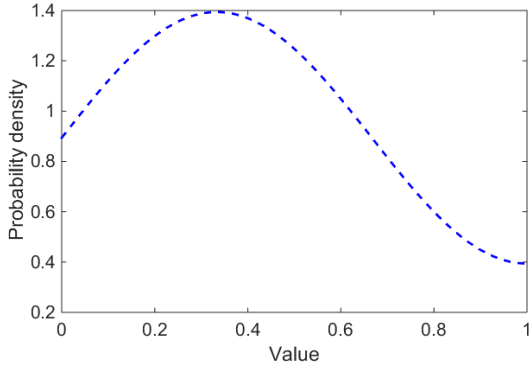
Fig. 2. Continuous PDF curve.
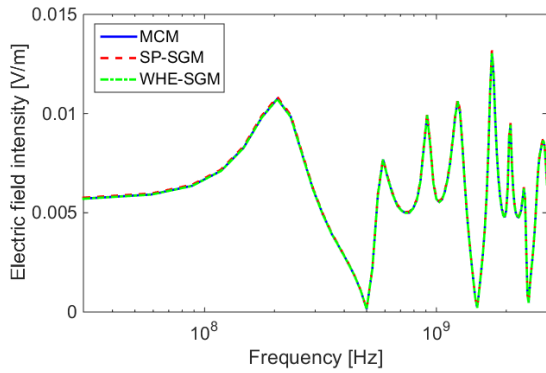
Fig. 3. The expectation results in continuous probability density case.
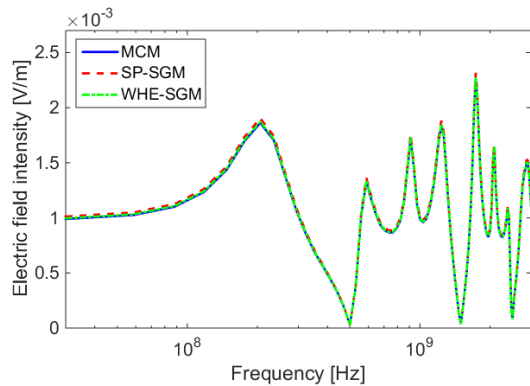
Fig. 4. The standard deviation results in continuous probability density case.

The Total-GDM results of SP-SGM and WHE-SGM in Fig. 3 and Fig. 4 are given in Table 2. It is shown that all the values in Table 2 are less than 0.1. Thus, it indicates that all the results are "Excellent" match with the results given by MCM according to Table 1. Furthermore, it indicates the conclusion that both SP-SGM and WHE-SGM can be as good as the MCM in this continuous probability density case.

Table 1: Relationship between Total-GDM and Quantitative Description [14]

Total-GDM (Quantitative)	FSV Interpretation (Qualitative)
Less than 0.1	Excellent
Between 0.1 and 0.2	Very Good
Between 0.2 and 0.4	Good
Between 0.4 and 0.8	Fair
Between 0.8 and 1.6	Poor
Greater than 1.6	Very Poor

Table 2: The Total-GDM values in continuous probability density case

	SP-SGM	WHE-SGM
Expectation	3.32×10^{-3}	6.47×10^{-4}
Standard deviation	0.026	0.027

The simulation time of the MCM is 1.35 hours, SP-SGM takes 1.14 minutes, and WHE-SGM uses 2.32 minutes. Thus, it is proved that the computational efficiencies of SP-SGM and WHE-SGM are much higher than that of MCM. The reason is that MCM needs thousands of times of the FDTD analysis, in order to make sure the calculation is converged. In this example, 2000 times are used. SP-SGM or WHE-SGM only needs one augmented FDTD analysis, so the simulation time is the several times of one common FDTD analysis. Thus, SP-SGM and WHE-SGM are in high computational efficiency.

Furthermore, the computational efficiency of SP-SGM is a little better than WHE-SGM. The reason is that SP-SGM needs less chaotic polynomials than WHE-SGM. Thus, the augmented FDTD analysis of the SP-SGM is easier than that of the WHE-SGM.

B. Discontinuous probability density case

The discontinuous PDF of the random variable should be:

$$PDF_{unc}(\xi) = \begin{cases} 4, & 1 \le \xi \le 1.2 \\ 0.075 \times [-2(\xi-17)^2 + 8(\xi-17) - 6], & 18 \le \xi \le 20. \quad (27) \\ 0, & \text{others} \end{cases}$$

In contrast to the continuous case in (26), the values are dispersed in two places. One is near the value 1.1, and the other is near the value 19. Figure 5 shows the discontinuous PDF curve. In some cases, if a material parameter is uncertain due to the lack of knowledge and

it has two kinds of inherent discrete states, the random variable can be presented by such discontinuous PDF since that we cannot judge which state it should be. Thus, the discontinuous PDF form is also frequently appeared in uncertainty analysis.
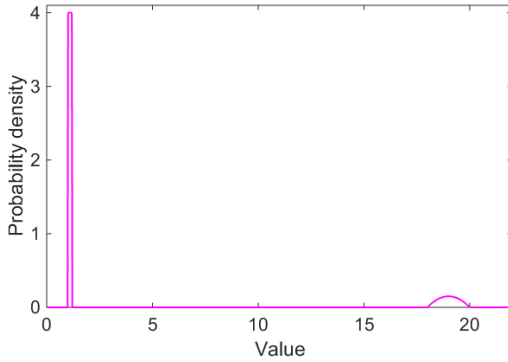
Fig. 5. The discontinuous PDF curve.

In the similar way, MCM, SP-SGM and WHE-SGM are undertaken for the uncertainty analysis. Fig. 6 and Fig. 7 give the expectation results and the standard deviation results in discontinuous probability density case.
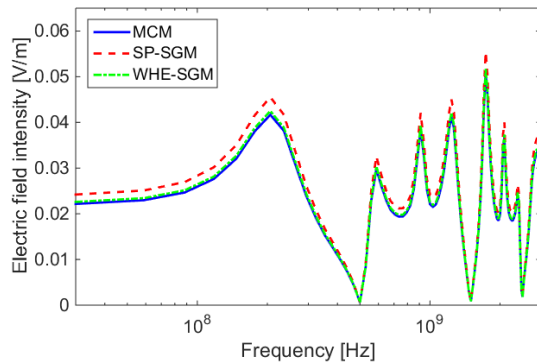
Fig. 6. The expectation results in discontinuous probability density case.
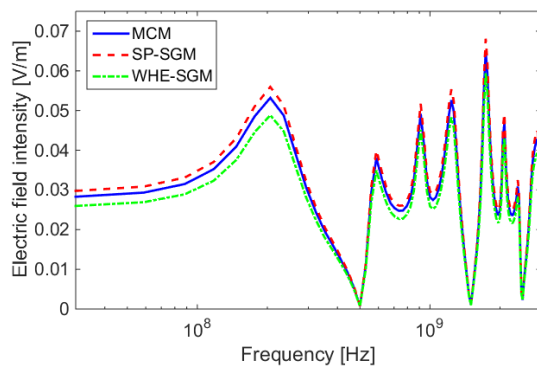
Fig. 7. The standard deviation results in discontinuous probability density case.

The Total-GDM results in Fig. 6 and Fig. 7 are presented in Table 3. As to the expectation results, the SP-SGM receives a "Very good" evaluation and the WHE-SGM has an "Excellent" result. It indicates that the WHE-SGM does better than the SP-SGM in expectation results in discontinuous probability density case. Considering the standard deviation results, the SP-SGM is an "Excellent" match with the MCM. On the contrary, the WHE-SGM only presents a "Very good" match. Consequently, the SP-SGM does better in standard deviation calculation.

It is worth noting that the expectation is the basic results of the uncertainty analysis results. Admittedly, the importance of the expectation results outweighs that of the standard deviation results. As a whole, the WHE-SGM performs better in discontinuous probability density case.

No matter SP-SGM or WHE-SGM, the simulation results in the discontinuous case are not good enough as that in the continuous case. The reason is that the discontinuous PDF leads the more complex uncertainty analysis outputs, so the truncation of the chaotic polynomials may cause a little bigger error.

Table 3: The Total-GDM values in discontinuous probability density case

	SP-SGM	WHE-SGM
Expectation	0.122	0.027
Standard deviation	0.069	0.112

The simulation time of the MCM is 1.59 hours, SP-SGM takes 1.47 minutes, and WHE-SGM uses 2.89 minutes. Thus, it would give the same conclusion with the continuous case in computational efficiency.

V. CONCLUSION

In this paper, two constructing orthogonal basis methods, Stieltjes procedure and Wiener Haar expansion, are applied into the Stochastic Galerkin Method (SGM) in order to perform uncertainty analysis with the arbitrary probability density inputs in Electromagnetic Compatibility simulation based on the Finite Difference Time Domain analysis. By simulating an electromagnetic wave propagation example with stochastic excitation source included, the following conclusions can be obtained according to the Feature Selective Validation results.

Firstly, when Probability Density Function is continuous, both Stochastic Galerkin Method with Stieltjes procedure (SP-SGM) and Stochastic Galerkin Method with Wiener Haar expansion (WHE-SGM) can provide the accurate results like the Monte Carlo Method (MCM). But the computational efficiency of the SP-SGM is a little better than that of the WHE-SGM.

Secondly, when Probability Density Function is discontinuous, the WHE-SGM does better in calculating

the expectation of the uncertainty analysis results, and the SP-SGM can give more accurate in the variance information. To sum up, the WHE-SGM performs better than the SP-SGM in this case.

Finally, it also indicates that the computational efficiencies of both SP-SGM and WHE-SGM are much better than that of MCM.

REFERENCES

[1] N. V. Kantartzis, "Multi-frequency higher-order ADI-FDTD solvers for signal integrity predictions and interference modeling in general EMC applications," *Applied Computational Electromagnetics Society Journal*, vol. 25, no. 12, pp. 1046-1060, 2010.

[2] R. I. Macpherson and N. J. Ryan, "Reducing electromagnetic coupling in shielded enclosures using a genetic algorithm - Finite-difference time-domain solver," *Applied Computational Electromagnetics Society Journal*, vol. 18, no. 3, pp. 144-150, 2003.

[3] C. Jullien, et al., "Advanced modeling of crosstalk between an unshielded twisted pair cable and an unshielded wire above a ground plane," *IEEE Transactions on Electromagnetic Compatibility*, vol. 55, no. 1, pp. 183-194, 2013.

[4] G. Spadacini and S. A. Pignari, "Numerical assessment of radiated susceptibility of twisted-wire pairs with random nonuniform twisting," *IEEE Transactions on Electromagnetic Compatibility*, vol. 55, no. 5, pp. 956-964, 2013.

[5] B. Jinjun, Z. Gang, W. Lixin, and A. Duffy, "Uncertainty analysis in EMC simulation based on stochastic collocation method," *2015 IEEE International Symposium on Electromagnetic Compatibility*, pp. 930-934, 2015.

[6] J. J. Bai, et al., "Uncertainty analysis in EMC simulation based on improved method of moments," *Applied Computational Electromagnetics Society Journal*, vol. 31, no. 1, pp. 66-71, 2016.

[7] Z. Zubac, D. De Zutter, and D. Vande Ginste, "Scattering from two-dimensional objects of varying shape combining the method of moments with the stochastic Galerkin method," *IEEE Transactions on Antennas and Propagation*, vol. 62, no. 9, pp. 4852-4856, 2014.

[8] R. S. Edwards, A. C. Marvin, and S. J. Porter, "Uncertainty analyses in the finite-difference time-domain method," *IEEE Transactions on Electromagnetic Compatibility*, vol. 52, no. 1, pp. 155-163, 2010.

[9] X. L. Wan and G. E. M. Karniadakis, "Multi-element generalized polynomial chaos for arbitrary probability measures," *SIAM Journal on Scientific Computing*, vol. 28, no. 3, pp. 901-928, 2006.

[10] O. P. Le Maître, et al., "Uncertainty propagation using Wiener–Haar expansions," *Journal of Computational Physics*, vol. 197, no. 1, pp. 28-57, 2004.

[11] D. Xiu and G. Em Karniadakis, "The Wiener-Askey polynomial chaos for stochastic differential equations," *SIAM Journal on Scientific Computing*, vol. 24, no. 2, pp. 619-644, 2002.

[12] R. S. Edwards, "Uncertainty Analyses in Computational Electromagnetism," *Ph.D. Dissertation*, University of York, 2009.

[13] IEEE Standard for Validation of Computational Electromagnetics Computer Modeling and Simulations. *IEEE STD 15971-2008*, pp. 1-41, 2008.

[14] IEEE Recommended Practice for Validation of Computational Electromagnetics Computer Modeling and Simulations. *IEEE STD 15972-2010*, pp. 1-124, 2011.

An Effective Sparse Approximate Inverse Preconditioner for the MLFMA Solution of the Volume-Surface Integral Equation

Jinbo Liu [1], Zengrui Li [1], Mang He [2], and Jianxun Su [1]

[1] School of Information and Communication Engineering
Communication University of China, Beijing, 100024, P. R. China
liuj@cuc.edu.cn, zrli@cuc.edu.cn, sujianxun_jlgx@163.com

[2] School of Information and Electronics
Beijing Institute of Technology, Beijing, 100081, P. R. China
hemang@bit.edu.cn

Abstract ─ In the framework of the multilevel fast multipole algorithm (MLFMA), effective construction of the sparse approximate inverse preconditioner (SAIP) for the volume-surface integral equation (VSIE) is discussed. A high quality SAIP for the entire VSIE matrix is constructed by using the sub-matrix of the near-field interactions between the surface basis and testing functions arising from the surface integral equation alone. In addition, a simple sparse pattern selection scheme based on the geometrical information of nearby basis functions and octree regrouping strategy is proposed to enhance the efficiency of the SAIP. In contrast to the existing sparse pattern selection schemes, the proposed scheme utilizes the near-field matrix in the MLFMA more effectively with only one tuning parameter. Numerical results indicate that with the proposed scheme, both the memory usage and setup time for constructing an effective SAIP are significantly reduced without compromising the efficiency and robustness.

Index Terms ─ Method of moments (MoM), multilevel fast multipole algorithm (MLFMA), sparse approximate inverse preconditioner, volume-surface integral equation (VSIE).

I. INTRODUCTION

The volume-surface integral equation (VSIE) [1], in conjunction of the method of moments (MoM) [2], is one of the most attractive methods to calculate the electromagnetic (EM) scattering or radiation of composite objects involving both conductors and inhomogeneous dielectrics. For the objects with electrically large sizes, fast EM algorithms, such as the multilevel fast multipole algorithm (MLFMA) [1], are highly required to alleviate the computation overhead. Based on the addition theorem of Green's function and diagonalization of the translation operator, the MLFMA drastically reduces the overall computational complexity from the order of $O(N^2)$ to $O(N\log N)$, where N is the number of unknowns [1]. During the implementation of MLFMA, the MoM matrix equation is decomposed into two parts as:

$$Z_{near}I + Z_{far}I = V, \qquad (1)$$

where Z_{near} and Z_{far} are the $N{\times}N$ impedance matrices representing the reactions between the basis and testing functions in the neighbor and far leaf boxes at the finest level of the MLFMA, and I and V are the $N{\times}1$ vectors of unknown expansion coefficients and generalized voltage, respectively. Besides, only the near-field matrix Z_{near} is explicitly computed and stored, while the far-field interaction part $Z_{far}I$ is implicitly computed through three processes: aggregation, translation, and disaggregation.

Although the VSIE is a second-kind integral equation, it is still necessary to apply the preconditioning techniques to speed up the convergence during the iterative solution of the matrix equation. Among related preconditioning techniques, the sparse approximate inverse preconditioner (SAIP), which is based on directly approximating the inverse of the preconditioning matrix, has been proved that it is not only one of the most effective preconditioners for the surface integral equation (SIE), but also easy for parallelization [3-6]. In the MLFMA, utilizing Z_{near} can provide effective SAIP. Further, benefited from the octree structure of the MLFMA, the setup time for constructing the SAIP can be decreased substantially [3, 4]. But meanwhile, the construction process of SAIP is very sensitive to the average number of unknowns belonging to the leaf boxes. Especially for the VSIE, because of the three-dimensional volumetric unknowns which are densely distributed in each non-empty leaf box, the setup time for SAIP will be very long. To reduce the time cost, several sparse pattern selection schemes have been reported. In

[5], performances of various selection schemes based on algebraic or geometrical information were compared through a large set of numerical experiments, while it was concluded that the ones based on geometrical information of the basis function distributions are more effective.

However, most of the existing discussions on the SAIP were focused on its applicability in the solution of SIE, while its effectiveness on the VSIE is rarely studied. In this paper, how to effectively use the SAIP in the VSIE solution is investigated. Based on the geometrical information of nearby basis functions and octree regrouping strategy, an effective sparse pattern selection scheme for the SAIP construction is proposed. Compared to the conventional selection schemes, the proposed one is more effective and robust with only one tuning parameter.

II. SAIP FOR THE VSIE

In the MLFMA, only the near-interaction matrix Z_{near} needs to be stored explicitly [1]. If we use $\bar{Z}$ to denote the preconditioning matrix extracted from Z_{near} to construct the SAIP, then the preconditioner M can be constructed as an approximate inverse matrix of $\bar{Z}$. During the construction process, the Frobenius norm minimization is usually chosen since it can decouple the entire constrained minimization problem into N independent linear least-square problems as:

$$\min \left\| E - \bar{Z}M \right\|_F^2 = \min \sum_{k=1}^{N} \left\| e_k - \bar{Z}m_k \right\|_2^2 , \qquad (2)$$

which can be parallelized naturally. In (2), E is the identity matrix, and e_k and m_k are the kth column of the matrices E and M, respectively, while M is constrained by a certain sparse pattern. Since $\bar{Z}$ is sparse, as done in [3, 4], let J denote the column structure of nonzero elements of $\bar{Z}$, and I denote the set of row indices of the nonzero entries of $\bar{Z}(:, J)$, the least-square problems in (2) are reduced into:

$$\min \sum_{k=1}^{N} \left\| e_k - \bar{Z}m_k \right\|_2^2 \Rightarrow$$
$$\min \sum_{k=1}^{N} \left\| e_k(I) - \bar{Z}(I,J)m_k(J) \right\|_2^2 \qquad (3)$$

which can be efficiently solved by QR factorization, and the computational complexity is determined by the size of $\bar{Z}(I, J)$. The QR factorization requires asymptotically $n_1 n_2^2$ flops, where n_1 and n_2 are the number of elements in the sets I and J, respectively. If we assume that each row of $\bar{Z}$ has n nonzero entries in average, both n_1 and n_2 are the order of $O(n)$. Thus, the total computational complexity of (3) is in the order of $O(Nn^3)$. In the context of the MLFMA, when we choose $\bar{Z}=Z_{near}$, it is found that any testing function in a given leaf box will couple with the same set of basis functions located in the boxes of the

near-interaction list of the given box [3]. By using this fact, the computation overhead of (3) can be reduced to $O(N_g n^3)$, where N_g is the number of non-empty leaf boxes. Therefore, the setup time for constructing M can be reduced several-fold without any loss of accuracy. On the other hand, $O(N_g n^3)$ indicates that the SAIP setup time is very sensitive to n. In other words, when n is relatively large, the setup time for constructing M will be very high. To alleviate this problem, after careful investigation, we find that there are two possible ways to reduce the SAIP computational effort for the VSIE.

The first way is to choose appropriate sub-matrices to construct the SAIP. In the VSIE, particularly, Z_{near} can be represented by four sparse sub-matrices as:

$$Z_{near} = \begin{bmatrix} Z_{SS} & Z_{SV} \\ Z_{VS} & Z_{VV} \end{bmatrix}, \qquad (4)$$

where Z_{SS}, Z_{SV}, Z_{VS} and Z_{VV} denote the self/mutual interactions between two types of basis/testing functions in the near-interaction lists (S stands for surface functions and V for the volume ones). Because the SAIP can be applied to any square matrix, there are three optional schemes to construct the preconditioner M: using Z_{SS} only (denoted by SS), using both Z_{SS} and Z_{VV} ($SS\&VV$), and using the entire Z_{near} matrix (Tot). For composite objects involving open conducting structures, Z_{SS} stands for the interactions between surface basis and testing functions used in the electric field integral equation (EFIE) which is a first-kind of integral equation, while Z_{VV} represents the interactions between volume basis and testing functions for the volume integral equation (VIE) that is second-kind. In general, Z_{VV} is more well-conditioned than Z_{SS}. Therefore, it is reasonable that applying SAIP to the sub-matrix Z_{SS} alone to improve the condition number of Z_{SS} might be enough for the calculation of composite objects. Besides, compared with $SS\&VV$ and Tot, SS is apparently the most memory- and time-efficient for constructing M. During the implementation of SS, M is considered as:

$$M = \begin{bmatrix} M_{SS} & \\ & 1 \end{bmatrix}, \qquad (5)$$

where M_{SS} is an approximate inverse matrix of Z_{SS} as:

$$Z_{SS}M_{SS} \approx E , \qquad (6)$$

which can be efficiently solved using (2).

On the other hand, the objects including thin conducting structures are needed to be discretized by fine meshes. If $\bar{Z}$ is still chosen the same as Z_{near}, $\bar{Z}$ will be very dense, resulting in a large n as well as high computation complexity of (3). In order to overcome this difficulty, it is necessary to select effectual sparse pattern from Z_{near}, i.e., extracting a sparser matrix $\bar{Z}$ from Z_{near} by pre-filtering technique before constructing M, which can evidently reduce the value of n. There are two main types of schemes reported to achieve this goal: 1) dropping entries with tiny magnitudes in Z_{near} as done in

[6]. However, improper setting of the dropping threshold may even degrade the convergence [5]. Thus, this scheme is not widely used; 2) dropping entries based on the geometrical information during the MLFMA implementation as done in [3]. Specifically, for a given testing function X_k located in the leaf box G, when drops the entries from Z_{near} to reduce into $\bar{Z}(I, J)$, two filtrations are used to determine the sparse pattern for X_k as:

$$\begin{array}{l} J = \left\{ j \middle| j \in S \quad \mathrm{dist}(G, j) \le \tau_1 \right\} \\ I = \left\{ i \middle| i \in S \quad \mathrm{dist}(i, J) \le \tau_2 \right\} \end{array}, \qquad (7)$$

where S is the sparse pattern of Z_{near}, $\mathrm{dist}(G, j)$ is the distance between the center of box G containing X_k and that of the jth basis function, and $\mathrm{dist}(i, J)$ is the distance between the center of the ith testing function and that of boxes containing all basis functions whose index $j \in J$. Thus, in order to select $\bar{Z}(I, J)$ for X_k, we need to draw a sphere of radius τ_1 with the same center of box G. The jth column entries $\bar{Z}(:, j)$ will be kept in $\bar{Z}(:, J)$ if the jth basis function is exactly contained in this sphere, otherwise $\bar{Z}(:, j)$ will be dropped. The similar procedure is also executed in the second filtration for row indices selection with a sphere of radius τ_2. However, during the first filtration, if the testing function X_k and two basis functions X_{j_1}, X_{j_2} reside in the MLFMA leaf boxes (black line) as shown in Fig. 1, then the distance between X_k and X_{j_1} will be smaller than τ_1, which leads to a strong mutual interaction Z_{kj_1}. But according to the selection criterion (7), Z_{kj_1} is dropped. In contrast, although the distance between X_k and X_{j2} is larger than τ_1, the resultant matrix entry Z_{kj_2} that represents a relatively weak interaction between X_k and X_{j_2}, is still included in $\bar{Z}(I, J)$. The similar situation will occur once again during the second filtration. Therefore, this two-parameter filtration scheme may not utilize the nonzero entries reasonably and effectively in some situations.
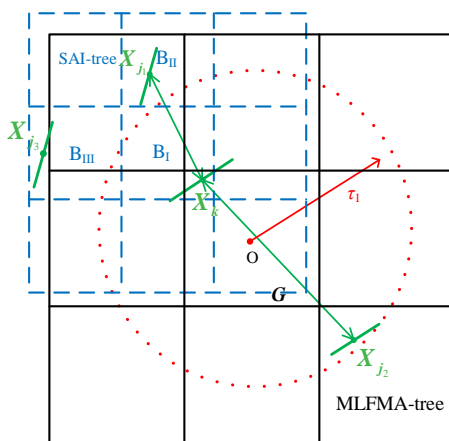
To solve this problem, we build a new octree structure with smaller box size R_{SAI} compared with the MLFMA leaf box, called SAI-tree which is shown in Fig. 1 (blue dashed line), to construct the SAIP. That is to say, we can use the SAI-tree to control the sparse pattern and to generate the matrix $\bar{Z}$, i.e., $\bar{Z}$ is considered as the near-field matrix in the SAI-tree. As shown in Fig. 1, in the SAI-tree, box B_{II} that contains X_{j1} is one of the neighbor boxes of box B_I containing X_k, so the entry Z_{kj1} representing strong interaction between X_k and X_{j1} will be included in $\bar{Z}$. On the contrary, since X_{j2} does not belong to any neighbor box of B_I, Z_{kj2} that denotes the relatively weak interaction between X_k and X_{j2} will be naturally filtered. On the other hand, however, in some extreme situations as shown in Fig. 1, in the SAI-tree the box B_{III} that contains X_{j_3} is one of the neighbor boxes of the box B_I containing X_k, while in the original octree of the MLFMA, the entry Z_{kj_3} representing the interaction between X_k and X_{j_3} is not included in the near-field matrix Z_{near}. In this situation, Z_{kj_3} needs to be calculated individually during generating $\bar{Z}$.

The proposed sparse pattern selection scheme exhibits two advantages over the conventional ones:

(1) Effective utilization of the nonzero entries. The proposed scheme can more "accurately" keep the generally strong interactions and drop the weak ones based on the geometrical information provided by the SAI-tree.

(2) Easy implementation. It has only one tuning parameter R_{SAI}, while R_{SAI} can be chosen to be smaller than the size of the leaf box in the MLFMA. If we still use N_g and n to denote the number of non-empty boxes in the SAI-tree and the average number of nonzero entries in each row of $\bar{Z}$ respectively, a smaller R_{SAI} leads to a larger N_g and a smaller n, which will further decrease the SAIP setup time since the computational complexity is about $O(N_g n^3)$ as mentioned previously. Furthermore, the value of R_{SAI} can be automatically fixed according to the average discretized mesh size, which will greatly simplify the process of tuning an appropriate parameter for a certain problem. It is worth mentioning that the proposed scheme needs additional time to construct the SAI-tree, but due to the utilization of the fast binary-tree searching algorithm, the additional time is very limited.

Applying the proposed sparse pattern selection scheme based on the SAI-tree, the implementation process of constructing M is described as follows:

(1) Determine the value of R_{SAI} according to the average discretized mesh size. According to a large amount of numerical experiments, R_{SAI} is recommended to be two times of the average mesh size.

(2) Build the SAI-tree in which the box size is set to R_{SAI}.

(3) Select the sparse pattern according to the index of near-field interactions in the SAI-tree.

Fig. 1. Locations of X_k, X_{j_1}, X_{j_2} and X_{j_3} in the MLFMA leaf boxes and in the SAI-tree.

(4) Generate $\bar{Z}$ according to the selected sparse pattern. If the entry in $\bar{Z}$ also belongs to Z_{near}, then extract it from Z_{near} directly; if not, calculate it individually.

(5) Construct the preconditioner M according to (2).

Moreover, for the objects with extremely large electrical size, Z_{near} becomes insufficient to approximate the entire impedance matrix, due to the inefficiency of the preconditioners constructed from Z_{near}. One way to alleviate this problem is to use the far-field interactions during constructing the preconditioners [7, 8]. In these approaches, a cheaper MLFMA version called approximate MLFMA is used as the preconditioner to iteratively solve a closely related matrix equation. In the practical process, a secondary preconditioner is needed to accelerate the iterative solving process of the closely related matrix equation. The SAIP applying the proposed sparse pattern selection scheme can be adopted as this secondary preconditioner.

III. NUMERICAL RESULTS

To validate the effectiveness of the proposed SAIP, EM radiation and scattering of composite dielectric-conductor objects are calculated. In our implementation, the RWG [9] and SWG [10] basis functions are used to model the equivalent surface and volume currents, respectively. The restarted GMRES with a restart parameter m is used as the iterative solver to reach convergence with relative residual error of 0.001 [11-13]. Zero vector is taken as initial approximate solution for all calculations. The leaf box size of the MLFMA is 0.25λ (λ is the wavelength in the free space). All computations are in single precision and carried out on a workstation with 2.4 GHz CPU and 384 GB RAM.

A. Microstrip patch antenna array

The first example is the EM radiation of an antenna array composed of 64 microstrip patch antennas at the operating frequency of 14.5 GHz as shown in Fig. 2. All antennas are excited with the same magnitude and phase. The relative dielectric constant is $\varepsilon_r=2.2-j0.00198$. The average mesh size is about 0.08λ, and the number of discrete triangles, tetrahedrons and unknowns are 9,375, 21,062 and 63,340, respectively, while the octree of MLFMA has 6 levels. The restart parameter of GMRES is $m=100$. To compare with other kinds of preconditioners limited to sequential implementation such as the preconditioners based on incomplete Lower-Upper decomposition (ILU), the whole computation process is executed serially. Table 1 shows the performance details of three schemes to construct SAIP from selecting different sub-matrices (*SS*, *SS&VV*, and *Tot*) with various tuning parameter R_{SAI}. This table contains the memory usage of preconditioner (PC-Mem), the additional time to construct the SAI-tree and generate $\bar{Z}$ (T_{add}), the setup time (T_{PC}) to construct preconditioner, the average number of basis functions in the non-empty boxes of the

SAI-tree (Δ), and so on. Besides, *none* means that the computation is executed without any preconditioner. From Table 1, the first finding is that the three different sub-matrix selection schemes need similar number of iterations to reach the target convergence, while the memory usage and setup time for constructing M by *SS* are much less than those by *SS&VV* and *Tot*. Therefore, for the VSIE solution, using sub-matrix Z_{SS} alone to construct the SAIP might be an appropriate choice.

Fig. 2. The structure of antenna array composed of 64 microstrip patch antennas at the operating frequency of 14.5 GHz.

The second finding is that large value of R_{SAI} does not always mean less total computation time, while the proper value of R_{SAI} is found to be about twice as large as the average mesh size. The reason is that enlarging the value of R_{SAI} will make $\bar{Z}$ denser, which would dramatically increase the setup time and the memory requirement for constructing preconditioner M. This phenomenon also demonstrates that enlarging the number of nonzero entries in matrix $\bar{Z}$ does not always lead to better preconditioning performance. It is worth to point out that some effective preconditioners can be constructed based on the Schur complement, which are specially designed to work in conjunction with the VSIE [14]. However, this kind of preconditioners usually needs to calculate both of the inverse of Z_{SS} and Z_{VV} directly or approximately. Thus, it is concluded that the memory usage and setup time of this kind of preconditioners based on the Schur complement are on the same level as SAIP by *SS&VV*, which are evidently larger than *SS*. For this reason, this kind of preconditioners does not be adopted in this paper.

From the above, we may draw the conclusion that in the VSIE solution, using Z_{SS} alone to construct the SAIP is an appropriate choice. However, whether this *SS* scheme can be successfully utilized to other kinds of preconditioners is worthwhile of further research. Table 2 lists the detailed computation information with various kinds of preconditioners on the first example, such as the SAIP with two tuning parameters τ_1, τ_2 reported in [3] (denoted by *conv*), the ILUT preconditioner [15] which is based on a dual dropping rule with two tuning parameters: the fill-in p and the threshold drop tolerance τ, and the variant approach of ILUT, called SuperLU [16], with three tuning parameters: the fill-ratio γ, the threshold drop tolerance τ, and the pivoting threshold η. Besides, only Z_{SS} is used to construct the preconditioner.

For *conv*, the parameter setting refers to [3]. Since the leaf box size of the MLFMA is 0.25λ, then,

$$0.125\lambda \le \tau_1, \tau_2 \le 0.5\lambda \quad \text{and} \quad \tau_1 \le \tau_2 . \qquad (8)$$

For the ILU type preconditioners, as stated in [15, 16], a more effective and robust ILUT or SuperLU preconditioner can be constructed with larger p or γ. In fact, when the preconditioning matrix is denser, it is indeed necessary to set a relatively larger p or γ in the ILUT factorization to achieve better performance. For this calculated antenna array, since it contains thin structures, dense meshes are needed to model the details, due to a relatively dense Z_{near} as well as Z_{SS}. As a consequence, p or γ needs to be set to a large value. From Table 2, it is obtained that when $p<200$ or $\gamma<10$, the ILUT or SuperLU preconditioner will be failure. Another finding is that the value of τ does not affect very much

the convergence rate during the iterative solution, which is in accordance with [15]. Comparing Table 1 with Table 2, it is found that different kinds of preconditioners improve the convergence in varying degrees. Comparing the proposed scheme (*prop*, i.e., SAIP with *SS* scheme) with *conv*, when an appropriate combination of tuning parameters is used ($R_{SAI}=0.15\lambda$ versus τ_1, $\tau_2=0.25$, 0.5), *prop* shows less iterations (169 versus 384) and less total time (188s versus 323s) to achieve convergence with similar memory usage (1141.8 MB versus 1139.4 MB). Compared with ILUT and SuperLU, *prop* shows the similar robustness, while the memory usage of SAIP is several times less than that of ILUT or SuperLU. More importantly, *prop* can be naturally parallelized, while the ILU-type preconditioners are limited to sequential implementation.

Table 1: Detailed performance of different sub-matrix selection schemes and R_{SAI} on the proposed SAIP

SAIP Style	R_{SAI} (λ)	PC-Mem (MB)	T_{add} (s)	T_{PC} (s)	n	N_g	Δ	Solution Time (s)	Iterations	Total Time (s)	Peak Memory (MB)
None			——					549	897	592	1130.6
SS	0.125	8.26	0.72	5.97	82.2	2228	5.9	521	757	583	1138.4
	0.15	11.70	1.54	19.2	116.4	1479	8.9	125	169	188	1141.8
	0.2	19.74	1.73	29.8	196.7	987	13.3	116	151	190	1198.3
	0.25	29.54	0.17	81.5	294.3	732	18.0	101	129	232	1209.4
SS&VV	0.125	113.8	0.73	306	252.5	2939	21.6	556	753	914	1294.9
	0.15	174.3	3.28	811	361.0	2048	30.9	134	163	987	1356.7
	0.2	299.5	4.21	2421	619.5	1152	55.0	132	149	2599	1478.1
	0.25	447.7	0.23	5342	926.4	785	80.7	119	127	5501	1627.2
Tot	0.125	183.3	0.74	816	379.3	2939	21.6	581	739	1442	1364.3
	0.15	261.5	3.92	1641	541.1	2048	30.9	136	161	1823	1443.9
	0.2	447.9	4.56	4713	923.5	1152	55.0	137	144	4892	1629.1
	0.25	699.5	0.24	10852	1385.5	785	80.7	124	121	11021	1881.3

Table 2: Detailed performance of different types of preconditioners

Preconditioner Style	Parameters	PC-Mem (MB)	T_{PC} (s)	Solution Time (s)	Iterations	Total Time (s)	Peak Memory (MB)
Conv (τ_1, τ_2)	0.2, 0.4	6.94	5.01		*		1137.7
	0.2, 0.5	7.92	8.66	358	512	402	1138.6
	0.25, 0.5	8.79	9.33	269	384	323	1139.4
	0.3, 0.5	19.8	19.6	262	355	325	1150.3
ILUT (p, τ)	150, 0.001	38.6	8.2		*		1213.9
	200, 0.001	42.7	10.4	146	178	201	1218.1
	200, 0.0001	62.8	30.3	133	165	206	1237.6
	300, 0.001	46.6	11.9	139	172	194	1220.2
SuperLU (γ, τ, η)	5, 0.001, 0.5	76.1	24.3		*		1223.1
	10, 0.001, 0.5	108.8	32.2	138	140	216	1254.0
	10, 0.0001, 1.0	149.0	42.9	140	135	239	1293.5
	15, 0.001, 0.5	113.2	38.1	125	127	208	1259.8

Note: "*" refers to no convergence after 1000 iterations.

As mentioned before in this paper, the restarted GMRES, which is a famous Krylov subspace method for solving nonsymmetric linear systems, is used as the iterative solver. However, as argued in [11-13], the

restart parameter m will deeply influence the convergence of this Krylov subspace method. In order to investigate how m influences the performance, Fig. 3 shows the iterations for four preconditioners (*prop*, *conv*, ILUT, SuperLU) with respect to different values of m, while the relative residual error is fixed to 0.001. It is observed that when m is too small, none of the four preconditioners can prompt GMRES to reach the target convergence after 1000 iterations. Along with the increase of m, the iterations will sharply decrease, and be followed by a steady decrease. When m is about 30, *prop* can achieve the convergence after hundreds of iterations, while for other three preconditioners, *conv*, ILUT and SuperLU can achieve the same convergence when m is about 60, 50 and 40, respectively. This illustrates that compared with *conv*, ILUT and SuperLU, *prop* is cooperated with a relatively small m, which has a low memory usage during using the GMRES to solve the matrix equation. Another finding is that when the value of m is suitably fixed, the convergence rate of *prop* is on the same level as that of the ILU type of preconditioners, while the *conv* is relatively slow. Therefore, Fig. 3 illustrates the robustness and efficiency of the proposed approach.
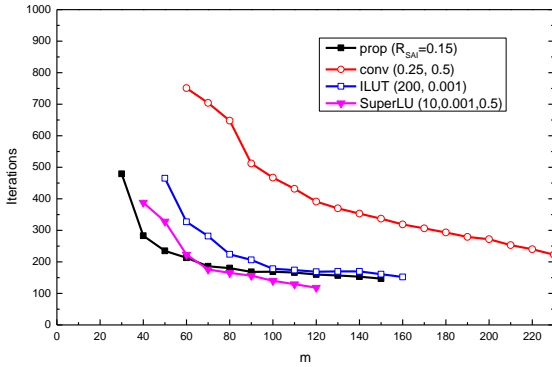
Fig. 3. Number of iterations for different preconditioners with respect to different restart parameter m in the GMRES.

B. Dielectric coated conducting sphere

The second example is the calculation of bistatic radar cross section (RCS) of a dielectric coated conducting sphere. The radius of the conducting sphere is 10λ, and the thickness of the coating dielectric is 0.05λ. The average mesh size is about 0.085λ and the total number of triangles, tetrahedrons and unknowns are 168,650, 934,261 and 2,447,096, respectively. R_{SAI} is set to 0.17λ which is about twice as large as the average mesh size. In this calculation, the OpenMP parallel technology is adopted and 16 cores are involved [17]. To verify the performance of SAIP, combined field integral equation (CFIE) or EFIE is adopted to disperse the conducting sphere part, which can be combined with VIE to yield the CFIE-VIE or EFIE-VIE type of VSIE. Since the matrix equation generated by EFIE-VIE is very

ill-conditioned, the restart parameter of GMRES is set to m=200 for EFIE-VIE which is a relatively large value, while m=30 when CFIE-VIE is adopted. Figures 4 and 5 show the number of iterations and solution time required by the SAIP with the three selection schemes (*SS*, *SS&VV* and *Tot*) to achieve convergence when the relative dielectric constant ε_r varies from 1.5 to 9.0, respectively. Besides, when EFIE-VIE is adopted without any preconditioner (*none*), ε_r=9 cannot achieve convergence after 5000 iterations. From Fig. 4 and Fig. 5, it is clear that the proposed SAIP can accelerate the convergence rate obviously, while *SS*, *SS&VV* and *Tot* need comparable iterations and solution time to reach the target convergence. Table 3 lists the computational details in terms of the memory usage of preconditioner (PC-Mem), the additional time to construct the SAI-tree and generate $\bar{Z}$ (T_{add}), the SAIP setup time (T_{PC}), and the peak memory usage with m=200 for *none*, *SS*, *SS&VV* and *Tot*. It is found that the memory usage and setup time for SAIP by *SS&VV* or *Tot* are several times as those by *SS*, which illustrates the efficiency of *SS*. When ε_r=2, the numerical results are shown in Fig. 6, while the exact result from Mie series is also given as a reference. It is observed that these numerical results have very high calculating precision.
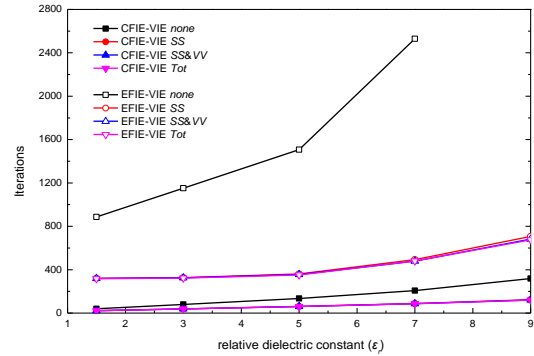
Fig. 4. Number of iterations for various ε_r, sub-matrix selection schemes, and VSIE formulations.
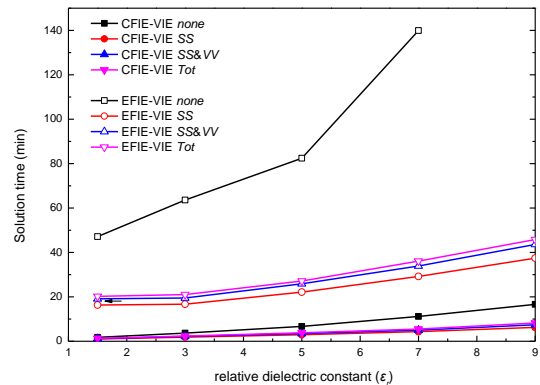
Fig. 5. Solution time for various ε_r, sub-matrix selection schemes, and VSIE formulations.
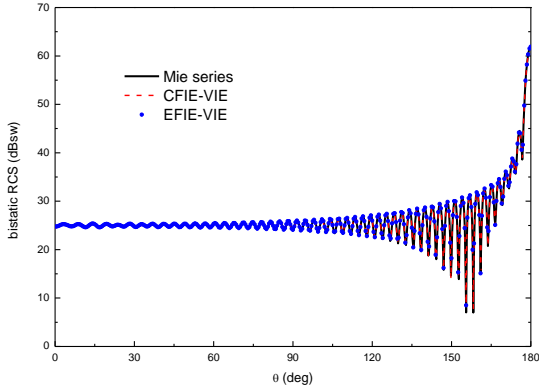
Fig. 6. Bistatic RCS of a conducting sphere of radius 10λ coated with 0.05λ thick homogeneous dielectric (ε_r=2) at φ=0 plane, illuminated by a θ-polarized plane wave with the incident angle θ^i=0, φ^i=0.

Table 3: Details of different selection schemes from the proposed SAIP with R_{SAI}=0.17λ and m=200 for a conducting sphere of radius 10λ coated with 0.05λ thick homogeneous dielectric

SAIP Scheme	PC-Mem (MB)	T_{add} (s)	T_{PC} (s)	Peak Memory (GB)
None		———		70.2
SS	210.1	1.3	11.8	70.4
SS&VV	15808.7	19.8	9986.6	86.0
Tot	19387.2	23.2	14086.8	89.5

C. Dielectric coated conducting almond

The monostatic RCS of a coated PEC almond is calculated, the geometric equation of which is listed in [18], while its position in the Cartesian coordinate is shown in Fig. 7. The length of the PEC almond is 10λ, the coating thickness is 0.05λ, and the relative dielectric constant of the coated dielectric is ε_r=3.38-j0.0338. After discretization, the average mesh size is about 0.075λ and the total number of triangles, tetrahedrons and unknowns are 30,880, 93,085 and 263,508, respectively. The coated almond is illuminated by a θ- or φ-polarization plane wave, and the observation range is θ=90° and 0≤φ≤90° with 91 observation points. During the calculation, R_{SAI} is set to 0.15λ, the OpenMP parallelization with 16 cores is applied, and CFIE-VIE or EFIE-VIE is adopted to disperse the object, while the restart parameter of GMRES is set to m=100 for the EFIE-VIE or m=30 for the CFIE-VIE. Table 4 shows the computational details in terms of the memory usage of SAIP (PC-Mem), the SAIP setup time (T_{PC}), and the peak memory usage with m=100 for the calculation process without any preconditioner (*none*) or with

SAIP by different sub-matrix selection schemes (*SS*, *SS&VV* and *Tot*), while Table 5 shows the total time of the whole process in terms of different incident wave polarization modes and different VSIE types. From Table 4, it is found that except *none*, *SS* shows the least peak memory usage and setup time, while Table 5 shows that *SS* leads to the minimum total time for both VSIE types and both polarization modes. Figure 8 shows the number of iterations with respect to different observation angles for different polarizations and VSIE types, respectively. It is observed that compared with *none*, the SAIP with each selection scheme (*SS*, *SS&VV* or *Tot*) can significantly accelerate the convergence. In addition, in terms of the acceleration performance, *SS* is on the same level as *SS&VV* or *Tot*. However, *SS* needs the least setup time and memory usage. This example illustrates that even for the calculation of monostatic RCS whose solution time occupies most of the total calculation time, *SS* also shows competitive effect.
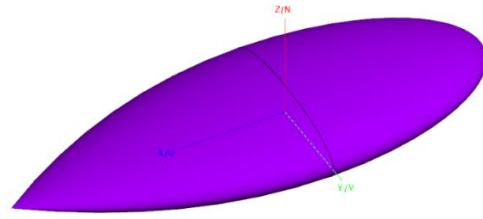
Fig. 7. The coated PEC almond in the Cartesian coordinate.

Table 4: Details of different selection schemes from the proposed SAIP with R_{SAI}=0.15λ and m=100 for a conducting 10λ length almond coated with 0.05λ thick homogeneous dielectric

SAIP Scheme	PC-Mem (MB)	T_{PC} (s)	Peak Memory (GB)
None		———	8.83
SS	58.1	7.1	8.89
SS&VV	1330.9	642.5	10.1
Tot	1874.4	1802.3	10.6

Table 5: The total time of the whole calculation process for a conducting 10λ length almond coated with 0.05λ thick homogeneous dielectric (unit: minutes)

VSIE Type	CFIE-VIE		EFIE-VIE	
Polarizations	θ	φ	θ	φ
None	39.7	36.0	885.5	372.3
SS	17.2	14.1	125.1	56.8
SS&VV	27.9	23.9	134.8	65.1
Tot	48.2	46.0	151.5	82.7
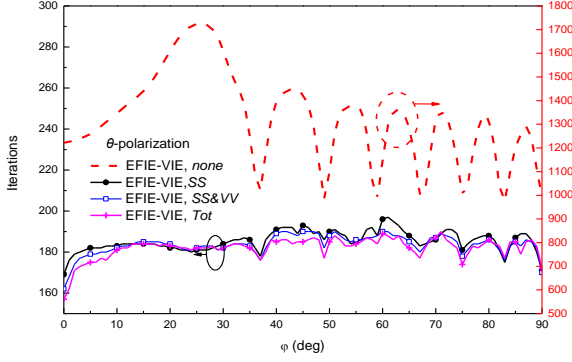
(a) θ-polarization incident wave and EFIE-VIE type
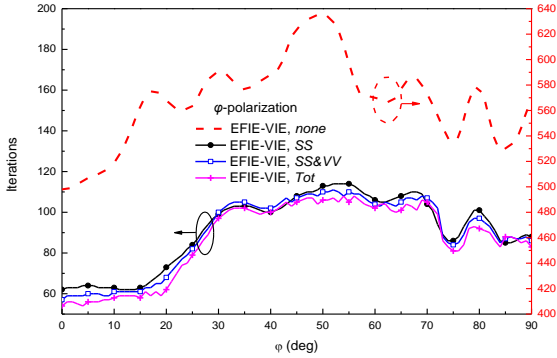
(b) φ-polarization incident wave and EFIE-VIE type
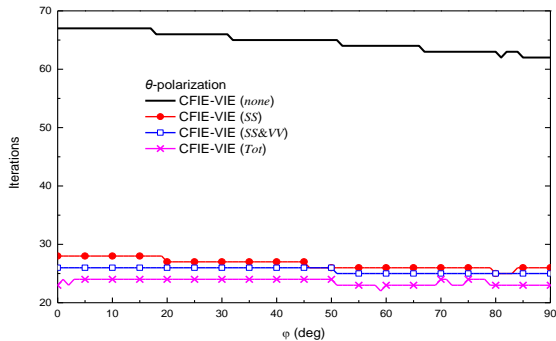
(c) θ-polarization incident wave and CFIE-VIE type
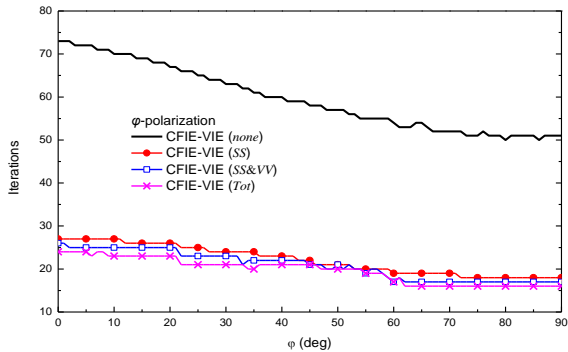
(d) φ-polarization incident wave and CFIE-VIE type

Fig. 8. Number of iterations as a function of incident angles for different polarizations and VSIE types.

IV. CONCLUSIONS

The sub-matrix selection schemes to construct the SAIP for the VSIE solution are discussed. For the VSIE, a high-quality SAIP can be constructed by utilizing the sub-matrix of surface-to-surface interactions in the near-field matrix alone, which significantly reduces the memory usage and setup time. Besides, an effective sparse pattern selection scheme with only one tuning parameter based on the geometrical information provided by the introduced SAI-tree is proposed. Numerical results show that compared with the reported SAIP and ILU-type preconditioners, the proposed SAIP reduces the number of iterations and total computation time with enhanced flexibility and stability, while the one tuning parameter can be automatically set according to the average mesh size.

REFERENCES

[1] W. C. Chew, J. M. Jin, E. Michielssen, and J. M. Song, *Fast and Efficient Algorithms in Computational Electromagnetics*, Boston, MA: Artech House, 2001.

[2] R. F. Harrington, *Field Computation by Moment Methods*, New York: MacMillan, 1968.

[3] P. L. Rui and R. S. Chen, "An efficient sparse approximate inverse preconditioning for FMM implementation," *Microwave Opt. Technol. Lett.*, vol. 49, No. 7, pp. 1746-1750, July 2007.

[4] B. Carpentieri, I. S. Duff, L. Giraud, and G. Sylvand, "Combining fast multipole techniques and an approximate inverse preconditioner for large electromagnetism calculations," *SIAM J. Sci. Comput.*, vol. 27, no. 3, pp. 774-792, 2005.

[5] B. Carpentieri, I. S. Duff, and L. Giraud, "Sparse pattern selection strategies for robust Frobenius-norm minimization preconditioners in electromagnetism," *Numer. Linear Algebra Appl.*, vol. 7, pp. 667-685, 2000.

[6] J. Lee, J. Zhang, and C. C. Lu, "Sparse inverse preconditioning of multilevel fast multipole algorithm for hybrid integral equations in electromagnetics," *IEEE Trans. Antennas Propag.*, vol. 52, no. 9, pp. 2277-2287, Sept. 2004.

[7] T. Malas, O. Ergul, and L. Gurel, "Sequential and parallel preconditioners for large-scale integral-equation problems," *2007 IEEE Computational Electromagnetics Workshop*, pp. 35-43, Aug. 2007.

[8] O. Ergul, T. Malas, and L. Gurel, "Solutions of large-scale electromagnetics problems using an

iterative inner-outer scheme with ordinary and approximate multilevel fast multipole algorithms," *Progress in Electromagnetics Research*, vol. 106, pp. 203-223, 2010.

[9] S. M. Rao, D. R. Wilton, and A. W. Glisson, "Electromagnetic scattering by surfaces of arbitrary shape," *IEEE Trans. Antennas Propag.*, vol. 30, no. 5, pp. 409-418, May 1982.

[10] D. H. Schaubert, D. R. Wilton, and A. W. Glisson, "A tetrahedral modeling method for electromagnetic scattering by arbitrarily shaped inhomogeneous dielectric bodies," *IEEE Trans. Antennas Propag.*, vol. 32, no. 1, pp. 77-85, Jan. 1984.

[11] Y. Saad, *Iterative Methods for Sparse Linear Systems*, 2nd ed., Philadelphia: SIAM, 2003.

[12] W. Joubert, "On the convergence behavior of the restarted GMRES algorithm for solving non-symmetric linear systems," *Numerical Linear Algebra with Applications*, vol. 1, no. 5, pp. 427-447, 1994.

[13] A. H. Baker, E. R. Jessup, and Tz. V. Kolev, "A simple strategy for varying the restart parameter in GMRES(m)," *Journal of Computational and Applied Mathematics*, vol. 230, no. 2, pp. 751-761, 2009.

[14] S. Tao, "Block matrix preconditioner for the coupled volume-surface integral equation," *ACES Journal*, vol. 29, no. 8, pp. 602-610, Aug. 2014.

[15] J. Lee, J. Zhang, and C. C. Lu, "Incomplete LU preconditioning for large scale dense complex linear systems from electromagnetic wave scattering problems," *Journal of Computational Physics*, vol. 185, pp. 158-175, Feb. 2003.

[16] X. S. Li and M. Shao, "A supernodal approach to incomplete LU factorization with partial pivoting," *ACM Trans. Math. Software*, vol. 37, no. 4, Article no. 43, Apr. 2011.

[17] J. Liu, M. He, K. Zhang, B. Wang, and Q. Qiu, "Parallelization of the multilevel fast multipole algorithm by combined use of OpenMP and VALU hardware acceleration," *IEEE Trans. Antennas Propag.*, vol. 62, no. 7, pp. 3884-3889, July 2014.

[18] A. C. Woo, H. T. G. Wang, M. J. Schuh, and M. L. Sanders, "EM programmer's notebook-benchmark radar targets for the validation of computational electromagnetics programs," *IEEE Antennas Propag. Magazine*, vol. 35, no. 1, pp. 84-89, Feb. 1993.

Uncertainty Analysis of the EMC Simulation Based on the Non-Intrusive Galerkin Method

Jinjun Bai [1], Gang Zhang [2], and Lixin Wang [2]

[1] College of Marine Electrical Engineering
Dalian Maritime University, Dalian, 116026, China
baijinjun@dlmu.edu.cn

[2] School of Electrical Engineering and Automation
Harbin Institute of Technology, Harbin, 150001, China
zhang_hit@hit.edu.cn, wlx@hit.edu.cn

Abstract ─ Recently, as a high-efficient uncertainty analysis method, the Stochastic Galerkin Method has been widely applied in EMC simulations. In this method, the original solver must be changed during uncertainty analysis. Thus, the realization of the Stochastic Galerkin Method may become impossible in some cases. In this paper, a novel method named Non-Intrusive Galerkin method is proposed in order to sove this problem. The performance of the proposed method can be clearly shown by calculating a published example.

Index Terms ─ Non-Intrusive Galerkin Method, Stochastic Galerkin Method, Uncertainty Analysis, EMC simulation.

I. INTRODUCTION

In actual engineering environment, uncertainties exist extensively as the random changes of the geometry condition or operating parameters. In order to model such situation precisely, stochastic modeling techniques have been widely introduced into the Electromagnetic Compatibility (EMC) simulation [1]. In this case, the inputs of the EMC models are uncertain parameters, and many uncertainty analysis methods have been introduced to deal with the variability in model inputs.

The Monte Carlo Method (MCM) is the most widely used uncertainty analysis method, and it has been testified accurate in the EMC simulation [2, 3]. However, low computational efficiency makes the MCM uncompetitive. The Method of Moments [4] and the Perturbation Method [5] are another two uncertainty analysis methods, and both of them cannot achieve high accuracy.

In recent years, the Stochastic Galerkin Method (SGM), which is based on the generalized Polynomial Chaos (gPC) expansion theory [6, 7], has caught some researchers' attention in EMC field. In the references

[8, 9], the SGM is presented to solve the stochastic Transmission Line Model. The crosstalk calculation of the random cables is presented in [8], and the field line coupling affection simulation with uncertain parameters in field is given in [9]. In the references [1, 10], the SGM is introduced into the finite-difference time-domain (FDTD) method to solve the stochastic Maxwell's equations. In the examples of the recent research, the SGM shows good accuracy and high efficiency [6-10].

However, during the uncertainty analysis of the SGM, the original solver must be changed. There is no doubt that it will be difficult to realize the SGM when the solver becomes complex. Especially in some cases, the solver can't be changed like the EMC software, and the using of the SGM will become impractical. This paper presents a novel method named Non-Intrusive Galerkin Method (NIGM), which improves the SGM by using the Numerical integration [11]. After calculating a published example in reference [12], the performance of the proposed method can be shown obviously by the use of the Feature Selective Validation [13].

The structure of the paper is as follows. Section II employs a brief description of the Stochastic Galerkin Method; the Non-Intrusive Galerkin Method can be seen in Section III; algorithm validation is presented in Section IV; Section V provides a summary of this paper.

II. THE STOCHASTIC GALERKIN METHOD

In the traditional EMC simulation, all the input parameters are supposed certain. However, in some cases, some input parameters need to be regarded as uncertain parameters, in order to improve the reliability of the EMC simulation results. If the inputs of the models are uncertain, the output parameters will be no longer deterministic too. And how to obtain such outputs is what the uncertainty analysis methods do.

The Maxwell's Equations in 1D are taken for example, as (1) and (2) shown. It is the wave propagating in a linear isotropic homogeneous material along the z-axis,

$$-\frac{\partial E_x(z,t)}{\partial z} = \mu \frac{\partial H_y(z,t)}{\partial t}, \qquad (1)$$

$$-\frac{\partial H_y(z,t)}{\partial z} = \varepsilon \frac{\partial E_x(z,t)}{\partial t} + \sigma E_x(z,t), \qquad (2)$$

where, $E_x(z, t)$ represents the electric field intensity orienting in the x direction, at a position z and time t. Similarly, $H_y(z, t)$ is the magnetic field orienting in the y direction. The symbols μ, ε, and σ stand for the permeability, permittivity and conductivity of the medium in which the electromagnetic fields propagate.

It is obviously that $E_x(z, t)$ and $H_y(z, t)$ are output parameters which we are interested in. The material parameters, like μ and ε, are the input parameters.

Suppose that the input parameters μ and ε are uncertain because of the lack of the knowledge. Thus, it is suitable to use the Uniform distribution parameters or the Gaussian distribution parameters to replace input parameters, rather than use a certain estimated value. In this situation, the lack of the knowledge is called a random event θ. Several random variables can be used to model the random event θ as (3) shown,

$$\xi(\theta) = \{\xi_1(\theta), \ \xi_2(\theta), \ \cdots, \ \xi_n(\theta)\}, \qquad (3)$$

where, $\xi(\theta)$ is the random variable space which is made up by the random variables. $\xi_i(\theta)$ is the random variable, and every variable has its own distribution.

After modeling by the random variables, the stochastic Maxwell's equations are obtained like (4) and (5):

$$-\frac{\partial E_x(z,t,\xi)}{\partial z} = \mu(\xi)\frac{\partial H_y(z,t,\xi)}{\partial t}, \qquad (4)$$

$$-\frac{\partial H_y(z,t,\xi)}{\partial z} = \varepsilon(\xi)\frac{\partial E_x(z,t,\xi)}{\partial t} + \sigma E_x(z,t,\xi). \qquad (5)$$

The parameters $\mu(\xi)$ and $\varepsilon(\xi)$ are uncertain inputs. Thus, the output parameters $H_y(z, t, \xi)$ and $E_x(z, t, \xi)$ will be influenced by the uncertainty of the inputs.

According to the gPC theory, firstly, the output parameters are expressed in the form of polynomial as (6) shown,

$$H_y(z,t,\xi) = h_0\varphi_0(\xi) + h_1\varphi_1(\xi) + h_2\varphi_2(\xi), \qquad (6)$$

where, $\varphi_i(\xi)$ is the Chaos polynomial which is determined by the Askey rule, shown in Table 1, and it is in the form of the polynomial of the random variables. More details about the Askey rule can be seen in reference [6, 7]. The coefficient h_i is under calculated. In a word, the solving process of the gPC theory is a kind of Undetermined Coefficients method.

The polynomials provided by the Askey rule satisfy the perpendicularity to each other like (7) and (8):

$$\langle \varphi_i, \ \varphi_j \rangle = \langle \varphi_i^2 \rangle \delta_{ij}, \qquad (7)$$

$$\delta_{ij} = \begin{cases} 1 & (i = j) \\ 0 & (i \neq j) \end{cases}. \qquad (8)$$

The inner product computation in (7) can be seen in (9):

$$\langle \varphi_i, \ \varphi_j \rangle = \int \varphi_i(\xi)\varphi_j(\xi)w(\xi)d\xi, \qquad (9)$$

where, $w(\xi)$ is the weight function, which can be obtained by calculating the joint probability density of the random variables.

Table 1: The Askey rule

Random Variables	Wiener-Askey Chaos	Support
Gaussian	Hermite-chaos	$(-\infty, +\infty)$
Gamma	Laguerre-chaos	$[0, +\infty)$
Beta	Jacobi-chaos	$[a,b]$
Uniform	Legendre-chaos	$[a,b]$

The Galerkin projection equations by using the SGM can be given by (10) and (11):

$$-\frac{\partial}{\partial z}\begin{bmatrix} e_0 \\ e_1 \\ e_2 \end{bmatrix} = \begin{bmatrix} M_{\mu 0,0} & M_{\mu 1,0} & M_{\mu 2,0} \\ M_{\mu 0,1} & M_{\mu 1,1} & M_{\mu 2,1} \\ M_{\mu 0,2} & M_{\mu 1,2} & M_{\mu 2,2} \end{bmatrix}\frac{\partial}{\partial t}\begin{bmatrix} h_0 \\ h_1 \\ h_2 \end{bmatrix}, \qquad (10)$$

$$-\frac{\partial}{\partial z}\begin{bmatrix} h_0 \\ h_1 \\ h_2 \end{bmatrix} = \begin{bmatrix} M_{\xi 0,0} & M_{\xi 1,0} & M_{\xi 2,0} \\ M_{\xi 0,1} & M_{\xi 1,1} & M_{\xi 2,1} \\ M_{\xi 0,2} & M_{\xi 1,2} & M_{\xi 2,2} \end{bmatrix}\frac{\partial}{\partial t}\begin{bmatrix} e_0 \\ e_1 \\ e_2 \end{bmatrix} + \sigma\begin{bmatrix} e_0 \\ e_1 \\ e_2 \end{bmatrix}, (11)$$

where, e_i and h_i are the coefficients of the Chaos polynomial, which are under calculated. And they are the abbreviation of $e_i(z, t)$ and $h_i(z, t)$. $M_{\mu i,j}$ means the product computation result of $\langle \mu(\xi)\varphi_i(\xi), \ \varphi_j(\xi)\rangle$. Similarly, $M_{\varepsilon i,j}$ means the product computation result of $\langle \varepsilon(\xi)\varphi_i(\xi), \ \varphi_j(\xi)\rangle$.

Obviously, the original solver is changed due to the Galerkin projection in SGM process. And after calculating the coefficients of (6), the uncertainty analysis results can be easily acquired by sampling in terms of the distributions of the random variables in (3). More details about the SGM can be seen in the references [6-10].

Due to the Galerkin Process, the solver must be changed during the SGM. This character severely limits the application of the SGM. In next section, another coefficient calculating method is given, and the original solver would not be changed in this method.

III. THE NON-INTRUSIVE GALERKIN METHOD

In the NIGM, numerical integration is introduced to improve the SGM.

The inner product computation with $\varphi_0(\xi)$ is carried out in both sides of (6), and (12) is obtained,

$$\langle \varphi_0(\xi), H_y(t,z,\xi) \rangle = h_0 \langle \varphi_0(\xi), \varphi_0(\xi) \rangle$$
$$+ h_1 \langle \varphi_0(\xi), \varphi_1(\xi) \rangle + h_2 \langle \varphi_0(\xi), \varphi_2(\xi) \rangle. \quad (12)$$

Using the orthogonal property of the Chaos polynomial in (7), $\langle \varphi_0(\xi), \varphi_0(\xi) \rangle = 1$, $\langle \varphi_0(\xi), \varphi_1(\xi) \rangle = 0$, and $\langle \varphi_0(\xi), \varphi_2(\xi) \rangle = 0$ can be gotten. Then (13) is obtained:

$$e_0 = \langle \varphi_0(\xi), H_y(t,z,\xi) \rangle. \quad (13)$$

In a similar way, the coefficients calculation can be replaced by the integration calculations, shown as (14):

$$e_k = \int_{a(\xi)}^{b(\xi)} \varphi_k(\xi) H_y(t,z,\xi) w(\xi) d\xi, \quad (14)$$

where, $a(\xi)$ and $b(\xi)$ are the lower bound and the upper bound of the integration calculation.

In the NIGM, Numerical integration is provided to calculate the integration in order to remove the random variables. Numerical integration is an approximate numerical method, which is used to calculate the integration when the integrand function is in a complex form. By this way, the coefficients calculation turns to be (15):

$$e_k = \sum_{i=1}^{n+1} A_i \varphi_k(NI_i) H_y(t,z,NI_i), \quad (15)$$

where, the integration points NI_i satisfy the character $a(\xi) \le NI_1 < NI_2 < \cdots < NI_{n+1} \le b(\xi)$, and A_i stands for the integration weight of the Numerical integration. The integration points are chosen according to the Gaussian Quadrature formula [11], and the total number of the integration points is supposed $n + 1$. $H_y(t, z, NI_i)$ presents making the certain EMC simulation result in point NI_i. Thus, the uncertainty ξ in input is replaced by the certain value NI_i. In another word, the random variable disappears. The value of $\varphi_0(NI_i)$ can be easily calculated by substituting NI_i into it.

Due to the numerical integration, the uncertain EMC simulation is replaced by several certain EMC simulations in numerical integration points NI_i. Thus, a steady EMC solver is enough for the NIGM, and the solver can be regarded as a 'black box'. There is no doubt that the realization of the NIGM is much easier than the SGM, and the NIGM can be introduced into the EMC software to make the uncertainty analysis.

IV. ALGORITHM VALIDATION

In this section, two typical examples are simulated in order to present the performance of the NIGM. Because of the high accuracy of the MCM, the uncertainty analysis results given by the MCM will be regarded as the standard data.

The first example is one-dimension wave propagation example published in reference [12], as shown in Fig. 1. The certain EMC simulation method FDTD is used to solve the Maxwell's equations.

The space step of the FDTD is $1.5 \times 10^{-2} m$ and the time step is $5.0 \times 10^{-11} s$. The number of discrete points in the electric field intensity is 151, and it is 150 in the magnetic field intensity. The sine excitation source is in the first discrete point with the amplitude $2.7 \times 10^{-3} V/m$ and the frequency $1.0 \times 10^9 Hz$. The total number of the time steps is 100.
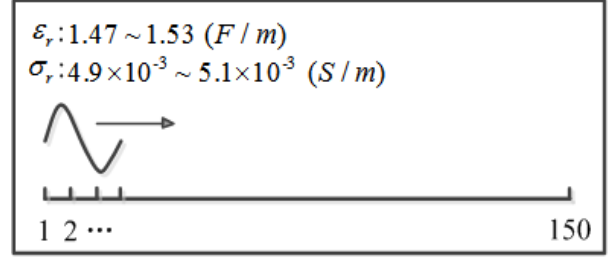
Fig. 1. One-dimension wave propagation model with uncertain inputs in medium parameters.

The dielectric coefficient ε_r and the conductivity σ_r are supposed to be the uncertain parameters, and they are both in the Uniform distribution. The dielectric coefficient obeys $U[1.47, 1.53](F/m)$, and the conductivity is $U[4.9 \times 10^{-3}, 5.1 \times 10^{-3}](S/m)$.

Such random event in the inputs can be modeled by two random variables ξ_1 and ξ_2 like (16) and (17). Both of the variables are in the Uniform distribution with the bound [-1, 1]:

$$\varepsilon_r = \varepsilon_r^* \times (1 + 0.02 \times \xi_2), \quad (16)$$

$$\sigma_r = \sigma_r^* \times (1 + 0.02 \times \xi_1), \quad (17)$$

where, the mean values of the input parameters are $\varepsilon_r^* = 1.5 \ (F/m)$ and $\sigma_r^* = 5 \times 10^{-3} \ (S/m)$.

For the SGM, six terms of the Chaos polynomial are given in (18). It is the tensor product of one-dimension Chaos polynomial, more details can be found in [9]:

$$\varphi_0(\xi) = 1$$
$$\varphi_1(\xi) = \sqrt{3} \times \xi_1$$
$$\varphi_2(\xi) = \sqrt{3} \times \xi_2$$
$$\varphi_3(\xi) = \frac{\sqrt{5}}{2} \times (3 \times \xi_1^2 - 1) \quad (18)$$
$$\varphi_4(\xi) = 3 \times \xi_1 \times \xi_2$$
$$\varphi_5(\xi) = \frac{\sqrt{5}}{2} \times (3 \times \xi_2^2 - 1)$$

According to [11], the numerical integration points in the NIGM are given by the Table 2, and the integration weight A_i is also presented.

The Probability Density Function (PDF) curve of the electric field intensity at the 100th discrete point simulation results are shown as Fig. 2.
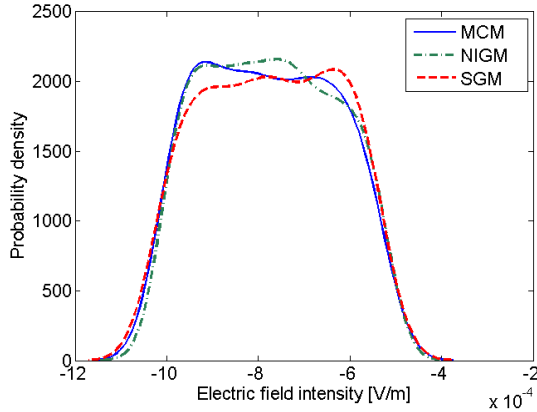
Fig. 2. The PDF of electric field intensity at the 100th discrete point.

Table 2: The numerical integration points (ξ_1, ξ_2)

Number	1	2	3
Point	$\left(-\dfrac{\sqrt{15}}{5}, -\dfrac{\sqrt{15}}{5}\right)$	$\left(-\dfrac{\sqrt{15}}{5},\ 0\right)$	$\left(-\dfrac{\sqrt{15}}{5}, \dfrac{\sqrt{15}}{5}\right)$
Weight	$\dfrac{25}{324}$	$\dfrac{40}{324}$	$\dfrac{25}{324}$
Number	4	5	6
Point	$\left(0, -\dfrac{\sqrt{15}}{5}\right)$	$(0,0)$	$\left(0, \dfrac{\sqrt{15}}{5}\right)$
Weight	$\dfrac{40}{324}$	$\dfrac{64}{324}$	$\dfrac{40}{324}$
Number	7	8	9
Point	$\left(\dfrac{\sqrt{15}}{5}, -\dfrac{\sqrt{15}}{5}\right)$	$\left(\dfrac{\sqrt{15}}{5}, 0\right)$	$\left(\dfrac{\sqrt{15}}{5}, \dfrac{\sqrt{15}}{5}\right)$
Weight	$\dfrac{25}{324}$	$\dfrac{40}{324}$	$\dfrac{25}{324}$

The results of the MCM are treated as the standard data, and 10,000 times of certain EMC simulations were done to make sure the convergence of the MCM.

Furthermore, the Fig. 3 shows the expectation value of all 200 discrete points, and the Fig. 4 presents the variance information. The expectation value means the most possible value, and the variance information presents the magnitude of the uncertainty.

Using the Feature Selective Validation, the Total Global Difference Measure (Total-GDM) values are shown in Table 3.

According to the qualitative rule in the Feature Selective Validation, if the Total-GDM value is less than 0.1, it means that the simulation results are in the 'Excellent' level. Thus, all the four values in Table 3 are in 'Excellent' level, and it is proved that the accuracy of the NIGM and the SGM in this example is the same as the MCM. It is worth noting that though the Total-GDM value of the SGM is less than that of the NIGM, the accuracy of the SGM and the NIGM is still in the same level. That is the opinion of the Feature Selective

Validation [13].
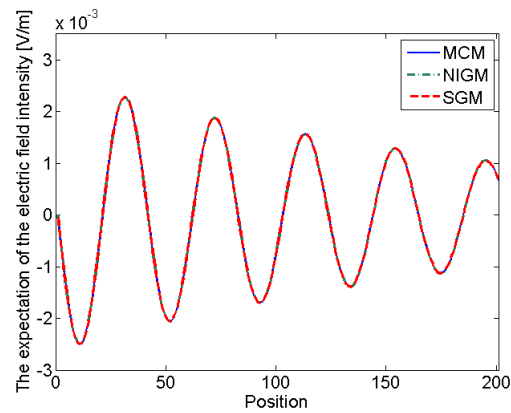
Fig. 3. The expectation values of all 200 discrete points.
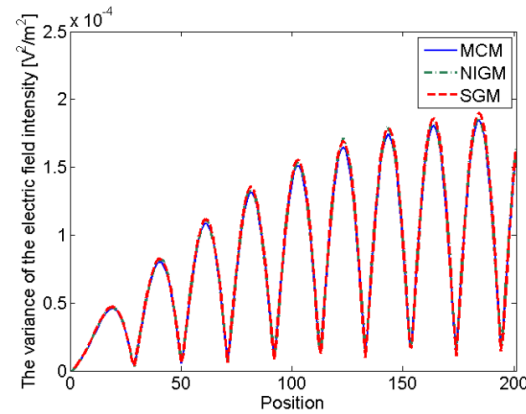
Fig. 4. The variance values of all 200 discrete points.

Table 3: The Total-GDM value of the results

Results	SGM	NIGM
Expectation	0.006	0.01
Variance	0.037	0.05

The simulation time of the MCM is 63.2 s, and the SGM takes 1.12 s. The NIGM wastes 0.65 s. It is proved that the computational efficiency of the SGM and the NIGM are in the same level, and much better than the MCM.

The second example is the shielding effectiveness calculation of a Perfect Electric Conductor (PEC) box with the random hole. In actual situation, the position of the hole and the size of the hole might be uncertain because of the existence of the manufacturing tolerance. Thus, the inputs of simulation model must be random in order to model the situation better.

In this example, the EMC software, CST Studio Suite, is applied to calculate the shielding effectiveness. As the solver of the software is not open source, the SGM cannot be used in this case. Thus, only the results of the

NIGM and the MCM are presented.

The material of the box is supposed the PEC, other space is supposed vacuum. The size of the solution space is $0.2m \times 0.2m \times 0.2m$. If the step of is supposed $2 \times 10^{-3}m$, the space can be described like $100 \times 100 \times 100$. The box is in the shape of cube located in the middle of the solution space, the length of side is $0.12m$. The wall thickness is $6 \times 10^{-3}m$, 3 times of space step.

The shielding effectiveness calculation at 100 MHz is obtained by the NIGM and the MCM. The position of the excitation source is at the point (6, 64, 64) of the space. And the excitation source is sinusoidal electric field source at single frequency 100 MHz. The shielding effectiveness reference point is in the middle of the solution space, that is the point (50, 50, 50). The model is given in Fig. 5.
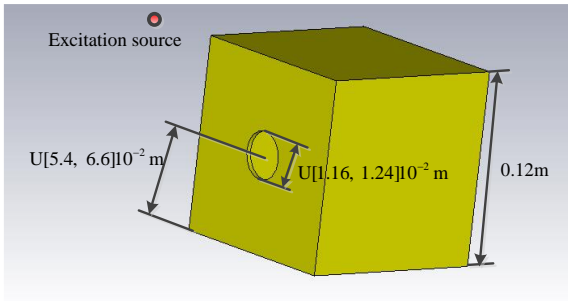
Fig. 5. The model of the PEC box with an uncertain hole on the surface.

The random variables for modeling the random event are similar as (16) and (17) shown. Thus, the numerical integration points and the weight are same as the Table 2 shown. Figure 6 gives shielding effectiveness results of the NIGM and the MCM.
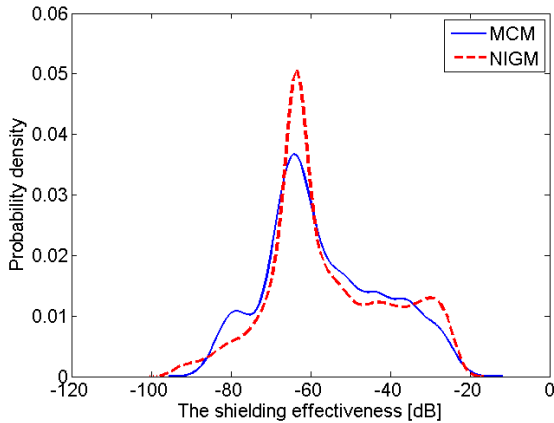
Fig. 6. The shielding effectiveness results given by the NIGM and the MCM.

In this example, the result is in the form of PDF. The PDF curve has the character that the area surrounded by the curve and the horizontal axis is 1. That means that the PDF curve will be 'wane and wax', unlike the results in Fig. 3 and Fig. 4. Thus, judging the accuracy of the simulation result by means of comparing the difference of two PDF curves is not reasonable. Furthermore, the Feature Selective Validation is not suitable at the same time.

The mean value and the variance comparison of the NIGM and the MCM are proposed. The mean value of shielding effectiveness values calculated by the MCM is -56.7 dB, and the variance information of the MCM is $14.6 \, dB^2$. Meanwhile, the mean value of the results given by the NIGM is -55.8 dB, and the variance information of the NIGM is $15.3 \, dB^2$. The error in mean value is 1.6%, and that in variance is 4.8%.

It is demonstrated that the NIGM is as accurate as the MCM in the second example.

The certain simulation times of the MCM are 5,000, and these of the NIGM are only 9. It is seen that the computational efficiency of the NIGM is much higher than the MCM.

In short, the NIGM is as accurate as the MCM and the SGM. Like the SGM, the NIGM owns high computational efficiency, and much better than the MCM. Like the MCM, the NIGM can realize the uncertainty analysis without changing the original solver. Thus, the application scope of the NIGM is much wider than the SGM.

V. CONCLUSION

This paper proposed a novel method named the Non-Intrusive Galerkin Method, aiming at realizing the uncertainty analysis in EMC simulations without changing the original solver. By using the Feature Selective Validation, it is clearly demonstrated that the proposed method is as accurate as the Stochastic Galerkin Method in a published example. Furthermore, it is proved that the proposed method can be generalized into the EMC software like the Monte Carlo method, but Stochastic Galerkin Method can't. It means that the proposed method is much better than the Stochastic Galerkin Method in the scope of application.

REFERENCES

[1]   R. S. Edwards, A. C. Marvin, and S. J. Porter, "Uncertainty analyses in the finite-difference time-domain method," *IEEE Transactions on Electromagnetic Compatibility*, vol. 52, no. 1, pp. 155-163, 2010.

[2]   D. Bellan and S. A. Pignari, "Efficient estimation of crosstalk statistics in random wire bundles with lacing cords," *IEEE Transactions on Electro-*

magnetic Compatibility, vol. 53, no. 1, pp. 209-218, 2011.

[3] C. Jullien, P. Besnier, M. Dunand, et al., "Advanced modeling of crosstalk between an unshielded twisted pair cable and an unshielded wire above a ground plane," *IEEE Transactions on Electromagnetic Compatibility*, vol. 55, no. 1, pp. 183-194, 2013.

[4] R. W. Walters and L. Huyse, "Uncertainty analysis for fluid dynamics with applications," *ICASE Report no. 2002-1, NASA/CR-2002-211449, REC Warangal*, Feb. 2002.

[5] P. E. Kloeden and E. Platen, *Numerical Solution of Stochastic Differential Equations*. Springer-Verlag, Berlin, 1999.

[6] D. Xiu, "Numerical methods for stochastic computations," *Princeton University Press*, pp. 1-23, 2010.

[7] D. Xiu and G. E. Karniadakis, "The Wiener Askey polynomial chaos for stochastic differential equations," *SIAM Journal on Scientific Computing*, vol. 24, no. 2, pp. 619-644, 2002.

[8] P. Manfredi and F. G. Canavero, "Numerical calculation of polynomial chaos coefficients for stochastic per-unit-length parameters of circular conductors," *IEEE Transactions on Magnetics*, vol. 50, no. 3, pp. 74-82, 2014.

[9] P. Manfredi and F. G. Canavero, "Polynomial chaos for random field coupling to transmission lines," *IEEE Transactions on Electromagnetic Compatibility*, vol. 54, no. 3, pp. 677-680, 2012.

[10] R. S. Edwards, "Uncertainty analyses in computational electromagnetism," *University of York*, 2009.

[11] R. A. Perez, "Uncertainty analysis of computational fluid dynamics via polynomial chaos," *Virginia Polytechnic Institute and State University*, 2008.

[12] B. Jinjun, Z. Gang, et al., "Uncertainty analysis in EMC simulation based on Stochastic collocation method," *2015 IEEE International Symposium on Electromagnetic Compatibility*, pp. 930-934, 2015.

[13] IEEE Recommended Practice for Validation of Computational Electromagnetics Computer Modeling and Simulations, *IEEE STD 15972-2010*, pp. 1-124, 2011.

A New Approach for Improving the Load Current Characteristic of Cascaded Magnetic Flux Compression Generator

Mohammad Jafarifar, Behrooz Rezaeealam*, and Ali Mir

Department of Electrical Engineering
Lorestan University, Khorramabad, Iran
*rezaee.bh@lu.ac.ir

Abstract – Helical magnetic flux compression generators (HFCGs) are widely used to generate extremely high-power pulses. Two most important output characteristics of HFCGs in their use as pulsed power generators are maximum value of load current and the rise time of that current. In this paper, an approach is proposed to improve the output characteristic of a Cascaded-HFCG. The approach is based on time-varying primary winding of dynamic transformer and addition of a gradually incremental resistance in series with the first stage winding. It is demonstrated analytically using simulation results that the output current and its rise-time improve by minimizing energy returned from secondary winding to primary winding of dynamic transformer. The results are compared to conventional Cascaded-HFCG that has a non-destructive winding in its structure. A finite element model is considered to calculate the self-inductances, mutual inductance and resistances of the generator. A new approach is proposed to gradually increase in the resistance of primary winding of dynamic transformer.

Index Terms ─ Dynamic transformer, explosive charge, helical magnetic flux compression generator, incremental resistance, load characteristic.

I. INTRODUCTION

Helical magnetic flux compression generators (HFCG) are widely used to produce very high current pulses in the recent past decades. These generators convert the chemical energy of explosive charge into magnetic energy in the form of current pulses. They are used in a variety of applications like nuclear research, X-Ray source, high power microwave, high power laser, rail gun, and so on. Some applications of HFCGs require shorter pulse width (shorter rise-time), higher voltage, higher current, higher energy gain and higher instantaneous power delivered to load [1]. Several approaches are proposed in literatures to achieve these requirements. For example, an increase in the axial length of winding increases current gain and energy gain of the generator but causes wider pulse width [2].

Another approach to get the higher current and energy gain is to increase the diameter of armature, which cause increase in cost and explosive pressure [2]. As mentioned, many applications require a rise-time of output current pulses in the range of one microsecond or less. In order to achieve shorter pulse width (less rise-time of pulse), the inductance of winding should be rapidly reduced (dL/dt reaches a maximum value). In the past few decades, several approaches have been proposed to increase the rate of inductance changing in HFCGs. One approach that is especially useful in larger HFCGs is to use areal or simultaneous initiation of the explosive charge [3], which may be achieved in either outside-in or inside-out detonations. Generally, the outside-in initiation is used for high magnetic field experiments [4]. The inside-out simultaneous initiation systems are successfully used in several generator designs [4]. Another approach is to taper the stator diameter to an angle less than the armature expansion angle. This technique is used in larger generators as well. Disadvantages of this approach include finite length systems and the difficulties in fabrication and assembly of the tapered stator [4]. Short pulse width can usually be achieved by using a conventional HFCG coupled with a pulse-forming circuit, such as an opening switch or fuse. Opening switches are difficult to design and fabricate and add greatly to the complexity of the experiment [5]. In [6], a new method is proposed to reach an arbitrary pulse width using two explosive current-opening switches (EOS) combined with HFCG. An EOS is used to form the leading edge of current pulse, while an explosive current interrupter (EOI) switched in-series to electrical circuit provides the duration of current pulse and the formation of its trailing edge. The most important advantage of this method is the production of a pulse with controlled amplitude and duration with a trapezoidal shape. Because of existence of two EOSs in this method, its manufacturing is very complicated, time consuming and expensive.

The first idea to overcome the aforementioned problems was to use inductively coupled Cascaded generators using air-cored transformer [7]. After that, in

1979, among several ideas and opinions, Chernyshev proposed the use of a dynamic transformer and its combination with Cascaded generator [8]. A Cascaded generator consists of two or more FCGs connected in-series with an air transformer or dynamic transformer, where each FCG is the load of the previous generator. A schematic of Cascaded-HFCG is shown in Fig. 1. It is composed of two conventional HFCGs, which are coupled magnetically using dynamic transformer.
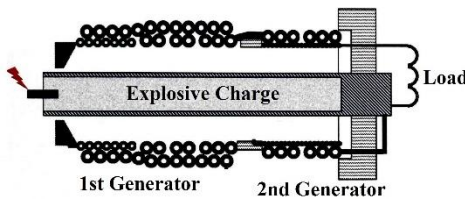
Fig. 1. Schematic of Cascaded Helical Magnetic Flux Compression.

The electrical equivalent circuit of Cascaded-HFCG after starting the explosion is shown in Fig. 2.
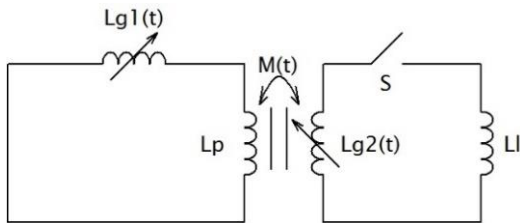
Fig. 2. Electrical Circuit of Cascaded-HFCG.

In the circuit shown above, $L_{g1}(t)$ is winding of first stage, L_P is primary winding of dynamic transformer, $L_{g2}(t)$ is winding of second stage (secondary of dynamic transformer) and L_l is load inductance. A seeding system (usually a capacitor bank) introduces an initial magnetic flux into generator by injecting current directly into first stage winding. When the explosion starts, the armature is expanded, and the injected flux is compressed. At the end of the first stage operation, switch S is closed, and the magnetic flux is trapped by $L_{g2}(t)$ using a dynamic transformer. At the same time, load current appears and increases rapidly to form a current pulse. The rise-time of load current is smaller than that of first stage current due to lower axial length of $L_{g2}(t)$ compared to $L_{g1}(t)$. Another advantage of Cascaded-HFCG is that it can be used as a voltage pulse generator with arbitrary amplitude because of the existence of step-up transformer (dynamic transformer) in its structure [8].

Actually, a Cascaded-HFCG is composed of two conventional HFCGs, which are connected in series and coupled magnetically; thus, its efficiency is expected to be a number close to the product of efficiency of each

individual HFCG. However, experimental results show that the efficiency of Cascaded-HFCG is about 30% less than the expected value [2]. One of the reasons of this lower efficiency is magnetic flux loss at the moment of flux trapping in second stage (this moment is called crowbar). Adequately, high mutual inductance between dynamic transformer windings can decrease flux losses and consequently increase the generator efficiency. There are many factors that maximize mutual inductance between two windings, such as turns number of windings, pitch of winding, axial length of windings and so on [9]. Although, high mutual inductance decreases magnetic flux losses, it can increase transferred energy between two windings. As we know, in Cascaded-HFCGs, after starting the second stage operation, the first stage current is still ongoing. Given that two stages are magnetically coupled through dynamic transformer, a part of energy returns to the first stage. Since there is no electrical connection between load and first stage winding, the returned energy leads to increase in current of first stage winding instead of reaching to load. In [10], a flux-trapping HFCG is considered, which is structurally similar to Cascaded-HFCGs. Simulation results show that close to the end of the generator operation, mutual inductance between main winding (which is similar to second stage winding in Cascaded-HFCG) and field winding (which is similar to first stage winding in Cascaded-HFCG) is high enough for a great amount of energy to return to the field winding circuit. The returned energy causes an increase the current of field winding more than the usual (as can be seen from Fig. 5 of [10]). It should be noted that in the described flux-trapping HFCG, the field winding only covers the first 50% of the main winding, which helps to decrease the coupling between the two windings before an appreciable amount of energy is transferred to the field-winding circuit. In [11], a Cascaded-HFCG is considered, in which primary winding of dynamic transformer covers 100% of the second stage winding. Simulation results show that due to the high amount of energy returned to the first stage winding, its current increases irrationally (Fig. 6 in [11]).

It can be concluded from the above discussion that one of the main issues about the lower efficiency of Cascaded-HFCG is the increase in first stage current more than the common value after crowbar instance and increase in ohmic losses. In [12], it is proposed to rapidly cut off current of the first stage by an EOS. On the other hand, it is shown that in this case, a surge voltage is produced in the generator, which causes electrical break down in generator insulators [13].

This paper proposes an approach to overcome the problems described above. In order to minimize the energy returned to the first stage, mutual inductance between two windings of dynamic transformer should tend to a very small value after starting the second stage operation. In conventional Cascaded-HFCG, the two

windings of dynamic transformer do not essentially decouple during the generator run time. If each turns of primary winding of dynamic transformer wipes out simultaneously with turns of second stage winding and armature expansion, the two windings can decouple more quickly, and the returned energy decreases significantly. Actually, the primary winding of the dynamic transformer should have time-varying behavior like the other windings of generator ($L_P \rightarrow 0$). In the case of time-varying L_P, the self-inductance of first stage winding reaches zero at the end of generator operation (in the conventional Cascaded-HFCG, the self-inductance of L_P is a non-zero value), therefore, the maximum value of the current of first stage winding increases too. To prevent the unusual increasing in the first stage current, a gradually incremental resistance should be introduced in-series with L_P. Added resistance restricts the maximum value of first stage current, which causes an increase in the load current. These claims are proved analytically and using simulation results. The mathematical model proposed in [11] is used for simulation of Cascaded-HFCG. Resistances of windings are calculated by the method presented in [14]. Time varying self-inductances and mutual inductance are calculated using finite element method (FEM) and validated by comparing with 2-D filamentary method described in [15].

II. MODELING OF CASCADED-HFCG

According to the model proposed in [11], the operation of Cascaded-HFCG can be divided into two distinct phases. The first phase of the operation begins by starting the explosion. Kirchhoff's voltage equation for the loop containing first-stage winding can be written as:

$$[L_{g1}(t)+L_p]\frac{dI_{g1}(t)}{dt}+[R_{g1}(t)+\alpha_1\frac{d(L_{g1}(t)+L_p)}{dt}]I_{g1}(t)=0, \quad (1)$$

where α_1 is the flux conservation coefficient, accounting for intrinsic flux losses in the first stage.

The second phase begins after the closure of switch S and lasts until the end of generator operation. Kirchhoff's voltage equation for the loops are as follows:

$$[L_{g1}(t)+L_p]\frac{dI_{g1}(t)}{dt}+[R_{g1}(t)+\alpha_1\frac{d(L_{g1}(t)+L_p)}{dt}]I_{g1}(t)+M(t)\frac{dI_{g2}(t)}{dt}+I_{g2}(t)\frac{dM(t)}{dt}=0, \quad (2)$$

$$[L_{g2}(t)+L_1]\frac{dI_{g2}(t)}{dt}+[R_{g2}(t)+R_1+\alpha_2\frac{dL_{g2}(t)}{dt}]I_{g2}(t)+M(t)\frac{dI_{g1}(t)}{dt}+I_{g1}(t)\frac{dM(t)}{dt}=0. \quad (3)$$

In (3), α_2 is the flux conservation coefficient accounting for intrinsic flux losses of the second stage. By solving the equations above, the time-varying current in the circuits can be calculated. However, the time variations of the inductances and resistances of windings should be obtained and the values of α_1 and α_2 should be determined in advance.

III. INDUCTANCE AND RESISTANCE CALCULATION

While there are many analytical formulas for the calculation of self-inductance and mutual inductance of the two air-cored helical windings, there is almost no explicit formula that produces accurate results when a magnetic core such as an aluminum armature is added inside the windings. The reason for this is that inductance calculation in the presence of magnetic core requires the use of formulas involving elliptic integrals or infinite series, which can be very complicated. Numerical methods can be used to avoid the calculation these complicated and time-consuming integrals.

In [14], a zero-dimensional method of calculating time varying inductances based on working volume collapse during armature expansion is introduced. This method is very simple and fast and is thus sufficient for designing purpose.

In [15], a method called 2-dimensional filamentary is introduced for the calculation of the self-inductance and mutual inductance of HFCG. According to this model, the armature and both windings of the generator are decomposed into the same number rings. The inductance of each winding involves the superposition of the self-inductance of rings and mutual inductance between them. In this model, the higher number of rings for armature provide further accuracy in inductance calculation, but this is more time-consuming, and the simulation becomes more complicated.

In [16], a 2-dimentional method based on the concept of equivalent impedance is proposed. Equivalent impedance can be calculated in each step of the generator operation through the division of voltage phasor by current phasor in an equivalent frequency. This method is only proposed for the calculation of self-inductance of conventional HFCG.

The most useful formula for the computation of self-inductance of a system involves calculating the total magnetic energy using (4):

$$E_m=\int_V \frac{B^2}{2\mu_0}dv=\frac{1}{2}\int_V \overline{A}.\overline{J}dv,$$
$$E_m=\frac{1}{2}LI^2. \quad (4)$$

For a linear magnetic system, the volume integral of (4) can be calculated analytically, but for nonlinear systems, there is no analytical solution for this integral and it should be calculated using numerical methods [10].

An appropriate method to calculate the mutual inductance of the two windings is to consider the system as a four-terminal device. A known current is applied at the input terminals of device (one of the windings), which induces a voltage across the output terminals (the other winding). The induced voltage can be calculated

from the magnetic potential vector using Faraday's law. The calculated voltage can be used to compute the mutual inductance via:

$$\text{mutual inductance} = \frac{\text{induced voltage}}{j(\text{angular frequency of supply}) \times (\text{applied current})}. \quad (5)$$

Considering (4) and (5), in order to achieve self and mutual inductances, it is necessary to calculate magnetic vector potential (A). Using the Maxwell equations, the magnetic potential vector can be written in the form of (6) for a system with certain boundary conditions:

$$\nabla^2 \bar{A} = -\mu_0 \bar{J}, \quad (6)$$

where μ_0 represents the magnetic permittivity of the vacuum, $\bar{J} = \sigma \bar{E} = -\sigma(\partial \bar{A}/\partial t)$ represents the vector of current density and σ special electrical conductivity. By replacing $\bar{J}$, the (6) obtains in the form of (7):

$$\nabla^2 \bar{A} - \sigma \mu_0 \frac{\partial \bar{A}}{\partial t} = 0. \quad (7)$$

In other regions where there is no current ($\sigma = 0$), (6) converts to the Laplace equation:

$$\nabla^2 \bar{A} = 0. \quad (8)$$

A helical flux compression generator is cylindrical and thus, using a cylindrical coordinate system is suitable for its analysis. Considering the symmetry of the helical generators, (6) can be expressed in the various parts of the generator in the form of (7):

$$\frac{\partial^2 A}{\partial z^2} + \frac{\partial^2 A}{\partial r^2} + \frac{1}{r}\frac{\partial A}{\partial r} - \frac{A}{r^2} = 0, \qquad \textit{for free space}$$

$$\frac{\partial^2 A}{\partial z^2} + \frac{\partial^2 A}{\partial r^2} + \frac{1}{r}\frac{\partial A}{\partial r} - \frac{A}{r^2} - \sigma\mu_0\frac{\partial A}{\partial t} = 0, \qquad \textit{for armature} \quad (9)$$

$$\frac{\partial^2 A}{\partial z^2} + \frac{\partial^2 A}{\partial r^2} + \frac{1}{r}\frac{\partial A}{\partial r} - \frac{A}{r^2} - \sigma\mu_0\frac{\partial A}{\partial t} = -\sigma\mu_0 J. \quad \textit{for windings}$$

By solving (9), the magnetic potential vector is calculated and using the (4) and (5) we can obtain the self and the mutual inductance.

In this paper, the self-inductance and mutual inductance of windings are calculated using FEM. The two stages of the generator, dynamic transformer and armature are modeled in 3-D as shown schematically in Fig. 3. The modeled domain is surrounded by a region of infinite elements, which is a way to truncate a domain that stretches to infinity. Each winding is modeled as a hollow cylinder that can be considered as a multi-turn winding. The armature is modeled as an aluminum hollow cylinder that can be considered as a single-turn coil passing the current of generator stages. The free space between windings and armature (called working volume) is considered as air.

Figure 4 shows a typical 2D axisymmetric schematic for the modeled Cascaded-HFCG demonstrated in Fig. 3.

Self-inductance calculation of the first-stage winding can be carried out by neglecting the second-stage winding. A known current (for example 1A) is

introduced to the first-stage winding. Using (4), the time-varying inductance profile can be calculated. Figure 5 shows the calculated time-varying self-inductance profile of the first-stage winding using the described FEM. In order to verify the validation of the calculated profiles, a simulation is performed using the 2-D filamentary method described in [15] and the results are compared. As we can see, there is an approximately good agreement between the calculated inductance profile using the FEM method and 2-D filamentary method.
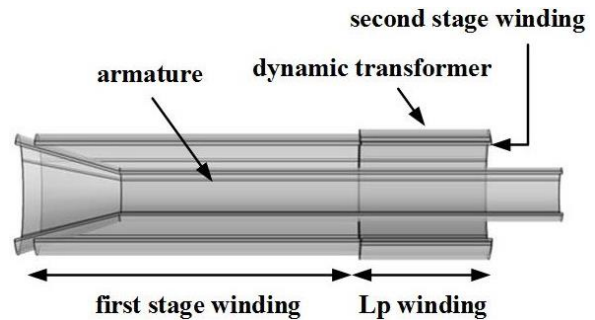
Fig. 3. FEM model of Cascaded-HFCG used to calculate inductances.
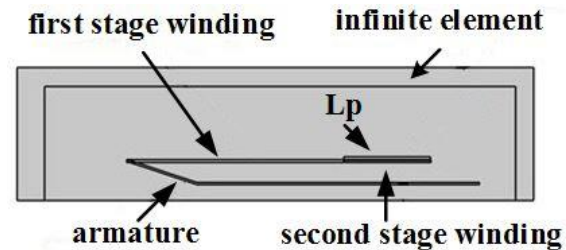
Fig. 4. 2D axisymmetric for the modeled Cascaded-HFCG.
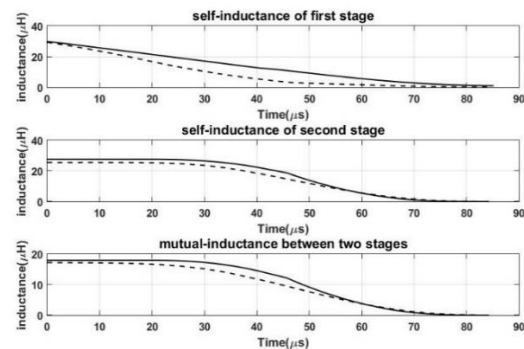
Fig. 5. Calculated time-varying inductances: (solid line) for FEM method; (dashed line) for 2-D filamentary method.

Inductance calculation procedure for second-stage winding is similar to the one described for the first stage.

First-stage winding is the neglected and a known current is fed to second-stage winding. The self-inductance profile of second-stage winding is similar to that of the first stage. But the difference is that during first-stage operation, there is no contact between second-stage winding and armature, as a result of which inductance is approximately constant. After closure of switch S, all turns of the winding are wiped out one by one and inductance tends to zero at the end of the generator operation. Figure 5 shows the calculated time-varying self-inductance of second-stage winding.

There are two accurate methods in literature to calculate the mutual inductance of two windings in the presence of armature. The first one is to fabricate the generator and measure inductance. This method is very time-consuming and expensive. Also, it is only possible to measure initial inductance experimentally because there is no device to measure mutual inductance during the generator operation. The second method is numerical simulation, such as electromagnetic field (EF) solver. In our model, the first-stage winding is fed by a current as the input of the four-terminal device. The second-stage winding is considered to be open-circuit and the induced voltage across its terminals is calculated using FEM. Finally, the mutual inductance is calculated using (5). Figure 5 shows time-varying mutual inductance of Cascaded-HFCG calculated by FEM.

In [14], a simple method is proposed to calculate the resistance for each winding of HFCG,

$$R(t)=R_{dc}(t)\times K_T \times K_{skin} \times K_{proximity}. \tag{10}$$

In this equation, $R_{dc}(t)$ is the DC resistance of winding, K_T is the temperature correction of conductivity, K_{skin} is correction for skin effect, and $K_{proximity}$ is correction for proximity effect. In our FEM model, a known current (a simple current source of 1A) is connected in series to each winding and electrical voltage between its two terminals is calculated using FEM. The DC resistance of the windings is equal to the electrical voltage between terminals over the applied current (in this case, 1A). The equation for the calculation of these corrections is described in [14].

IV. ANALYTICAL SOLUTION

In this section, an analytical analysis is performed to describe an approach to increase the load current of Cascaded-HFCG and decrease the rise-time of load current. The results are validated by simulation in the next section. For simplification, ohmic resistances of windings and armature are assumed to be negligible. Suppose that at the starting of generator operation, initial flux $\Phi(0)$ is introduced to first-stage winding by initial energy supply. For time interval $(0, t_1)$, where t_1 is crowbar time of the second stage, flux equation for the left loop of Fig. 2 can be written as:

$$\Phi(0)=(L_p+L_{g1}(0))I_{g1}(0).$$
$$\Phi(t)=(L_p+L_{g1}(t))I_{g1}(t)=\Phi(0). \tag{11}$$

At the end of the flux compression procedure in the first stage, self-inductance of first-stage winding vanishes ($L_{g1}(t_1) \to 0$). Thus, (11) changes as follow:

$$\Phi(t_1)=L_pI_{g1}(t_1)=\Phi(0). \tag{12}$$

After the closure of switch S at the moment t_1, the following system of flux equations is valid for two loops of Fig. 2:

$$L_pI_{g1}(t)+M(t)I_{g2}(t)=L_pI_{g1}(t_1), \tag{13}$$

$$(L_{g2}(t)+L_l)I_{g2}(t)+M(t)I_{g1}(t)=M(t_1)I_{g1}(t_1). \tag{14}$$

The right term in (14) is magnetic flux trapped by second stage due to mutual inductance between the windings. Solving (13) and (14) using (12), we can find the current of second stage of the generator:

$$I_{g2}(t)=\Phi(0)\frac{\frac{1}{L_p}\left[M(t_1)-M(t)\right]}{L_l+L_{g2}(t)\left(1-\frac{M^2(t)}{L_pL_{g2}(t)}\right)}. \tag{15}$$

At the end of the generator operation, the value of $L_{g2}(t)$ and $M(t)$ tend to zero, and the (15) changes as follows:

$$I_{g2}(t_{end})=\Phi(0)\frac{\frac{1}{L_p}M(t_1)}{L_l} = \Phi(0)\frac{M(t_1)}{L_pL_l}. \tag{16}$$

It can be concluded from (16) that the final value of load current depends on three factors. The impact of $\Phi(0)$ and $M(t_1)$ on load current is considered in many existing articles [9]. The third effective factor on load current is the inductance of primary winding of dynamic transformer (L_P). It is obvious that smaller L_P results higher load current. According to the design criteria's, and to maximize the flux trapped by dynamic transformer, L_P should not have very small initial value. If inductance of L_P decreases after the crowbar of second stage operation and simultaneously with armature expansion, the load current increases consequently. In a conventional Cascaded-HFCG, inductance of L_P is approximately constant; however, a destructive structure using a very thin explosive substrate located over or under the L_P can sweep out turns of L_P and cause to inductance of L_P to decrease ($L_P \to 0$) [13].

As previously mentioned, the current of the first stage winding after second stage crowbar causes a decrease in the efficiency of Cascaded-HFCG and consequently decreases load current. To overcome this problem, we propose adding a gradually incremental resistance in-series with L_P. The advantage of added resistance is explained analytically in the following. Let (3) be rearranged as:

$$[L_{g2}(t)+L_1]\frac{dI_{g2}(t)}{dt}+[R_{g2}(t)+R_1+\alpha_2\frac{dL_{g2}(t)}{dt}]I_{g2}(t)$$

$$=-M(t)\frac{dI_{g1}(t)}{dt}-I_{g1}(t)\frac{dM(t)}{dt}. \quad (17)$$

In (17), $I_{g1}(t)$ has a positive sign and $dM(t)/dt$ is negative during the generator operation; thus, the term $-I_{g1}(t)(dM(t)/dt)$ (shown as term A for convenience) is a positive quantity for the whole duration of generator operation. In return, $-M(t)(dI_{g1}(t)/dt)$ (term B) can be considered in two cases as follows:

    a)   In conventional Cascaded-HFCG (with no added series resistance), $I_{g1}(t)$ increases for the whole duration of generator operation, so $dI_{g1}(t)/dt$ has positive sign. On the other hand, $M(t)$ is positive too, so the sign of term B becomes negative. In this condition, the right side of (13) is equal to A-B.

    b)   Adding series resistance with L_p cause current to become descending and $dI_{g1}(t)/dt$ gets negative sign in this case, so the sign of term B becomes positive and the right side of (17) is equal to A+B.

It is obvious that for the case (b), the right side of (17) has a greater value than the case (a), due to which load current becomes greater.

Another advantage of added incremental resistance is the decreasing in rise-time of load current. Ohmic resistance of load and second stage can be negligible, so (17) can be written as:

$$\frac{dI_{g2}(t)}{dt}=\frac{-M(t)\frac{dI_{g1}(t)}{dt}-I_{g1}(t)\frac{dM(t)}{dt}-I_{g2}(t)\frac{dL_{g2}(t)}{dt}}{L_{g2}(t)+L_1}. \quad (18)$$

With the same analysis as before, if $dI_{g1}(t)/dt$ is a negative quantity, the numerator of (18) becomes larger and this means smaller rise-time of current. This is one of the goals of the optimization of Cascaded-HFCG.

V. SIMULATION RESULTS AND DISSCUSION

As previously mentioned, L_p has a great impact on generator efficiency in Cascaded-HFCGs because of its participation in energy transfer to second stage winding and load. The (16) shows that if each turn of L_p is wiped out simultaneously with armature operation and second stage winding, the load current increases. On the other hand, coupling between L_p and second stage winding decreases gradually; thus, the returned energy to L_p decreases, which can increase the generator efficiency. The self-Inductance profile of first stage winding for the case of time varying L_p which calculated using FEM is shown in Fig. 6.
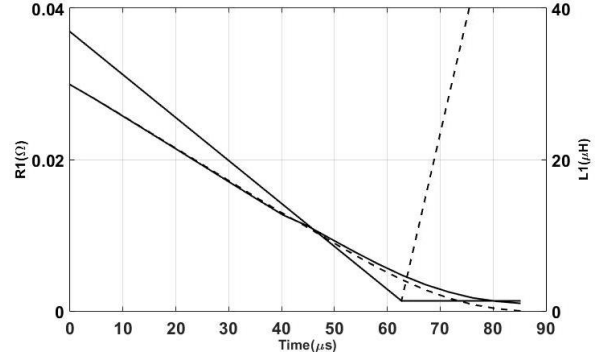
Fig. 6. Self-inductance and resistance profile of first-stage winding; (solid line) conventional generator; (dashed line) generator with added resistance and time-varying L_P.

The procedure of the inductance calculation for this case, is similar to previously described in Section III. The only difference is that L_p must be time varying and burns out after generator operation. As we can see, self-inductance tends to zero at the end of generator operation while it reaches a non-zero value for conventional generator.

Since the first stage current passes a return conductor and does not get to load, its continuation causes more energy loss and decreases generator efficiency; therefore, this current should be interrupted after starting second stage operation. Sudden interruption of current may cause electrical break down in generator insulations [13]. It may be better to gradually decrease current of L_p using an incremental resistance in-series with that. In this paper a resistance increasing linearly from zero to 50 $m\Omega$ is added in-series with L_p. It is described how we can increase the resistance practically at the end of this section. Figure 6 shows the resistance profile of the first stage winding in the case of added resistance in comparison with conventional Cascaded-HFCG.

The equivalent electrical circuit of Cascaded-HFCG changes as Fig. 13 considering the proposed approach.
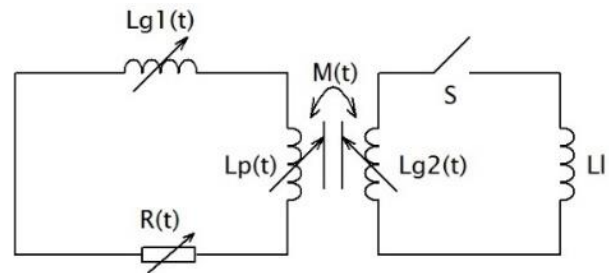
Fig. 7. Electrical circuit of cascaded-HFCG considering added resistance and dynamic L_p.

In order to validate the theoretical analysis performed in the previous section, a computer code is programmed based on the model demonstrated in Section II and electrical equivalent circuit of Fig. 7. A brief description of the modeled Cascaded-HFCG is needed here. The first stage winding is a single-pitch winding composed of 42 turns and has 300 mm length. Primary winding of dynamic transformer has 4 turns and 120 mm length. The inner diameter of first stage winding is 115 mm and the aluminum armature placed inside winding has an outer diameter of 50 mm. Armature wall thickness is 3.8 mm. The second stage winding has 30 turns and 120 mm length, which is located under first stage winding and ends at the same location as the ending of primary winding of dynamic transformer. The initial current of first stage winding is supplied by a 6 μF energy storage capacitor charged to about 20 KV. The load inductance is 25 nH. Detonation velocity is 6400 m/s.

Figure 8 shows the simulation results obtained from computer code for modeled Cascaded-HFCG. As we can see, current of first stage reaches a maximum value about 400 KA with rise time of current close to 65 μs, whereas maximum value of load current is 200 KA with rise time of current smaller than 15 μs for conventional generator. It is obvious that after starting second stage operation (about 50 μs) the current of first stage rises sharply and reaches an extremely high value. The reason for this excessive current is the high mutual inductance between the two windings and the energy returned to L_p, as previously discussed in detail.
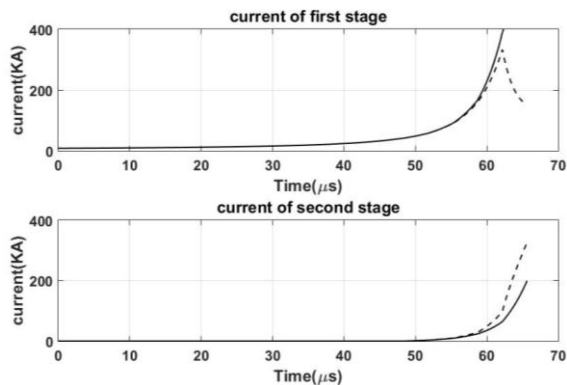
Fig. 8. Simulation results of conventional generator (solid line) and generator with time-varying L_P and incremental resistance (dashed line).

The simulation of the generator using the proposed method is done using self-inductance profile and resistance profile of first-stage winding, as demonstrated in Fig. 8. It can be seen that, after adding the resistance to the circuit, current of first stage follows a decreasing trend and causes an increase in load current. The maximum load current is 300 KA-i.e. 100 KA greater

than previous case. Current of first stage is limited to 300 KA due to the added resistance in-series with first stage winding. On the other hand, because of destructive behavior of L_p in this case and minimization of returned energy, the generator efficiency becomes greater. It is obvious that there is a considerable improvement in the di/dt and the rise time of the load current.

As we know, internal voltage in FCGs could reach about hundred kilovolts depending on some factors such as generator size, law of inductance change, and initial energy of system [17]. Actually, high internal voltages develop in HFCGs because of three reasons: high initial inductance of first stage winding, very small rise-time of current, and high value of inductance variation over time (dL/dt). For the proposed approach in this paper, dL/dt becomes greater than conventional Cascaded-HFCG because of the dynamic behavior of L_P, due to which the internal voltage becomes greater. Figure 9 shows internal voltage of the analyzed generator for two cases. The maximum value of internal voltage is 55 KV, which is much smaller than the critical value (critical value of internal voltage is 150 KV for HFCG [2]).
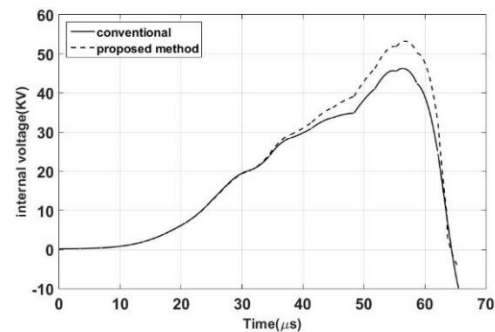
Fig. 9. Internal voltage for conventional generator (continued line) and proposed method (dashed line).

As for feasibility of the above behavior of incremental resistance and time varying L_P, it's better to describe the operation of a simple Exploded Opening Switch (EOS) first. The scheme of the device where current carrying foil is broken at its casting onto a ribbed dielectric barrier using high explosive (called EOS in literature) is shown in Fig. 10.
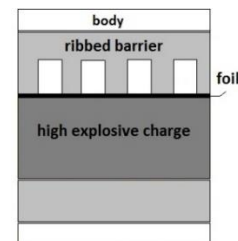
Fig. 10. Cross-section of exploded opening switch.

In the above described EOS, when the current carrying path is cut off by a ribbed barrier under the pressure of explosion, the current drops to zero sharply and a voltage surge is produced in the windings [12]. It may be better to find a way to increase the resistance slowly and simultaneous with armature expansion to prevent voltage surge formation in generator. In the following an approach is proposed to how we can increase the resistance in-series with first stage winding of Cascaded-HFCG gradually.

Fig. 11. Hollow cylinder conductor.

As we know, if a potential difference is applied to the ends of a hollow cylinder, electrical current can flow through its side surface azimuthally (Fig. 11). In this case, the cross-sectional area is $A = \pi(b^2 - a^2)$, thus the resistance is calculated from (19):

$$R = \rho \frac{L}{A} = \frac{\rho L}{\pi\left(b^2 - a^2\right)}, \qquad (19)$$

From (19), the resistance of the cylinder is proportional to the length of conductor (L). If the cylinder is cut from one end helically, the length of the current carrying path increases, which causes an increase in resistance (Fig. 12).

Fig. 12. Cylindrical conductor which is cut helically.

In order to practical implement of the above-mentioned idea, we can consider a structure like that shown in Fig. 13.
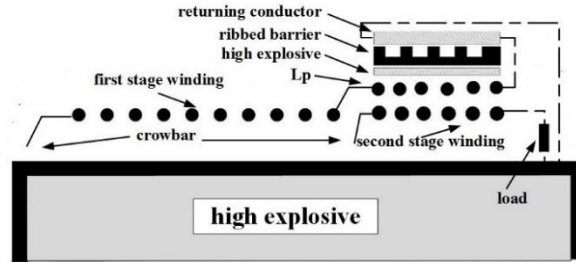
Fig. 13. Cascaded-HFCG with incremental resistance and time-varying L_P.

As we can see, a very thin hollow cylinder which is located over the L_P winding and coaxial with it, is considered as the returning conductor. The returning conductor is connected to L_p winding from one hand and to armature from the other hand. A ribbed barrier with helical grooves is located under the returning conductor which is faced to cylinder. The ribbed barrier is placed on explosive substrate. Detonation in substrate is initiated by an impact from expanding armature. The detonation propagates along cylinder and barrier, so pushed the grooves on the cylinder. Under the pressure of the grooves, the cylinder is cut in the form of helical and cause to an increase in the length of current path. Figure 14 shows a cross sectional representation of the ribbed barrier with helical grooves which can be used for our purpose. The ribbed barrier can be located over the cylindrical conductor too. In this case, the explosive charge should be located inside the cylindrical conductor. The mechanism of this device is similar to the EOS presented in Fig. 10.
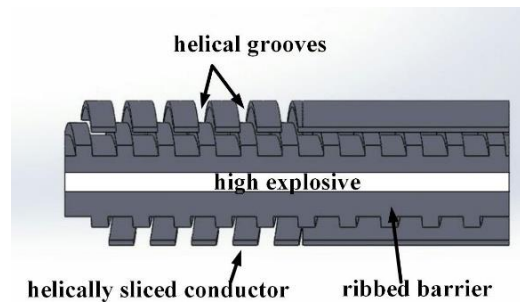
Fig. 14. Cross section of the ribbed barrier with helical grooves.

VI. CONCLUSION

Based on an analytical analysis, a new approach is proposed to improve the performance of Cascaded-HFCG. According to the proposed approach, each turn of the primary winding of the dynamic transformer should be wiped out simultaneously with armature expansion. This causes the primary winding to decouple from the secondary winding, which minimizes energy returning to the primary winding. On the other hand, a

gradually incremental resistance should be added in-series with the primary winding of the dynamic transformer. Added resistance restricts current increasing in primary winding, which causes lower energy loss, greater load current, and shorter pulse width of current. A quick numerical model is used to validate the performance of the proposed approach. Self-inductance and mutual inductance of the winding are calculated using FEM and compared to the results obtained by the 2-D filamentary method. FEM is an accurate and very fast method to calculate time-varying inductances in HFCGs.

REFERENCES

[1] L. L. Altgilbers, M. D. Brown, I. Grishnaev, B. M. Novac, I. R. Smith, I. Tkach, and Y. Tkach, *Magnetocumulative Generators*, Springer-Verlag, New York, 1999.

[2] A. A. Neuber (Editor), *Explosivley Driven Pulsed Power, Helical Magnetic Flux Compression Generators*, Springer-Verlag, Berlin, 2005.

[3] R. S. Caird and C. M. Fowler, "Conceptual design for a short-pulse explosive-driven generator," *Proc. 4th Megagauss Magnetic Field Generation and Pulsed Power Applications*, pp. 425, 1986.

[4] B. L. Freeman, L. L. Altgilbers, A. D. Luginbill, and J. C. Rock, "Development of small, tapered stator helical magnetic flux compression generators," *Electromagnetic Phenomena*, vol. 3, no. 3 (11), 2003.

[5] V. K. Chernyshev, G. S. Volkov, V. A. Ivanov, and V. V. Vakharushev, "Study of basic regularities of formation of multi-MA-current pulses with short risetime by EMG circuit interruption," in *Megagauss Physics and Technology*, pp. 663-675, Boston, 1980.

[6] P. V. Duday, A. A. Zimenkov, V. A. Ivanov, A. I. Kraev, S. V. Pak, A. N. Skobelev, and A. Y. Fevralev, "Method of generating a mega-ampere current pulse to accelerate a liner by a magnetic field," *J. Appl. Mech. Tech. Phys.*, vol. 56, no. 1, pp. 103-107, 2015.

[7] S. D. Gilev and V. S. Prokopiev, "Generation of electromagnetic energy in a magnetic cumulation generator with the use of inductively coupled circuits with a variable coupling coefficient," *J. Appl. Mech. Tech. Phys.*, vol. 58, no. 4, pp. 571-579, 2017.

[8] D. Q. Chen, "Research on Dynamic-Cascaded Helical Explosively-Driven Magnetic Flux Compression Generators," *Ph.D. Dissertation*, Changsha, P. R. China, 2015.

[9] A. Young, A. Neuber, and M. Kristiansen, "Design consideration for flux-trapping helical flux compression generator energized by capacitive discharge," *Pulsed Power Conference (PPC)*, pp. 527-531, Chicago, 2011.

[10] A. Young, A. Neuber, and M. Kristiansen, "Modeling and simulation of simple flux-trapping FCGs utilizing PSpice software," *IEEE Trans. Plasma Sci.*, vol. 38, no. 8, Aug. 2010.

[11] Y. Wang, J. Zhang, D. Chen, S. Cao, and D. Li, "Fast modeling of flux trapping cascaded explosively driven magnetic flux compression generators," *Rev. Sci. Instrum.*, 84, 014703, 2013.

[12] A. V. Shurupov, V. E. Fortov, A. V. Koslov, A. A. Leont'ev, N. P. Shurupova, V. E. Zavalova, S. V. Dudin, V. B. Mintsev, and A. E. Ushnurtsev, "Cascade explosive magnetic generator of rapidly increasing current pulses," in *14th International Conference on Megagauss Magnetic Field Generation and Related Topics*, pp. 1-5, 2012.

[13] A. A. Bazanov, "Helical magnetocumulative generators with magnetic flux amplification: comparative advantages of amplification schemes and the operational efficiency of generators with dynamic transformation," *Tech. Phys.*, vol. 56, no. 9, pp. 1339-1344, 2011.

[14] B. M. Novac and I. R. Smith, "A zero-dimensional computer code for helical flux-compression generators," *Electromagnetic Phenomena*, vol. 3, no. 4, 2003.

[15] B. M. Novac, I. R. Smith, M. C. Enache, and H. R. Stewardson, "2D modeling of inductively coupled helical flux-compression generators - FLUXAR systems," *Laser Part. Beams*, vol. 15, no. 3, pp. 397-412, 1997.

[16] M. H. Khanzade, Y. Alinejad-Beromib, and A. Shoulaie, "Calculation of time-varying equivalent inductance and resistance of helical flux compression generators using the 2D filamentary method and dynamic matrix concept in the frequency domain," *Chin. Phys. B*, vol. 19, no. 1, 2010.

[17] V. A. Demidov, "Problems of creation of high-efficient magnetocumulative generators electric strength of helical magnetocumulative generators," *IEEE Trans. Plasma Sci.*, vol. 38, no. 8, pp. 1773-1779, 2010.

A Novel Chebyshev Series Fed Linear Array with High Gain and Low Sidelobe Level for WLAN Outdoor Systems

Tang The Toan [1], Nguyen Minh Tran [2], and Truong Vu Bang Giang [3]

[1] University of Hai Duong, Haiduong, 170000, Vietnam
toantang@uhd.edu.vn

[2] Sungkyunkwan University, Suwon, 16418, KOREA
minhtran.uet@gmail.com

[3] Vietnam National University, Hanoi, 100000, Vietnam
giangtvb@vnu.edu.vn

Abstract ─ In this paper, we propose a novel linear microstrip array antenna with high gain and low sidelobe level (SLL) for outdoor WLAN applications. The array antenna includes of two main parts: a linear array and a reflector. Specifically, the array is linearly constructed with 10 elements; those are placed on Rogers RT/Duroid 5870^{tm} substrate with the dimensions of $422 \times 100 \times 10.15$ mm^3. Furthermore, to acquire the SLL reduction, a series fed network is designed to have the output signals being proportional to the Chebyshev distributions (with the preset SLL of -30 dB). On the optimization of the single element, Yagi antenna theory is applied by adding two directors above each element to increase its directivity. Additionally, we put a reflector at the back side of the proposed array. Simulation results indicate that the array operates well at 5.5 GHz with the high gain of 17.5 dBi and a low SLL of -26 dB. A prototype has been fabricated and measured to validate the simulation results. Good agreement between simulation and measurement data have been obtained. This proves that the presented array antenna can be a good candidate for WLAN applications.

Index Terms ─ Fan-beam, linear array, low sidelobe.

I. INTRODUCTION

Printed antenna arrays are usually used in telecommunication systems such as point to point and point to multipoint, in radar microwave, and millimeter systems. However, combining antenna elements in an array may lead to larger in size and the side lobe level (SLL) will be high, which is the main drawback of such kind of antenna. The high SLL in the array may be caused by: tolerances in fabrication, mutual coupling between radiating elements, limitations in feasibility of feeding network realization, surface wave effect as well as parasitic radiation from a feeding network.

Several techniques to reduce the SLL of the array have been investigated and proposed in the literature [1-3]. In the digital beamforming (smart antennas) or radar systems, Binomial, Chebyshev and Taylor distributions have been commonly applied in power excitation of the array to get low SLL. In the ordinary arrays, the same thing can be achieved by designing the feeding network which has output power corresponding to these distributions. Among several types of array feeding structures, there are two common types of feeding network for the array: corporate fed and series fed. The discontinuities, bends and power dividers in the corporate fed array may cause spurious radiation that raises the SLL to high levels, especially in large arrays. In some cases, a single high-directive element is used to avoid the spurious effect of the feeding network [4, 5]. In opposite with the corporate one, the series fed, which employs shorter and fewer transmission lines, leads to an array antenna with smaller size, lower attenuation loss and spurious radiation from the feed lines.

Recently, several attempts have been done to suppress the SLL in the printed array antennas [6-16]. A novel aperture coupled microstrip antenna array has been proposed in [8]. The antenna consists of a total 100 microstrip elements that are arranged in two rows of 50 elements, with element spacing of 0.51 free-space wavelength. A SLL of -20.9 dB has been obtained. However, due to using a large number of elements, the size of the whole array is considerably large while the SLL is not low. In [13], Saputra et al. have introduced a sidelobe suppression method for X-band antenna array by designing a novel feeding network with Chebyshev distribution. The array operates at 9.3 GHz and can give -19.4 dB SLL. As the complexity of the feeding network and the limited number of elements, the gain is only 12.3 dBi and the SLL is still high. Another 6 elements array antenna with linear series fed has been presented in [12]. A wideband of 6.5 % has been obtained, but the SLL

and the gain acquired are still not good, which are -20 dB and 14.2 dBi, respectively. Lower SLLs have been tackled and obtained in [9, 14]. By using the optimized distribution coefficients through differential evolution algorithm, a wideband and lower SLL have been achieved in slot antenna with series fed network in [9]. The antenna includes of 10 elements which are arranged in a series feeding network. The SLL and half power beam-width (HPBW) are -25.3 dB and 8.4⁰, respectively. However, the gain achieved is only 14.5 dBi. In addition, the authors in [14] have proposed a low SLL and wideband series fed dielectric resonator antenna (DRA) array. The proposal can get a very low SLL of -30 dB and high gain of 19 dBi. Nevertheless, the large number of elements (up to 22 dielectric resonators have been used) result in a large size. Besides, the fabrication could be complicated as complex design techniques have been used. Similarly, two other DRA arrays have been introduced in [11, 16]. The array [16] works at 60 GHz, while the counterpart operates at 7.4 GHz. The SLL are -27.7 dB and -23 dB, respectively. Bayderkhani and Hassani have presented two linear series fed Yagi-like array samples in [10, 15]. The arrays have 22 similar Yagi line elements, which can provide the gain of 15.3 dBi and the SLL of about -27 dB. In spite of using a huge number of single elements and the Chebyshev distribution with the SLL preset to -35 dB, the gain and the SLL is not noticeably good. Hassani and his other colleagues have continuously proposed two other low SLL arrays [6, 7]. The sample in [7] has the SLL of 20 dB, while the lower SLL (-33.2 dB) has been obtained in [6]. However, the gain in [7] is remarkably high with 18.2 dB compared to just -15.9 dBi in [6].

In this paper, a high gain, low SLL, microstrip linear antenna array will be introduced. The design procedure from single element, feeding network and the complete array will be specifically demonstrated. The array consists of 10 single elements, which are double-sided printed dipoles (DSPD). The low SLL is obtained by designing the series fed network with the output power corresponding to the Chebyshev coefficients (preset SLL of -30 dB). As can be seen from the simulation results, the antenna operates well at 5.5 GHz with the bandwidth of 212 MHz. Moreover, a high gain of 17.5 dBi has also been acquired, while the SLL is low at -26 dB. Fabrication and measurement have been done, and simulated results have been validated with the corresponding measured data. Good agreements between simulation and measurement have been shown.

II. ANTENNA DESIGN AND STRUCTURE

A. Design of the single element

To build an array, a single element should be first selected and designed. In this work, to guarantee the requirements in both size and performance, DSPD has been used as the single element of the array. In authors'

previous work [17], we have presented and analyzed this kind of antenna in details. Figure 1 gives the proposed DSDP used as single elements in the array construction. The length of the feed line and the patch can be given by approximately a quarter of the wavelength ($\lambda_g/4 = c/4f_0\sqrt{\varepsilon_r}$). The width of the patch can be calculated by equation (1):

$$Z_a \approx 90 \frac{\varepsilon_r^2}{\varepsilon_r - 1}\left(\frac{L}{W}\right)^2, \qquad (1)$$

where, $\qquad Z_a = \frac{Z_0^2}{Z_{in}}, Z_{in} = 50 \ \Omega$

$$Z_{0(parallelstrip)} = 2Z_{0(microstrip)}\left(h = \frac{d}{2}\right).$$

In this paper, the DSDP is placed on the Roger RT/Duroid 5870tm (thickness of 1.575 mm and ε_r = 2.33), and has been adjusted to work at 5.5 GHz with the impedance $Z_d = 100\Omega$ at the center frequency. The final dimensions of the single element are given in Table 1.

The simulated S_{11} and radiation pattern of the DSDP are shown in Fig. 2 and Fig. 3, respectively. It is clear that the DSDP can work well at 5.5 GHz with the gain of 5.27 dBi. This DSDP will be used as the single element of the array in this work.

Table 1: The parameters of the single element

Parameters	Value (mm)	Parameters	Value (mm)
W_{e1}	0.8	L_{e1}	8.5
W_{e2}	9.1	L_{e2}	6.0
W_{e3}	10.0	a	2.5
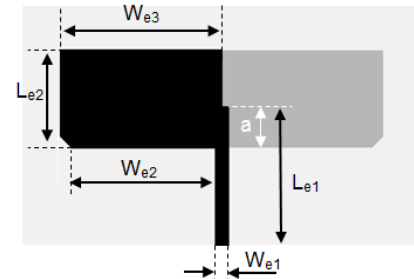
Fig. 1. The proposed single element.
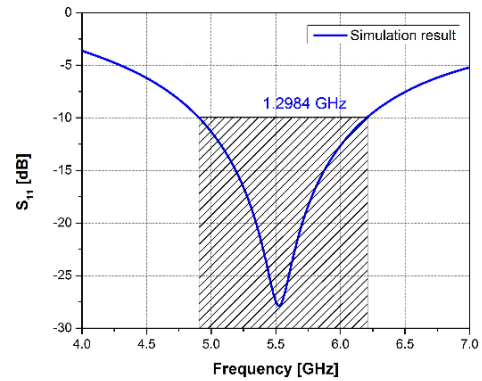
Fig. 2. Simulated S_{11} of the DSPD.
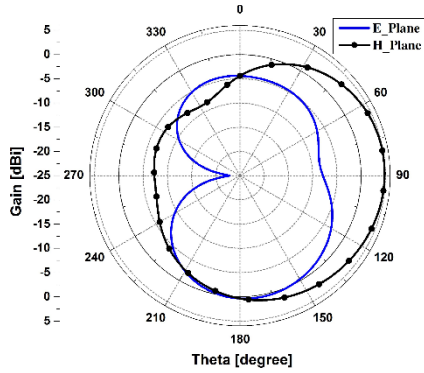
Fig. 3. Radiation pattern of the DSPD.

B. Design of the feeding network

This section will present the procedure to design the feeding network using in the array. The series fed network for the linear array is designed to match with the single element in the previous section to form a 10×1 array antenna. The Chebyshev distribution with preset SLL of -30 dB has been utilized as the output coefficients' target. In order to obtain the Chebyshev distribution in the series fed network, different shunt stubs have been added to the feed line so that the amount of signal flowing out each output port can be easily controlled. The operation and the equivalent circuit of the stub in the antenna are given in the Fig. 4. According to [18], the equivalent shunt capacitor of shunt stub can be calculated by:

$$Y_{in} = jY_c \tan\left(\frac{2\pi}{\lambda_g}l\right) \approx jY_c\left(\frac{2\pi}{\lambda_g}l\right) = j\omega\left(\frac{Y_c l}{v_p}\right), \quad (2)$$

where Y_c is the equivalent admittance of the stub, l is the length of the stub v_p is the phase velocity, λ_g is the wavelength in the substrate.
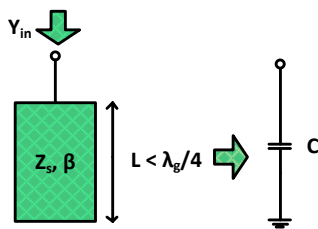
Fig. 4. The equivalent capacitor of shunt stub.

As the symmetrical properties of Chebyshev distribution, the proposed feeding network has a mirror like structure. Indeed, the feed has a main line which is fed by the 50Ω line at the center. To form the symmetrical geometry, the same feeding line and shunt stubs are equally distributed on each side of the central line. These stubs serve as shunt capacitors and play as impedance matching to control the output amplitude excited at each element. Due to the effect of shunt stubs in the impedance matching point, the S parameters at each port related to

the input port will be easily handled. It means that the energy flowing out each output port can be controlled [19]. The feed model at one side and the equivalent circuit are shown Fig. 5.

(a) The feed model with shunt stubs

(b) The equivalent circuit
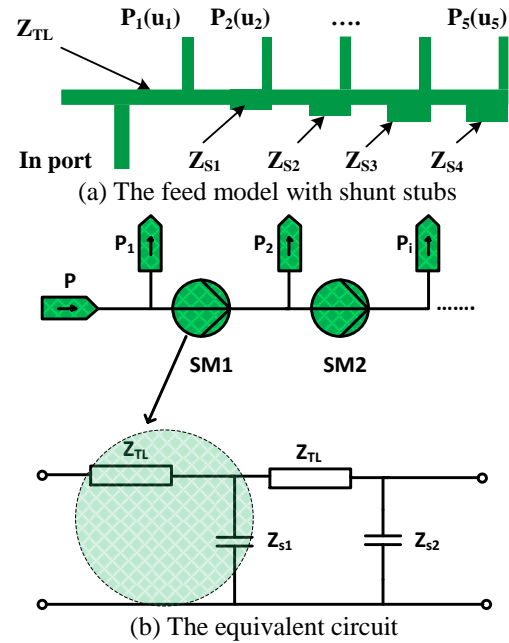
Fig. 5. The series fed network and its equivalent circuit.

In this work, the feeding network has been designed for 10×1 antenna array with the Chebyshev amplitudes corresponding to SLL of -30 dB. The Chebyshev amplitudes for 10 elements are given in the Table 2.

Table 2: Chebyshev amplitude weights for 10×1 linear array (SLL = -30 dB)

Element No.	u_1	u_2	u_3	u_4	u_5
Amplitude	1	0.8780	0.6692	0.43	0.2575
Characteristic Impedances	Z_{TL}	Z_{s1}	Z_{s2}	Z_{s3}	Z_{s4}
Element No.	u_6	u_7	u_8	u_8	u_{10}
Amplitude	1	0.8780	0.6692	0.43	0.2575
Characteristic Impedances	Z_{TL}	Z_{s5}	Z_{s6}	Z_{s6}	Z_{s8}

The impedance of the shunt stubs (Z_{s1}, Z_{s2} ,…, Z_{s4}) can be determined using theory given in [20] as follow: $Z_{s1}/Z_{TL} = u_2/u_1 = 0.8780$; $Z_{s2}/Z_{TL} = u_3/u_1 = 0.6692$; $Z_{s3}/Z_{TL} = u_4/u_1 = 0.4300$; $Z_{s4}/Z_{TL} = u_5/u_1 = 0.2575$. For determining the value of impedances and the value of shunt stubs, the main line should be first selected. The different values of the main line have been simulated, and the results are given in Fig. 6. The wider bandwidth has been achieved with the main line impedance of 178Ω. Hence, the main line has been designed with the impedance of 178Ω. Eventually, these values of Z_{si} have been calculated as

given in Table 3.
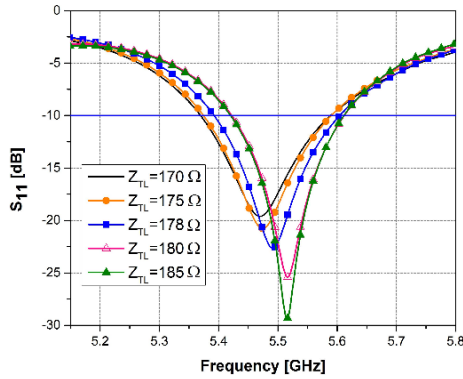
Fig. 6. The simulated reflection coefficient of different main line impedances.

Table 3: Characteristic impedances of the series fed network

Characteristic impedances	Z_{TL}	Z_{s1}	Z_{s2}	Z_{s3}	Z_{s4}
Value (Ω)	178	156.11	118.98	76.454	45.78
Characteristic impedances	Z_{TL}	Z_{s5}	Z_{s6}	Z_{s7}	Z_{s8}
Value (Ω)	178	156.11	118.98	76.454	45.78

Figure 7 shows the final series fed network of 10 elements designed on Roger RT/Duroid 5870tm substrate (the height of 1.575 mm and the permeability of 2.33) with the dimensions of 55×385×1.575 mm^3. Synthesized parameters of 10×1 series fed network is given in Table 4 [21].

Table 5 gives the simulated amplitude and phase data at each output port. It is clear that the simulated amplitude coefficients coincide with the Chebyshev distribution with small negligible differences. The normalized radiation pattern of simulated coefficients

from the feed and the corresponding one from theory have been presented in Fig. 8. This series fed network can be combined with single elements to construct a linear antenna array which has the SLL suppressed to -27 dB.

Table 4: Synthesized parameters of 10×1 series fed network

Parameters	Value (mm)	Parameters	Value (mm)
d	38.8	w_{s4}	7.00
l_s	3.75	W_1	2.00
w_{s1}	1.14	W_2	0.80
w_{s2}	3.30	g	7.20
w_{s3}	5.13		

Table 5: The simulated amplitudes and phases of the series fed network

Element No.	u_{1-6}	u_{2-7}	u_{3-8}	u_{4-9}	u_{5-10}
Amplitude	1.0000	0.9238	0.6726	0.4150	0.1863
Phase	-50.48^0	-53.67^0	-53.10^0	-55.75^0	-51.12^0
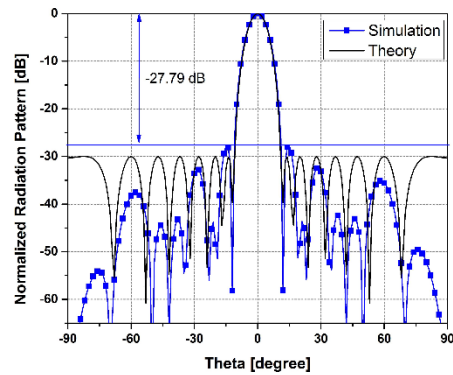
Fig. 8. Normalized radiation patterns with respect to the output power coefficient (solid line) and theoretical one (dotted line) [21].

Fig. 7. 10×1 series fed network [14].

C. Design of the array

The array structure is obtained by combining optimized single elements and the series fed network developed in the previous sections.

So as to increase the gain, two techniques are being applied in the design of the array. Firstly, as the inspiration of Yagi theory, directors are being added into the elements of the array [20]. Hence, according to the theory given in [20] that the directors in Yagi antenna should be around 0.4λ to 0.48λ, each single element has been integrated with three directors, which have the same size of 2.5×15 mm ($0.42\lambda_g \times0.07\lambda_g$), at both sides of the DSDP. The number of directors can be designed

larger subject to the trade off between gain and dimensions required in the array. The simulated results of the gain and the SLL with respect to the sample with and without directors will be specifically presented and discussed. Secondly, a reflector is being placed at the back of the main array with the distance of $g \approx \lambda_g/4$ (as shown in Fig. 9 (c)) so as to boost up the gain of the whole array. The overall size of the proposed array is $422\times100\times10.15$ mm^3 as given in Fig. 9.

The optimized array has been fabricated and measured in the laboratory as shown in the Fig. 10. In Section 3, the detailed results will be compared and discussed.
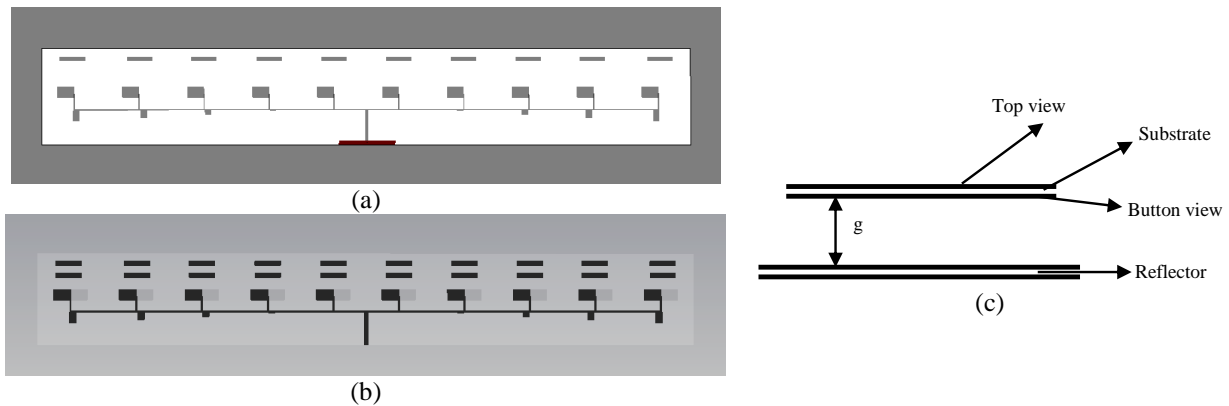
Fig. 9. Structure of the proposed array: (a) top view, (b) button view, and (c) side view.

Fig. 10. Fabricated antenna array.

III. RESULTS AND DISCUSSION

A. Simulation results

In this work, the element and array are simulated using the CST Studio Suite 2016 in the notebook computer with the configuration as given in Table 6. The total time required to completely run the simulation in this computer is nearly 10 minutes.

Figure 11 shows the simulated S_{11} of the array. The proposed antenna operates at 5.5 GHz with the bandwidth of 212 MHz at -10 dB of S_{11}. Though the single element can provide wide bandwidth (about 1.3 GHz bandwidth), the constructed array antenna can just operate at a part of the full bandwidth of the applications. This may result

from the effect of the feed or the mutual coupling between the elements when combined.

Table 6: Computer configuration

Brand Name	Lenovo - T440S
Max Screen Resolution	1600 x 900 pixels
Processor	2.1 GHz Intel Core i7
RAM	8 GB DDR3L SDRAM
Memory Speed	1600 MHz
Hard Drive	256 GB Serial ATA-600
Graphics Coprocessor	Intel HD Graphics 4400
Operating System	Windows 10
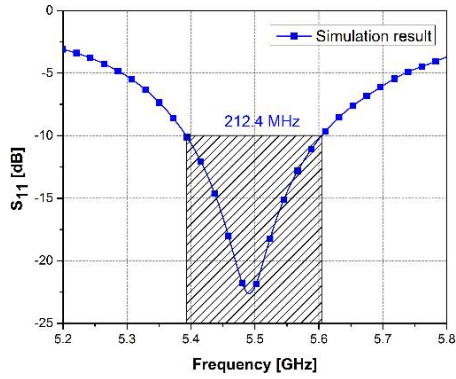
Fig. 11. Simulated S_{11} of the array [15].

The radiation pattern, gain and SLL over the operating frequency have also been demonstrated in Figs. 11 and 12. As can be seen from Fig. 12, a narrow HPBW of 10.4^0 is acquired over 5.4 GHz - 5.65 GHz band.

The stable gain at about 17 dBi, and the SLL, which is lower than -20 dB, are obtained over the bandwidth as given in Fig. 13. At 5.5 GHz, the gain of 17.5 dBi and low SLL of -26.0 dB have been acquired. In comparison with those from theory and the feeding in [21], the SLL of the array in this paper is 1.79 dB higher (see Fig. 8). It proves the capability of applying the series fed network to simultaneously obtain high gain and low SLL arrays.
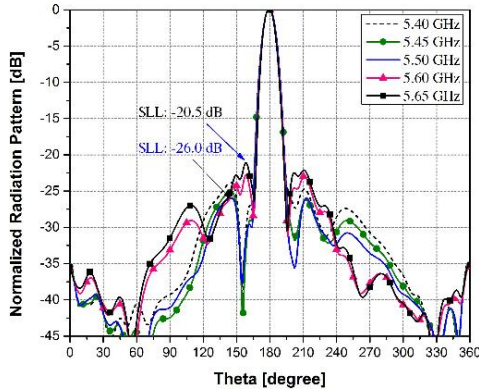
Fig. 12. The radiation pattern over different frequencies.

It is noticable that the SLL and gain in the case with added directors are better compared to that of the array without directors. Therefore, the benefits of high gain in Yagi antenna has been successfully leveraged and

employed in this proposal, and approximate 1 dB gain higher is achieved by using 3 additional directors.
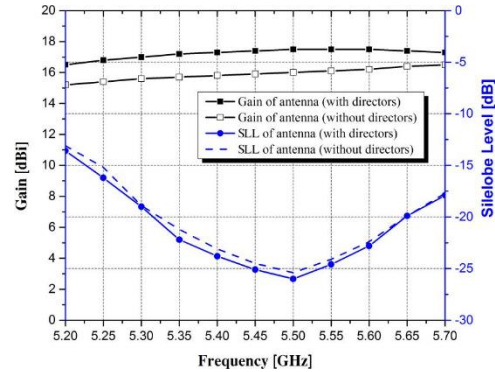
Fig. 13. The gain and SLL over the operating bandwidth.

The gain over operating frequency band of the sample with and without the reflector is shown in Fig. 14. The array with the reflector definitely has higher gain (about 3 dB) compared to the one having no reflector. Hence, the use of the reflector has a great advantage in terms of gain enhancing.
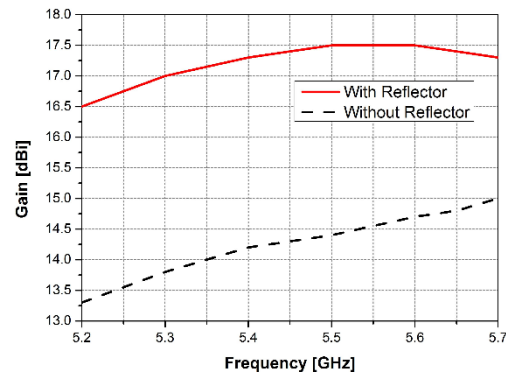
Fig. 14. Comparison of gain between the array with and without reflector.

B. Experimental results

The measurement of the prototype has been done and the measured data has been compared to that of the simulation.

Figure 15 shows the simulated and measured return loss of the antenna. It can be seen that the operating frequency of the antenna is 5.5 GHz with the bandwidth (at S_{11} = -10 dB) of 212 MHz.
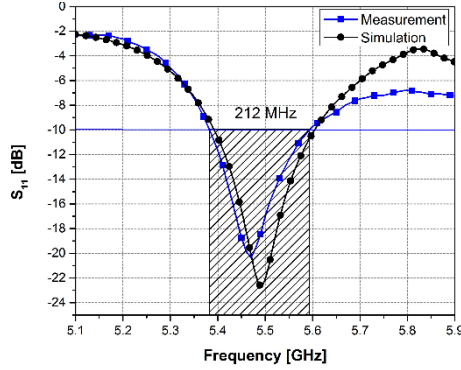
Fig. 15. The reflection coefficient of the array antenna.

The simulated and measured radiation patterns in E and H plane are also compared and presented in Fig. 16.

(a) H_plane

(b) E_plane
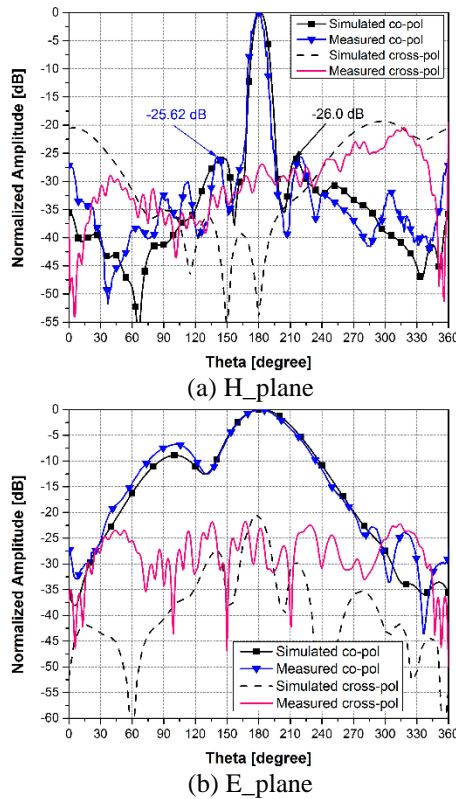
Fig. 16. Normalized radiation pattern of proposed array antenna at 5.5 GHz.

It is clear that simulated data have agreed well with measured ones. Indeed, the gain in simulation and measurement are 17.5 dBi and 17.1 dBi, respectively. Moreover, the low SLL in measurement has been also achieved with about -25.62 dBi compared to -26 dB from the simulation. The cross polarization in both simulation and measurement has also been given and they are both lower than -20 dB.

The results in this work have also been collated with the other works from the literature as shown in Table 7.

Table 7: The comparison between references and this work

References	[9]	[16]	[11]	[This Work]
Element no.	10×1	10×1	8×1	10×1
Size (λ)	6.01×1.1	---	---	7.7×1.83×0.19
Freq. (GHz)	9.0	60	7.54	5.5
Bandwidth (%)	1.3	36.1	31.9	3.9
Gain (dBi)	14.5	15.7	15.7	17.5
SLL (dB)	-25.3	-27.7	-23.1	-26.0
Cross-po. (dB)	-25.0	---	-30.0	-20.0

It can be seen that with the same number of elements, the proposed array has the gain of 17.5 dBi, which is higher than that of [9] with just 14.5 dBi and [16] with about 15.7 dBi. Moreover, the SLL in this work is 0.7 dBi lower than that in [9] but 1.7 dBi higher than that in [16]. In comparison with the work in [9], our array has better results in terms of both gain and SLL, but honestly the proposed array size is larger than that in [9] in term of wavelength.

IV. CONCLUSIONS

In this paper, a novel high gain and low sidelobe level linear microstrip antenna array for outdoor WLAN applications has been proposed. The design procedure from the single element to full array construction has been presented in details. In order to get low SLLs, Chebyshev weighting method has been deployed in the feeding network of the antenna. The Chebyshev excitation coefficients have been obtained in the feed by using the shunt stubs added at the feed line of each element. The simulated results show that the array can operate at 5.5 GHz with the bandwidth of 212 MHz and has a high gain of 17.5 dBi with the low SLL of about -26 dB. A prototype has also been fabricated and measured to validate the simulation results. It is clear from the comparison that simulated and measured data agree well with each other.
''

REFERENCES

[1] C. A. Balanis, "Antenna Synthesis and Continuous Sources," in *Antenna Theory Analysis and Design*, N. Jersey, Ed., John Wiley & Sons, Inc, pp. 385-421, 2016.

[2] D. G. Fang, "Design of Conventional and DBF Microstrip Antenna Arrays," in *Antenna Theory and Microstrip Antennas*, Ed: CRC Press, Taylor Francis Group, LLC, pp. 207-252, 2010.

[3] D. M. Pozar and B. Kaufman, "Design considerations for low sidelobe microstrip arrays," *EEE*

Transactions on Antennas and Propagation, vol. 38, pp. 1176-1185, 1990.

[4] J. M. J. W. Jayasinghe, J. Anguera, and D. N. Uduwawala, "Genetic algorithm optimization of a high-directivity microstrip patch antenna having a rectangular profile," *Radioengineering*, vol. 22, no. 3, pp. 700-707, Sep. 2013.

[5] J. Anguera, A. Andújar, S. Benavente, J. Jayasinghe, and S. Kahng, "High-directivity microstrip antenna with mandelbrot fractal boundary," *IET Microwaves, Antennas & Propagation*, vol. 12, pp. 569-575, 28 Mar. 2018.

[6] R. Bayderkhani and H. R. Hassani, "Wideband and low sidelobe slot antenna fed by series-fed printed array," *IEEE Transations on Antennas and Propagation*, vol. 58, no. 12, pp. 3898-3904, 2010.

[7] N. Bayat, H. R.Hassani, and S. M. A. Nezhad, "Sidelobe level reduction in microstrip patch antenna array," presented at the *2011 Loughborough Antennas & Propagation Conference*,Loughborough, UK, 2011.

[8] J. Xiao, G. Dong, and M. H. Zhu, "Novel aperture coupled microstrip antenna array with low cross-polarization, low sidelobe and backlobe," presented at the in *2004 4th International Conference on Microwave and Millimeter Wave Technology Proceedings*, 2004.

[9] J. Yin, Q. Wu, C. Yu, H. Wang, and W. Hong, "Low sidelobe level series-fed microstrip antenna array of unequal inter-element spacing," *IEEE Antennas and Wireless Propagation Letters*, vol. 16, pp. 1695-1698, 2017.

[10] R. Bayderkhani and H. R. Hassani, "Wideband and low sidelobe linear serises fed Yagi – like antenna array," *Progress In Electromagnetics Research B*, vol. 17, pp. 153-157, 2009.

[11] J. Lin, W. Shen, and K. Yang, "A low sidelobe and wideband series fed linear dielectric resonator antenna array," *IEEE Antennas and Wireless Propagation Letters*, vol. 16, pp. 513-516, 2017.

[12] C. Niu, J. She, and Z. Feng, "Design and simulation of linear series-fed low sidelobe microstrip antenna array," *in Proceedings of Asia-Pacific Microwave Conference*, 2007.

[13] Y. P. Saputra, F. Oktafiani, Y. Wahyu, and A. Munir, "Side lobe suppression for X-band array antenna using Dolph-Chebyshev power distribution," *in The 22nd Asia-Pacific Conference on Communications (APCC2016)*, 2016.

[14] M. R. Nikkhah, J. Rashed-Mohassel, and A. A. Kishk, "A low sidelobe and wideband series-fed dielectric resonator antenna array," presented at the in *The 2013 21st Iranian Conference on Electrical Engineering (ICEE)*, May 2013.

[15] R. Bayderkhani and H. R. Hassani, "Low sidelobe wideband series fed double dipole microstrip antenna array," *IEICE Electronics Express*, vol. 6, no. 20, pp. 1462-1468, Oct. 2009.

[16] W. Shen, J. Lin, and K. Yang, "Design of a V-band low sidelobe and wideband linear DRA array," presented at the in *2016 Progress in Electromagnetic Research Symposium (PIERS)*, Shanghai, China, 2016.

[17] T. T. Toan, N. M. Tran, and T. V. B. Giang, "A new approach to design and optimize double-sided printed dipole antennas," in *in The 2016 National Conference on Electronics, Communications, and Information Technology*, Hanoi, Vietnam, pp. 2/21-2/24, 2016.

[18] T. L. Wu, "Microware filter design," Ed. *Department of Electrical Engineering National Taiwan University*, 2014.

[19] T. T. Toan, N. M. Tran, and T. V. B. Giang, "A low sidelobe fan-beam series fed linear antenna array for IEEE 802.11ac outdoor applications," in *The 2017 International Conference on Advanced Technologies for Communications (ATC-2017)*, Quy Nhon, Vietnam, pp. 161-165, 2017.

[20] Y. Huang and K. Boyle, *Antennas From Theory to Practice*. John Wiley & Sons Ltd, 2008.

[21] T. T. Toan, N. M. Tran, and T. V. B. Giang, "Designing a feeding network of linear antenna arrays using Chebyshev distribution weights for a sidelobe level of -27 dB," in *Vietnam Japan Microwave 2017 Conference*, Hanoi, Vietnam, pp. 45-49, 2017.

Tang The Toan was born in 1976. He received his B.Sc. degree in Electronics and Physics, and M.Sc. degree in Electronics and Telecommunications from Hanoi National University of Education, Hanoi, VN, in 1998 and 2011, respectively. Currently, he is a Ph.D. student in the Faculty of Electronics and Telecommunications, University of Engineering and Technology, VNU.

His research interests are microstrip antennas design and analysis, electromagnetics and propagation, metamaterials.

Nguyen Minh Tran received the B.Sc. and M.Sc. in Electronics and Telecommunications Technology from the University of Engineering and Technology, VNU, Cau Giay, Hanoi, VN, in 2014 and 2016, respectively. He has served as a Research Assistant at the Laboratory

of Modeling and Simulation. He is currently pursuing his Ph.D. degree in the Department of Electrical and Computer Engineering, School of Electronics and Communications Engineering, Sungkyunkwan University, Suwon, Korea.

His research interests include of microstrip antennas analysis and design, RF circuits, wireless power transfer.

Truong Vu Bang Giang received the B.S. and M.S. degree from the VNU-University of Sciences, in 1994 and 1997, respectively, and the Dr.-Ing. (Ph.D.) degree in Electrical Engineering from the Hamburg-Hamburg University of Technology, Hamburg, Germany, in collaboration with the Institute of Communications and Navigation, German Aerospace Center, in 2006.

He is now the Deputy Director of Science and Technology Department of Vietnam National University, Hanoi and as the Secretary of the National Research Program for Sustainable Development of North-West Region of Vietnam.

He is a Member of IEEE MTTs and APS. He has served as the Steering Committee (Co-Chair), Organizing Committee (Chair and Co-Chairs) or Technical Committee of ATC, REV-ECIT, VJMW, VJISAP conferences in Vietnam; Scientific and Technical Committee, International Transaction Journal of Engineering, Management, & Applied Sciences & Technologies (ITJEMAST).

His current research interests include Microstrip Antennas for Mobile and Handheld Devices; Analysis and Design of Conformal Antennas; Digital Beamforming and Beamsteering for Smart Antennas; Metamaterial Antennas; Design of RF Devices and Systems.

A Novel Herringbone Circularly Polarized Quasi Lumped Antenna Array

Yazeed Qasaymeh [1], Khaled Issa [2], Abdullah Alahmadi [1], and Mohamadariff Othman [3]

[1] Department of Electrical Engineering
Majmmah University, Al-Majmmah, 11952, Kingdom Saudi Arabia
*y.qasaymeh@mu.edu.sa, a.alahmadi@mu.edu.sa

[2] KACST-TIC in Radio Frequency and Photonics for the e-Society (RFTONICS)
Electrical Engineering Department, King Saud University, Riyadh, Kingdom Saudi Arabia
kissa@ksu.edu.sa

[3]Department of Electrical Engineering, Faculty of Engineering
University of Malaya, Kuala Lumpur, 50603, Malaysia
mohamadariff@um.edu.my

Abstract — Herein, a series herringbone fed traveling wave quasi-lumped circularly polarized antenna array is presented. The proposed quasi-element antenna comprises a narrow strip inductor parallel to the interdigital capacitor. The inductor was placed at the center finger and shorted across the interdigital capacitor with pad capacitors connected at both ends of the structure. Circular polarization was achieved by feeding the quasi elements at the corners with a 90° phase difference along a travelling wave microstrip feed line. The proposed quasi-lumped element antenna has the potential to realize significant size reductions, and it will ultimately be lightweight, small volume, and inexpensive. The antenna characteristics of the array antenna, including return loss and radiation patterns, were characterized. The size of the antenna structure was 21 mm × 38 mm, allowing for potential use in wireless communication systems that use the 5 GHz ISM band.

Index Terms — Array, circularly polarization, gain, herring fed, quasi lumped, radiation pattern, return loss.

I. INTRODUCTION

In modern communication systems, circularly polarized (CP) antennas are favored over linearly polarized (LP) antennas owing to their flexibility in terms of steering angle between the transmitting and receiving antenna [1]. CP antennas are more suitable for several applications including mobile and fixed satellite systems, remote control, telemetry, wireless communication, and radar systems in which the multi-path fading, absorption, and reflectivity are major concerns [1–5].

Over the past two decades, researchers have developed several CP antennas designs that suffer from narrow axial ratio bandwidth for lower frequency ranges [1–6]. To enhance the CP radiation, different shapes of patches and slots were prepared, including L-shaped [3] and lightning-shaped slots [5], and the insertion of inverted and stepped L- or T-shaped strips was reported [6,7]. In [7–10], different phase feeding topologies featuring seven quarter-wave transformers in circular [3] and circular arc-shaped patterns [8]. An overall improvement of the CP array performance can be achieved using the sequential rotation phase feeding method. A sequential rotation feed network is typically designed using different power divider circuits. Furthermore, multi-band and single antenna topologies have been reported to enhance bandwidth [11–13].

To date, many feeding techniques have been reported for achieving improved CP properties in microstrip antenna arrays. For instance, series feed [14], parallel feed [15], and sequential rotation feed [16] techniques have been developed. Parallel and corporate feeds have advantages in terms of excitation networks for printed antenna arrays and exhibit design flexibility and facile formation of two-dimensional arrays [15]. However, these methods have some drawbacks during prototyping, including unbalanced pattern and mutual coupling effects between the elements and feed network. The series feed topology represents a more concise network because it requires shorter transmission lengths and less junctions, resulting in lower insertion loss. However, it experiences narrow bandwidth and inherent phase differences caused by the differences in feed line lengths [17].

The purpose of this article is to acquire a circular polarization and to reduce array size. The circular polarization produced will use the herringbone feeding technique and the quasi-lumped elements used to reduce array size.

Section 2.1 shows the configuration of a single radiating element. The array used for the herringbone feeding technique is presented in Section 2.2. In Section 3, the S11 and radiation pattern results are presented.

II. SINGLE ELEMENT ANTENNA GEOMETRY

By definition, lumped elements are much smaller than their respective wavelengths. Thus, microstrip shorts and stubs with physical lengths of less than a quarter-wavelength at the operating frequency are required for approximate microwave operation of lumped elements in microstrip structures and are referred to as quasi-lumped. A schematic of the quasi-lumped element resonator is shown in Fig. 1. Whilst, the equivalent lumped circuit is shown in Fig. 2. The proposed resonator antenna consists of a narrow straight strip inductor in parallel with an interdigital capacitor [18].

(a)

(b)
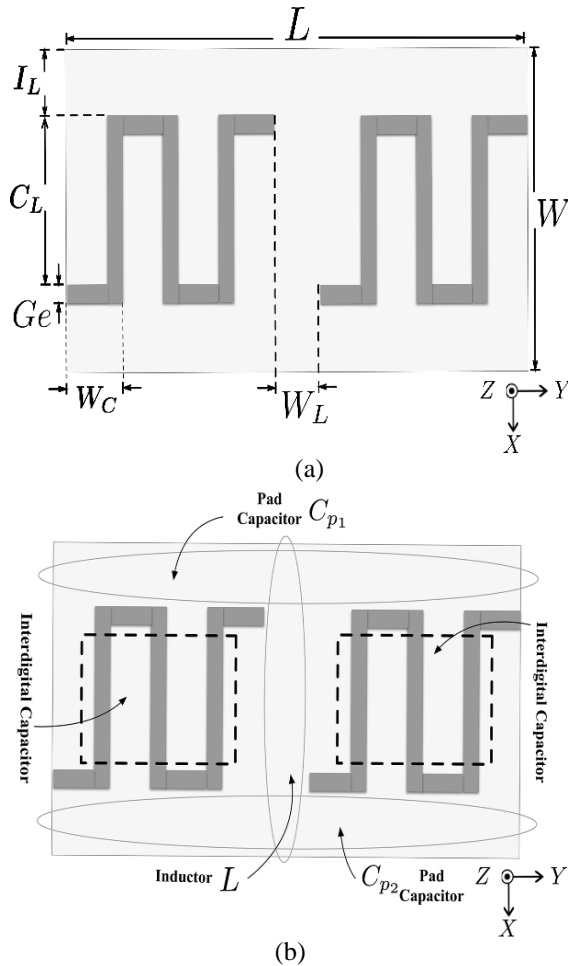
Fig. 1. The proposed resonator antenna: (a) the allocation of equivalent lumped elements, and (b) the parameters used to calculate the equivalent lumped elements.
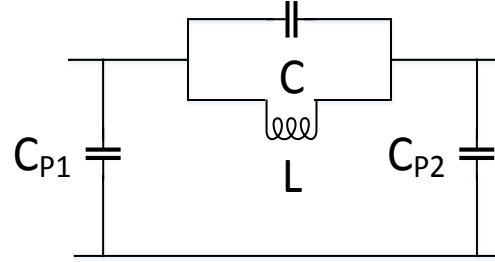
Fig. 2. Equivalent circuit of the proposed antenna.

The equation used to determine the resonant frequency of the proposed antenna has been previously reported [19,20,21]:

$$f=\frac{1}{2\pi\left[\sqrt{\left(L\left(C_{p1}C_{p2}/(C_{p1}+C_{p2})\right)+C\right)}\right]}. \quad (1)$$

From Equation (1), the resonance frequency is determined by the equivalent lumped elements L, C_{p_1}, C_{p_2} and C. These lumped elements were calculated by solving Equations (2) to (6) in an iterative manner using Matlab®.

The inductor L is a single, narrow and straight conductor positioned at the center. The inductance can be calculated by Equation (2):

$$L=200\times10^{-9}I_L\left[\ln\left(\frac{2I_L}{W_L+h}\right)+0.50049+\frac{W_L}{3I_L}\right]. \quad (2)$$

Where h is the substrate thickness.

The interdigital capacitor, C, is a multi-finger periodic structure and the capacitance arises across a narrow gap between the conductors. These gaps are very long and can be folded to reduce the area and form a lumped element. The equation used to determine the series capacitance of the interdigitated structure is Equation (3):

$$C=\varepsilon_0\left(\frac{\varepsilon_r+1}{2}\right)\left[(N-\Delta)C_L\right]. \quad (3)$$

Where,

N is the fingers number,

Δ is the correction factor $\Delta=0.5\left(w_{eff}-w\right)$,

$w_{eff}=1.5\times10^{-3}$, w is the finger width.

The length of interdigital finger C_L is calculated by Equation (4). Whilst, the width of the whole structure is calculated by Equation (5):

$$I_L=C_L+g_e, \quad (4)$$

$$w=2\times I'_L+I_L. \quad (5)$$

The parasitic capacitors C_{p_1} and C_{p_2} connected at both ends of the structure, act as capacitors to ground. By adjusting the parasitic capacitors, the resonant frequency

of the resonator can be tuned. Equation to determine pad capacitances is given in Equation (6):

$$C_P = \left[\frac{2.85\varepsilon_{eff}}{\ln\left[1+(1/2)(8h/\varepsilon_{eff})\left[(8h/\varepsilon_{eff})+\sqrt{(8h/\varepsilon_{eff})^2+\pi^2}\right]\right]} \right] \times \frac{1}{25.4\times10^{-3}},$$

(6)

where h is the substrate height.

The radiating element dimensions were obtained from Equations (2) – (6). Table 1 shows the dimensions of a single quasi lumped antenna at the targeted resonance. The parameters were determined using Equations (2) – (6) at a resonant frequency of 5.8 GHz, whereas the resonant frequency was calculated using Equation (1). Table 2 presents the equivalent lumped elements for single quasi lumped antenna.

Table 1: The proposed antenna quasi-lumped element parameters

Parameter	Dimension [mm]
W_C	0.35
I_L	3.35
C_L	3.05
N	8
I_L'	1.23
g_e	0.3
W_L	1.2
L	5.4
W	5.8
h	0.813

Table 2: The proposed antenna design parameters

C	C_{P1}	C_{P2}	L
0.347 PF	0.17 PF	0.17 PF	1.74 nH

III. CONFIGURATION OF ARRAY FEED

The proposed herringbone antenna design comprises four identical resonating elements. These resonators consist of resonant quasi-lumped elements fed in a quadrature at a design center frequency of 5.8 GHz. The resonators were oriented at ±45° with respect to the feeding line. The quadrature feed yields in the excitations were 90° out of phase. Hence, the technique naturally exhibits circular polarization [22]. The resonators were allocated by to achieve a quadrature phase. In each resonator, the return phase of the reflection from the second element was 180° out of phase with the reflected wave from the initial element [23].

Thus, reflection enhancement is inherently achieved by the resonator design. The first resonator trigger along the feed line dictates the leading phase and the circular polarization orientation. The herringbone antenna has a shorter feeding line than that of a meandering antenna, resulting in array size reduction [24]. Figure 3 presents the prototyped antenna array in CST Microwave Studio.
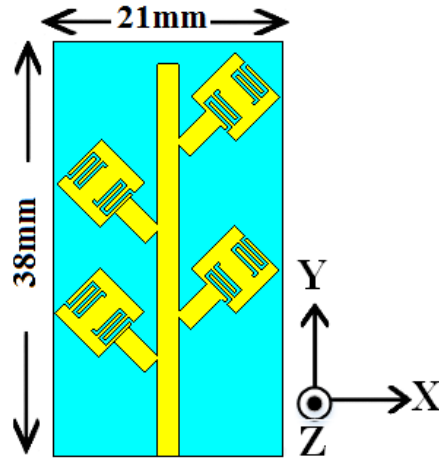
Fig. 3. The 5.8 GHz proposed herringbone array. [Microstrip length is 36 mm].

IV. RESULTS AND DISCUSSIONS

Figure 4 shows the fabricated antenna array on an RO4003C microwave substrate with a relative permittivity of 3.38 and a thickness of 0.813 mm.
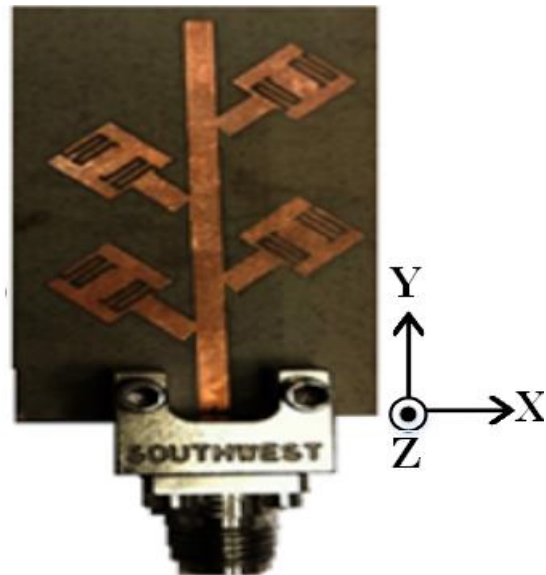
Fig. 4. The 5.8 GHz prototyped herringbone array.

The simulation and measurement results for the input return loss are shown in Fig. 5. The minimum

simulated input return loss for a frequency fine-tuned to 5.788 GHz was –14.21 dB, whereas the minimum measured return loss was approximately –15.84 dB at 5.79 GHz. These results indicate the antenna was resonating at the designed frequency.
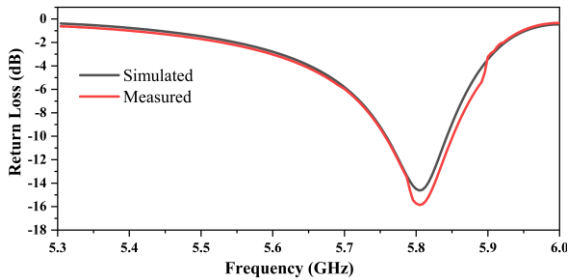
Fig. 5. The simulated and measured return loss results.

Figure 6 shows the simulated and measured co-polarization and cross-polarization patterns in the xz-plane at 5.788 GHz. Cross-polarization was higher than co-polarization by approximately 20 dB in the broadside direction, which is characteristic of left-hand circular polarized (LHCP) radiation. The gain of the array was improved to 5.28 dBi compared to that of a single element, which showed a gain of 1.33 dBi.
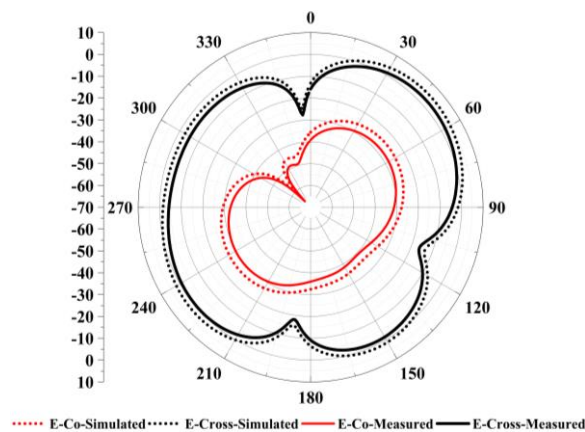
Fig. 6. The simulated and measured results for E-co. and E-cross. polarized.

V. CONCLUSION

Herein, a novel feeding technique for the preparation of a CP quasi lumped antenna was presented. The proposed array was fed by a herringbone microstrip orienting the elements ±45° from the feed line to achieve CP radiation. A noticeably reduced size of the array was achieved compared to that of conventional microstrip antennas. Table 3 shows a notable size reduction comparing the proposed array with various designs reported in literature.

Table 3: A size comparison between the proposed design and several designs reported in the literature

Reference	Array Size [mm]
[25]	85×110
[26]	70×70
[27]	70×70
[28]	70×70
[29]	60×60
Proposed work	21×38

REFERENCES

[1] P. Xu, Z. H. Yan, T. L. Zhang, and X. Q. Yang, "Broadband circularly polarized slot antenna array using a compact sequential-phase feeding network," *Prog. Electromagn. Res.*, vol. 47, pp. 173-179, 2014.

[2] X. Quan, R. Li, and M. M. Tentzeris, "A broadband omnidirectional circularly polarized antenna," *IEEE Trans. Antennas Propag.*, vol. 61, no. 5, pp. 2363-2370, 2013.

[3] S. Fu, S. Fang, Z. Wang, and X. Li, "Broadband circularly polarized slot antenna array fed by asymmetric CPW for L-band applications," *IEEE Antennas Wirel. Propag. Lett.*, vol. 8, pp. 1014-1016, 2009.

[4] T. Yu, H. Li, X. Zhong, T. Yang, and W. Zhu, "A wide bandwidth circularly polarized micro-strip antenna array using sequentially rotated feeding technique," *In Antennas & Propagation (ISAP), 2013 Proceedings of the International Symposium, IEEE*, vol. 2, pp. 743-745, Oct. 23, 2013.

[5] S. Gao, Y. Qin, and A. Sambell, "Low-cost broadband circularly polarized printed antennas and array," *IEEE Antennas Propag. Mag.*, vol. 49, no. 4, pp. 57-64, 2007.

[6] J. Pourahmadazar, C. Ghobadi, J. Nourinia, N. Felegari, and H. Shirzad, "Broadband CPW-fed circularly polarized square slot antenna with inverted-L strips for UWB applications," *IEEE Antennas Wireless Propag. Lett.*, vol. 10, pp. 369-372, 2011.

[7] J. R. James and P. S. Hall, *Handbook of Microstrip Antennas*. IEEE Electromagnetic Waves Series, 1989.

[8] J. Pourahmadazar and V. Rafii, "Broadband circularly polarised slot antenna array for L-and S-band applications," *Electron. Lett.*, vol. 48, no. 10, pp. 542-543, 2012.

[9] P. Mohammadi and V. Rafii, "High gain and

broadband circularly polarized square slot antenna array," *Prog. Electromagn. Res.*, vol. 43, pp. 105-113, 2013.

[10] C. A. Balanis, *Antenna Theory, Analysis and Design*. Wiley India Edition, Third edition, 14, 2005.

[11] P. N. Shinde and B. K. Mishra, "Design of triple band slot antenna for 802.11 a/b WLAN and upper UWB application using pentagon tuning stub," *Int. J. Microw. Opt. Technol.*, vol. 8, no. 1, pp. 17-1, 2013.

[12] P. N. Shinde and B. K. Mishra, "Compact thin ground plane UWB antenna with dual band stop characteristics," *Microw. Opt. Technol. Lett.*, vol. 55, no. 5, pp. 1045-1049, 2013.

[13] P. N. Shinde and J. P. Shinde, "Design of compact pentagonal slot antenna with bandwidth enhance-ment for multiband wireless applica-tions," *AEU-Int. J. Electron. Commun.*, vol. 69, no. 10, pp. 1489-1494, 2015.

[14] K. Sood, R. Jyoti, and S. B. Sharma, "Linear array modules with prescribed excitations using wave-guide shunt slot-fed microstrip patch elements," *Int. J. Microw. Wirel. Technol.*, vol. 5, no. 5, pp. 637-644, 2013.

[15] J. Huang, "A parallel-series-fed microstrip array with high efficiency and low cross-polarization," *Microw. Opt. Technol. Lett.*, vol. 5, no. 5, pp. 230-233, 1992.

[16] J. Pourahmadazar and V. Rafii, "Broadband circularly polarised slot antenna array for L-and S-band applications," *Electron. Lett.*, vol. 48, no. 10, pp. 542-543, 2012.

[17] Z. Q. Jianfang, L. Wei, W. Lei, and X. Shanjia, "Dual-linearly-polarized microstrip array based on composite right/left-handed transmission line," *Microw. Opt. Technol. Lett.*, vol. 48, no. 7, pp. 1366-1369, 2006.

[18] I. J. Bahl, *Lumped Elements for RF and Micro-wave Circuits*. Boston: Artech House, 2003.

[19] F. Huang, B. Avenhaus, and M. J. Lancaster, "Lumped-element switchable superconducting filters," *IEE Proc.-Microw. Antennas Propag.*, vol. 146, no. 3, pp. 229-233, 1999.

[20] E. Bogatin, IEEE Trans. Compon. Hybrids mfg Technol. CHMT-11, 253 (1988). Microelectronics Reliability, vol. 29, no. 6, 1989.

[21] H. T. Su, M. J. Lancaster, F. Huang, and F. Wellhofer, "Electrically tunable superconducting quasilumped element resonator using thin-film ferroelectrics," *Microw. Opt. Technol. Lett.*, vol. 24, no. 3, pp. 155-158, 2000.

[22] J. R. James, P. S. Hall, and C. Wood, *Microstrip Antenna Theory and Design*. Stevenage, U.K.: Peregrinus, Ch. 5, 1981.

[23] M. Guglielmi and D. R. Jackson, "Broadside radiation from periodic leaky-wave antennas," *IEEE Trans. Antennas Propag.*, vol. 41, no. 1, 31-37, 1993.

[24] P. M. Haskins and J. S. Dahele, "Squinted-beam 'herringbone' array," *IEEE Antennas and Propagation Society International Symposium*, 1998.

[25] M. K. Nayan, M. F. Jamlos, and M. A. Jamlos, "Circularly polarized MIMO antenna array for point-to-point communication," *Microw. Opt. Technol. Lett.*, vol. 57, no. 1, pp. 242-247, 2015.

[26] C. L. Tang, H. T. Chen, and K. L. Wong, "Small circular microstrip antenna with dual-frequency operation," *Electron. Lett.*, vol. 33, no. 13, pp. 1112-1113, 1997.

[27] J. Y. Sze, K. L. Wong, and C. C. Huang, "Coplanar waveguide-fed square slot antenna for broadband circularly polarized radiation," *IEEE Trans. Antennas Propag.*, vol. 51, no. 8, pp. 2141-2144, 2003.

[28] J. Y. Sze and Y. H. Ou, "Compact CPW-fed square aperture CP antenna for GPS and INMARSAT applications," *Microw. Opt. Technol. Lett.*, vol. 49, no. 2, pp. 427-430, 2007.

[29] C. C. Chou, K. H. Lin, and H. L. Su, "Broadband circularly polarised crosspatch-loaded square slot antenna," *Electron. Lett.*, vol. 43, no. 9, pp. 485-486, 2007.

Yazeed Mohammad Qasaymeh received B.Sc.Eng. degree from Mutah University, Karak, Jordan, in 2006, M.Sc.Eng. degree in Eng-ineering from College of Electrical and Computer Engineering, Uni-versity Sains Malaysia, Pinang, Malaysia, in 2009, and Ph.D. degree in the College of Electrical and Electronic Engineering, Universiti Sains Malaysia, Pinang, Malaysia. He is currently an Assistant Professor in College of Engineering, Al-majmaah University at Aaudia Arabia. His research interest is antennas array, wireless communication MIMO, distributed antenna systems.

Khaled Issa received the B.Sc. degree (Hons.) from the Prepara-tory Institute of Scientific and Technical Studies (IPEST), Tunisia, in 2006, and the M.Sc. degree in Physics and the Ph.D. degree (Hons.) with the Faculty of Science Monastir, Tunisia, in 2008 and 2016, respectively. He was an Electro-Optic Research

Engineer with IPEST and the Institute of Nano-technology of Lyon (INL), France, and the Laser Center Jussieu, Université Pierre et Marie Curie, France, from 2004 to 2006. He was a Photonic Engineer with INL, France, from 2008 to 2009. He was a Teacher Assistant with the Faculty of Science of Monastir from 2008 to 2014. His main research interests during the Ph.D. were the atomic, molecular interaction and systems, advanced quantum studies, and rare gas clusters. He joined as a Researcher with KACSTRFTONICS, KSU, Saudi Arabia, in 2014. He has authored, presented and submitted peer-reviewed conferences and journal papers. He supervised under-graduate student's projects in optical telecommunication and renewable energy areas. He co-supervised graduate students. He mainly involved on antenna analysis, synthesis and characterization projects, nano-fabrication and nano-characterization of nano-structures, and various funded research projects by NSTIP and RFTONICS-TIC.

Abdullah Saad Al-Ahmadi received BSc.Eng. degree from Saba University, Sanaa, Yemen, in 2005, M.Sc.Eng. degree in Engineering from College of Electrical, Universiti Teknologi Malaysia, Johor, Malaysia, in 2008, and Ph.D. degree from the College of Electrical and College of Engineering, Universit, Pinang, Malai Teknologi Malaysia, Johor, Malaysia. He is currently and Assistant Professor in College of Engineering, Majmaah University in Saudi Arabia. His research interest are location determination systems and wireless communication.

Mohammadariff Bin Othman received BSc.Eng. degree from Multimedia University, M.Sc.Eng. degree in Engineering from College of Electrical and Computer Engin-eering, University Sains Malaysia, Pinang, Malaysia, in 2009, and Ph.D. degree in the College of Electrical and Electronic Engineering, Universiti Sains Malaysia, Pinang, Malaysia 2015. He is currently a Senior Lecturer in College of Engineering, Malaya University at Malaysia.

An Estimation Method for the SLF/ELF Field Strength with L-type Horizontal Line-Current Antennas over Inhomogeneous Anisotropic Ground

Bin Li [1,2], Chao Liu [2], Hua-ning Wu [2], and Bo Zhang [3]

[1] National Key Laboratory of National Defense Technology for Integrated Ship Power Technology
Naval University of Engineering, Wuhan, 430033, China
libin521002@sina.com

[2] Department of Electronic Engineering
Naval University of Engineering, Wuhan, 430033, China
chaoliunue@sina.com, wuhuaning007@163.com

[3] Naval Academy of Armament
Shanghai, 200436, China
zbdtc123123@sina.com

Abstract ─ In this study, the radiation characteristics of the control source of extremely low frequency (CSELF) horizontal line-current antennas are studied by the reciprocity theorem. The radiation field strength expressions of the CSELF L-type horizontal line-current antenna are derived on the basis of a field-direction coefficient in the spherical earth-ionosphere cavity. The estimation results of the super low frequency/extremely low frequency (SLF/ELF) wave are provided with regard to the conductivity, the propagation distances and the water-depth. The propagation characteristics of the CSELF wave are calculated under different conditions and are compared to Bannister's method. The effectiveness of the proposed method is validated by a case study.

Index Terms ─ Control source of extremely low frequency (CSELF), earth-ionosphere cavity, ground resistivity, horizontal dipole antenna.

I. INTRODUCTION

The control source of extremely low frequency (CSELF) method is a key technique for underwater communications and electromagnetic exploration [1-4], especially for earthquake prediction and oil and gas exploration. Compared with other electromagnetic detection technologies, SLF/ELF detection has greater advantages regarding the detecting depth and precision and can be applied to geomagnetic high-energy radiation and underground exploration fields [5, 6]. The effective radiation of the SLF/ELF electromagnetic wave is a crucial component of the CSELF method. Horizontal line-current antennas have been implemented extensively as effective transmitting antennas in the

SLF/ELF band. As shown in Fig. 1, a horizontal line-current antenna is low-slung in a high ground resistivity region, and grounding electrodes are at the two ends of the cable, which transmits a sinusoidal alternating current underground. Thus, a huge amperage current loop is formed by the tens of kilometers of the cables and the ground currents. For a long dipole horizontal antenna with fixed length at a specific frequency, an antenna ground with high equivalent resistivity can enhance the effective skin depth. The magnetic moment of the current loop is large, which is equivalent to increasing the electrical size of the line-current antenna. Therefore, the horizontal line antenna can be seen as a horizontal magnetic dipole (HMD) in the Earth-ionosphere cavity [7, 8].

Generally, the apparent resistivity of the control source station affects the radiation characteristics of the ELF electromagnetic waves in the Earth-ionosphere cavity. A high ground resistivity in the antenna path area is an important factor to improve the performance of the SLF/ELF transmission system [9]. The crust is affected by geological structures such as bedrock strike, gullies, and fault zones. Hence, the resistivity of the earth's crust is actually anisotropic and inhomogeneous [10]. Due to the constraint of the geological structure, CSELF horizontal line-current antennas, which may have a length of up to tens of kilometers, usually consist of several L-type folded lines. Many numerical analyses have focused on the geo-electric magnetic field strength (MFS) and the distribution of the surface-induced electric field strength (EFS) of the horizontal electric dipole (HED) [11-13]. However, the radiation field of the L-type horizontal line-current antenna over inhomogeneous anisotropic ground has not received

sufficient attention, especially in the ocean environment. Therefore, this study focuses on the radiation field of the CSELF and proposes a low-complexity estimation method for the field intensity of the L-type horizontal line-current antenna over inhomogeneous anisotropic ground based on the waveguide theory. Solving the radiation field of the SLF/ELF provides an approximate solution for remote sensing of the underground and underwater environment.

This paper is organized as follows. Section 2 briefly describes the electrical characteristics of the horizontal line-current antenna path and proposes the closed-form solution for the CSELF radiation field of the L-type horizontal line-current antenna. In Section 3, we present the calculated results and illustrate the radiation characteristics of the CSELF L-type horizontal line-current antenna. The conclusions of this paper are presented in Section 4.
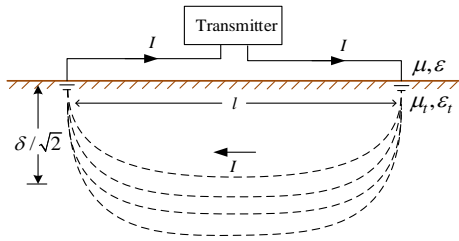
Fig. 1. A horizontal line-current antenna grounded at each end.

II. ANALYTICAL FORMULAS FOR THE CSELF RADIATION FIELD

A. The electrical characteristics of the CSELF antenna path

Generally, the surface geometries of the antenna path have no significant influence on the SLF/ELF propagation. However, the conductivities of the CSELF antenna path from the land surface to a certain depth have a great effect on the propagation of the SLF/ELF electromagnetic wave [14]. Therefore, it is necessary to study the electrical characteristics of the CSELF antenna path. As part of the input resistance, the resistance of the ground loss determines the CSELF radiation efficiency of the horizontal L-type line-current antenna. In most of the medium models, the resistivity of the ground is represented by the horizontal layered structure or the half-space homogeneous structure [15-18].

A SLF/ELF electromagnetic wave has a deeper skin depth underground. Hence, it cannot be considered that the electrical properties of the ground are homogeneous. In a Cartesian coordinate system, the vertical plane waves propagate vertically downward (along the positive z-axis). When the time variation factor is set as $e^{j\omega t}$, the electromagnetic waves can be expressed in the x-axis direction [19]:

$$\partial^2 E_x / \partial z^2 - k^2 E_x = 0. \tag{1}$$

$k^2 \approx -j\omega\mu_{xl}\sigma_{xl}$, ω denotes the angular frequency, μ_{xl} denotes the permeability tensor element, and σ_{xl} denotes the conductivity tensor element. When z is infinite, the general solution of Equation (1) is:

$$E_x = Ae^{-kz}. \tag{2}$$

A denotes a constant. Based on the differential formula of Faraday's law $\nabla \times E = -j\omega\mu \cdot H$; the component of the MFS in the direction of the y-axis can be obtained by:

$$H_y = -\frac{A}{\sqrt{j\omega\mu_{xl}\rho_{xl}}} e^{-kz}. \tag{3}$$

Using Equations (2) and (3), the impedance of the plane wave can be represented as:

$$\eta_{xy} = -\sqrt{\omega\mu_{xl}\rho_{xl}} \cdot e^{-j\pi/4}. \tag{4}$$

ρ_{xl} denotes the ground equivalent resistivity along the x-axis. It can be seen that the wave impedance is closely related to the resistivity and the ground equivalent resistivity can be determined by the magnetotelluric method [20].

B. The estimation method for the CSELF in the Earth-ionosphere cavity

The total path of the SLF/ELF long dipole antenna with high power can reach hundreds of kilometers. The L-type emission source has a higher resolution than the horizontal long loop source and the ring source [21]. The ionosphere disturbances have a great influence on the amplitude and phase of the ELF/very low frequency (VLF) electromagnetic wave [22-24]. Using a horizontal line-current antenna as a model, other forms of artificial sources can be made up of multiple horizontal antennas. We regard the horizontal line-current antenna as a HED in the Earth-ionosphere cavity. The radiation field of the electric dipole is a transverse magnetic (TM) wave. For an observer located in the far field, the relative wave-number is $k_r \geq 1$. The effective reflection height of the ionosphere to the SLF/ELF wave is far less than the wavelength of the SLF/ELF wave in free space. The MFS component H_r is very small and negligible compared to the H_θ component and the H_φ component; therefore, the SLF/ELF electromagnetic wave is a transverse electromagnetic (TEM) wave in the far field.

In a flat earth-ionosphere cavity, the vertical EFS component of the short vertical current source on the ground can be obtained from the perpendicular EFS component of a line-current source, which is in an infinite medium, with an infinite length and a uniform line as in the following:

$$E_z(\rho) = -\frac{\omega\mu_e Il}{4h_i} H_0^{(2)}(Sk_0\rho). \tag{5}$$

I denotes the antenna current, l denotes the length of the short vertical current source, h_i denotes the ionosphere

height, and $H_0^{(2)}(Sk_0\rho)$ denotes the second kind of the Hankel function.

As shown in Fig. 2, the horizontal line-current source Il_1 and Il_2 are placed on the surface of the earth in a Cartesian coordinate system, and the source Il_1 points in the positive direction of the x-axis which originates from the coordinate origin o. The experimental vertical electrical dipole (VED) source is placed at the point o'. When the principal axis of the surface impedance is regarded as the normal direction of the $x'o'y'$ plane in a Cartesian coordinate system, φ denotes the angle between the radial direction and the x-axis and φ' denotes the angle between the radial direction and the x'-axis. The two sources are set in the same space. According to the reciprocity theorem [12, 19], the electromagnetic field produced by the horizontal line-current sources and the VED satisfies:

$$\int_l \boldsymbol{E} \cdot \hat{\boldsymbol{r}} I_1 \mathrm{d}l_1 = \int_l \boldsymbol{H} \cdot \hat{\boldsymbol{y}} I' \mathrm{d}l'. \tag{6}$$

Based on Equation (6), in the flat earth-ionosphere cavity, the vertical EFS component of the current source is given as:

$$E_z' = -E_\rho \cos\varphi' = \eta_g H_\phi \cos\phi'. \tag{7}$$

E_ρ denotes the horizontal EFS at Il_1, produced by the vertical current source $I'l'$. In the Earth-ionosphere cavity, we assume $I'l' = Il_1$. When the distance ρ between the field point and source point is greater than the ionosphere height h_i, the location of the field point is not near the antipodal point. Based on Equations (5) and (7), the radial EFS of the direct wave can be expressed as follows:

$$E_r^d = -\mathrm{j}\frac{IlSk_0}{4h_i}\left(\frac{\omega\mu\rho_g}{\mathrm{j}}\right)^{1/2}$$
$$\cdot\left[\frac{\rho/a_e}{\sin(\rho/a_e)}\right]^{1/2} \mathrm{H}_1^{(2)}(Sk_0\rho)\cos\varphi. \tag{8}$$

$\left[\frac{\rho/a_\varepsilon}{\sin(\rho/a_\varepsilon)}\right]^{1/2}$ denotes the spherical focusing factor. Using the Maxwell equation, the magnetic field in a spherical cavity can be obtained as follows:

$$\boldsymbol{H}^d = -\frac{IlSk_0}{4h_i\eta_e}\left(\frac{\omega\mu\rho_g}{\mathrm{j}}\right)^{1/2}\left[\frac{\rho/a_e}{\sin(\rho/a_e)}\right]^{1/2}\left\{\hat{\boldsymbol{\theta}}\frac{1}{Sk_0\rho}\right.$$
$$\cdot\mathrm{H}_1^{(2)}(Sk_0\rho)\sin\varphi + \hat{\boldsymbol{\varphi}} \tag{9}$$
$$\left.\cdot\left[\mathrm{H}_0^{(2)}(Sk_0\rho) - \frac{1}{Sk_0\rho}\mathrm{H}_1^{(2)}(Sk_0\rho)\right]\cos\varphi\right\}.$$

k_0 is the wave number, a_ε is the earth radius, and S is the parameter of the cavity. Similarly, the EFS and MFS of the direct wave of the source Il_2 can be obtained by Equations (8) and (9). However, the field opponent differs for the source Il_2 and the source Il_1 due to the folded angle. The field-direction coefficient can be expressed as follows:

$$S_f \approx \begin{cases} (\cos\varphi + \cos(\pi - \gamma_n - \varphi)), & 0 \le \varphi \le \pi/2. \\ (\cos\varphi + \cos(\pi - \gamma_n + \varphi)), & -\pi/2 \le \varphi < 0. \end{cases} \tag{10}$$

γ_n denotes the folded angle of the nth fold line between the radial direction and the positive x-axis. We assume that the angle γ is in the range of $[\pi/2, 3\pi/2]$. The waves of the multiple circulations are negligible because of the attenuation in the cavity. Using the approximate expression of the Hankel function, we simplify the EFS expression of the L-type line-current antennas as:

$$|(E_r)^d| \approx \frac{fI}{2h_i}\left(\frac{2\pi\mu}{c_0}\right)^{\frac{1}{2}} \cdot \left[\frac{\frac{\rho}{a_e}}{\sin(\frac{\rho}{a_e})}\right]^{\frac{1}{2}}\frac{e^{-\alpha\rho}}{(\rho\frac{c_0}{v_p})^{\frac{1}{2}}}$$
$$\begin{bmatrix} l_1\sqrt{\rho_{gn}}\cos\varphi - \sum_{n=2}^m l_n\sqrt{\rho_{gn}} \\ \cdot\begin{cases}\cos(\gamma_{n-1}-\varphi), & -\pi/2 \le \varphi \le 0, \\ \cos(\gamma_{n-1}+\varphi), & 0 \le \varphi \le \pi/2, \end{cases} \end{bmatrix}, \tag{11}$$

where l_n and ρ_{gn} denote the length and the equivalent ground resistivity respectively of the nth fold line, c_0 denotes the speed of light in a vacuum, and v_p denotes the wave velocity in the waveguide. The approximate expressions for the radial magnetic field strength can be derived from the wave impedance and Equation (11), which is similar to Bannister's expression [25]. According to Equation (11), when the length of the antenna is determined, the electrical parameter that determines the radiation capability of the CSELF antenna is mainly the ground resistivity of the antenna path.
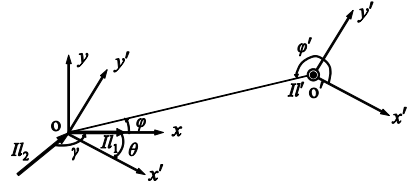
Fig. 2. Reciprocal relationship between an L-type line-current antenna and a VED.

III. NUMERICAL RESULTS AND DISCUSSION

In this section, the characteristics of the radiation field of the CSELF antenna are simulated in detail. As shown in Fig. 3, using an L-type horizontal antenna as an example, we assume that the CSELF horizontal L-type line-current antenna is placed in the xoy plane. The lengths of the two L-type lines are $l_1 = 80$ km and $l_1 = 120$ km. The first L-type line is parallel to the x-axis. The fold angle is $\gamma = 150°$. A horizontal line antenna with an equivalent length is placed on the x-axis and is calculated by Bannister's method for comparison. A homogeneous ground with a resistivity of 5000 Ω is selected as the ground dielectric model. The alternating current of the artificial source is 300 A and the operating

frequencies are 70 Hz and 130 Hz, respectively. The effective reflection height of the ionosphere is 75 km.
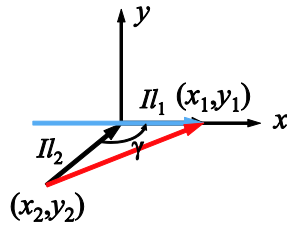
Fig. 3. Simulation model of the L-type line-current antenna.

The field strength values of the antenna are shown in Fig. 4. Figure 4 (a) indicates that the EFS and MFS of the CSELF are increasing with increasing values of the apparent resistivity at 7000 km. Compared with the EFS and MFS values of the horizontal line antenna, the fold line antenna has a lower field strength value. When the apparent resistivity is above 5000 Ω, the field strength values of the CSELF source do not increase considerably and the differences in the field strength are less than 3 dBV/m in the far field. Therefore, a high apparent resistivity improves the field strength of the CSELF source. The frequencies have little effect on the field strength in the SLF/ELF band. Figure 4 (b) shows that the field strength of the CSELF decreases as the propagation distance increases in the Earth-ionosphere cavity. With a decrease in the frequency, the initial EFS decreases and the decay rate of the field strength decreases slightly. Hence, within 7000 km, the higher-frequency portion of the SLF/ELF wave is better suited for communication purposes. Beyond 7000 km, the low-frequency portion of the SLF/ELF should be used to obtain relatively higher signal strength. Near the air-seawater interface, the wave on the interface is dominated by the vertical electric field component. The communication at sea depends mainly on the horizontal component of the field strength.
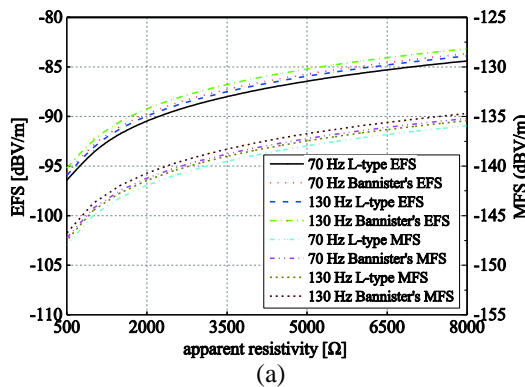
(a)
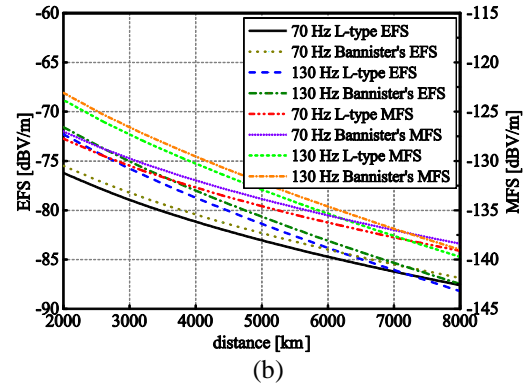
(b)

Fig. 4. (a) EFS and MFS of the CSELF versus apparent resistivity at x=7000 km, and (b) EPS and MFS of the CSELF versus the distance.

Figure 5 (a) shows the horizontal component of the EFS with respect to the propagation distance. Compared with the EFS values in Fig. 4 (b), the field strength values of the waves are strongly attenuated by four orders of magnitude at the air-seawater interface. Figure. 5 (b) shows that the EFS values of the CSELF are decreasing with increasing depth. When the SLF/ELF wave propagates in the single-mode region of the Earth-ionosphere cavity (2000–8000 km), the higher the frequency is, the faster the attenuation and the lower the penetration depth is. The EFS horizontal component of the SLF/ELF waves exhibits slight differences in shallow water. However, when the SLF/ELF wave signals are transmitted to a larger depth, a lower frequency is required. Considering the limited capacity of the channel, maintaining a balance between the penetration and the communication capability represents a problem of shore based CSELF in underwater communications.

The simulations indicate that the results of the proposed method are basically consistent with the results of the Bannister's expression. We believe that these consistencies are mainly caused by the waveguide theory and the similar simulation environments. The field strength of the fold line antenna is relatively smaller than the field strength derived by Bannister's expression. Because the fold line antenna is equivalent to the dipole signed by the red dotted line in Fig. 3, the φ angle is larger for the equivalent antenna than for the compared antenna. Moreover, the ground conductivity is assumed as the homogenous ground in the above case. The numerical solution of the fold line antennas can be obtained by the equivalent antenna. Therefore, the equivalent conductivity is regarded as a practical solution procedure of the inhomogeneous anisotropic ground conductivity. Note that these simulation results

are obtained under specific conditions (earth-ionosphere cavity) and that the effect of inhomogeneous anisotropic ground conductivity on the L-type line-current antenna requires further study.
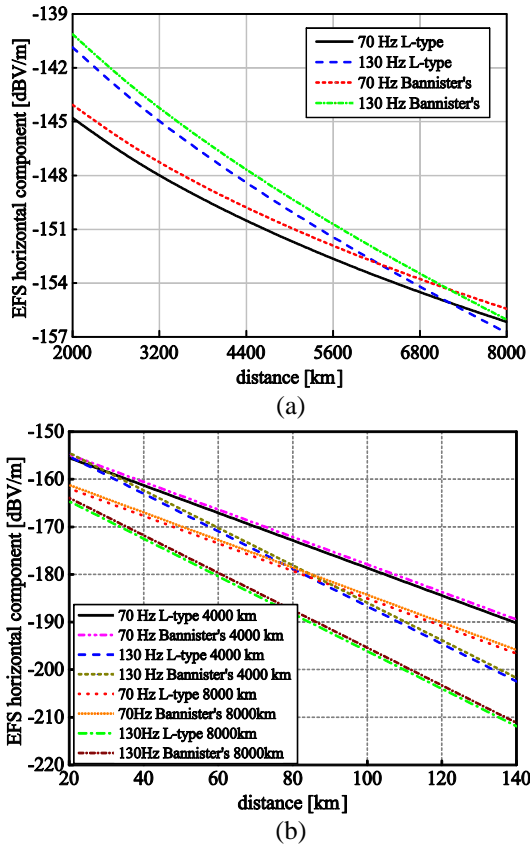
Fig. 5. (a) EFS horizontal component of the CSELF versus distance at the air-seawater interface, and (b) EPS horizontal component of the CSELF versus sea–water depth.

IV. CONCLUSIONS

In this study, the radiation characteristics of the CSELF in the Earth-ionosphere cavity are investigated and a novel low-complexity estimation method for the CSELF with an L-type horizontal line-current antenna is proposed. Using the reciprocity theorem, the EFS and MFS closed-form expressions of the CSELF are given in a spherical earth-ionosphere cavity. A simulation of the proposed closed-form solution shows that the ground resistivity of the control source station has a large effect on the SLF/ELF field intensity in the far field. A high apparent resistivity improves the field strength of the CSELF source. When the SLF/ELF waves pass from the air to the water, the SLF/ELF waves are attenuated strongly by the seawater surface. The higher the frequency, the smaller the penetration depth is. It is verified by a theoretical analysis and simulations that the proposed estimation method predicts the field strength of

the CSELF accurately.

REFERENCES

[1] S. Coco, A. Laudani, F. R. Fulginei, and A. Salvini, "A new neural predictor for ELF magnetic field strength," *IEEE Transactions on Magnetics*, vol. 50, no. 2, pp. 69-72, Feb. 2014.

[2] G. Lucca, "Analytical evaluation of sub-sea ELF electromagnetic field generated by submarine power cables," *Progress in Electromagnetics Research B*, vol. 56, pp. 309-326, Dec. 2013.

[3] N. Damiano, L. Yan, B. Whisner, and C. Zhou, "Simulation and measurement of through-the-earth (TTE), extremely low-frequency signals using copper-clad, steel ground rods," *IEEE Transactions on Industry Applications*, vol. 53, no. 5, pp. 5099-5095, Sept.-Oct. 2017.

[4] Y. Wang, Y. Zhou, and Q. S. Cao, "Study of ELF propagation parameters based on the simulated Schumann resonances," *IEEE Antennas and Wireless Propagation Letters*, vol. 13, pp. 63-66, Dec. 2013.

[5] K. Shiokawa, Y. Yokoyama, A. Ieda, Y. Miyoshi, et al., "Ground-based VLF/ELF chorus observations at subauroral latitudes - VLF-CHAIN campaign," *Journal of Geophysical Research Space Physics*, vol. 119, no. 9, pp. 7363-7379, Sept. 2015.

[6] G. Z. Zhao, L. F. Wang, J. Tang, X. B. Chen, et al., "New experiments of CSELF electromagnetic method for earthquake monitoring," *Chinese Journal of Geophysics*, vol. 53, no. 3, pp. 479-486, Mar. 2010.

[7] C. Liu, B. Wang, H. Q. Xu, and Y. L. Liu, "The impedance characteristics of ELF line-current antenna over inhomogeneous anisotropic ground," *Applied Mechanics and Materials*, vol. 548-549, pp. 771-775, June 2014.

[8] M. L. Burrows and C. W. Niessen, "ELF communication system design," *Engineering in the Ocean Environment, Ocean 72 - IEEE International Conference on*, Newport, RI, pp. 95-109, Sept. 1972.

[9] M. L. Burrows, "Surface impedance and the efficiency of horizontal-dipole extremely low frequency (ELF) antenna arrays," IEEE Transactions on Communications, vol. 22, no. 4, pp. 475-483, Apr. 1974.

[10] W. D. Xu, X. M. Zhang, Z. Li, S. F. Zhao, and W. Zhang, "Statistical analysis of the propagation characteristics of VLF electromagnetic waves excited by the artificial transmitter," *Chinese*

Journal of Geophysics, vol. 59, no. 5, pp. 1578-1584, May 2016.

[11] Y. X. Wang, R. H. Jin, J. P. Geng, and X. L. Liang, "Exact SLF/ELF underground HED field strengths in earth-ionosphere cavity and Schumann resonance," *IEEE Transactions on Antennas and Propagation*, vol. 59, no. 8, pp. 3031-3039, Aug. 2011.

[12] C. Liu, L. G. Zheng, and Y. P. Li, "A closed-form solution for ELF radiated fields of a line-current antenna in earth-ionosphere waveguide," *International Conference on Wireless Communications, Networking and Mobile Computing*, Beijing, pp. 2506-2509. Sept. 2009.

[13] M. Hayakawa and T. Otsuyama, "FDTD analysis of ELF wave propagation in inhomogeneous subionospheric waveguide models," *Applied Computational Electromagnetics Society Journal*, vol. 17, no. 3, pp. 239-244, Nov. 2002.

[14] S. V. Makki, T. Z. Ershadi, and M. S. Abrishamian, "Determining the specific ground conductivity aided by the horizontal electric dipole antenna near the ground surface," *Progress in Electromagnetics Research B*, vol. 1, pp. 43-65, Jan. 2008.

[15] A. Kulak and J. Mlynarczyk., "ELF propagation parameters for the ground-ionosphere waveguide with finite ground conductivity," *IEEE Transactions on Antennas and Propagation*, vol. 61, no. 4, pp. 2269-2275, Apr. 2013.

[16] D. L. Paul and C. J. Railton, "Spherical ADI FDTD method with application to propagation in the earth ionosphere cavity," *IEEE Transactions on Antennas and Propagation*, vol. 60, no. 1, pp. 310–317, Jan. 2012.

[17] G. Lucca, "Analytical evaluation of sub-sea ELF electromagnetic field generated by submarine power cables," *Progress in Electromagnetics Research B*, vol. 56, pp. 309-326, Dec. 2013.

[18] H. Y. Li, J. Zhan, Z. S. Wu, and P. Kong, "Numerical simulations of ELF/VLF wave generated by modulated beat-wave ionospheric heating in high latitude regions," *Progress in Electromagnetics Research M*, vol. 50, pp. 55-63, Jan. 2016.

[19] Y. P. Wang, *Engineering Electrodynamics*, Xidian University Press, Xi'an, 2007.

[20] P. S. Greifinger, V. C. Mushtak, and E. R.Williams, "On modeling the lower characteristic ELF altitude from aeronomical data," *Radio Science*, vol. 42, no. 2, pp. 1–12, Apr. 2007.

[21] C. M. Fu, Q. Y. Di, C. Xu, and M. Y. Wang, "Electromagnetic fields for different type sources with effect of the ionosphere," *Chinese Journal of Geophysics*, vol. 55, no. 12, pp. 3958-3968, Dec. 2012.

[22] M. S. Zhdanov, *Geophysical Electromagnetic Theory and Methods*, Elsevier Science, New York, 2009.

[23] T. B. Jones, K. Davies, and B. Wieder, "Observations of D region modification at low and very low frequencies," *Nature*, vol. 238, no. 5358, pp. 33-34, Jul. 1972.

[24] G. Z. Li, T. T. Gu, and K. Li, "SLF/ELF electromagnetic field of a horizontal dipole in the presence of an anisotropic earth-ionosphere cavity," *Applied Computational Electromagnetics Society Journal*, vol. 29, no. 12, pp. 1102-1111, Dec. 2014.

[25] P. R. Bannister, "ELF propagation update," *IEEE Journal of Oceanic Engineering*, vol. oe-9, no. 3, pp. 179-188, Jul. 1984.
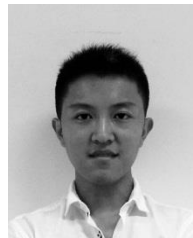
Bin Li received his M.S. and Ph.D. degrees from Naval University of Engineering, Wuhan, China, in 2015 and 2019.

He currently serves as a Research Assistant at Naval University of Engineering. His current research interests include SLF/ELF wave propagation and electromagnetic interference.

Chao Liu received the M.S. and Ph.D. degrees in Electromagnetic Field and Microwave Technology from Xidian University, Xi'an, China.

He was a Professor at Naval University of Engineering. His research interests include VLF communication, antenna design and numerical analysis for electromagnetic fields.

Hua-ning Wu received his M.S. and Ph.D. degrees from Naval University of Engineering, Hubei, China, in 2012 and 2015.

He currently serves as a Lecturer at Naval University of Engineering. His research interests include antenna array pattern synthesis, intelligent antenna design.

Bo Zhang received his M.S. degree from Naval University of Engineering, Hubei, China, in 2015.

He currently served as an Engineer at Naval Academy of Armament. His research interests include electronic control and circuit design, intelligent antenna design.

A Low Profile Circularly Polarized Antenna based on Stepped Open-ended Slot Radiator

Ping Wang [1], Qi Wu [1], Yu Shao [1], and Dong Huang [2]

[1] School of Communications and Information Engineering
Chongqing University Posts and Telecommunications, Chongqing, 400065, China
wp@cqupt.edu.cn, 641837048@qq.com, shaoyu@cqupt.edu.cn

[2] Chongqing Institute of Green and Intelligent Technology
Chinese Academy of Sciences, 400714, China
chenyijia000011@163.com

Abstract — A compact wide band and low profile circularly polarized antenna is presented based on stepped open-ended slotline in this paper. The antenna is composed of four open-end-slotted patches and a feed network. Four open-end-slotted patches are sequentially rotated and vertically soldered on the ground plane of the feed network, and are excited by a wide band transition from strip-line to slot-line with short pin in antenna element. The CP radiation of the proposed antenna is realized by four output ports of the feed network which transmit four signals that have equal amplitude with quadrature phase difference (0^0, 90^0, 180^0, and 270^0). Simulation results are compared with the measurements, and a good agreement is obtained. The measured results show that the proposed antenna can provide broad impedance bandwidth of 73.4% (3.5 GHz–7.56 GHz) (reflection coefficient less than -10 dB), a maximum gain of 4.74 dBi, and a 3-dB axial ratio (AR) bandwidth of about 35.1% (3.65 GHz–5.2 GHz).

Index Terms — Circularly polarized (CP) antenna, low profile, open-ended slotline, stepped slotline, feed network, wide band.

I. INTRODUCTION

Due to the unique features that circularly polarized (CP) antenna can increase orientation diversity and reduce the loss caused by the multi-path effects between transmitting and receiving antennas, CP antenna has been researched widely over the past decades. One most typical example of CP antenna is various shaped patch with a slight structure perturbation at a specific location to form two orthogonal linear polarizations with a 90^0 phase shift [1-3], but these antennas have inherent narrow impedance and axial ratio (AR) bandwidth (typically 1%-4%). In order to enhance the bandwidth, commonly one method is the use of parasitic elements [4-9]. In [4], a design realizes the circularly polarized performance using a stacked arrangement of the corner-truncated rectangular patch, where AR bandwidth of better than 11% and impedance bandwidth of better than 27% were obtained. In [5], a micro-strip-fed hexagonal patch with a slant slot-line is proposed for CP application, where a parasitic element with different size was introduced to broaden 3dB AR bandwidth to 5%. Fang et al. investigated the cut-corner stacked path antenna, in which a horizontally meandered strip (HMS) feed technique is proposed to obtain impedance bandwidth of 25.8% and 3-dB AR bandwidth of 13.5% for universal ultrahigh frequency (UHF) RF identification applications [6]. A hybrid combination of coupling feed technique and parasitic element was also introduced to achieve larger 3dB AR bandwidth, such as slot coupling (2.8%) [7], T-shaped strip coupling (0.98%, 4.275%, 0.8869%, and 1.35% in four distinct bands) [8], and L-shaped strip coupling (10%) [9, 10]. However, the aperture coupled antenna needs a reflecting plate to block back radiation, which increases the complexity of the antenna configuration. In addition, the effects of the length of the vertical and horizontal portion of the L-shaped or T-shaped strip on input resistance and reactance are dependent, which result in complex design process. It is seen that though the antennas have a low profile structure, the AR bandwidth is still very narrow.

Another example of CP antenna is the sequentially multi-fed-rotated CP antenna presented in [11-15], in which generally a hybrid feed network need be designed to provide a relative phase shift of 90 degree and equal amplitude in the output port. In [11], a 2×2 circularly polarized stacked patch array was proposed, but only 12% impedance and 8% 3dB AR bandwidths are achieved. Single radiation patch fed by a complex feed network without 100Ω isolation resistor to realize a high gain and wide axial ratio beam-widths was also presented in [12], whereas only 11% AR bandwidth is achieved owing to the narrow band characteristic of single patch. In [13],

Shen et al. presented a low profile CP antenna based on quarter-mode substrate integrated wave guide, but the antenna provides the only 5.8% AR bandwidth. It is important to note that a circularly polarized antenna array based on anti-podal Vivaldi antenna was proposed, and exhibits 10-dB return loss and 3-dB AR bandwidths from 1 GHz to 10 GHz [14]. However, its size is too large, especially in profile size of 173 mm. A size reduction based on halved Vivaldi antenna is also presented in [15], but the profile size of $0.42\lambda_L$ (λ_L is the free-space wavelength at the center frequency) is still large for some wireless communication systems.

In this paper, we present a wide band and low profile circularly polarized antenna with a profile size of only $0.19\lambda_L$ (λ_L is the free-space wavelength corresponding to lowest operating frequency).The antenna is formed by four sequentially rotated rectangle patches with open-ended slot-line, and is fed by using four output ports of feed network to realize the CP performance. The antenna is studied using the package ANSYS high-frequency structure simulator (HFSS), which is based on the finite element method. An antenna prototype is fabricated and measured to verify the simulation and findings.

II. PROPOSED ANTENNA CONFIGURATION AND DISCUSSION

Figure 1 shows the geometry of the overall CP antenna prototype. In this design, an FR-4 substrate (dielectric constant = 4.4, loss tangent = 0.02) with a thickness of 0.8 mm was employed as the system circuit board and the overall dimension is about 60 mm×60 mm. A system ground plane with a same size is printed on the top layer of the substrate, whereas the feed network resides on the bottom layer of the substrate. The feed network is composed by the Wilkinson power divider, 90 degree delay line, and 180 degree delay lines, and brings into sequential rotation of current on the radiation patch for CP radiation. One end of the 50-Ω feeding strip-line is connected to the inner conductor of a 50-Ω SMA connector for testing the antenna, while the other end is connected to the Wilkinson power divider. The external metal shell of the SMA connector is soldered to the system ground plane.

Four rectangle-supported substrate boards, which also are fabricated by FR-4 substrate with a thickness of h=0.5 mm, are integrated together to form a hollow square-ring wall and are located on system ground plane vertically. Four rectangle patches are printed on four exterior face of the supported dielectric wall respectively and the bottom edge of that is soldered to the system ground plane, whereas three slot-lines with different slot widths are etched on each rectangle patch to form a stepped open-ended slot radiator. On the interior face of the supported dielectric wall, coupling micro-strip line is

printed and one end of that is extended to couple the stepped slot-line, and then is connected through the short circuit pins (E, F, G, H) to the rectangle patch. Other end of the coupling micro-strip line is connected to the output ports of the feed network that have equal amplitude with quadrature phase difference (0^0, 90^0, 180^0, and 270^0). It should be mentioned that to fix the rectangle-supported dielectric wall vertically on the system ground plane two tips on each substrate boards were deliberately made and inserted into the etched slot on system ground plane, and the existence of the tip slightly affects the resonant frequency and radiation patterns, which can be included in the full-wave simulation.
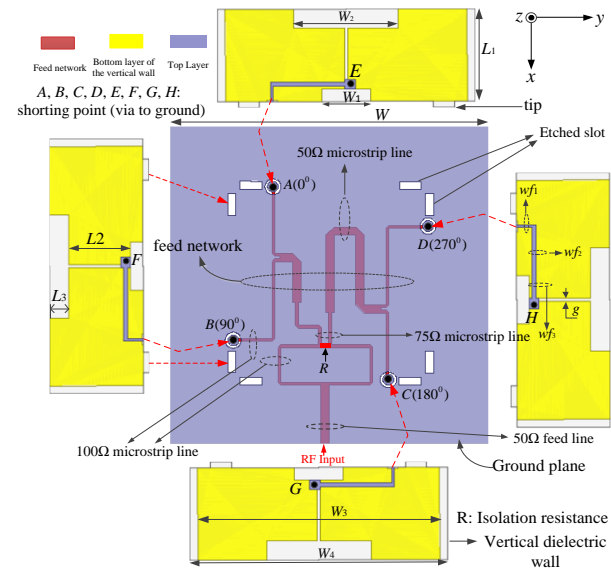
Fig. 1. Geometry and dimensions of the proposed antenna: W=60, w_1=7, w_2=15, w_3=36, w_4=37, wf_1=0.31, wf_2=0.67, wf_3=1.5, L_1=15, L_2=9.9, L_3=3.1. (Unit: mm).

To study the functions of the stepped configuration, the following cases, i.e., Ant 1(slot-line structure with metal wall and dielectric wall, which means that four rectangle patches encircle into a square ring wall successively), Ant 2 (stepped slot-line structure with metal wall and dielectric wall) and Ant 3 (stepped slot-line structure with dielectric wall and four separated rectangle patches) as shown in Fig. 2, are analyzed. The simulated results of |S11| of Ant 1, Ant 2 and Ant 3 are shown in Fig. 2. It is clear from the figure that Ant 1 produces wider impedance bandwidth owing to the extension of the effective current path on the metal wall formed by interconnected four rectangle patches, but the 3 dB AR bandwidth is poor. When the stepped slot-line structure is used in Ant 1, Ant 2 is formed. Although the impedance bandwidth is narrower, the axial ratio is improved. Ant 3 is formed by truncating the vertical edge of the rectangle patch in Ant 2, which shows that the

metal wall in Ant 2 is decomposed into four separated patches with same size. Because coupling between radiation patches is reduced, Ant 3 achieves better impedance bandwidth and 3 dB AR bandwidth, as shown in Fig. 2.

Figure 3 demonstrates the impact of varying the function of L_3 on the reflection coefficient of the antenna. The figure shows that when increasing L_3 the resonance band is shifted downward, and vice versa, i.e., the lowest working frequency is 3.82 GHz when $L_3=0$, the lowest working frequency is 3.65 GHz as the L_3 is added from 0 to 3.1 mm, and 3.37 GHz as L_3 is increased from 3.1 mm to 8.1 mm. Therefore, L_3 should be selected appropriately to compromise on good impedance matching and low profile requirement.
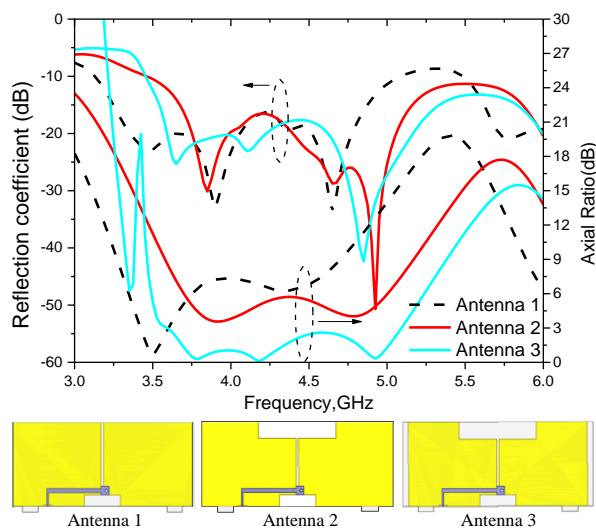
Fig. 2. Simulated reflection coefficient and axial ratio of Ant 1, Ant 2, and Ant 3.
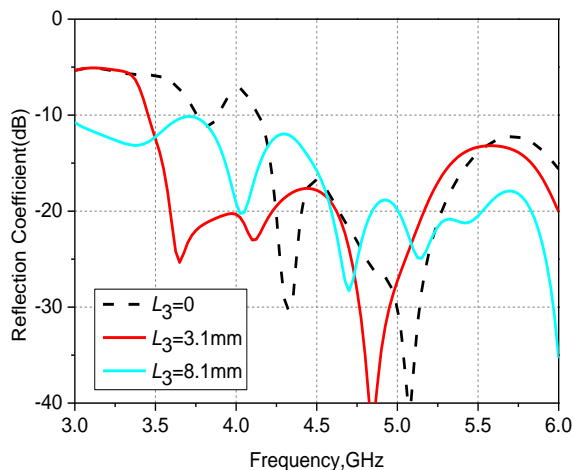
Fig. 3. Simulated reflection coefficient for the proposed antenna as a function of L_3.

Figure 4 shows the reflection coefficient and axial ratio performance versus frequency for different w_2 when other parameters are kept unchanged. It is clearly known from the figure that varying the parameter w_2 has less effect on impedance matching, whereas w_2 is increased from 5 mm to 20 mm, the AR bandwidth are slightly changed and three lowest AR values (f_1, f_2, f_3) are produced. It is also observed that with variety of w_2 results in significant shifts up of the first resonance (f_2), shifts downward of the second resonance (f_2), almost no change of third resonances (f_3). To have a wider and proper AR bandwidth, the parameter w_2 needs to be well optimized.
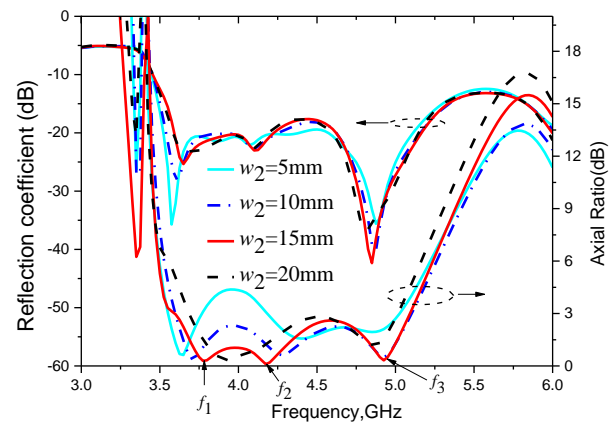
Fig. 4. Simulated reflection coefficient and axial ratio for the proposed antenna as a function of w_2.
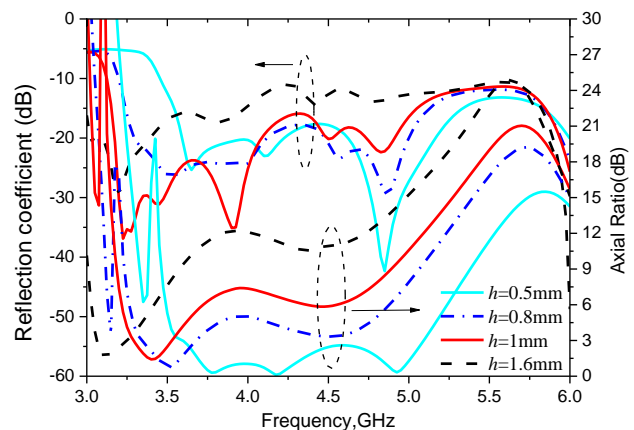
Fig. 5. Simulated reflection coefficient and axial ratio for the proposed antenna as a function of h.

The effect of the thickness of the supported dielectric wall (h) on reflection coefficient and axial ratio is illustrated in Fig. 5. It is found that the parameter h has large effect on the reflection coefficient and axial ratio. When the parameter h is increased, the curves of both reflection coefficient and axial ratio are shifted

downward, and the AR performance becomes worse. Results have revealed that the best performance is obtained when h=0.5 mm.

III. SIMULATED AND EXPERIMENTAL RESULTS

To verify the effectiveness of the design, a prototype of the proposed antenna with the dimensions shown in Fig. 1 was fabricated. A photograph of the fabricated antenna is displayed in Fig. 6 (a). The radiation performance of the antenna was measured in an anechoic chamber using the NSI300V-30X30 far-field measurement system and The VSWR results of the proposed antenna are measured using a calibrated Agilent vector network analyzer N5230A.

(a)

(b)
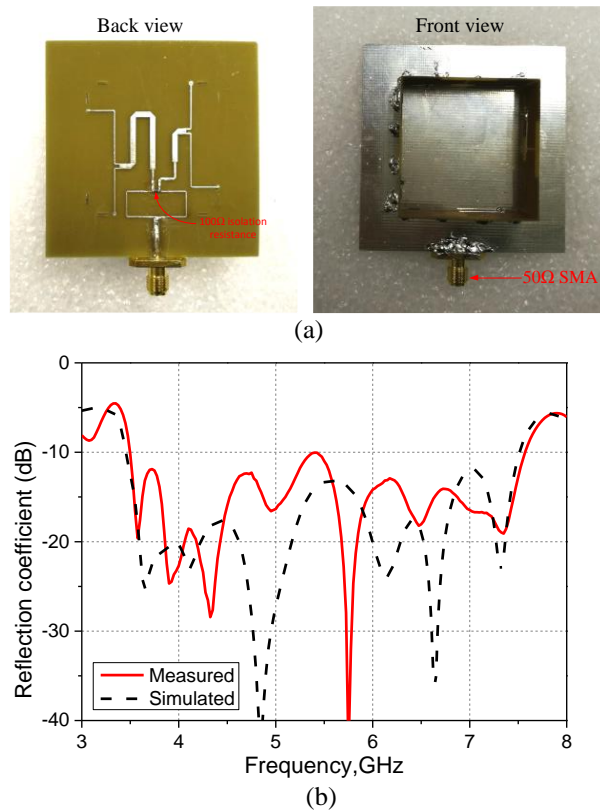
Fig. 6. (a) Fabricated antenna, and (b) comparison of simulated and measured reflection coefficient of the proposed antenna.

A. Reflection coefficient, axial ratio, and realized gain

Measured and simulated reflection coefficient for the proposed antenna are shown in Fig. 6 (b), which shows a little discrepancy due to the error of substrate parameters of the FR-4 substrate and tolerance in manufacturing. It is seen clearly that the measured reflection coefficient is less than -10 dB over the frequency ranges of 3.5 GHz–7.56 GHz (73.4%), which

is complied with simulated results. Figure 7 shows the comparison between the simulated and measured AR at broadside direction (+z). The measured 3-dB AR bandwidth of 3.65 GHz–5.2 GHz or 35.1% is obtained. Within the frequency range, the measured gain of the proposed antenna is 2.52 dBi on average and 4.27 dBi at maximum when the operating frequency is 5.2 GHz. A gain increased slightly over the operating band is found experimentally.

B. Radiation pattern

Figure 8 shows the comparison between the simulated and measured radiation patterns at 3.8 GHz, 4.2 GHz, and 4.95 GHz, in the xz-plane and yz-plane, respectively. It is seen that the proposed antenna radiates a right-hand circular polarization (RHCP), and has an approximately symmetrical radiation pattern across the operating bandwidth. The symmetrical radiation pattern should be attributed to the square ring-shaped radiator and system ground plane, whereas the back lobe and cross-polarization (left-hand circular polarization, LHCP) components are unsymmetrical in the working bands due to the effect of parasitical radiation of feed network and edge diffraction of compact ground plane. The measured and the simulated results of the RHCP radiation pattern are in good agreement, and its maximum beam is always directed to the +z-axis direction, which have great advantages in practical applications.

Fig. 7. Simulated and measured peak realized gain and axial ratio.

xz-plane   (a) 3.8 GHz yz-plane

xz-plane   (b) 4.2 GHz   *yz*-plane

xz-plane   (c) 4.95 GHz   *yz*-plane

— — LHCP(Simulation)   —— RHCP(Simulation)

— · — LHCP(Measurement) , —— RHCP(Measurement)

Fig. 8. Normalized radiation patterns at three resonant frequencies: (a) 3.8 GHz, (b) 4.2 GHz, and (c) 4.95 GHz.

C. Performance comparison

The performance of the proposed antenna is compared with previous designs in the literature in terms of fractional bandwidth, AR bandwidth, profile size, gain, as shown in Table 1. It is seen that our proposed antenna has the widest impedance bandwidth, while maintaining a low profile. More importantly, the designed antenna also shows good circularly polarized characteristics. From comprehensive view, our antenna is suitable for practical application environments. The design in [5] has a small AR bandwidth, though its profile is smaller than that of our antenna. The antenna in [12], constructed by using square patch, uses a four-feed network to equal amplitude and quadrature phase difference, while its bandwidth is still smaller a than that of our proposed antenna. The design in [13] has a very impressive low profile, though its bandwidth is very small, only 5.8%. Based on Vivaldi antenna structure, a wideband circularly polarized antenna is proposed in [15], but the profile size of $0.42\lambda_L$ is larger than that of our antenna. Compared with the works in [16, 17], our proposed antenna exhibits larger bandwidth.

Table 1: Performance comparison between the proposed antenna and other reported CP antennas

Reference	VSWR	Lowest Operating Frequency (λ_L is Referencing Wavelength)	Impedance Bandwidth	AR Bandwidth	Profile Size (mm)	Gain (dBi)
[5]	<2	1.54 GHz (194.8 mm)	11%	5%	24.8 ($0.127\lambda_L$)	>6.5
[12]	<1.5	0.86 GHz (348.8 mm)	19.7%	11%	34 ($0.097\lambda_L$)	8.36~9.65
[13]	<2	5.02 GHz (59.76 mm)	8.4%	5.8%	2.84 ($0.048\lambda_L$)	~5.58
[15]	<2	3.45 GHz (86.95 mm)	57.3%	41.4%	36.8 ($0.42\lambda_L$)	>6.9
[16]	<2	2.8 GHz (107.1 mm)	34%	34%	1.6 ($0.02\lambda_L$))	5.3~7.5
[17]	<2	3.45 GHz (86.95 mm)	13.5%	8%	1.6 ($0.02\lambda_L$))	4~7.8
This work	<2	3.65 GHz (82.2 mm)	73.4%	35.1%	15.5 ($0.19\lambda_L$)	0.69~4.74

IV. CONCLUSION

A low profile circularly polarized antenna based on stepped open-ended slot radiator has been presented in this paper. The antenna is formed by sequentially rotating four isolated rectangle patches with stepped slot-line, and encircle into a square ring structure, then is located vertically on a square ground plane. To realize broadband CP performance, Wilkinson power dividers, 90 degree delay line, and 180 degree delay lines are used to form a feed network of four output ports with a relative phase shift of 90 degree and equal amplitude, in which each output port is sequentially connected to the coupling micro-strip line on the interior face of the vertical dielectric wall. The optimized antenna has achieved a broad impedance bandwidth of 73.4% (3.5 GHz–7.56 GHz) (reflection coefficient less than -10 dB), a maximum gain of 4.74 dBi, and a 3-dB axial ratio (AR) bandwidth of about 35.1% (3.65 GHz–5.2 GHz). Moreover, the antenna is compact and its profile size is only about 0.19λ. The results indicate that the proposed antenna is an excellent candidate for various wireless systems.

Education Committee (No. KJ1600409).

REFERENCES

[1] I. Taha, K. Ayyuce, and S. ismail, "Circularly polarized microstrip patch antenna slits," *Appl. Comp. Electromagnetics Society (ACES) Conference*, EM Simulations Using Sonnet-I, 2010.

[2] Nasimuddin, Z. N. Chen, and X. M. Qing, "Asymmetric-circular shaped slotted microstrip antennas for circular polarization and RFID applications," *IEEE Trans. Antennas Propag.*, vol. 58, no. 12, pp. 3821-3828, 2010.

[3] K. F. Tong and T. P. Wong, "Circularly polarized U-slot antenna," *IEEE Trans. Antennas Propag.*, vol. 55, no. 8, pp. 2382-2385, 2007.

[4] S. Shekhawat, P. Sekra, D. Bhatnagar, V. K. Saxena, and J. S. Saini, "Stacked arrangement of rectangular microstrip patches for circularly polarized broadband performance," *IEEE Trans. Wireless Propag. Lett.*, vol. 9, pp. 910-913, 2010.

[5] T. Mondal, S. Samanta, R. Ghatak, and S. R. B. Chaudhuri, "A novel hexagonal wideband circularly polarized stacked patch microstrip antenna," *Microwave Opt. Technol. Lett.*, vol. 57, no. 11, pp. 2548-2554, 2015.

[6] Z. B. Wang, S. J. Fang, S. Q. Fu, and S. L. Jia, "Single-fed broadband circularly polarized stacked patch antenna with horizontally meandered strip for universal UHF RFID applications," *IEEE Trans. Microw. Theory Tech.*, vol. 59, no. 4, pp. 1066-1073, 2011.

[7] A. R. Weily and N. Nikolic, "Circularly polarized stacked patch antenna with perpendicular feed substrate," *IEEE Trans. Antennas Propag.*, vol. 61, no. 10, pp. 5274-5278, 2013.

[8] D. K. Singh, B. K. Kanaujia, S. Dwari, G. P. Pandey, and S. Kumar, "Novel quad-band circularly polarized capacitive-fed microstrip antenna for C-band applications," *Microwave Opt. Technol. Lett.*, vol. 57, no. 11, pp. 2622-2628, 2015.

[9] S. L. S. Yang and K. M. Luk, "A wideband L-probes fed circularly-polarized reconfigurable microstrip patch antenna," *IEEE Trans. Antennas Propag.*, vol. 56, no. 2, pp. 581-584, 2008.

[10] K. M. Luk, K. F. Lee, and H. W. Lai, "Development of wideband L-probe coupled patch antenna," *Appl. Comp. Electromagnetics Society (ACES) Journal*, vol. 22, no. 1, pp. 620-625, 2007.

[11] A. Kumar and M. V. Kartikeyan, "A circularly polarized stacked patch aperture coupled microstrip antenna for 2.6GHz band," *Int. J. Infrared Milli. Waves*, vol. 28, no. 1, pp. 13-23, 2007.

[12] P. Wang, G. Wen, J. Li, Y. Huang, L. Yang, and Q. Zhang, "Wideband circularly polarized UHF RFID reader antenna with high gain and wide axial ratio beamwidths," *Prog. Electromagn. Res.*, vol. 129, pp. 65-385, 2012.

[13] C. Jin, Z. X. Shen, R. Li, and A. Alphones, "Compact circularly polarized antenna based on quarter-mode substrate integrated waveguide subarray," *IEEE Trans. Antennas Propag.*, vol. 62, no. 2, pp. 963-967, 2014.

[14] K. K. M. Chan, A. E. C. Tan, and K. Rambabu, "Decade bandwidth circularly polarized antenna array," *IEEE Trans. Antennas Propag.*, vol. 61, no. 11, pp. 5435-5443, 2013.

[15] Y. J. Hu, Z. M. Qiu, B. Yang, S. J. Shi, and J. J. Yang, "Design of novel wideband circularly polarized antenna based on Vivaldi antenna structure," *IEEE Trans. Wireless Propag. Lett.*, vol. 14, pp. 1662-1665, 2015.

[16] M. H. Rasekhmanesh, A. Piroutiniya, and P. Mohammadi, "Wideband circularly polarized antenna array using sequential phase feed structure and U-shape radiating patch elements for S-band applications," *Microwave Opt. Technol. Lett.*, vol. 59, no. 11, pp. 2806-2812, 2017.

[17] M. H. Rasekhmanesh, P. Mohammadi, and A. Piroutiniya, "A circularly polarized miniaturized array using combination of circle and rectangular lines in the sequential phase feed structure," *Appl. Comp. Electromagnetics Society (ACES) Journal*, vol. 32, no. 4, pp. 339-343, 2017.

Ping Wang was born in Chongqing, China. He received his M.S. degree in Theoretical Physics from Chongqing University of China in 2008 and the Ph.D. degree in University of Electronic Science and Technology of China (UESTC) in 2013, respectively. Currently, he is working in Chongqing University of Posts and Telecommunications, China. His current research interests include patch antennas, wide band antennas, and arrays.

Qi Wu, master degree candidate of Chongqing University of Posts and Telecommunications. His main research direction is circularly polarized antenna, tag antenna, end-fire antenna, metamaterial, and electromagnetic theory and application in communication.

Yu Shao was born in Kunming, Yunnan Province, China. He received his M.Eng. degree in Electromagnetic Field and Microwave Technology from Wuhan University, Wuhan, China, in 2009 and the Ph.D. degree in Electrical Engineering from Auburn University, USA, in 2015. Currently, he is working in Chongqing University of Posts and Telecommunications, China. His research interests include computational electromagnetics, antennas and bio-electromagnetics.

Dong Huang was born in Chongqing, China. He currently is working in Chongqing Institute of Green and Intelligent Technology, Chinese Academy of Sciences, China. His research interests include computational electromagnetics, antennas and wireless communications.

Wearable Antennas for Body-Centric Communications: Design and Characterization Aspects

**Abdullah G. Al-Sehemi [1,2], Ahmed A. Al-Ghamdi [3], Nikolay T. Dishovsky [4],
Nikolay T. Atanasov [5], and Gabriela L. Atanasova [5]**

[1] Research Center for Advanced Materials Science (RCAMS)
King Khalid University, Abha, 61413, Saudi Arabia
agsehemi@kku.edu.sa

[2] Department of Chemistry
King Khalid University, Abha, 61413, Saudi Arabia
agsehemi@kku.edu.sa

[3] Department of Physics
King Abdulaziz University, Jeddah, Saudi Arabia
aghamdi90@hotmail.com

[4] Department of Polymer Engineering
University of Chemical Technology and Metallurgy, Sofia, 1756, Bulgaria
dishov@uctm.edu

[5] Department of Communication and Computer Engineering
South-West University 'Neofit Rilski', Blagoevgrad, 2400, Bulgaria
natanasov@windowslive.com, gatanasova@windowslive.com

Abstract ─ Wearable antennas exhibit numerous challenges in terms of design and optimization due to the specific environment in which they operate. Therefore, the design of such antennas is a non-trivial task, as multiple constraints have to be satisfied. We present an algorithm for design-and-optimization of flexible wearable antennas with high radiation efficiency and low specific absorption rate, that takes into account the dielectric loading of the human body. It provides a list of feasible antenna designs, not just a single solution, and identifies the optimal wearable antenna design. Numerical examples on the design and optimization of a wearable antenna (based on a dipole structure with a reflector) to demonstrate the validity and efficiency of the proposed algorithm are given. The optimal antenna design shows robust on-body performance and provides a suitable balance between small antenna size (antenna surface is 2214 mm^2), high radiation efficiency (57.73%), and low value of the maximum 10 g average SAR (0.112 W/kg) on a homogeneous semisolid phantom. Finally, the optimal antenna design is fabricated. The antenna performance is studied under different conditions: on a homogeneous semisolid phantom, on a liquid phantom, on a three-layer semisolid phantom, on a human arm and in the free space. A good agreement between simulated and measured antenna performance is observed.

Index Terms ─ Antenna characterization, antenna design, optimization, radiation efficiency, SAR, wearable antenna.

I. INTRODUCTION

Body-centric wireless communications (BCWCs) are held to have the potential to improve the quality of life and could offer significant benefits in commercial, military and medical applications, personal entertainment, and so on and so forth [1-6]. They will also play an important role in the upcoming era of the Internet of Things. Such systems provide short range low-power, and highly reliable wireless connectivity between devices worn on (or implanted in) the human body, or between two devices (body-to-body or body-hub) in close proximity. Consequently, three wireless communication channels (in-, on-, and off-body) exist.

The wearable antenna and radio wave propagation constitute the basic elements of the on- and off-body wireless channel. They determine reliability of the wireless link and have a great impact on the quality-of-

service offered by the whole system [7]. Therefore, the antenna design is a topic of great importance.

The wearable antennas exhibit numerous challenges in terms of design and optimization. For example, to achieve a good performance in a BCWCs system the wearable antenna should be insensitive to the effects of the human body in order to minimize detuning of the resonant frequency and degradation of the radiation efficiency. At the same time, the impact of the wearable antenna on human tissues also needs to be addressed, such as the maximum allowed specific absorption rate (SAR) [8]. The wearable antennas also should be compact, lightweight, and flexible, possibly allowing for integration with clothes and garment accessories [9]. Another limitation in the design of wearable antennas in which substrates are from textiles or polymer materials is finding of electromagnetic properties of the materials. In addition, these antennas have to show good radiation characteristics and high radiation efficiency [4]. Consequently, in wearable antenna design and optimization problems, several goals (impedance matching, bandwidth, compact size, high radiation efficiency, and low SAR) must be satisfied simultaneously in order to obtain an optimal solution.

An algorithm for flexible and wearable antenna design has been proposed in [10]. The proposed design procedure is mainly focused on the selection of the materials and on the analysis of the antenna structure in the free space, without to investigate the effect of the human body proximity on the antenna performance. In [11] the problem of optimization design of a microwave wearable antenna jointly with the model of human body that is located in the proximity of the antenna has been investigated. The presented optimization procedure uses full wave simulator based on finite difference time domain method (FDTD) to improve antenna design with respect to its impedance matching for several values of the antenna-to-body distance. In both [10] and [11], the antenna efficiency is not reported.

Recently, a number of algorithms like, ant colony optimization (ACO) [12], genetic algorithm (GA) [13, 14], and particle swarm optimization (PSO) [13] have been introduced for antennas aimed at either improving the current design or at speeding up the design process [15]. All of these algorithms are random search algorithms that are guided by biological principles. They all maintain a collection of possible solutions and use biologically based rules to search the objective function space for the best solution [13]. However, as the number of variables increase, the search space size grows exponentially, making it harder for these algorithms to find a suitable solution [16].

Multi-objective optimization has been presented for problems with more than one objective and its application to antennas for ground penetrating radar, satellite broadcast communications, and RFID tags has been reported in [17].

In this work, we firstly propose an improved algorithm for wearable antenna numerical design-and-optimization. The algorithm is based on the ideas in [13, 17] and has the advantage to provide a list of feasible antenna designs and to find the optimal solution that meets specifications. Next it is demonstrated using a planar dipole antenna. The presented algorithm can be quickly adopted in practice and applied to any wearable antenna structure.

The novelty in our work lies in the fact that we present a fast design of compact and flexible wearable antennas with high radiation efficiency and low SAR, that takes into account the dielectric loading of the human body.

II. NUMERICAL DESIGN-AND-OPTIMIZATION ALGORITHM

In this section in Fig. 1, we describe the proposed algorithm for wearable antenna numerical design-and-optimization. The principal difficulty in the design of a compact flexible wearable antenna is that both the human body and size miniaturization may affect antenna performance (such as resonant frequency, bandwidth and/or radiation efficiency).

Taking into consideration the above factors the first step in wearable antenna design is the selection of design goals and stopping criteria. We propose the following design goals: (1) minimization of the overall antenna size, (2) minimization of the reflection coefficient magnitude ($|S_{11}|$) at the desired resonant frequency (f_r), (3) maximization of the antenna radiation efficiency (RE), and (4) minimization of the specific absorption rate (SAR). The stopping criteria associated with these design goals can be expressed as: (1) First stopping criteria: $|S_{11}| \leq$ -15 dB at f_r, $|S_{11}| \leq$ -10 dB within the frequency band of interest, and $f_L \leq f_r \leq f_U$, (2) Second stopping criteria: RE $\geq$ 50 % and SAR $\leq$ 0.5 W/kg.

The next steps in the wearable antenna design are the selection of antenna topology and a suitable selection of materials, both for the conductive and nonconductive parts of the antenna [18]. A detailed review of available topologies for wearable antennas can be found in [3, 18-21] and a survey of the different types of materials for wearable antennas can be found in [3, 18, 21]. As mentioned above, the wearable antennas should be designed on flexible materials. Flexible materials like fabrics, polymers, and papers have been widely used in the existing wearable antennas. Consequently, the next important step when designing antennas on fabrics or polymer materials is a characterization of the electromagnetic (EM) properties of the materials like complex relative permittivity and/or permeability, loss tangent, and electric conductivity.

Once the antenna topology and materials for the conductive and nonconductive parts of the antenna

are selected and their electromagnetic properties are characterized, the next step is to provide an initial design of the wearable antenna. The initial antenna design has to originate from human experience, knowledge, innovation [22], and from a set of dimensional formulas. It includes techniques to design antenna elements and for generating a set of preliminary input design data for numerical full-wave EM analysis. Once the initial design of the antenna is known, the geometrical parameters for the optimization process have to be carefully selected and defined. In the next step third stopping criteria associated with geometrical parameters of the antenna (lower bound ≤ antenna geometrical parameters ≤ upper bound) also have to be provided.

Moreover, the design of one antenna for body-centric communications has to be carried out taking into account the human body effects [23]. Consequently, experimental and numerical phantoms of the human body have to be developed and their EM properties have to be extracting. A detailed review of various types of phantoms is presented in [9, 24]. The phantoms shapes, size, and electrical properties of the tissue-equivalent liquids are also provided in EN 62209-2-2010 [25], IEEE Std. 1528-2003 [26], and FCC 865664 D01 [27].

The next step in the numerical design-and-optimization algorithm is to build a numerical model of the antenna and phantom taking into account the electromagnetic properties of the materials. The last step before launching the EM simulations is the simulation parameters setup (boundary conditions, excitation, meshing). This is presented in Fig. 1 through the block labelled "Preprocessor". Various numerical methods are available in the literature, each with specific advantages and drawbacks, making them suitable for analysis, modeling, simulation, design and visualization of wearable antennas. These methods include Finite-Difference Time-Domain, Integral Equations/Method of Moments (MoM), Finite Element Method (FEM) [22].

The FDTD is probably the most popular technique for the analysis of wearable antennas. Reasons for its popularity include its versatility, low computational complexity, ability to accurately determine near- and far-field antenna characteristics over a wide frequency bandwidth from a single time domain simulation in the presence of complex materials (anisotropic, inhomogeneous and frequency dispersive). One drawback of the FDTD is the approximation of curved surfaces, due to the "staircasing" caused by the use of cubic cells [9].

MoM can be applied to structures made either of good conductors such as a wire antenna or being well described by an impedance boundary condition. This method is inefficient for the analysis of wearable antennas with complex materials (anisotropic and inhomogeneous) and its numerical cost grows very fast with increase of the upper corner frequency.
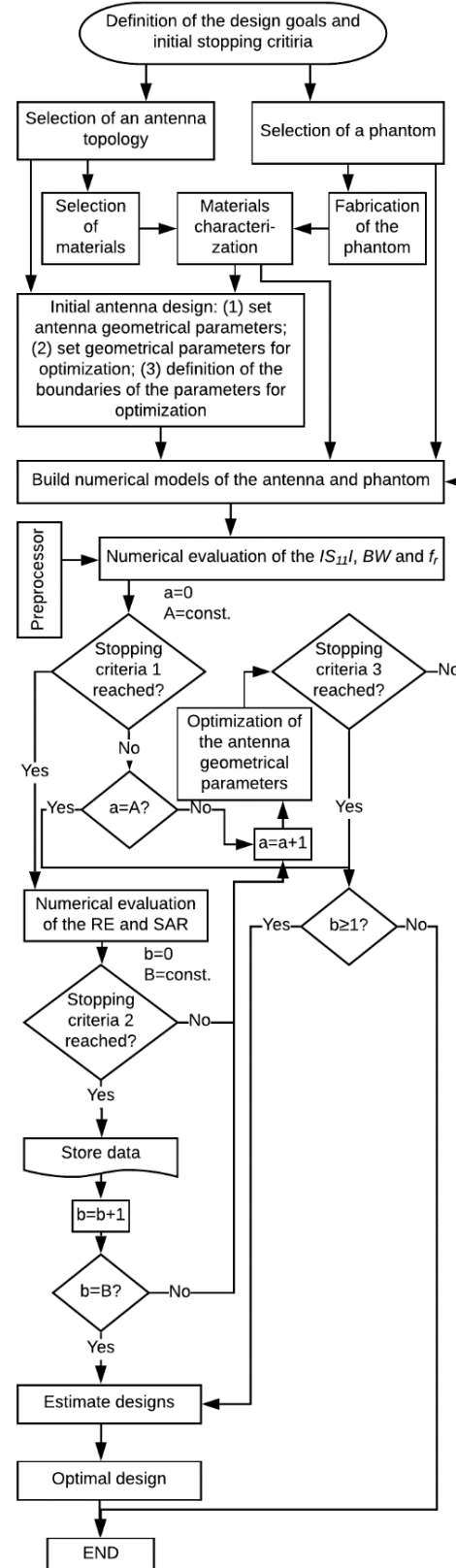
Fig. 1. A flowchart of the proposed design-and-optimization algorithm.

FEM is a frequency domain technique for the analysis and design of highly complicated antennas. The advantages of FEM are the flexibility in terms of modeling any complex geometries, irregular shapes, and inhomogeneous or dispersive materials. However, for geometrically and electrically large structures (such as the human body), the mesh can become very complex with many tetrahedral mesh cells. This in turn leads to huge matrices to solve which can require very large amounts of computer memory.

The optimization procedure starts from a cycle that selects new antenna design that satisfies the first stopping criteria ($|S_{11}| \leq$ -15 dB at f_r, $|S_{11}| \leq$ -10 dB within the frequency band of interest, and $f_L \leq f_r \leq f_U$), evaluates it, and subsequently updated numerical antenna model continues until a threshold is met or when the number of iterations exceeds a predefined maximum number of iterations (A = max number of iterations). The optimal antenna design obtained in the previous iteration of the optimization procedure is utilized as a starting point for the next optimization cycle. The cycle selects an antenna design that satisfies the second stopping criteria and stops when a threshold (finding the B = defined number of designs that satisfy second stopping criteria or after a defined maximum number of iterations) is met.

III. ILLUSTRATION EXAMPLES

In this section, we demonstrate the proposed algorithm for wearable antenna numerical design-and-optimization using a planar dipole structure, providing a compact flexible antenna with high radiation efficiency and low SAR for on-/off-body communications in the 2.4-2.48 GHz industrial, scientific, and medical (ISM) band.

The design goals for our first example are: (1) minimization of the overall antenna size, (2) minimization of the reflection coefficient magnitude at f_r = 2.44 GHz, (3) maximization of the antenna radiation efficiency, and (4) minimization of the specific absorption rate.

The proposed stopping criteria have been applied. In this example a dipole structure with a reflector has been selected and used as a candidate for evaluation of the proposed algorithm. The initial design of the antenna geometry is based on our earlier work [23] which demonstrated that the dipole antenna with a reflector is less affected by the presence of a human body model and consequently it is suitable for BCWCs.

Figure 2 (a) illustrates the geometry of dipole structure and microstrip line applied in the design of the wearable antenna. They are described by means of 10 geometrical parameters. Figure 2 (b) illustrates the overall geometry of the proposed wearable antenna. It is comprised of two components: (1) a planar dipole and a microstrip line which are placed on the first and second layer of a three-layer flexible dielectric material, and (2)

a metallic reflector which is placed on the third layer of the dielectric material. The overall geometry of the proposed wearable antenna is described by two geometrical parameters – width (W) and length (L). Stopping criteria 3 associated with geometrical parameters of the antenna is defined: 37.5 mm $\leq$ W $\leq$ 44 mm and 48 mm $\leq$ L $\leq$ 56 mm.
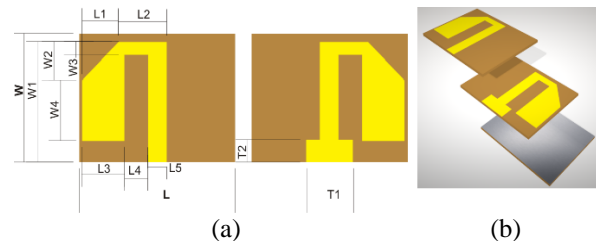
Fig. 2. The geometry of the: (a) dipole structure and (b) wearable antenna.

A brass foil with a thickness of 0.05 mm (for the radiating elements) and an aluminum foil with a thickness of 0.01 mm (for the reflector) are selected and used for the conductive parts of the antenna. For nonconductive parts of the antenna a composite based on natural rubber mixed with kaolin as a filler is synthesized and used. The rubber composite is selected as the antenna's substrate due to its notable features, such as high flexibility, ability to withstand mechanical strains and low dielectric loss. The electromagnetic parameters of the synthesized rubber composite were measured by the resonant perturbation method which is a well-known method for extracting electromagnetic properties of dielectrics, semiconductors, magnetic materials, and composite materials [28]. The real part of the relative permittivity is 2.481, imaginary part is 0.015, and the dielectric loss angle (tanδ) is 0.006 at 2.56 GHz.

Three different types of the human body phantoms are developed and fabricated. The first one is a homogeneous semisolid (gel) phantom with dimensions 100 mm × 47 mm × 117 mm and measured EM parameters to emulate human muscle tissue (relative permittivity $\varepsilon_r' = 40.81$ and conductivity $\sigma = 2.33$ S/m at 2.56 GHz). The EM properties of the phantom are in agreement with those of 2/3 muscle [29] (relative deviation within 15%). The second one is a liquid phantom. This phantom is widely used in SAR evaluation and can quite well represent tissues with high water content. The liquid phantom is a rectangular box with dimensions 300 mm × 150 mm × 360 mm made of Plexiglas having 2 mm thickness (phantom shell), filled with deionized water. The EM parameters of the liquid numerical phantom at 2.45 GHz are $\varepsilon_r' = 78.69$, $\sigma = 1.44$ S/m [26] for deionized water and $\varepsilon_r' = 2.67$, tanδ = 0.007 for the phantom shell. The third one is a three-layer semisolid model, consisting of skin, fat and muscle tissue

layers. The EM parameters and thickness of the different tissue layers of three-layer phantom in numerical calculation at 2.45 GHz are presented in Table 1 and assumed to be in [29].

Table 1: Material properties and thickness of three-layer semisolid phantom in numerical calculation

	ε_r'	σ (S/m)	ρ (kg/m³)	Thickness (mm)
Skin	38.006	1.464	1020	1.0
Fat	5.280	0.105	918	6.0
Muscle	53.574	1.81	1040	40.0

The numerical models of the antenna and homogeneous phantoms (semisolid and liquid) are simulated in XFdtd (xFDTD, Remcom Inc., State College, PA, USA) a software that utilizes the finite-difference time-domain method. Each simulation is accomplished under the following conditions: a non-uniform cubic-cell mesh (cell size of 0.5 mm and 5 mm) and a perfectly matched layer (7 layers) is used at the boundaries of the computational domain. The 12-field components approach is used to calculate SAR in the voxel.

To simplify antenna geometry generation, the numerical models of the dipole structure and microstrip line are first optimized on the homogeneous semisolid phantom and all 10 variables of the geometrical parameters are updated to meet the design specifications. The resulting design parameter values have been achieved in 152 iterations and are listed in Table 2. The antenna is directly placed onto the surface of the semisolid phantom, as in Fig. 3 (a).

Table 2: Parameter values of the dipole structure and microstrip line, which have been optimized by dint of the proposed algorithm for wearable antenna design

Parameter	Value (mm)	Parameter	Value (mm)
L1	12.0	W2	12.0
L2	15.5	W3	4.0
L3	13.5	W4	19.0
L4	7.5	T1	15.0
L5	6.0	T2	7.0

Next numerical optimization of the wearable antenna is performed in two steps. In the first step a number of solutions (optimized antenna structures) that satisfy the first stopping criteria are found. These are obtained through update of the parameters W and L of the numerical antenna model in an iterative way until a threshold (the number of solutions exceeds 25) is met or when the number of iterations exceeds 50. At each

iteration is generated a new numerical model of the antenna directly placed onto the surface of the numerical semisolid phantom and a simulation in XFdtd is launched. Figure 4 shows the obtained number of 22 solutions. Each point denotes a feasible design solution with three coordinates. Each design solution is denoted by the geometrical parameters W (mm) x L (mm) (width (mm) x length (mm)) of the antenna. From Fig. 4, it can be seen that the antenna size is reduced from 2,464 mm² to 1,968 mm² (miniaturization ratio of 20%). The designs are utilized as starting points for the next step of the algorithm.

(a)

(b)

(c)
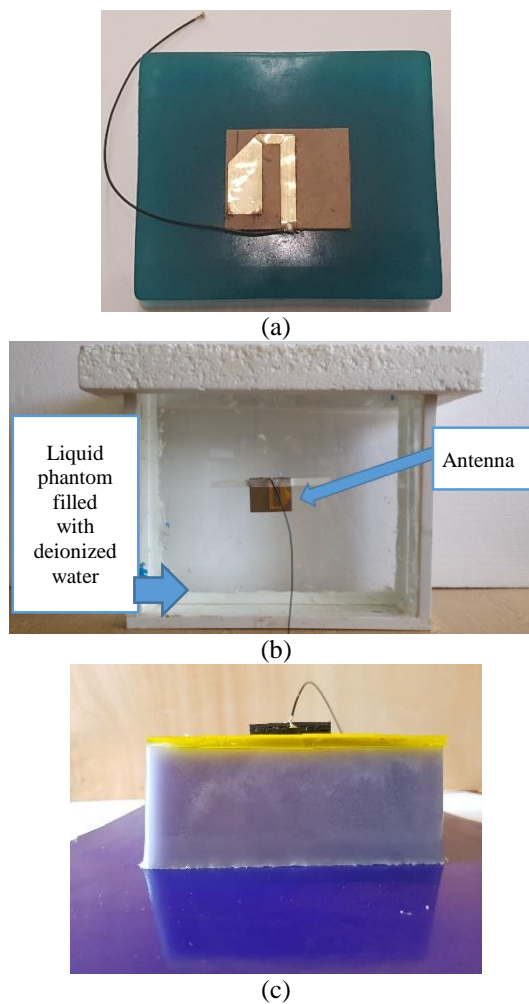
Fig. 3. Photographs of the fabricated human body phantoms with a prototype of the wearable antenna: (a) homogeneous semisolid, (b) liquid, and (c) three-layer semisolid.

In the next step radiation efficiency and SAR of the optimized antenna structures are estimated. The cycle selects antenna designs that satisfy second stopping criteria. Figure 5 shows the obtained number of 22

solutions (optimized antenna structures) after 40 iterations.

Design 44 x 56 provides the highest radiation efficiency (60.23%) and lowest maximum 10 g average SAR (0.103 W/kg) among all designs but no benefits in antenna size reduction (antenna surface is 2,464 mm^2) and bandwidth. Design 41 x 48 shows a significant size reduction (about 20%) and bandwidth enhancement compared with other designs, but it presents also lowest radiation efficiency (52.54%). Consequently, there is a large trade-off between the achieved size reduction and the radiation efficiency. Design 41x54 is an optimal antenna design that provides a suitable compromise between the small antenna size (antenna surface is 2,214 mm^2), high radiation efficiency (57.73%) and low value of the maximum 10 g average SAR (0.112 W/kg) in the ISM band.

The next verification of the proposed algorithm involved the design and optimization of a wearable antenna directly placed on the surface of a liquid phantom.

The design goals are same as for the first example. Again, first a number of solutions (optimized antenna structures) that satisfies the first stopping criteria are found and utilized as starting points for the next step.

In the next step radiation efficiency and SAR of the optimized antenna structures are estimated. Figures 6 and 7 show the obtained number of 20 solutions. It can be observed that the antenna size is reduced from 2,464 mm^2 to 1,920 mm^2 (miniaturization ratio of 22%). Designs 41 x 50 - to - 41 x 56 have the same SAR values (0.094 W/kg) but they are different in terms of radiation efficiency and bandwidth. Similarly, as for the previous example, design 44 x 56 provides the highest radiation efficiency (59.31%) and lowest maximum 10 g average SAR (0.059 W/kg) among all designs but no benefits in antenna size reduction (antenna surface is 2,464 mm^2) and bandwidth.

Design and optimization of the proposed wearable antenna on the homogeneous liquid phantom lead to negligible enhancement of the bandwidth and reduction of maximum 10 g average SAR values compared to the semisolid phantom. The reason to obtain these results can be explained by the location of the antenna to the phantoms. For the semisolid phantom, the antenna touches to the surface of the phantom, and this makes the higher SAR values. Compared to the semisolid phantom, the liquid phantom has a thin shell (2 mm), which does not allow the estimation of the SAR on the phantom surface.

The last verification of the proposed algorithm involved the design and optimization of a wearable antenna directly placed on the surface of a three-layer phantom. The design goals and steps are same as for the first and second example. Figures 8 and 9 show the obtained number of 22 solutions.
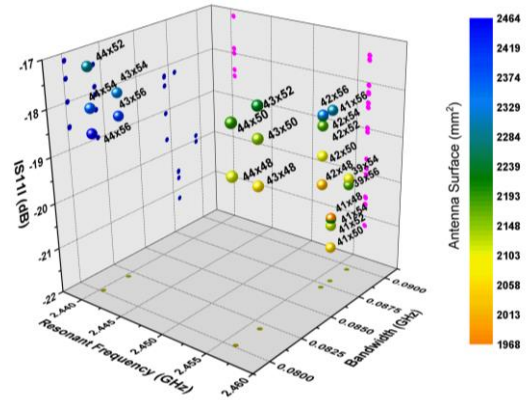
Fig. 4. A set of solutions satisfying constraints in first stopping criteria, obtained using the proposed algorithm. The wearable antenna is placed on a homogeneous semisolid phantom.
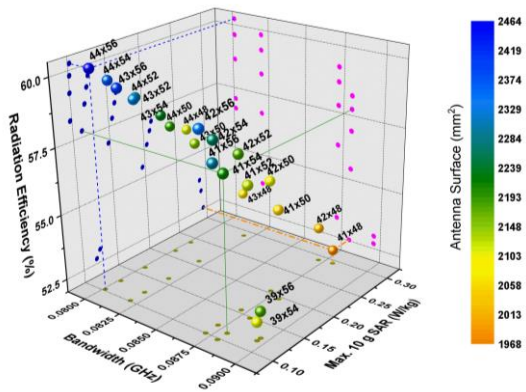
Fig. 5. A set of solutions satisfying constraints in second stopping criteria, obtained using the proposed algorithm. The wearable antenna is placed on a homogeneous semisolid phantom.
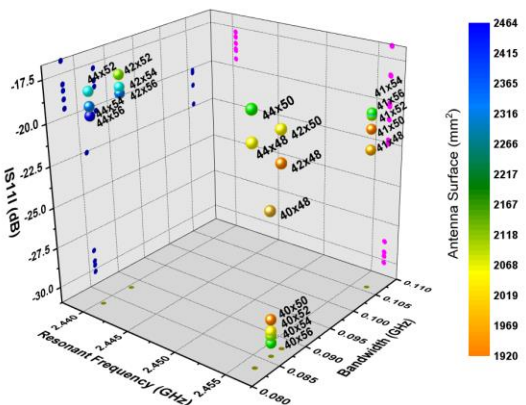
Fig. 6. A set of solutions satisfying constraints in first stopping criteria, obtained using the proposed algorithm. The wearable antenna is placed on a liquid phantom.
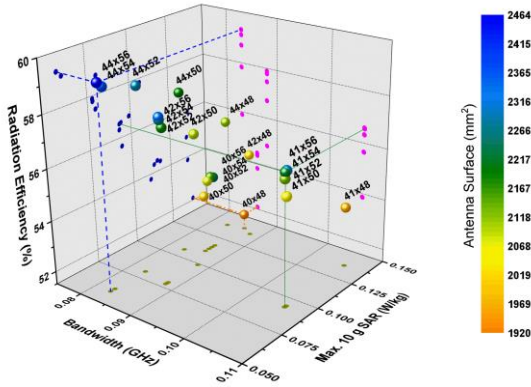
Fig. 7. A set of solutions satisfying constraints in second stopping criteria, obtained using the proposed algorithm. The wearable antenna is placed on a liquid phantom.
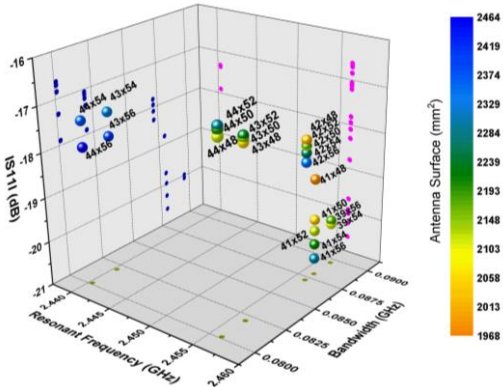
Fig. 8. A set of solutions satisfying constraints in first stopping criteria, obtained using the proposed algorithm. The wearable antenna is placed on a three-layer semisolid phantom.
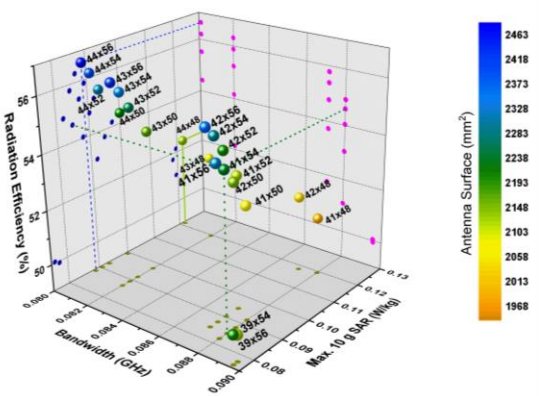
Fig. 9. A set of solutions satisfying constraints in second stopping criteria, obtained using the proposed algorithm. The wearable antenna is placed on a three-layer semisolid phantom.

Design and optimization of the proposed wearable antenna on the three-layer phantom lead to negligible reduction of the radiation efficiency (from 60.23% on homogeneous phantom to 56.20% on three-layer phantom for design 44 x 56) and reduction of maximum 10 g average SAR values compared to the homogeneous semisolid phantom.

IV. EXPERIMANTAL VALIDATION

In order to verify the proposed algorithm a prototype of the selected design 41 x 54 (width (mm) x length (mm) of the antenna) of the wearable antenna has been fabricated. The antenna performance in terms of reflection coefficient magnitude, bandwidth and radiation efficiency is analyzed under different conditions.

The measured and simulated $|S_{11}|$ curves of the optimized design are shown in Fig. 10. The experimental results are obtained when the antenna is mounted on the surface on the semisolid phantom and on the shell of the liquid phantom, as shown in Fig. 3. The results for antenna performance in the free-space and on human arm are also presented in Fig. 10 for comparison. It can be seen that, the measured $|S_{11}|$ curves agree well with the simulated curves. Moreover, the antenna exhibits a measured operating ($|S_{11}| \leq$ -10 dB) bandwidth of 118 MHz on the semisolid phantom, 119 MHz on the liquid phantom, 119 MHz on human arm and 95 MHz in the free space. The simulated operating bandwidth of the proposed antenna on the semisolid phantom is 88 MHz, 106 MHz on the liquid phantom and 94 MHz in the free space. A good agreement between simulated and measured results is observed.
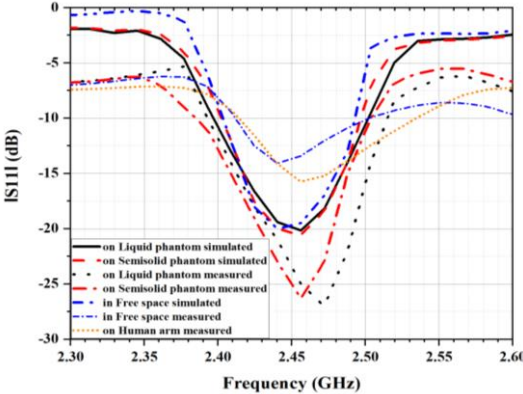
Fig. 10. The plot of reflection coefficient magnitude of selected design 41 x 54 when the antenna is placed on human body phantoms, human arm, and in the free space.

In addition, Table 3 shows measured and simulated radiation efficiency, and simulated maximum 10 g average SAR for design 41 x 54 at 2.44 GHz. In the Fig.

11 are presented 3D radiation patterns of the selected design at 2.44 GHz in four different conditions.

Table 3: Radiation efficiency (%) and maximum 10 g average SAR (W/kg) of the optimized wearable antenna

Phantom	Semisolid	Liquid	Three-Layer	Free Space
Measured RE (%)	50.21	49.87	-	58.53
Simulated RE (%)	57.73	56.55	54.60	64.36
Simulated SAR (W/kg)	0.112	0.093	0.085	-

From Fig. 11 can be seen that the 3D radiation patterns are very similar even with three different body phantoms except for minor differences in the direction of the phantom (backward direction). The antenna in the free space has a 7.23 dB front-to-back ratio, which increases to 16.27 dB, 17.55 dB, and 23.38 dB when the antenna is placed on a three-layer semisolid, on a homogeneous semisolid, and on a liquid phantom, respectively. In the backward direction the lowest radiation is obtained for liquid phantom, due to the larger size and attenuation. The peak antenna gain is 5.565 dBi on the homogeneous semisolid, 4.570 dBi on three-layer, and 5.225 dBi on the liquid phantom, while in the free space the peak antenna gain is 4.504 dBi. The peak gain of the antenna increases (about 1 dB) when the antenna is placed on a phantom due to reflections of propagating waves from the phantom, however the efficiency is decreased [1].

(a)   (b)
(c)   (d)
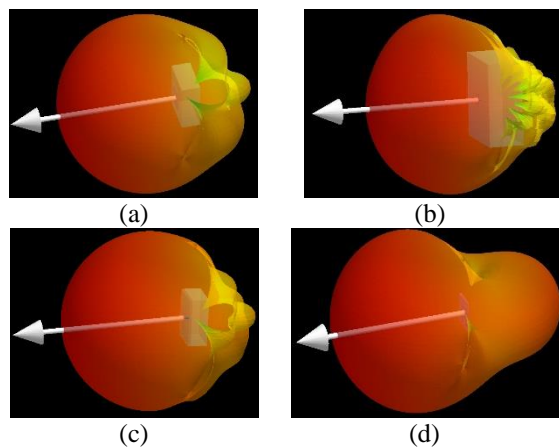
Fig. 11. 3D radiotion pattern of selected design 41 x 54: (a) on the semisolid phantom, (b) on the liquid phantom, (c) on the three-layer phantom, and (d) in the free space.

V. CONCLUSION

In conclusion, we have proposed a novel algorithm to design-and-optimization of flexible wearable antennas with high radiation efficiency and low SAR, that takes into account the dielectric loading of the human body. It provides a list of feasible antenna designs, not just a single solution and identifies the optimal wearable antenna design. The proposed algorithm has been validated using a planar dipole antenna with a reflector placed on a homogeneous semisolid phantom, a three-layer phantom and on a liquid phantom. The optimal antenna design was constructed, and antenna performance was studied under different conditions. The antenna shows robust on-body performances. Measured results demonstrate that a bandwidth of 118 MHz on semisolid phantom, 119 MHz on the liquid phantom, 119 MHz on the human arm, and 95 MHz in the free space is achieved. Moreover, measured radiation efficiency of 50.21%, 49.87%, and 58.53% is realized when the antenna is placed on the surface of semisolid and liquid phantom, and in the free space, respectively. Hence, optimization results achieved with described algorithm show that antenna size reduction is obtained without compromise in radiation efficiency, bandwidth and SAR. The presented algorithm can be quickly adopted in practice and applied to any wearable antenna structure.

The next step of the research work is to apply the algorithm in the case of more complex wearable antennas such a fractal antennas or antenna over a metasurface.

REFERENCES

[1] P. Hall and Y. Hao, *Antennas and Propagation for Body-Centric Wireless Communications*, 2nd ed., Artech House, London, 2012.

[2] Q. H. Abbasi, M. U. Rehman, K. Qaraqe, and A. Alomainy, *Advances in Body-Centric Wireless Communication: Applications and State-of-the-Art*, IET, London, 2016.

[3] N. F. M. Aun, P. J. Soh, A. A. Al-Hadi, M. F. Jamlos, G. A. E. Vandenbosch, and D. Schreurs, "Revolutionizing wearables for 5G," *IEEE Microwave Magazine*, vol. 18, no. 3, pp. 108-124, May 2017.

[4] A. Y. I. Ashyap, Z. Z. Abidin, et al., "Inverted E-shaped wearable textile antenna for medical applications," *IEEE Access*, vol. 6, pp. 1-9, June 2018.

[5] K. Ito, N. Haga, M. Takahashi, and K. Saito, "Evaluations of body-centric wireless communication channels in a range from 3 MHz to 3 GHz,"

Proceedings of the IEEE, vol. 100, no. 7, pp. 2356-2363, July 2012.

[6] W. -C. Chen, B. DeLong, R. Vilkhu, and A. Kiourti, "Enabling batteryless wearables and implants," *ACES Journal*, vol. 33, no. 10, pp. 1106-1108, Oct. 2018.

[7] S. Dumanli, L. Sayer, E. Mellios, X. Fafoutis, G. S. Hilton, and I. J. Craddock, "Off-body antenna wireless performance evaluation in a residential environment," *IEEE Trans. on Antennas and Propagt.*, vol. 65, no. 11, pp. 6076-6084, Nov. 2017.

[8] G. Conway, S. Cotton, and W. Scanlon, "An antennas and propagation approach to improving physical layer performance in wireless body area networks," *IEEE J. on Selected Area in Comm.*, vol. 27, no. 1, pp. 27-36, Jan. 2009.

[9] A. Pellegrini, A. Brizzi, et al., "Antennas and propagation for body-centric wireless communications at millimeter-wave frequencies: A review," *IEEE Antennas and Propagt. Magazine*, vol. 55, no. 4, pp. 262-287, Aug. 2013.

[10] H. Khaleel, *Innovation in Wearable and Flexible Antennas*, WIT press, Southampton, 2015.

[11] Ł. Januszkiewicz, P. D. Barba, and S. Hausman, "Optimization of wearable microwave antenna with simplified electromagnetic model of the human body," *OpenPhys.*, vol. 15, pp. 1055-1060, Nov. 2017.

[12] A. Zare and S. Baghaie, "Application of ant colony optimization algorithm to pattern synthesis of uniform circular antenna array," *ACES Journal*, vol. 30, no. 8, pp. 810-818, Aug. 2015.

[13] P. Rocca and R. Haupt, "Biologically inspired optimization of antenna arrays," *ACES Journal*, vol. 29, no. 12, pp. 1047-1059, Dec. 2014.

[14] K. Fertas, H. Kimouche, M. Challal, H. Aksas, R. Aksas, and A. Azrar, "Design and optimization of a CPW-fed tri-band patch antenna using genetic algorithms," *ACES Journal*, vol. 30, no. 7, pp. 754-759, July 2015.

[15] Z. Li, Y. Erdemli, J. Volakis, and P. Papalambros, "Design optimization of conformal antennas by integrating stochastic algorithms with the hybrid Finite-Element method," *IEEE Trans. on Antennas and Propagt.*, vol. 50, no. 5, pp. 676-684, May 2012.

[16] D. Prado, J. Álvarez, M. Arrebola, M. Pino, R. Ayestarán, and F. Las-Heras, "Efficient, accurate and scalable reflectarray phase-only synthesis based on the Levenberg-Marquardt algorithm," *ACES Journal*, vol. 30, no. 12, pp. 1246-1255, Dec. 2015.

[17] X. Travassos, D. Vieira, and A. Lisboa, "Antenna optimization using multiobjective algorithm," *ISRN Communications and Networking*, vol. 2012, pp. 1-8, 2012.

[18] P. Nepa and H. Rogier, "Wearable antennas for off-body radio links at VHF and UHF bands: Challenges, the state of the art, and future trends below 1 GHz," *IEEE Antennas and Propagt. Magazine*, vol. 57, no. 5, pp. 30-52, Oct. 2015.

[19] N. H. M. Rais, P. J. Soh, F. Malek, S. Ahmad, N. B. M. Hashim, and P. S. Hall, "A review of wearable antenna," *Loughborough Antennas & Propagation Conference*, pp. 225-228, Nov. 2009.

[20] B. Gupta, S. Sankaralingam, and S. Dhar, "Development of wearable and implantable antennas in the last decade: A review," in *Proceedings of the 10th Mediterranean Microwave Symposium (MMS '10)*, pp. 251-267, Aug. 2010.

[21] S. Dhupkariya, V. K. Singh, and A. Shukla, "A review of textile materials for wearable antenna," *J. Microwave Eng. Technol.*, vol. 1, no. 3, pp. 2349-9001, Oct. 2015.

[22] C. A. Balanis editor, *Modern Antenna Handbook*, John Wiley & Sons, Inc., Hoboken, 2008.

[23] A. Al-Sehemi, A. Al-Ghamdi, N. Dishovsky, N. Atanasov, and G. Atanasova, "On-body of a compact planar antenna on multilayer polymer composite for body-centric wireless communications," *AEU – International Journal of Electronics and Communications*, vol. 82, pp. 20-29, Dec. 2017.

[24] T. Björninen, "Comparison of three body models of different complexities in modelling of equal-sized dipole and folded dipole wearable passive UHF RFID tags," *ACES Journal*, vol. 33, no. 6, pp. 706-709, June 2018.

[25] EN 62209-2, *Human exposure to radio frequency fields from hand-held and body mounted devices – Human models, instrumentation, and procedures - Part 2: Procedure to determine the specific absorption rate (SAR) for wireless communication devices used in close proximity to the human body (frequency range of 30 MHz to 6 GHz)*, IEC, 2010.

[26] *IEEE for Recommended Practice for Determining the Peak Spatial-Average Specific Absorption Rate (SAR) in the Human Head from Wireless Communications Devices: Measurement Techniques*, IEEE Standard 1528, 2003.

[27] FCC, *SAR measurement requirements for 100 MHz to 6 GHz*, Aug. 2015.

[28] L. Chen, C. Ong, C. Neo, V. V. Varadan, and V. K. Varadan, *Microwave Electronics: Measurement and Materials Characterization*, 1st ed., John Wiley & Sons, Ltd., 2004.

[29] https://transition.fcc.gov/fcc-bin/dielec_file

Abdullah G. Al-Sehemi is a Professor in the Department of Chemistry King Khalid University, Saudi Arabia. He received his Ph.D. from University of Leicester, UK. He is currently Member of the Saudi Consultative Council. He was the Dean of Scientific Research and Director of The Research Center for Advanced Materials Science (RCAMS). He is an author of over 200 publications, co-inventor of several patents and the editor of 6 books. He is working experimentally and computationally in the field of advanced functional materials, nanomaterials, stereochemistry, and drug design.

Ahmed A. Al-Ghamdi is a Staff Member at King Abdul Aziz University (KAU), Faculty of Science, Physics Department. He obtained his B.Sc. in Physics from KAU at 1981 and master's degree in 1985 from Tulane University, USA. The Ph.D. degree was obtained in 1990 from Sussex University, UK, in point defects created by ion implantation. He has 26 years of experience in academic and research activities in solid state physics. He worked in the various field of solid physics applications including photodiodes, gas sensors, biosensors, and various another field of applications. He is currently working in synthesis, characterization and applications in composites and nanocomposites.

Nikolay T. Dishovsky received the Ph.D. degree from the University of Chemical Technology and Metallurgy, Sofia, in 1983 and the Doctor of Science Degree from the same university in 1997. Since 2000 he is a Full Professor and Head of the Department of Polymer Engineering at the University of Chemical Technology and Metallurgy. He is the author of 8 books, more than 230 articles, and more than 45 patents for inventions. Dishovsky was a recipient of the Bulgarian Patent Office award for the Inventor of the Year 2015. His research interests include fillers and filled elastomers, rubber based nanocomposites, rubber based sensors and microwave absorbers.

Nikolay T. Atanasov received the M.Sc. and Ph.D. degrees from the Technical University of Sofia, Sofia, Bulgaria, in 1999 and 2013, respectively.

He is currently an Associate Professor in the Department of Communication and Computer Engineering, South-West University 'Neofit Rilski', Blagoevgrad, Bulgaria. His research interests include computational electrodynamics, SAR computation, design of antennas for wireless devices, medical diagnostic and therapeutic applications of EM. He is particularly interested in the characterization of the electromagnetic properties of the materials at microwave frequencies and investigation of the potential of conductive composites for the antenna applications.

Gabriela L. Atanasova received the M.Sc. and Ph.D. degrees from the Technical University of Sofia, Sofia, Bulgaria, in 1999 and 2013, respectively.

She is an Associate Professor in the Department of Communication and Computer Engineering, South-West University 'Neofit Rilski', Blagoevgrad, Bulgaria. Her research interests encompass theoretical and experimental studies for modeling interactions between EM fields and biological systems, as well as methods for the computer-aided analysis and design of high-frequency structures and antennas.

Modelling Approach to Predict the RFID Read Rates on a Complex Set of Materials

Renuka Nalinggam [1] and Widad Ismail [2]

[1] Faculty of Engineering & Information Technology, Southern University College
Jalan Selatan Utama, Off Jalan Skudai, 81300 Skudai, Johor
renukanalinggam@sc.edu.my

[2] Auto ID Laboratory, School of Electrical and Electronic Engineering, Universiti Sains Malaysia (USM)
Engineering Campus, 14300 Nibong Tebal, Pulau Pinang, Malaysia
eewidad@usm.my

Abstract ─ This research provides a platform to prove the potential of radio-frequency identification (RFID) technology for use in hypermarket payment systems. A 2.54 GHz ZigBee-based embedded passive and active RFID (EPARFID) system was developed to obtain experimental data and subsequently analyze passive RFID characteristics. A read rate prediction model based on materials permittivity value is proposed. Combining experimental data with analytical electromagnetic models improved the extrapolation of RFID read rates in a given environment. The modelling approach is a step toward the development of a robust methodology to predict RFID read rates on a complex set of materials. Results obtained from the proposed prediction modelling of read rates based on the Friis free space equation by quantifying uncertainties provide new insights into the nature of tag read rates.

Index Terms ─ Relative permittivity, RFID modelling, RFID on complex materials, RFID read rate prediction.

I. INTRODUCTION

Radio-frequency identification (RFID) technology is applied to the location and tracking of objects. Thus, RFIDs are used in a wide range of industrial fields, such as factory automation, distributed and process control, traceability management, supply chain management, real-time monitoring of health, and radiation check [1]. RFID has been recently applied to many location identification systems to detect the presence of tagged objects and/or people. Localization using an RFID reader is important to provide improved and efficient context-aware services [1]. Most studies related to RFID focus on the application of RFID technology to provide tag identification and for tracking purposes only [2].

Considering that studies focus on the development of a prototype to be applied at item-level tagging for retail applications, researchers have presented several comparisons based on previous literature findings on the RFID system application to retail tracking systems. This comparison review aims to determine the accurate problem encountered in a retail platform. Moreover, the review will contribute to the research by identifying priority factors that require attention and providing potential solutions for problems.

From the reviews [3-6], researchers anticipate and highly recommend the standardized RFID system for global application and tag performance (despite the material surface) as a highly recommended concern. Thus, the current research was conducted to offer potential solution for the issues highlighted in the review.

RFID is related to the procedure of transmitting and recognizing object in the form of a unique serial number through the RF wave. The range of an RFID system is determined by the power emitted by the reader antenna, the power available within the tag, the type of passive tag, the orientation of the antenna and the tag, and the surface of the material on which the tag is placed. The power available within the tag received from the reader will be converted into energy to activate the chip inside the tag. Tagged surface materials also play a vital role, because they may influence RFID performance in terms of distance and read rate because of the effect of various parameters, such as dielectric constant, radiation efficiency, and radiation impedance caused by the diversity of material properties [7]. Radio-frequency (RF) signals contain information that has been modulated from RF waves. The behavior of RF signals can be detected and predicted. They can be interfaced with other signals and react differently to various materials. Typical material reactions toward RF signals are reflection, absorption, and attenuation, which reduce the reliability and performance of RFID systems in terms of tag detection [8]. This phenomenon limits the implementation of RFID systems on material-related

applications. Different materials produce varying read rates in an RFID system.

Performing experiments on material reaction using the preferred materials is a highly effective means to obtain the read rate of each type of material. However, measuring the read rates of all materials available in hypermarkets is economically not feasible and time consuming. The lack of measured read rate data on a material of interest results in the development of power prediction models. Many models are available for predicting tag read rates [9-13].

Most models are developed by focusing only on available power in tags, reader-transmitted power, antenna gain, and distance estimation. To demonstrate the eligibility of RFID technology for hypermarket application, tag surface material parameters are the factors considered in a prediction model. Although numerous researchers have developed prediction models [9-13] (as summarized in Table 1) that can be used to predict tag read rates, uncertainties remain in selecting a suitable model that can be applied to research. Thus, real-time measurement results should be compared with a suitable prediction model to validate its accuracy. Each prediction model has advantages and limitations. A power prediction model should be modified on the basis of limitations observed in existing models. Therefore, determination of measured experimental data is an important requirement to select an optimum read rate prediction model.

The current research aims to develop a multi-band RFID by embedding the passive and active RFIDs as a single system platform (EPARFID), investigate the eligibility of the developed EPARFID system in hypermarkets' checkout payment system, and propose a suitable modified RFID read rate prediction model to predict tag read rate reliability on the basis of the materials' relative permittivity. RFID (passive system) and WSN are integrated into an active RFID (EPARFID) system to determine the existence of a significant improvement in monitoring. This process will provide an opportunity for the RFID technology to work in a wireless platform, with a long range, wide area, and in multi-hop communication [6], as shown in Fig. 1.
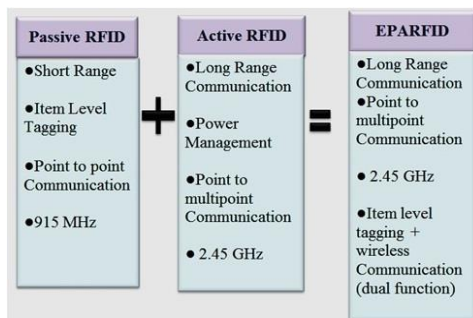
Fig. 1. Passive and active (EPARFID) system layout.

Table 1: Review on available RFID read rate prediction models

Research Title	Input Parameters	Outcome	Application
[9]	P_r, G_r, G_t, λ and d	Undefined	Experimental data presentation on critical aspects of the UHF RFID systems
[10]	Reader: P_r, P_T, G_r, G_T, and radar cross section of the RF tag	To quantify the effects on RF tag material attachment	RF tag designer
[11]	Impedance matching, coupling coefficient, and impedance-matching coefficient	To obtain power observed by the tag chip	Item-level tagging
[12]	EIRP, G_{Reader}, S_{11}, S_{22}, S_{21}, LF, R_2 and X_2	To predict power transmitted to the chip	To predict electromagnetic compatibility performance in complex aeronautic areas
[13]	Zc (chip input impedance) and Za (antenna input impedance)	To predict impedance matching between the reader antenna and the tag chip	Compact and low-profile tag for metal application
Proposed EPARFID System	P_r, G_r, G_t, ε_r, λ, and d	RFID read rate prediction based on dielectric permittivity	RFID system developers for hypermarket or supply chain application

The passive and active portions in the proposed EPARFID system are non-separable. They involve three main segments, namely, passive tag (tag on materials), active tag (payment counter), and active reader (display). The system must perform two types of communications to display the data. The first part of communication occurs between the passive and active tags. The second part of communication occurs between the active tag and the active reader. Then, the data can be displayed. During the first-part communication, passive RFID-related characteristics, such as distance between passive tag and reader, passive tag on materials, and passive tag surface are found. During the second part of the communication,

active RFID-related characteristics, such as multi-hop, throughput, self-healing, and latency were discovered.

Therefore, the actual experiments were conducted to identify the abovementioned characteristics and provide standard guidelines for the EPARFID system. On the basis of these characteristics, the power prediction model was modified. Moreover, the result was compared with the actual experiment data to determine efficiency. The power prediction model parameters focused on the passive RFID characteristics and not the active RFID. As stated previously, the segments in the EPARFID system are non-separable portions, and the research focused on hypermarket application. Thus, passive RFID characteristic parameters, such as placement of passive tag on materials, the materials' permittivity value, and the distance between passive tag and reader, become the main concerns in model modification. This finding is explained by the fact that the first segment communication (Passive RFID) of the EPARFID system affects the second segment communication (Active RFID) of the system.

This work aims to provide fundamental data on the design of experiments that involve a complete analysis related to standard packaging materials available in hypermarkets.

Many researchers [3, 4, 13-16] acknowledged that dielectric materials provide significant effects on RFID reading performance. Their studies are emphasized on tag surface dielectric permittivity value only. Tag surface dielectric permittivity value alone is insufficient for this research as packaging materials in retails contain a certain filling. Therefore, emphasis on the permittivity value of the surface (metal, glass, plastic, and cardboard) and the subsurface (water, powder, and paste) of packaging materials is an added novelty for this research. Table 2 presents the relative permittivity values of the surface and subsurface of the materials involved in this research.

In practical applications, quantities such as polarizabilities and scattered thicknesses are not the most convenient to use. Instead, it is preferable to play with the permittivity of the components of the mixture. The most common mixing rule is the *Maxwell Garnett* formula, which is written explicitly for the effective permittivity [17].

The mixing equation for general thin mixture is as follows:

$$\varepsilon_{eff} = \varepsilon_e + 3f\varepsilon_e \frac{\varepsilon_i - \varepsilon_e}{\varepsilon_i - 2\varepsilon_e}, \tag{1}$$

where f is the ratio between $\frac{\varepsilon_i}{\varepsilon_e}$, for the Maxwell Garnett prediction of the effective permittivity of a mixture with inclusions of permittivity, and ε_i in a background medium of permittivity, ε_e. Therefore, ε_i and ε_e are defined as subsurface and surface relative permittivities, respectively [17].

II. MODIFICATION OF A POWER PREDICTION MODEL

A simple propagation model is used as a reference to predict passive tag read rates at difference distances and tag surfaces. The modelling approach is one step toward the development of a robust methodology for predicting RFID read rates on a complex set of materials. Thus, a power prediction model equation, namely, equation (2), is modified to determine the power absorbed by an RFID tag chip. Simple dipole-like antennas are utilized in all ultra-high frequency (UHF) passive tags. These antennas can be easily fabricated, and their size is controlled due to the radiation wavelength. Efficient power delivery to the chip by the power available at the tag antenna will maximize tag performance [18].

In general, the power P_t received and available at the tag antenna output connector can be generally determined, as follows:

$$P_t = P_r . \rho . C, \tag{2}$$

where P_r is the power at the input connector of the reader antenna, ρ is the impedance-matching coefficient between the reader and its antenna, and C is the coupling coefficient between the reader's and tag's antennas [11].

In UHF RFID systems, critical conditions are met far from the reader's antenna, in which the maintenance of high-power levels is important to activate passive tags and ensure an observable backscattered signal [14]. Such configuration allows UHF systems to operate under far-field conditions at the reader and tag sides. Under these conditions, the radiated electric and magnetic fields propagate as plane waves perpendicular to one another and to the wave propagation direction.

When an ideal matching between the reader and its antenna ($\rho = 1$) is considered, P_t in Equation (2) (unit: dBm) changes into the following:

$$P_{t,dBm} = P_{r,dBm} + G_{t,dB} + G_{r,dB} + \rho_{dB} + 20 . \log_{10}\left(\frac{\lambda}{4\pi d}\right), \tag{3}$$

where G_r and G_t are the antenna gains of the reader and tag, respectively; ρ is the polarization mismatch coefficient between these gains; and d is the distance between the reader's antenna, which is the attenuation caused by propagation in space.

However, the tag antenna designed for a particular application, such as for mounting on a metallic surface, may be incompatible with a different surface, even that within the same class of products. This phenomenon is explained by the limit of the antenna's bandwidth, which leads to detuning when placed on a material with dielectric properties outside the design range.

In real-life applications, performance may deteriorate closer to the reader's antenna. In general, inferior performance can be expected with respect to distance, because parasitic effects (i.e., relative permittivity)

influence system behavior. Accordingly, this research focuses on the influence of dielectric permittivity on RFID read range performance [3]. Thus, the dielectric permittivity ($\mathcal{E}_r$) of tagged surfaces is a crucial parameter that should be included in Equation (3). When the wave penetrates the permittivity medium with relative permittivity $\mathcal{E}_r$, the wavelength becomes the following:

$$\lambda = \frac{1}{f\sqrt{\mu_0\varepsilon_0\varepsilon_r}}, \qquad (4)$$

where $\mathcal{E}_r$ is the relative permittivity value of the medium [18]. Table 2 provides the relative permittivity values of the materials involved in this research. This research focuses on the tag surface and subsurface of materials. Thus, Fig. 2 illustrates the emphasized tag surface and subsurface.
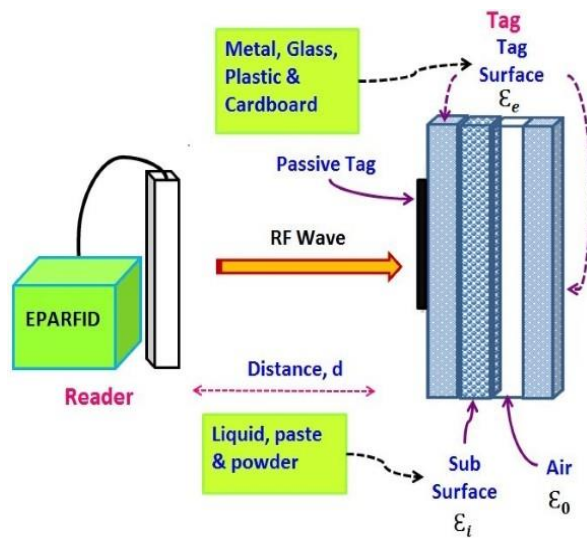
Fig. 2. Illustration of the emphasized tag surface and subsurface emphasized.

Tag surface permittivity and filling permittivity are combined based on (1). Tag surface (e.g., metal, glass, plastic, and cardboard) permittivity value is defined as environment permittivity $\mathcal{E}_e$. By contrast, the content of respective materials (e.g., water, paste, detergent, and powder) is assumed as inclusion permittivity $\mathcal{E}_i$. The value of f obtained for all the combinations is lower than 1. Hence, the respective material permittivity value is substituted into (1). Table 3 presents the $\mathcal{E}_{eff}$ value substituted into (4) as the $\mathcal{E}_r$ value based on the respective material's surface and subsurface values and the respective material's effective permittivity values. The terms provided in Table 3 are the small form of the standard packaging material's surface and subsurface, that is, MLA means the following: (M) stands for metal surface, (L) stands for liquid subsurface, and (A) is the tag type.

Table 2: Permittivity of respective materials

Materials	Dielectric Permittivity, $\mathcal{E}_r$
Metal (M)	9.7
Plastic (P)	2.5
Glass (G)	8
Cardboard (C)	2
Air	1
Water/Liquid (L)	78
Powder (P)	3.5
Paste (D)	50

Table 3: Absolute permittivity values of material combination in the research

Terms	Material Surface (Environment Permittivity, εe)	Material Subsurface (Inclusion Permittivity, εi)	εeff
MLA		78	66.01
MPA	9.7	3.5	6.50
MDA		50	39.31
GLA		78	67.76
GPA	8	3.5	4.41
GDA		50	50.00
PLA		78	74.43
PPA	2.5	3.5	2.71
PDA		50	50.00
CLA		78	75.11
CPA	2	3.5	2.50
CDA		50	40.67

A tag is assumed to be readable if P_t exceeds a power threshold P_{th}. When $P_t < P_{th}$, the available power is insufficient for the tag to respond [9]. The following is a summary of the main parameters. Their values are used to check the power absorbed by the tag at 0.3 m. In this scenario, the tag is placed on a cardboard filled with powder. $P_r = 30$ dBm; $G_r = 8$ dB; $G_t = 2.15$ dB; $\varepsilon_{eff} = 2.50$; $\lambda = 0.2073$ m; $d = 0.3$ m.

When the preceding parameters are substituted into (3), the prediction of the power absorbed by the tag is 11.981 dBm. The P_t value is higher than $P_{th} = -12$ dBm. Thus, the tag is assumed to be readable. The method is repeated at different distances of 0.5 and 0.7 m, as shown in Table 4. Figure 3 displays the layout design of the measurement setup of the embedded passive and active RFID (EPARFID) system with three different distances.

III. RESULT AND ANALYSIS OF THE MODIFIED POWER PREDICTION MODEL

Variations between 0 and 0.3 m, 0.3 and 0.5 m, and 0.5 and 0.7 m were implemented to obtain 10 average values of the tags that responded and those that did not respond. On the basis of the average value of the linear

equation, the respective distance was obtained as follows [19]:

$$P_t = 0.9478\varepsilon_{eff} + 9.5412 \text{ at } 0.3 \text{ m}, \quad (5)$$
$$P_t = 0.9478\varepsilon_{eff} - 10.549 \text{ at } 0.5 \text{ m}, \quad (6)$$
$$P_t = 0.9478\varepsilon_{eff} - 40.459 \text{ at } 0.7 \text{ m}. \quad (7)$$

Table 4: Received power level of the tag with respect to the effective permittivity ε_{eff} for the distances of 0.3, 0.5, and 0.7 m

Surface + Subsurface	ε_{eff}	Non-Line-of-Sight Transmission P_t (dBm)		
		0.3 m	0.5 m	0.7 m
CLA	75.11	−2.860	−5.782	−13.488
PLA	74.43	−2.820	−5.743	−13.449
GLA	67.76	−2.413	−5.335	−13.041
MLA	66.01	−2.299	−5.221	−12.928
CDA	47.18	−0.840	−3.763	−11.469
PDA	46.52	−0.779	−3.702	−11.408
GDA	40.67	−0.196	−3.118	−10.824
MDA	39.31	−0.048	−2.970	−10.677
MPA	6.50	7.768	4.846	−2.861
GPA	4.41	9.453	6.530	−1.176
PPA	2.71	11.567	8.645	0.939
CPA	2.50	11.918	8.995	1.289
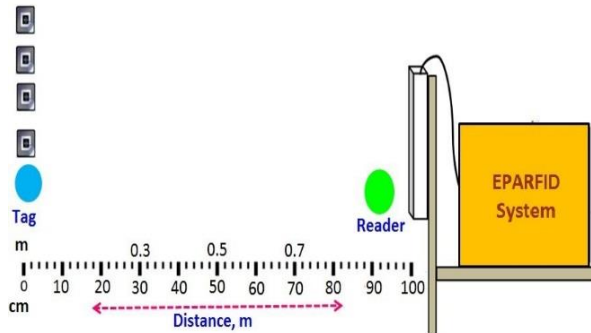
Fig. 3. Measurement setup of the EPARFID system with three different distances.

On the basis of Equations (5), (6), and (7), the graphs of the received power level of the tag with respect to the relative permittivity are plotted for the distances of 0.3, 0.5, and 0.7 m in Figs. 4 to 6. As shown in Fig. 4, the received power of the tag at all the relative permittivity values is higher than −12 dBm, which indicates that 100% of the tag detection is achieved at 0.3 m. As shown in Fig. 5, most of the values are maintained at a level higher than the threshold value. By contrast, Fig. 6 shows that the tag with a dielectric permittivity value of over 50 is not detected at 0.7 m.
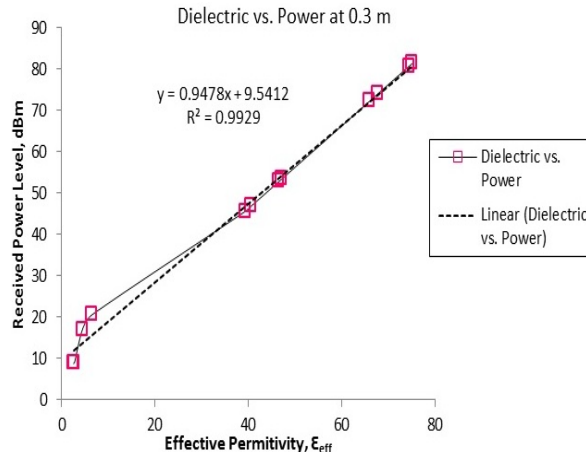
Fig. 4. Dielectric vs. received power of the tag at 0.3 m.

Ten average values obtained from the EPARFID system and predicted by the proposed model were compared at distances of 0.3, 0.5, and 0.7 m. In terms of detection percentage, the EPARFID system and the modelling achieved 100% at 0.3 m. At 0.5 m, the detection percentages achieved by the EPARFID system and the modelling are 90% and 96.8%, respectively. The detection achieved at 0.7 m by the EPARFID system is 65.5%, and that of the modelling is 68.7%. The modelling achieves 0 root mean square (RMS) value at an ideal distance, and the value increases with increasing distance. At low RMS value, the performance improves. The distance between the tag and the reader significantly affects system performance. Thus, higher RMS value is obtained at a longer distance.

The tag read rate reliability percentages of the EPARFID system and the proposed model are calculated as follows:

$$Read\ Rate\ Reliability\ (\%) = \frac{Responded\ Tag}{Total\ Tag} \times 100\%. \quad (8)$$

The responded tag in (8) indicates the total number of tags that successfully responded during the experiment. Total tag denotes the number of experiment repetitions. All the experiments were repeated 10 times to obtain 10 average data for analysis.

At 0.3 m, the modelling and EPARFID system achieved 100% tag detection. Thus, 0.3 m is the optimum distance between the tag and the reader regardless of the tag surface and orientation, as shown in Fig. 7. Moreover, the modelling and EPARFID system maintained a 100% detection percentage for tag surfaces with an effective permittivity of 2.5–20 at 0.5 m. The model and EPARFID system achieved 90% detection percentage for an effective permittivity of 20–60 and 80% for an effective permittivity of 60 and higher, as shown in Fig. 8. At 0.7 m, the EPARFID system

maintained 70% detection percentage for tag surfaces with an effective permittivity of 2.5–60. Then, the percentage dropped to 60% and 50% for effective permittivity of 60–70 and 70 and higher, respectively. By contrast, the proposed model achieved 80% detection percentage for an effective permittivity of 2.5–10, 70% for an effective permittivity of 40–60, and 60% for an effective permittivity of 60 and higher as shown in Fig. 9.
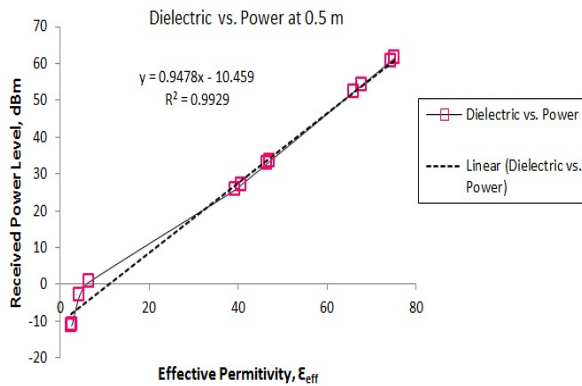
Fig. 5. Dielectric vs. received power of the tag at 0.5 m.
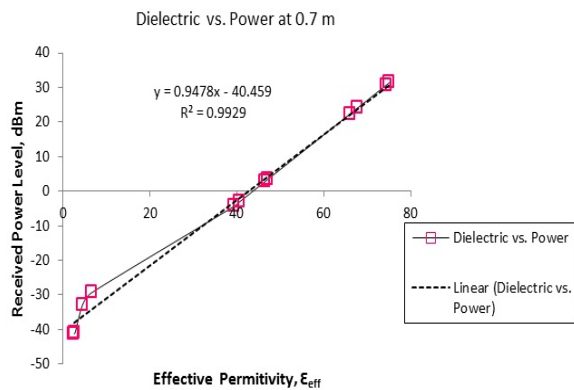
Fig. 6. Dielectric vs. received power of the tag at 0.7 m.
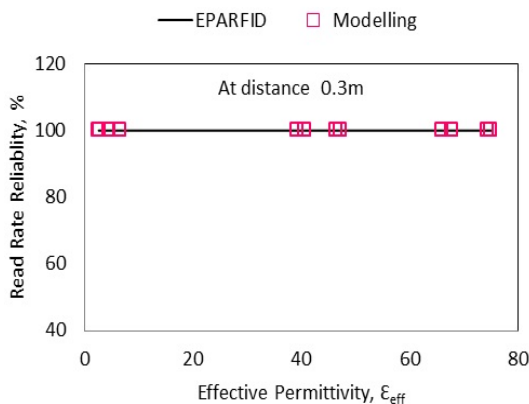
Fig. 7. EPARFID system vs. proposed model at 0.3 m.

The analysis demonstrates that the presence of dielectric materials on the tag surface can damage RF signal strength and reduce its read range performance, because the tag no longer works in free space. A tag antenna designed for a particular application, such as mounting on a metallic surface, may be incompatible with a different surface, even that belonging to the same class of products. This phenomenon is due to the bandwidth limit of the antenna. Detuning occurs when the tag is placed on a material with dielectric properties outside the designed range. Moreover, the thickness of a material affects the tuning of dielectric media with medium to high permittivity and varying thickness values. Therefore, fixing the distance between the tag and the reader can be a potential solution for selecting a standard RFID system and tag that can be applied to different materials. The analysis proves that the distance between the reader and the tag is a critical aspect that requires consideration during system performance. The optimum performance of the proposed system can be achieved by maintaining the distance between the tag and the reader at 0.3 m. As the distance between the tag and the reader increases, the performance percentage of the tag decreases or the tag becomes unreadable.
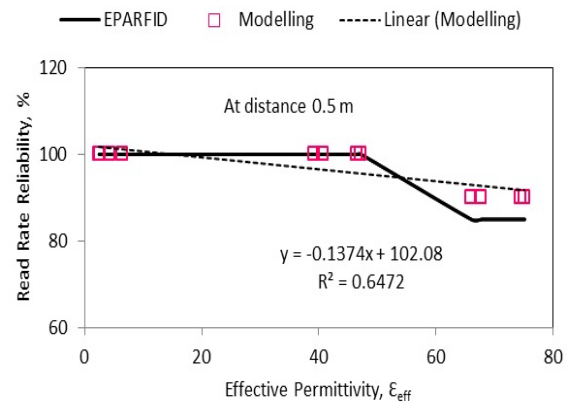
Fig. 8. EPARFID system vs. proposed model at 0.5 m.
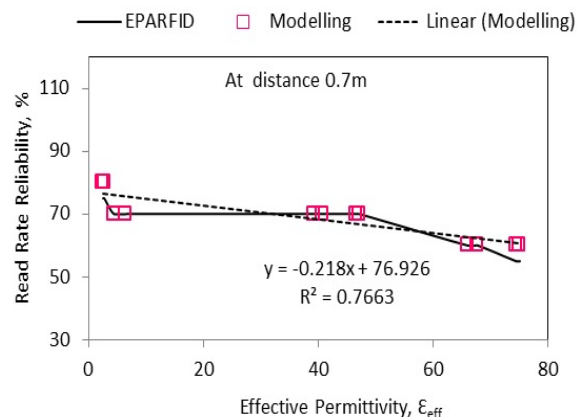
Fig. 9. EPARFID systems vs. proposed model at 0.7 m.

The analysis indicates that the power data predicted by the proposed model closely follow the experimental data obtained from the EPARFID system experiments, particularly at the ideal distance of 0.3 m. The confirmation of the closeness of the proposed model verified that the EPARFID system's experimental data can be observed at 0.5 and 0.7 m.

IV. CONCLUSION

This research successfully validates that RFID technology does not require line-of-sight transmission to detect passive tags. The tag detection results are precise regardless of orientation if the distance between the passive tag and the reader does not exceed 0.3 m, depending on the signal quality of the reader. The relative dielectric permittivity of the materials used in the experiment significantly affects EPARFID performance. Materials with low relative permittivity demonstrate consistent performance than materials with high relative permittivity. Perceiving trends on how read rate probabilities vary with distance, power level, and tag surface relative permittivity for a set of materials is remarkable. Combining experimental data with analytical electromagnetic models improves the extrapolation of RFID read rates in a given environment. The results obtained from the proposed prediction model of read rate based on Friis free space equation by quantifying uncertainties provide new insights into the nature of tag read rates. Furthermore, confirming the closeness of the results of the proposed modelling approach to the EPARFID system experimental data establishes the validity of the proposed modelling approach. In conclusion, the findings and discussions presented by this research possibly serve as a guideline for improving feasibility and eligibility of the EPARFID system development and framework and create awareness for retail application on item-level tagging.

ACKNOWLEDGEMENT

REFERENCES

[1] L. Wang, L. D. Xu, Z. Bi, and Y. Xu, "Data cleaning for RFID and WSN integration," *IEEE Transactions on Industrial Informatics*, 10(1), 408-418, 2014.

[2] D. De Donno, L. Catarinucci, and L. Tarricone, "A battery-assisted sensor-enhanced RFID tag enabling heterogeneous wireless sensor networks," *IEEE Sensors Journal*, 14(4): pp. 1048-1055, 2014.

[3] S. Shao, "Design approach for robust UHF RFID tag antennas mounted on a plurality of dielectric surfaces," *IEEE Antennas and Propagation Magazine*, vol. 56, 2014.

[4] M. Attaran, "Critical success factors and challenges of implementing RFID in supply chain management," *Journal of Supply Chain and Operations Management*, vol. 10, no. 1, 2012.

[5] A. Sabbaghi, "Effectiveness and efficiency of RFID technology in supply chain management: Strategic values and challenges," *Journal of Theoretical and Applied Electronic Commerce Research*, vol. 3, issue 2, 2008.

[6] P. C. Jain and K. P. Vijayagopalan, "RFID and wireless sensor networks," *Proceedings of ASCNT, CDAC*, Noida, India, 2010.

[7] L. H. Mei, et al., "Influence of UHF tags in the different material surface to RFID system," *Antennas and Propagation (APCAP), 2014 3rd Asia-Pacific Conference*, IEEE, 2014.

[8] M. N. O'Grady and J. P. Kerry, "Smart packaging technologies and their application in conventional meat packaging systems," in *Meat Biotechnology*, Springer, pp. 425-451, 2008.

[9] I. A. D. Chiara, "Analysis of performance and interferance effects in radio frequency identification systems," 2011.

[10] J. D. Griffin, et al., "RF tag antenna performance on various materials using radio link budgets," *IEEE Antennas and Wireless Propagation Letters*, 5(1): pp. 247-250, 2006.

[11] P. V. Nikitin, K. Rao, and S. Lazar, "An overview of near field UHF RFID," in *RFID*, 2007. *IEEE International Conference on*, 2007, *IEEE*, 2007.

[12] A. Piche, et al., "RFID equivalent model for prediction of functional and EMC performances in complex aeronautic environments," *Aerospace EMC (Aerospace EMC), 2016 ESA Workshop on*, IEEE, 2016.

[13] Y. Zhang, et al., "Design of miniaturized UHF RFID tag antenna attached to dielectric and metallic objects," *Antennas and Propagation & USNC/URSI National Radio Science Meeting, 2015 IEEE International Symposium on*, IEEE, 2015.

[14] J. Baker-Jarvis, M. D. Janezic, and D. C. Degroot, "High-frequency dielectric measurements," *IEEE Instrumentation & Measurement* Magazine, 2010.

[15] M. Periyasamy and R. Dhanasekaran, "Assessment and analysis of performance of 13.56 MHz passive RFID in metal and liquid environment," In *Communications and Signal Processing (ICCSP), 2014 International Conference on IEEE*, pp. 1122-1125, 2014.

[16] J. Xie, M. Wang, and J. Tan, "A novel method to evaluate the RFID system reliability," *Procedia Engineering*, 174, 465-469, 2017.

[17] A. Sihvola, "Mixing rules with complex dielectric

coefficients," *Subsurface Sensing Technologies and Applications,* (1)4: 393-415, 2000.

[18] L. A. Kosuru, "Optimum performance of UHF RFID tags in dielectric environment," *University of Kansas*, 2011.

[19] J. M. Govardhan, "Performance modeling and design of backscatter RFID systems: A statistical approach," *Oklahoma State University*, 2006.

Renuka Nalinggam obtained her B.S. in Engineering from Universiti Tenaga Nasional in 2005 and her M.Sc. from Universiti Sains Malaysia in 2012. She worked as a Lecturer in the Asian Institute of Medical, Science and Technology University from 2011 to 2012. She currently serves as a Lecturer in Southern University College, Skudai, Johor, while pursuing her Ph.D. in Universiti Sains Malaysia. Her research interests are machine-to-machine communication, radio-frequency identification, and wireless sensor networks.

Widad Ismail is a Professor and Project Coordinator for the Auto-ID Laboratory, Universiti Sains Malaysia. She obtained her B.S. in Engineering (First Class Honors in Electronics and Communication Engineering) from the University of Huddersfield, United Kingdom (1999). She obtained her Ph.D. in 2004 (Active Integrated Antenna with Image Rejection) in Electronics and Communication Engineering from the University of Birmingham, United Kingdom. She worked in the University of Birmingham from 2000 to 2003 as a postgraduate teaching assistant. She has been working as a Lecturer in Universiti Sains Malaysia since 2004. Her areas of research are wireless system design, radio-frequency identification, active integrated antennas, and radio-frequency and microwave systems engineering. She is also a member of the Institute of Electrical and Electronics Engineers and the Wireless World Research Forum.

Ultra Wideband Power Divider Design Implementing Microstrip with Slotted Ground

Norhudah Seman [1*], Khairul H. Yusof [2], Mohd H. Jamaluddin [1], and Tharek A. Rahman [1]

[1] Wireless Communication Centre, School of Electrical Engineering
University Teknologi Malaysia, 81310 UTM Johor Bahru, Johor, Malaysia
huda@fke.utm.my, haizal@fke.utm.my, tharek@fke.utm.my

[2] Faculty of Engineering and Information Technology, MAHSA University
42610 Jenjarom, Selangor, Malaysia
khairulhuda@mahsa.edu.my

Abstract ─ This article proposes a compact design of a two-section power divider, which operates over an ultra wideband frequency range of 3-11 GHz. The design approach of microtrip with slotline at the ground plane is applied to reduce the size of the circuit and to achieve wide bandwidth coverage. The rectangular slots are implemented at the ground plane, which is positioned symmetrically underneath the second and third arms of each microstrip quarter-wave transformer to reduce its length up to 33.34%. These attributes lead to an easily fabricated 20 mm x 23 mm compact power divider with a reduced size (by 23.33%). The bandwidth performance is improved up to 19.4% compared to a conventional divider. The design is realized by implementing the Rogers TMM4 substrate and simulated by using CST Microwave Studio. The power divider is verified by using a vector network analyzer (VNA). A good agreement between simulation and fabrication is achieved in terms of return loss, isolation and transmission coefficients across the UWB frequency range.

Index Terms ─ Microstrip-slot, power divider, two-section, ultra wideband.

I. INTRODUCTION

Nowadays, the general public desires faster mobile internet access, the latest communication gadgets, and unlimited communication and access to information. To date, avant-garde smartphones and tablets continue growing in demand, requiring more innovative multimedia capabilities. Consequently, the forthcoming fifth generation (5G) of wireless technology, which is presumed to arrive by 2020, is extensively studied. This future technology of 5G is expected to offer extremely high capacity and countless connections of billions of wireless gadgets with very low latency and response times. Hence, a massive multiple-input and multiple-output (MIMO) and distributed antenna system (DAS) technology are proposed for the respective indoor and outdoor applications of 5G architecture. These two approaches seem to be appropriate solutions for offering services with high data rates and quality [1]. In addition, to supporting for this requirement, various extensive research works are needed in component designs, including an alternative to a mixer as one of the important components in the wireless communication system. Commonly, a mixer consists of active devices that require a certain biasing circuit that leads to additional thorough design effort and complexity. Thus, a six-port network can be used as an alternative to the mixer-based approach. In contrast to the mixer, this six-port network can be formed by using only passive devices, such as a coupler, H-hybrid and power divider. Therefore, by having this network in the wireless communication system architecture, the complexity of the design can be reduced and, consequently, can increase the performance of the bandwidth.

The power divider is one of the important components in a six-port network, which requires a lot of effort to increase the bandwidth. One method has been introduced [2] that implements a multilayer technique formed by a microstrip-to-slot-to-microstrip transition. The design shows that the UWB operating frequency range from 3.1 to 10.6 GHz is achieved; however, the performance levels are degraded due to misalignment problems and the existence of an air gap between the two substrates [3]. Another method for achieving the desired wideband performance entails the use of a multi-section power divider [4]. To enhance the bandwidth performance and reduce the size of the circuit in a multi-section power divider design, a few other methods are added, such as compensation circuit [5], coupled line [6], combination of a coupled line and quasi-lumped element [7], least squares method [8], stub [9-11] and additional capacitance and inductance element [12].

Guo et al. proposed a novel design of a power divider, in which a coax balun transformer is used to replace the isolating resistor between the two output ports [5]. This technique increases the simulated bandwidth performance coverage from 490 to 830 MHz. However, the use of the coax balun transformer and dummy load in the proposed design leads to difficulty and complexity in the circuit design. In [6], a two-section coupled-line coupler at each of the quarter-wave transformer was proposed. The isolation performance of this design was improved up to 40 dB. However, the performance was limited to the narrowband frequency range. To overcome the bandwidth limitation by the design that was introduced in [6], Gruszczynski et al. proposed the quasi-lumped element technique for a multi-section coupled-line Wilkinson power divider design [7]. The structure is composed of a three-section coupled line with a quasi-lumped element approach. A wideband frequency response of 0.6 to 2.5 GHz and a small size circuit were achieved. However, to obtain the highest self-inductance per unit length, the width of the coupled strip at each coupled-line section had to be as narrow as possible to provide the shortest length of the coupled lines, which led to difficulties in the fabrication process. Meanwhile, in [8], Oraizi and Sharifi introduced a design and optimization procedure based on the method of least squares (MLS) for a multi-section Wilkinson power divider. The significant parts of the proposed method and design were that the performance of the phase difference between the two output ports operated well in a designated frequency band and that a minimization of the insertion loss could be incorporated into the expression of the error function. However, the performance was too narrow, which cover only 0.5-2.5 GHz.

The proposed power dividers in [9-11] utilized open-circuited stub on each branch in the designs. Design in [9] and [11] demonstrated good UWB performance from 3.1 to 10.6 GHz with well transmission coefficients, return losses and isolation. In contrast to [9, 11], design in [10] exhibited narrowband performance. Another UWB power divider reported in [12] was constructed using two sections of a four-way Wilkinson power divider, with one input port and four output ports. In addition to good UWB performance, band rejection was achieved in the design by using a symmetric spiral defect ground-slotted (DGS) structure. Even though [9, 12] offer UWB operation, the methods used has produced larger size circuits compared to the conventional two-section power divider. While [11] has compact size but its resistors that positioned further apart from the transmission may lead to fabrication difficulty.

Hence in this article, a new compact two-section UWB power divider formed by a microstrip-slot is proposed. By implementing this technique, a compact size of the power divider circuit with excellent ultra

wideband performance from 3 to 11 GHz is achieved. The use of the microstrip slot in the design leads to the reduction of the quarter-wave transformer length of the power divider up to 33.34%, which consequently results in a reduced-size circuit. The initial dimension was calculated by using mathematical equations, as described in [4], which were obtained by using even- and odd-mode analysis. The design of the two-section power divider utilized a Rogers TMM4 substrate with the following features: 0.508 mm thickness, a dielectric constant of 4.5, a loss tangent of 0.002 and conductor-coating thickness of 35 μm. The design and simulation were performed by using CST Microwave Studio, in which the time-domain solver is specifically applied. Meanwhile, open boundary and waveguide ports were chosen to be used in the simulation. Then, the measurement was conducted by using a vector network analyzer (VNA).

II. UWB POWER DIVIDER DESIGN

The configurations of the proposed power divider design are shown in Figs. 1 and 2. The design consists of two conductive layers: a top and bottom layer. The top layer incorporates the microstrip line with three ports, Port 1 (P1), Port 2 (P2), and Port 3 (P3), whereas the bottom layer consists of two rectangular-shaped slots underneath the microstrip lines. These microstrips and slots form two-section quarter-wave transformers. The rectangular-shaped microstrip line and slot are chosen to minimize fabrication errors since the fabrication is performed manually. Between each section of the quarter-wave transformer, two resistors (R_1 and R_2) are used to ensure that good isolation is achieved between the output ports, and any reflected power is dissipated at a wider frequency range. The width and length of the microstrip presented are denoted as W_m and L_m, respectively. Meanwhile, the width and length of the slot are denoted as W_s and L_s.
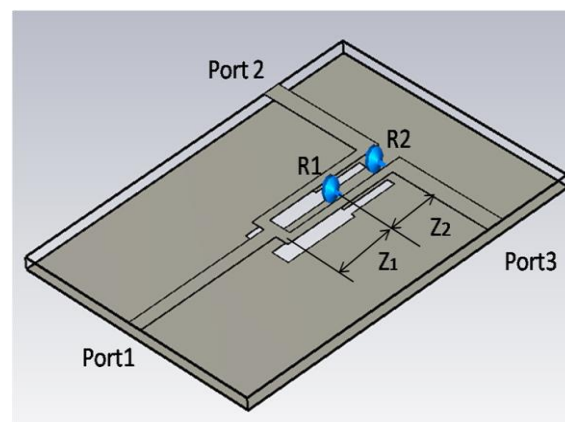
Fig. 1. The perspective view of the UWB two-section microstrip-slot power divider.

Figure 3 shows the equivalent circuit of the proposed designed power divider, which consists of impedance (Z_0), a capacitor (C), and a resistor (R) [4]. As observed from the figure, the circuit is divided into two output arms, in which each port has two fringe capacitances, C_g located between the slot edges at the ground plane in the air region. The fringe capacitance, C_g for the output arm P2 and P3, are denoted as C_{g1} and C_{g2}, and C_{g3} and C_{g4}, accordingly. Meanwhile, the parallel-plate capacitances, C_{p1}, C_{p2}, C_{p3}, C_{p4}, C_{p5}, and C_{p6} denote the vertical capacitance between the top layer microstrip line and the ground plane.
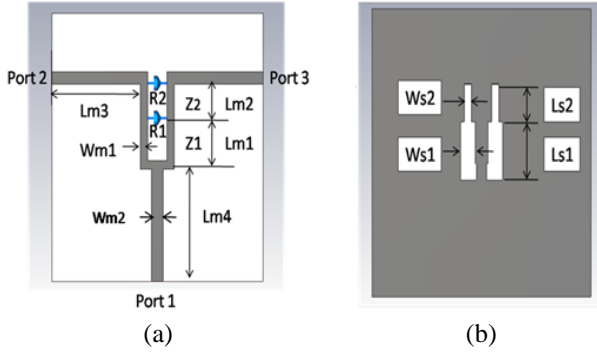
Fig. 2. The detail configuration of UWB two-section microstrip-slot power: (a) top and (b) bottom view.
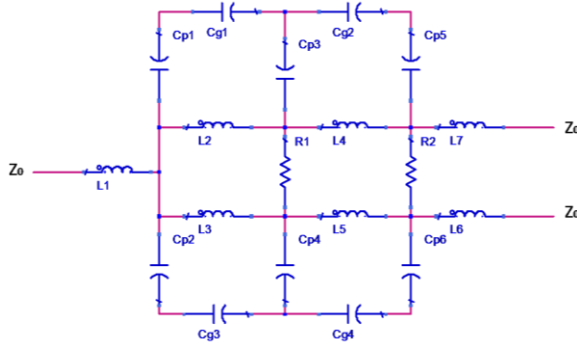
Fig. 3. The equivalent circuit of UWB two-section microstrip-slot power divider.

The characteristic impedances of the two-section quarter-wave transformers, Z_1 and Z_2, are determined through the binomial approach of the multi-section step impedance matching technique [4]. A binomial is chosen to obtain the maximal flat transmission coefficients of S21 and S31 across the designated frequency band. To calculate the value of Z_1 and Z_2, the value of Z_L/Z_0 must be known. The Z_L/Z_0 value can be computed through an even-mode analysis. As explained in [4], for the even-mode excitation, there is no current flow through the resistor R_1 and R_2. The value of Z_0 is assumed to be 50 Ω and the Z_L to be $2Z_0$, and Z_L/Z_0 is equivalent to 2.

Thus, the characteristic impedance of Z_1 and Z_2 can be computed from the respective equations (1) and (2) that redefined from the binomial multi-section step impedance matching equation in [4]:

$$\ln Z_1 = \ln Z_2 + 2^{-N} C_1^N \ln \frac{Z_L}{Z_0}, \quad (1)$$

$$\ln Z_2 = \ln Z_0 + 2^{-N} C_0^N \ln \frac{Z_L}{Z_0}, \quad (2)$$

where N is the number of sections of the quarter-wave transformer. The binomial coefficients, C_n^N, can be obtained by using equation (3) [4]:

$$C_n^N = \frac{N!}{(N-n)!n!}, \quad (3)$$

where n are 0 and 1. Note that, in this case, N is 2 and the required binomial coefficients from equation (3) are $C_0^2 = 1$ and $C_1^2 = 2$. Therefore, the computed Z_1 and Z_2 from equations (1) and (2) are 84.09 Ω and 59.46 Ω, respectively.

The value of the resistors, R_1 and R_2, can then be obtained by performing the odd-mode analysis, wherein the odd-mode analysis, a null voltage is excited along the middle of the circuit. This excitation ensures that the two points on the mid-plane are grounded. By simplifying the circuit, the R_1 and R_2 can be calculated by using equation (4) and (5), accordingly [13]:

$$R_1 = \frac{2Z_1 Z_2}{\sqrt{(Z_1 + Z_2)(Z_1 - Z_2 \cot^2 \varphi)}}, \quad (4)$$

$$R_2 = \frac{4R_1 Z_0 (Z_1 + Z_2)}{\sqrt{R_1(Z_1 + Z_2) - 2Z_1}}, \quad (5)$$

where φ can be obtained by using equation (6) [13]:

$$\varphi = \frac{\pi}{2}\left[1 - \frac{1}{\sqrt{2}}\left(\frac{f_2 - f_1}{f_2 + f_1}\right)\right], \quad (6)$$

where f_1 and f_2 are the start and stop frequencies of the designated band, respectively. Thus, the calculated values of the resistors R_1 and R_2 are 123.0 Ω and 201.91 Ω, accordingly.

As stated in the proposed design description, which is illustrated in Figs. 1 and 2, the two sections of the quarter-wave transformers with the characteristic impedance of Z_1 (84.09 Ω) and Z_2 (59.46 Ω) are used to achieve the bandwidth specification. This two-section of the quarter-wave is formed by a microstrip line with two rectangular slots underneath. This microstrip line with a slot underneath is named the microstrip-slot line, with the characteristic impedance of $Z_{m\text{-}s}$. The relationship between microstrip-slot impedance, $Z_{m\text{-}s}$ with the width of the slot, W_s and microstrip line impedance, Z_m can be expressed as in equation (7) [14]:

$$Z_{m-s} = 18.22W_s^2 + Z_m, \quad (7)$$

Table 1: Analysis of the effective length of the microstrip-slot quarter-wave sections 1 and 2 that correspond to the electrical length, $\theta = 90°$

Effective Length of Microstrip-slot Quarter-wave Sections 1 and 2, $\theta = 90°$	Parameters			
	Operating Frequency	Center Frequency, f_c	Microstrip-slot Wavelength, $\lambda_{m\text{-}s}$	Theoritical-slot Wavelength, λ_S
12.46 mm	1 - 4 GHz	2.5 GHz	49.8 mm	72.4 mm
6.23 mm	1 - 7 GHz	4 GHz	24.9 mm	45.2 mm
4.15 mm	3 - 11 GHz	7 GHz	16.6 mm	25.8 mm
3.15 mm	4 - 14 GHz	9 GHz	12.6 mm	20.1 mm
2.49 mm	6 - 16 GHz	11 GHz	10.0 mm	16.4 mm

This equation is derived by using the completing square curve fitting method. However, the equation is only valid for microstrip-slot impedance, $Z_{m\text{-}s}$ ranging from 40 Ω to 100 Ω, dielectric permittivity, ε_r between 2 and 5 and a substrate thickness, h of 0.508 mm. In the case of this proposed power divider design, the characteristic impedance of the microstrip slots, $Z_{m\text{-}s}$ are Z_1 (84.09 Ω) and Z_2 (59.46 Ω), which correspond to sections 1 and 2 of the quarter-wave transformer. In contrast, the characteristic impedance of microstrip line, Z_m is set to be 57.38 Ω that analogous to the microstrip width, $W_{m1} = 0.7$ mm. According to these values of Z_1, Z_2 and Z_m, the computed slot widths (W_{s1} and W_{s2}) of each section using equation (7) are 0.65 mm and 1.34 mm, respectively. Then, by using the obtained value of W_{s1} and W_{s2}, the impedance of a slot can be determined by implementing equation (8) [15]:

$$Z_s = 73.6 - 2.15\varepsilon_r + (638.9 - 31.37\varepsilon_r)(W_s/h)^{0.6}$$
$$\left(36.23\sqrt{\varepsilon_r^2 + 41} - 225\right)\frac{W_s/h}{W_s/h + 0.87\varepsilon_r - 2} + \quad , \quad (8)$$
$$0.51(\varepsilon_r + 2.12)\left(\frac{W_s}{h}\right)\ln\left(\frac{100h}{\lambda_0}\right) - 0.753\frac{\varepsilon_r(h/\lambda_0)}{\sqrt{W_s/h}}$$

where h and λ_0 are 0.508 mm and 46.15 mm, respectively. The formula in (8) is valid for the case of dielectric constant (ε_r) ranging from 3.8 to 9.8, $0.0015 < W_s/\lambda_0 < 0.075$ and $W_s/h > 1.67$. By applying equation (8), the slot impedance of each section is obtained to be 157.81 Ω and 125.83 Ω, respectively. In addition, the widths of the microstrip line at the top layer of the proposed design (W_{m1} and W_{m2}) can be obtained using (9) by setting the values of the microstrip-line impedance (Z) as follows: the quarter-wave transformer (Z_m) is equivalent to 57.38 Ω, and characteristic impedance (Z_0) is equivalent to 50 Ω [4]:

$$\frac{W_{mi}}{h} = \frac{2}{\pi}\left[\frac{377\pi}{2Z\sqrt{\varepsilon_r}} - 1 - \ln\left(\frac{377\pi}{2Z\sqrt{\varepsilon_r}} - 1\right)\right.$$
$$\left. + \frac{\varepsilon_r - 1}{2\varepsilon_r}\left\{\left(\frac{377\pi}{2Z\sqrt{\varepsilon_r}} - 1\right) + 0.39 - \frac{0.61}{\varepsilon_r}\right\}\right], \quad (9)$$

where $i = 1, 2$. Therefore, the values of W_{m1} and W_{m2} obtained from equation (9) are 0.7 mm and 1.069 mm, respectively. Once the initial dimensions of the proposed two-section power divider have been obtained, the optimization is carried out using CST Microwave Studio. Due to the limitation of available commercial resistors in the market, R_1 and R_2 are set to be 130 Ω and 200 Ω, respectively, despite the calculated values from (4) and (5). The details of the optimized microstrip and slot width dimensions of the proposed design are given as follows: $W_{m1} = 0.7$ mm, $W_{m2} = 1.07$ mm, $W_{s1} = 0.65$ mm, and $W_{s2} = 1.34$ mm. The effective length of the two-section quarter-wave, L_{m1}, L_{m2}, L_{s1} and L_{s2} (which correspond to an electrical length of $\theta = 90°$), is according to the designated operating frequency. To obtain the length of the two-section quarter-wave transformer that formed by the microstrip-slot lines, a simple analysis was conducted, which is summarized in Table 1.

By having an optimized microstrip and slot widths that represent the characteristic impedances, the length of the microstrip-slot quarter-wave sections 1 and 2 are varied to observe the changes in the operating and center frequency. In any wideband microwave design, this center frequency is used as the designed frequency accordingly. Similar lengths of section 1 and 2 are considered, which concern the lengths of 12.46 mm, 6.23 mm, 4.15 mm, 3.15 mm and 2.49 mm. The increment of length, as expected, shifts the operating and center frequency to the higher range. Then, the microstrip-slot wavelength, $\lambda_{m\text{-}s}$ is compared to the theoretical slot wavelength, λ_s. In this analysis, slot wavelength, λ_s is used, as its effective permittivity, ε_{es}, does not depend on the slot width and thickness of the substrate. This contrasts to the microstrip wavelength. The slot wavelength, λ_s can be computed from (10) [2]:

$$\lambda_s = \frac{c}{f_c\sqrt{\varepsilon_{es}}}, \quad (10)$$

where $\varepsilon_{es} = (\varepsilon_r + 1)/2$ and the speed of light, $c = 3 \times 10^8$ ms^{-1}. Therefore, by referring to Table 1, microstrip-slot wavelength, $\lambda_{m\text{-}s}$ is approximately 0.62 of slot wavelength, λ_s. Consequently, the microstrip-slot effective permittivity,

ε_{em-s} and microstrip-slot wavelength, λ_{m-s} can be estimated from (11) and (12):

$$\varepsilon_{em-s} = 1.3(\varepsilon_r + 1), \qquad (11)$$

$$\lambda_{m-s} = \frac{c}{f_c \sqrt{\varepsilon_{em-s}}}. \qquad (12)$$

Hence, the initial sections 1 and 2 lengths of the microstrip-slot quarter-wave can be computed from (12). Then, the optimization is performed to obtain the optimal effective length. The optimized length dimensions are $L_{m1} = L_{m2} = L_{s1} = L_{s2} = 4.153$ mm, while the lengths to ports are $L_{m3} = 9.65$ mm and $L_{m4} = 10$ mm. The overall size of the proposed design after the optimization is 20 mm x 23 mm. When all the requirements are met, the design is fabricated and tested. The simulation and measurement results of the proposed design are discussed in the next section.

III. RESULTS AND DISCUSSION

The prototype of the proposed UWB two-section power divider and its measurement setup using a VNA are presented in Fig. 4. Surface mount resistors, also known as SMD resistors, of 130 Ω and 200 Ω are used as R_1 and R_2 in this prototype, respectively. Referring to the measurement setup, the concerned ports are connected directly using special high-performance cables to the VNA, whilst other ports are terminated using an ultra wideband 50 Ω termination. Then, the obtained measurement results plotted in Figs. 5 and 6 are compared to the simulated ones and discussed.
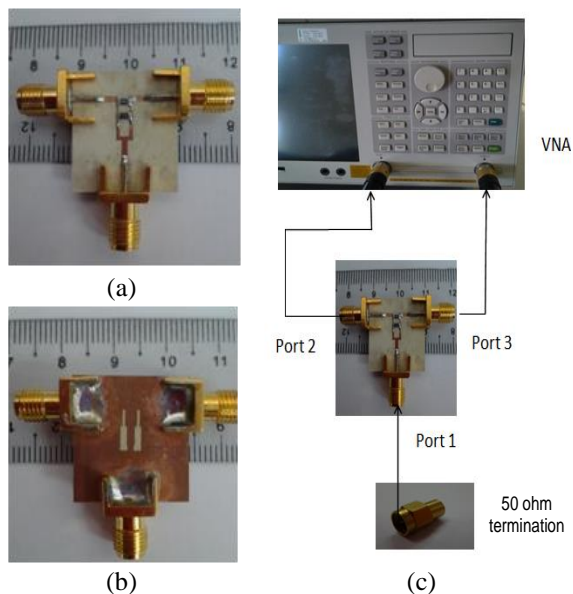
Fig. 4. (a) Top, (b) bottom view of the proposed UWB two-section power divider prototype, and (c) its configuration of measurement setup using a vector network analyzer (VNA).

(a)

(b)
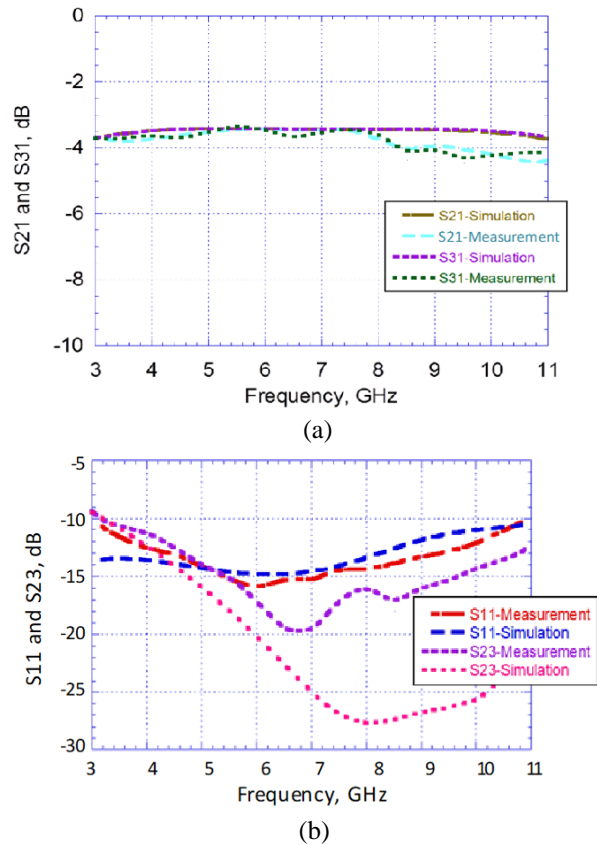
Fig. 5. Simulated and measured performance of the proposed UWB two-section power divider: (a) S21 and S31, and (b) S11 and S23.
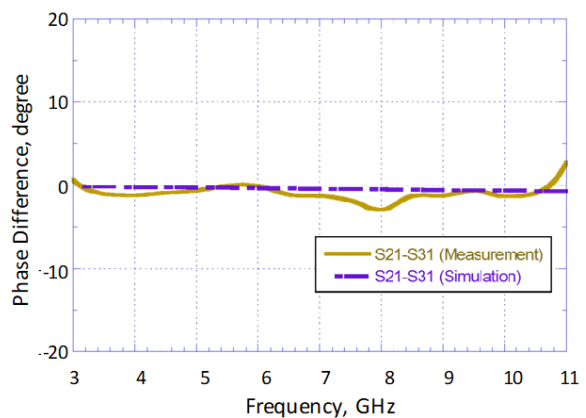
Fig. 6. The simulation and measurement results for phase difference between two output ports of the proposed two-section power divider.

The measurement and simulation performance levels of the transmission coefficients S21 and S31 are shown in Fig. 5 (a). It is noted that the results of S21 and S31 for simulation and measurement show almost

similar performance levels of -3.55 ± 0.15 dB and -3.8 ± 0.5 dB across 3 to 11 GHz, accordingly. Meanwhile, Fig. 5 (b) shows the simulated and measured results of the S11 and S23 of the proposed two-section power divider. By referring to the plotted simulation results, S11 and S23 are less than -10 dB for the whole band covering 3-11 GHz, whilst both the S11 and S23 results are lower than -10 dB for the same designated band. Furthermore, the simulation and measurement results for the phase difference between port 2 and 3 are depicted in Fig. 6. The plotted phase difference performance indicates the obtained simulation of 0° ± 0.2°. Meanwhile, the measurement result shows a comparable performance with a slight degradation of 0° ± 2° across 3 to 11 GHz. Then, the simulation and measurement results of S11, S21, S31, S23 and the phase difference between port 2 and 3 are summarized, as shown in Table 2.

Table 2: The comparison of the simulation and measurement results of the proposed two-section power divider

Parameter	Simulated Performance	Measured Performance
S11	≤ -12 dB	≤ -10 dB
S21 and S31	-3.55 ± 0.15 dB	-3.8 ± 0.5 dB
S23	≤ -10 dB	≤ -10 dB
Phase difference between Port 2 and 3	0° ± 0.2°	0° ± 2°

Referring to Table 2, it can be noted that both simulation and measurement results exhibit a good relative agreement even though there are slightly obvious differences due to the imperfect fabrication that was done in-house and additional losses contributed by the used connectors, terminations, and resistors. However, both simulation and measurement performances are acceptable and comply with the optimal power divider requirement across the designated UWB frequency range of 3-11 GHz.

Moreover, it is important to compare the proposed two-section microstrip-slot power divider to the conventional two-section power divider. The conventional power divider is designed at a center frequency of 6.85 GHz, which is similar to the proposed power divider. The comparisons are summarized in Table 3. In the conventional two-section power divider design, both section quarter-wave transformers have a length of 6.23 mm, which corresponds to a quarter-wavelength of microstrip $\lambda_m/4$ and an electrical length of θ of 90°. By implementing the rectangular-shaped slot underneath the microstrip line to form the quarter-wave transformer into the proposed power divider design, the length of both quarter-wave transformers can be reduced to 4.153 mm, which is equivalent to $\lambda_{m-s}/4$. This is due to

the defections in the ground layer that disturb the current distribution in the ground plane and at the same time increase the effective inductance and capacitance of the microstrip line [16]. This contributes to reducing the size of the power divider circuit up to 23.33%. In addition to that, the bandwidth performance is improved up to 19.4% compared to the conventional two-section power divider.

Furthermore, as observed in Table 3, the conventional power divider design has a narrower microstrip line width at the section 1 quarter-wave transformer, which is 0.28 mm. To ensure that a very strong performance is achieved by the proposed power divider, precision fabrication is required. This very narrow microstrip line may lead to difficulty in the fabrication stage with a limited in-house facility. By introducing the rectangular-shaped slot at the ground plane underneath the microstrip line to form the quarter-wave transformer, a wider microstrip line of 0.7 mm can be used, which indirectly offers a better degree of fabrication tolerance. To maintain the impedance levels of each section of the quarter-wave transformer at 59.46 Ω and 84.09 Ω, each slot needs to have different widths, which are 0.65 mm and 1.34 mm, respectively. Thus, the microstrip-slot lines are obliged to have higher impedance due to the increment of its effective inductance and higher slow-wave factor compared to the conventional transmission lines [16].

Nonetheless, by concerning its size reduction and operating frequency, the proposed design is compared to the other related and published works in [2, 7, 10, 11]. By referring to Table 4, the proposed design has the broadest bandwidth of 9 GHz that covering 3-11 GHz with comparable small size as the design in [11]. The designs in [2, 6, 10] have larger size with narrower bandwidth. Therefore, the implementation of the microstrip-slot technique in the design has realized the goals of size reduction and bandwidth enhancement.

Table 3: The performance comparison between proposed and conventional two-section power divider

Parameter		Conventional Power Divider	Proposed Power Divider
Microstrip line width of quarter-wave transformer (mm)	Section 1	0.28	0.7
	Section 2	0.65	0.7
Length of quarter-wave transformer (mm)	Section 1	6.23	4.153
	Section 2	6.23	4.153
Size circuit (mm²)		20 x 30	20 x 23
Bandwidth (GHz)		3-9.7	3-11

Table 4: Comparison of the proposed design with the related and published works in [2, 7, 10, 11]

Design	Technique	Size	% Claimed Size Reduction	Operating Frequency (GHz)
Proposed Design	Microstrip-slot	20 mm x 23 mm	23.33%	3 - 11 (BW = 8)
[2]	Multilayer microstrip-slot	24 mm x 40 mm	Not specified (larger)	2 - 6 GHz (BW = 4)
[6]	Coupled-line	6.33 mm × 22.1 mm	Not specified (smaller)	2.4
[10]	T-shaped step impedance transmission line	56 mm × 56 mm	53%	$f_1 = 0.450$ and $f_2 = k f_1$, where ($k = 6.3$, 6.7 and 7.3)
[11]	Small length transmission lines and open-circuited stubs	Not specified	Not specified (comparable)	3.1 - 10.6 (BW = 7.5)

*BW = Bandwidth

IV. CONCLUSION

The design of a compact UWB two-section power divider by implementing the microstrip-slot technique was presented in this article. The microstrip-slot technique, which includes a rectangular-shaped slotline underneath each quarter-wave transformer section of two microstrip output arms, led to the reduction of the circuit size up to 23.33% compared to the conventional power divider. The power divider was fabricated and practically tested in the laboratory. The fabricated power divider showed good results in terms of return loss, isolation, transmission coefficients and phase difference between the output ports over a UWB frequency band range between 3 and 11 GHz. Additionally, a bandwidth improvement of 19.4% was demonstrated by this proposed power divider. Hence, this power divider is suitable to be used in many wireless applications that are in high demand nowadays, and that high demand is expected to continue in the future.

REFERENCES

[1] C.-X. Wang, F. Haider, et al., "Cellular architecture and key technologies for 5G wireless communication networks," *IEEE Commun. Mag.*, vol. 52, no. 2, pp. 122-130, Feb. 2014.

[2] N. Seman and S. N. A. M. Ghazali, "Design of multilayer microstrip-slot in-phase power divider with tuning stubs for wideband wireless communication applications," *Wirel. Pers. Commun.*, vol. 83, no. 4, pp. 2859-2867, Aug. 2015.

[3] D. N. A. Zaidel, S. K. A. Rahim, N. Seman, R. Dewan, and B. M. Sa'ad, "New ultra-wideband phase shifter design with performance improvement using a tapered line transmission line for a butler matrix UWB application," *Appl. Comput. Electromagn. Soc. J.*, vol. 29, no. 8, pp. 611-617, July 2014.

[4] D. M. Pozar, *Microwave Engineering*, 4th Edition, Wiley, New York, 2011.

[5] Q. Guo, Y. Ma, and J. Ju, "A novel broadband high-power combiner," *Asia-Pacific Microwave Conference*, Suzhou, pp. 3495-3498, Dec. 2005.

[6] D. Kang, Y.-H. Pang, and H.-H. Chen, "A compact wilkinson power divider/combiner with two-section coupled lines for harmonics suppression," *Asia-Pacific Microwave Conference*, Kaohsiung, pp. 995-997, Dec. 2012.

[7] S. Gruszczynski and K. Wincza, "Miniaturized broadband multisection coupled-line wilkinson power divider designed with the use of quasi-lumped element technique," *International Caribbean Conference on Devices*, *Circuits and Systems*, Playa del Carmen, pp. 1-4, Mar. 2012.

[8] H. Oraizi and A.-R. Sharifi, "Design and optimization of broadband asymmetrical multi-section Wilkinson power divider," *IEEE Trans. Microw. Theory Tech.*, vol. 54, no. 5, pp. 2220-2231, May 2006.

[9] X.-P. Ou and Q.-X. Chu, "A modified two-section UWB Wilkinson power divider," *International Conference on Microwave and Millimeter Wave Technology*, Nanjing, pp. 1258-1260, Apr. 2008.

[10] A. Mahan, S. H. Sedighy, and M. Khalaj-Amirhosseini, "A compact dual-band planar 4-way power divider," *Appl. Comput. Electromagn. Soc. J.*, vol. 32, no. 3, pp. 243-248, Mar. 2017.

[11] S. Tsitsos, D. Efstathiou, P. Kyriazidis, and A. A. P. Gibson, "Design of an ultra wide-band power divider with harmonics suppression," *6th International Conference From Scientific Computing to Computational Engineering*, Athens, July 2014.

[12] M. F. Khajeh, S. A. Mirtaheri, and S. Chamaani, "Design and analysis of a band-notched UWB 1 to 4 Wilkinson power divider using symmetric defected ground structure," *European Conference on Antennas and Propagation*, Rome, pp. 860-864, Apr. 2011.

[13] S. B. Cohn, "A class of broadband three-port TEM-mode hybrids," *IEEE Trans. Microw. Theory Tech.*, vol. 19, no. 2, pp. 110-116, Feb. 1968.

[14] K. H. Yusof, N. Seman, M. H. Jamaluddin, and D. N. A. Zaidel, "Characterization and formulation of microstrip-slot impedance with different thickness and relative permittivity," *Applied Mechanics and Materials*, vol. 781, pp. 53-56, Aug. 2015.

[15] R. Janaswamy and D. H. Schaubert, "Characteristic impedance of a wide slotline on low-permittivity substrates," *IEEE Trans. Microw. Theory Tech.*, vol. 34, no. 8, pp. 900-902, Aug. 1986.

[16] L. G. Maloratsky, "Microstrip circuit with a modified ground plane," *High Frequency Electronic, Summit Technical Media*, pp. 38-47, 2009.

Norhudah Seman received the B.Eng. in Electrical Engineering (Telecommunications) degree from the Universiti Teknologi Malaysia, Johor, Malaysia, in 2003 and M.Eng. degree in RF/Microwave Communications from The University of Queensland, Brisbane, St. Lucia, Qld., Australia, in 2005. In September 2009, she completed her Ph.D. degree at The University of Queensland. Currently, she is an Associate Professor and Director (Communication Engineering) in School of Electrical Engineering and Research Fellow in HiCoE Wireless Communication Centre (WCC), Universiti Teknologi Malaysia. Her research interests concern the design of microwave/millimeterwave devices for biomedical and industrial applications, effects of electromagnetic field radiation including specific absorption rate (SAR), and mobile communications.

Khairul Huda Yusof received the diploma in Electrical Engineering (Telecomunication) and degree of B.Eng. in Electrical Engineering (Microelectronics) from Universiti Teknologi Malaysia in 2008 and 2011, respectively. Currently, she just completed her Ph.D. study in Electrical Engineering at Universiti Teknologi Malaysia, majoring in Telecomunication. She is now a Lecturer in Faculty of Engineering and Information Tehnology, MAHSA University, Malaysia.

Mohd Haizal Jamaluddin was born in Selangor, Malaysia. He received his Bachelor degree and Master degree in Electrical Engineering from Universiti Teknologi Malaysia (UTM), Malaysia in 2003 and 2006, respectively. He received the Doctoral degree in Signal Processing and Telecommunications from the University of Rennes 1, Rennes, France in 2010. He is currently an Associate Professor in UTM. His main field of interest is on antenna design especially on dielectric resonator antenna, reflect array antenna and lens antenna.

Tharek Abd Rahman is a Professor at Faculty of Electrical Engineering, Universiti Teknologi Malaysia (UTM). He obtained his B.Sc. in Electrical & Electronic Engineering from University of Strathclyde UK in 1979, M.Sc. in Communication Engineering from UMIST Manchester UK and Ph.D. in Mobile Radio Communication Engineering from University of Bristol, UK in 1988. He is the Director of Wireless Communication Centre (WCC), UTM. His research interests are radio propagation, antenna and RF design and indoors and outdoors wireless communication. He has also conducted various short courses related to mobile and satellite communication to the Telecommunication Industry and Government body since 1990. He has a teaching experience in the area of mobile radio, wireless communication system and satellite communication.

Optimization Design of Metamaterial Absorbers Based on an Improved Adaptive Genetic Algorithm

Sai Sui [1], Hua Ma [1], Hong-Wei Chang [1], Jia-Fu Wang [1], Zhuo Xu [2], and Shao-Bo Qu [1]

[1] College of Science
Air Force Engineering University, Xi'an, Shaanxi 710051, China
suisai_mail@foxmail.com

[2] Electronic Materials Research Laboratory, Key Laboratory of the Ministry of Education
Xi'an Jiao tong University Xi'an, Shaanxi 710049, China

Abstract — Most reported metamaterials are designed empirically by parameter sweep, which is time-consuming and ineffective. We propose an optimization method of designing metamaterial absorbers based on an improved adaptive genetic algorithm (IAGA), with the aim to get wideband absorption. Firstly, an IAGA optimization model is presented, of which the crossover probability is adaptively adjusted by introducing a nonlinear function, and the mutation probability is adaptively adjusted using complementary idea. Then, a wideband triple-layer metamaterial absorber in THz region is designed and optimized using IAGA, getting about 40.4% increasing of relative bandwidth compared with the results of reference [19]. A further comparison between IAGA and standard genetic algorithm (SGA) indicates that the IAGA is an effective method in improving convergence speed and stability, and can be used to optimize structure parameters of metamaterial absorbers with desired characteristics.

Index Terms — Absorber, adaptive genetic algorithm, metamaterial, optimization.

I. INTRODUCTION

In recent years, metamaterials have been investigated extensively by researchers all over the world. Metamaterials are artificially synthesized periodic structures with lattice constant that is much smaller than the wavelength of the incident electromagnetic wave, thus can be considered as effectively homogeneous media [1]. The effective parameters ($\varepsilon(\omega)$ and $\mu(\omega)$) can be tuned and controlled by the design of the resonance structure of unit cell. Thus, metamaterials can achieve many interesting and exotic electromagnetic properties or phenomena, and can apply to absorbers, frequency selective surfaces (FSS), gradient meta-surfaces, electromagnetic band gap structures(EBG) and artificial magnetic conductors(AMC) [1-8], etc. In 2008, the concept of prefect metamaterial absorber was proposed

by Landy et al. [5], of which the perfect absorption mainly arises from locally enhanced fields because of the strong electromagnetic resonance. The electric and magnetic responses can be tuned independently so as the impedance matches to that of free space by varying the geometry of metamaterial absorbers.

However, most reported metamaterial unit cells are obtained empirically based on intuition, experience or a large number of simulation, which is time-consuming, ineffective and expensive [1-3,5,7]. Usually, in the design process of a new device, optimization methods play important roles in assisting the designer to find the best solution efficiently. These methods vary in the design variables on which they performed. There are three main categories of methods. The first one is the parameter optimization method, which uses design parameters to get a solution whose geometry has been pre-defined by the designer; The second one is the shape optimization method, which changes the boundary between each sub-domain whose topology is defined by the designer; The third one is the topology optimization method, which uses parameters to describe material distribution inside a design space. All the above optimization methods are built on mature optimization algorithms such as genetic algorithm (GA), particle swarm optimization algorithm (PSO), and ant colony algorithm (ACA). GA is one of the earliest algorithms which applied to the optimization design of metamaterials [4-14]. In GA, the biology evolutionary steps are simulated by taking biological evolution process as the background, and the concepts of propagation, hybridization, variation, competition and selection are introduced. As GA uses a lot of evaluations during the process of optimization, many studies are aimed to decrease the time cost [15-16]. Dealing with the shortcomings of slow convergence speed and easily premature of GA, Srinivas put forward adaptive genetic algorithm (AGA) whose crossover and mutation probability can automatically change according to the fitness [17]. However, when AGA is used to solve

practical metamaterial optimization problems [18], the optimization process may be interrupted unexpectedly or even failed to achieve optimal results.

In this paper, we propose a metamaterial absorber design method based on an improved adaptive genetic algorithm (IAGA) technique, with the aim to wideband high-efficiency absorption. Firstly, an IAGA optimization model for wideband absorption is proposed. Then the effectiveness of the new technique is evidenced by a design example using IAGA and the comparison between IAGA and SGA.

II. IMPROVED ADAPTIVE GENETIC ALGORITHM

A. Adaptive genetic algorithm

AGA can adjust crossover and mutation probability adaptively based on individual fitness in the evolutionary process to improve the convergence. The crossover and the mutation probability, P_c and P_m are calculated as follows [17]:

$$P_c = \begin{cases} \frac{k_1(f_{max}-f)}{f_{max}-f_{avg}} & ,f \geq f_{avg} \\ k_2 & ,f < f_{avg} \end{cases}, \qquad (1a)$$

$$P_m = \begin{cases} \frac{k_3(f_{max}-f')}{f_{max}-f_{avg}} & ,f' \geq f_{avg} \\ k_4 & ,f' < f_{avg} \end{cases}, \qquad (1b)$$

where f_{max} and f_{avg} are respectively the largest and the average fitness of the current population, f is the fitness of individual being selected to participate in crossover, f' the fitness of individual being selected to participate in mutation, and k_1, k_2, k_3, k_4 the constants between 0 and 1, which are based on experience and practical problem [17].

In practical optimization design of metamaterials, standard adaptive genetic algorithm (SAGA) may cease unexpectedly or fail to achieve convergence solution. By analysis, we find that SAGA is prone to be interrupted during the process of evolution under improper setting of crossover and mutation probability. Specifically, the main problems are as follows.

(1) In the initial evolution stage of SAGA, the initial individual fitness may have a little difference,

$$f \approx f_{avg} \approx f_{max}, \qquad (2)$$

so the standard deviation of fitness of current population can be expressed as:

$$\sigma_f = \sqrt{\frac{1}{N}\sum_{i=1}^{N}(f_i - f_{avg})^2} \approx 0, \qquad (3)$$

where N is the current population size. In this situation, the adaptive crossover and the adaptive mutation probability cannot be calculated by Eq. (1) since arithmetic error. This may lead to abnormal interruption of the computing process and divergence of the algorithm.

(2) Theoretically, in the late evolution stage of SAGA, the algorithm gradually converges to the optimal solution,

$$\lim_{N\to\infty} f \approx f_{best}, \qquad (4)$$

such trend is what we expect. However, in the actual convergence process, there will be the same problem as what was mentioned in case (1). In this case, the algorithm get stagnated or even interrupted, which makes it converge fast to a local optimum.

(3) From the schema theorem of GA, the low order, short length, and high fitness mode can generate a global optimal solution ultimately with the genetic operators [11]. As the algorithm evolution proceeds, various individual similarity increases. However, the mutation operator is still in working, which will create new individuals of a higher order, resulting in oscillation problem.

To solve the above problems of using SAGA in metamaterial optimization design, we propose an IAGA as described in the next section.

B. Improved adaptive genetic algorithm

To deal with the divergence problem of SAGA, the elite preservation strategy is employed. This strategy preserves the elite individual from each previous generation to the next generation. Meanwhile, a duplicate of elite individual participates in crossover and mutation operation, which ensures the integrity of the elite individual. Based on this strategy, we propose a new adaptive method in which adaptive adjustment will occur in the process of making a new generation. The improved method includes two aspects: Firstly, we employ a nonlinear adjustment function, exponential function, to adjust crossover and mutation probability adaptively in real-time, which can solve the divergence problem in the early evolution stage. Secondly, we adjust mutation probability adaptively based on complementary idea, which reduces the order of populations, increase the search space of the algorithm, and solve convergence oscillation problem in the late evolutionary stage.

1) Exponential adjustment function

Exponential adjustment function (Eq. (5)) is a variation of the standard exponential function, where constants α and β are adjustment factor used to adjust the decline rate of the function; G is the generation number of GA:

$$h(G) = 1/(1 + e^{\frac{(G-\alpha*\beta)}{\alpha}}). \qquad (5)$$

Graphically, as shown in Fig. 1, at the initial stage, $h(G)$ is almost invariant; whereas with increasing G, $h(G)$ decreases gradually, which can be used to adjust the crossover and the mutation probability, to improve the convergence stability of the algorithm. The constant α controls the spread and shrink of $h(G)$. The greater α, the faster declines of $h(G)$. The constant β controls the

shift of $h(G)$, and $h(G)$ right shifts with increasing β.
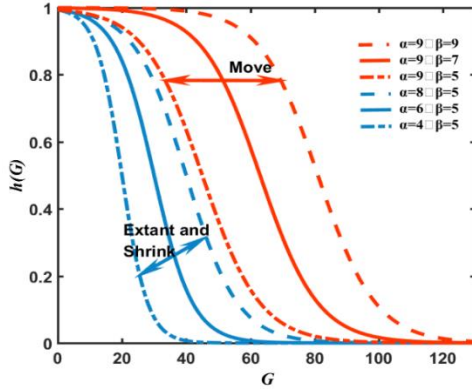
Fig. 1. The exponential adjustment function $h(G)$.

Introducing the exponential adjustment function, the crossover probability P_c of IAGA can be expressed as:

$$P_c = \begin{cases} \frac{1}{1+exp((G-\alpha*\beta)/\alpha)}*[k_0+\frac{(k_1-k_0)*(f_{max}(G)-f_{avg}(G-1))}{f_{max}(G)-f_{avg}(G)}] & ,f_{avg}(G)\geq f_{avg}(G-1) \\ k_2 & ,f_{avg}(G)<f_{avg}(G-1) \end{cases}, \quad (6)$$

where $f_{avg}(G)$ and $f_{max}(G)$ are respectively, the mean fitness and the largest fitness of all individuals in generation G; the constants k_0, k_1, and k_2 control the range of adaptive crossover probability within the scope of $[h(G)*k_0,h(G)*k_1]\cup k_2$. It should be noted that, Eq. (6) is coincident with Eq. (1) in a particular case: $h(G)=0$ and $k_0=0$. As scale factor, such an adjustment function can increase the overall coordination in the evolutionary process of SAGA, and adaptively decrease the crossover and mutation probability, reducing the probability of convergence oscillation problem in the late evolution stage.

Equation (6) indicates that in the initial stage of evolutionary algorithm, the effect of exponential adjustment function $h(G)$ on P_c is small, so the adaptive range of P_c is $[k_0,k_1]$. With G increasing, $h(G)$ decreases gradually and decrease crossover probability slightly in a nonlinear manner. In this paper, the parameters are fixed at $k_0=0.5,k_1=k_2=0.8$ as the experience value in which the GA works well for most of practical problems, and thus the adaptive crossover probability range is $[0.5,0.8]$.

2) Adaptive adjustment strategy based on the complementary idea

Adaptive adjustment of mutation operator is implemented with complementary idea. SGA mutation operator is based on a fixed number of individuals. But this is different from the real ecological environment, of which mutation number is stochastic. We adaptively

adjust the number of mutation individuals to simulate the stochastic mutation operation of the real ecological environment, according to complementary idea. The specific steps are as follows.

(1) Use the elite preservation strategy to determine *nEliteKids*, which means the number of preservation individuals. This principle allows the best individuals from the current generation to carry over to the next.

(2) Use Eq. (6) to calculate crossover probability and then determine the number of crossover individuals:

$$nXoverKids =[P_c * populationsize]. \quad (7)$$

(3) Determine the number of mutation individuals in accordance with the complementary idea:

$$nMutateKids = populationsize - nXoverKids - nEliteKids, \quad (8)$$

where *populationsize* is the population size that denotes the number of individuals in current generation.

According to schema theorem of GA, we analyze the convergence characteristic [11, 22] of IAGA. Suppose the crossover probability range is $[h(G)_{min} * k_0, k_1]$, where $h(G)_{min}$ is the minimum value of exponential adjustment function. The adaptive mutation probability can be estimated with complementary idea according to Eq. (7) and Eq. (8):

$$P_m = \frac{nMutateKids}{populationsize} = 1 - P_c - \frac{nEliteKids}{populationsize}. \quad (9)$$

Equation (9) indicates that the range of P_m is $[1-\frac{nEliteKids}{populationsize}-k_1,1-\frac{nEliteKids}{populationsize}-h(G)_{min}*k_0]$ and P_m will increase with decreasing P_c. According to theoretical analysis based on the genetic algorithm schema theorem, the changes of P_m versus P_c will reduce the populations order and accelerate the convergence speed.

From the analysis in section 2.2, we can get that the IAGA can adaptively adjust the crossover and mutation probabilities. The mutation probability increases with decreasing crossover probability, which helps to reduce the populations order, create new structures, and extend the algorithm search space; on the other hand, the mutation probability can be adaptively reduced when the crossover probability increases, thereby improving the convergence speed and stability. Particularly, in the late stage of IAGA, not only the crossover and mutation probability can be ensured properly, but also low order individual can be effectively avoided, leading to a better stability of the algorithm at the convergence value since the adjustment function $h(G)$.

III. OPTIMIZATION DESIGN OF WIDEBAND METAMATERIAL ABSORBERS

A. Initial design

A polarization insensitive and wide-band THz

metamaterial absorber is selected as the optimizing object, with the goal of achieving the maximum absorption bandwidth. The metamaterial absorber structure in Ref. [19] is shown in Fig. 2. The metamaterial absorber consists of two metallic pattern layers separated by a FR4 substrate. The metallic parts are copper with frequency independent conductivity $\sigma = 5.8 \times 10^7 \text{S/m}$ and thickness $ft = 0.017 \mu m$. The geometry parameters are denoted by a, b, c, u, n, w, h.
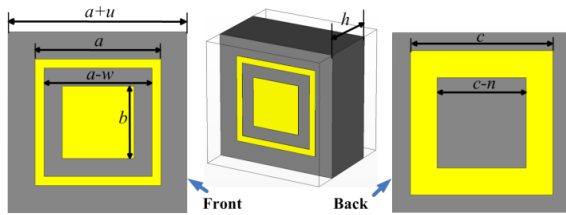
Fig. 2. The absorber unit cell structure in Ref. [19] and the geometry parameters.

1) Calculation of the absorption

The absorption can be calculated using:

$$A(\omega) = 1 - R(\omega) - T(\omega), \qquad (10)$$

where $A(\omega)$, $R(\omega)$, and $T(\omega)$ are the absorption, reflectivity, and transmissivity, respectively.

This metamaterial absorber can be modeled as a two-port network. Electromagnetic waves are incident in port 1 and exit through port 2. The reflectivity and transmissivity can be calculated by S-parameters of S_{11} and S_{21}:

$$R(\omega) = |S_{11}|^2, \qquad (11)$$

$$T(\omega) = |S_{21}|^2. \qquad (12)$$

2) The fitness function

The metamaterial absorber optimization design is a multi-objective optimization problem [20,21], so the working band, the bandwidth and the absorption should be considered synchronously in calculating the fitness function. In the simulation frequency range $\left[F_{min}, F_{max} \right]$ (where F_{max} and F_{min} are the upper and lower limit frequencies), the optimization goal is to make the absorption bandwidth as wide as possible and meanwhile the absorption meets a certain minimum requirement. Considering these two optimization goals, we set the absorption not less than 80%, and the fitness function is:

$$f = 1 - \frac{\sum_{i=1}^{n} \Delta F_i}{F_{max} - F_{min}}, \qquad (13)$$

where ΔF_i is the frequency interval distance which the absorption is not less than 80% continually. Equation (13) indicates that, the wider bandwidth, the smaller fitness value we will get, supposing the absorption is

more than 80%.

3) The structure and algorithm parameters and their constraints

To ensure getting the reasonable structure, we employ an inequality to constraint the geometric parameters, as follows:

$$\begin{cases} -a+b < 0 \\ -a+c-u < 0 \\ -a+b+w < 0 \\ -c+n < 0 \\ a,b,c,u,n,w,h > 0 \end{cases} \qquad (14)$$

Population size is generally in 20-40 preferably. In this paper, the population size is fixed at 20 as the minimum size in which the GA works well for most of practical problems, and its size makes it possible to perform faster computation, and the maximum generation is 30. The initial individual parameters assume the parameters in Ref. [19] and the rest initial individuals are created randomly to satisfy the constraint conditions.

B. Numerical simulation

The VBA interfaces provided by commercial electromagnetic simulation software CST and MATLAB are employed to establish an interactive simulation system [9, 20, 21]. Joint simulation flow chart with IAGA is shown in Fig. 3. The calculation configurations, in CST, are as follows: periodic boundary conditions, $2 \mu m$ near-field distance, frequency-domain solver, and the frequency range $3.5 - 6THz$.
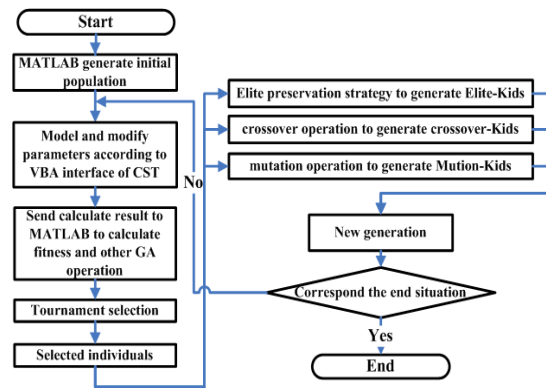
Fig. 3. Joint simulation flow chart.

C. Comparison and discussion
1) Optimization results

After 30 generations of evolution, the steady optimal individual results are obtained, as shown in Table 1 and Fig. 4.

Table1: Metamaterial absorber structure parameters

Parameters/μm	a	b	c	u	n	w	h
Before	9.75	9.00	12.10	8.25	1.00	0.25	5.00
After	8.63	7.40	12.93	5.50	4.98	0.16	5.25
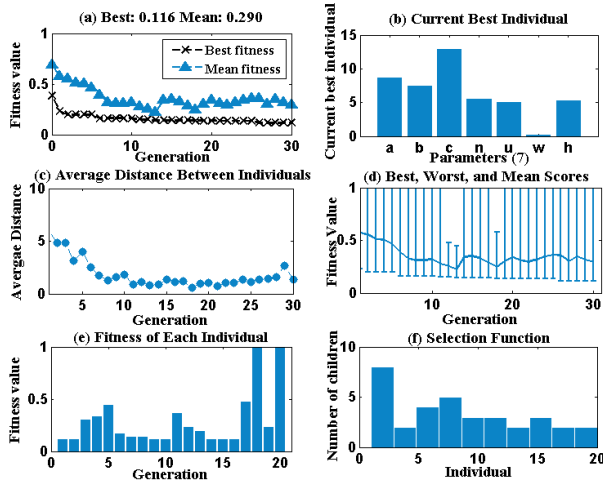
Fig. 4. The results of IAGA: (a) the best fitness value (cross mark) and the average fitness value (triangle mark) of each generation; (b) the best individual obtained from final optimization results; (c) the mean distance of all individuals in each generation (Hamming distance); (d) the optimum fitness value, the worst fitness value and average fitness value of each generation; (e) each individual fitness value of the current generation; (f) offspring quantity of the initial population.

2) Comparison with reference

As shown in Fig. 5, after the optimization, both the two resonances move to a higher position, due to the overall reduced size (Table 1). Compare to the results of Ref. [19], the absorption bandwidth increases, resulting in that the bandwidth with absorption more than 80% are increased from the original 0.805 THz to 1.604 THz with the relative bandwidth increasing of 40.4% [24]. These results demonstrate the feasibility of IAGA.
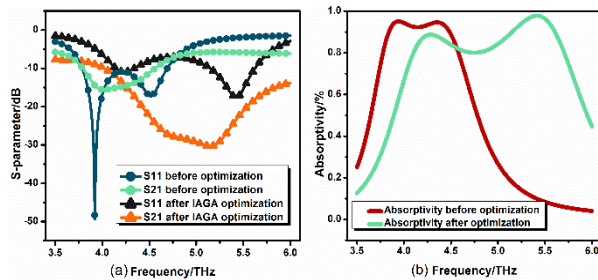
Fig. 5. (a) The S-parameter and (b) the absorption of before and after optimization.

3) Comparison between IAGA and SGA

Adopting the same structure as that of above metamaterial absorber, a real-coded SGA is employed to make a comparison with IAGA. Shown as Fig. 6, the IAGA optimal fitness value is less than SGA, which proves that the former algorithm has better global search capability. It is also found that the convergence speed of IAGA is much higher.
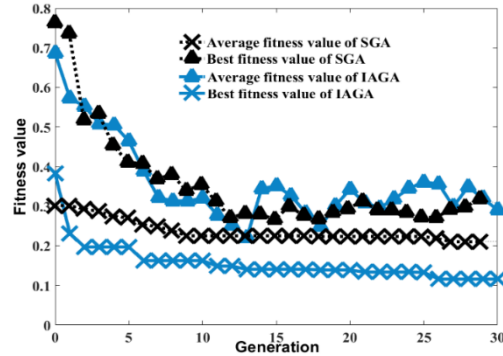
Fig. 6. Average fitness value and best fitness value of IAGA and SGA.

IV. CONCLUSION

An optimization method of designing metamaterial absorbers based on an improved adaptive genetic algorithm (IAGA) is proposed and is verified by example of THz metamaterial absorber. Firstly, a nonlinear self-adjustment function is employed to adjust crossover and mutation probability in real-time, which can solve the possible oscillation problem in the middle/late stage and the divergence problem in the early stage of SAGA. Secondly, mutation operator with the complementary idea is adjusted to decrease the population order and to create the new structure for population, improving the algorithm search space, convergence speed and stability. Lastly, the feasibility of the IAGA is verified by making comparisons with SGA, proving that the IAGA owns advantages of easy mobility, large search space, fast convergence speed and less design time. However, the IAGA has disadvantage of depending on the adjustment parameters and there is no experiment of the THz metamaterial absorber since experimental condition limitation, which is our next research direction. This method can also be extended to multi-object optimization problems such as the design of left-handed metamaterials, frequency selective surfaces, transmission line (TL) metamaterials, etc.

ACKNOWLEDGMENT

REFERENCES

[1] D. R. Smith and N. Kroll, "Negative refractive index in left-handed materials," *Physical Review Letters*, vol. 85, pp. 2933, 2000.

[2] J. B. Pendry, A. J. Holden, D. J. Robbins, and

W. J. Stewart, "Magnetism from conductors and enhanced nonlinear phenomena," *Microwave Theory and Techniques, IEEE Transactions on*, vol. 47, pp. 2075-2084, 1999.

[3] J. B. Pendry, A. J. Holden, W. J. Stewart, and I. Youngs, "Extremely low frequency plasmons in metallic mesostructures," *Physical Review Letters*, vol. 76, pp. 4773, 1996.

[4] E. Michielssen, J. M. Sajer, S. Ranjithan, and R. Mittra, "Design of lightweight, broad-band micro-wave absorbers using genetic algorithms," *Microwave Theory and Techniques, IEEE Transactions on*, vol. 41, pp. 1024-1031, 1993.

[5] N. I. Landy, S. Sajuyigbe, J. J. Mock, D. R. Smith, and W. J. Padilla, "Perfect metamaterial absorber," *Physical Review Letters*, vol. 100, pp. 207402, 2008.

[6] S. Cui, D. S. Weile, and J. L. Volakis, "Novel planar electromagnetic absorber designs using genetic algorithms," *IEEE Transactions on Antennas and Propagation*, vol. 54, pp. 1811-1817, 2006.

[7] M. Hua, Q. Shao-Bo, X. Zhuo, Z. Jie-Qiu, and W. Jia-Fu, "Material parameter equation for rotating elliptical spherical cloaks," *Chinese Physics B*, vol. 18, pp. 179, 2009.

[8] G. Chao, Q. Shao-Bo, P. Zhi-Bin, X. Zhuo, L. Jia, and G. Wei, "Multiband terahertz metamaterial absorber," *Chinese Physics B*, vol. 20, p. 017801, 2011.

[9] Z. Yu, Y. Feng, X. Xu, J. Zhao, and T. Jiang, "Optimized cylindrical invisibility cloak with minimum layers of non-magnetic isotropic materials," *Journal of Physics D: Applied Physics*, vol. 44, p. 185102, 2011.

[10] E. S. Hou, N. Ansari, and H. Ren, "A genetic algorithm for multiprocessor scheduling," *Parallel and Distributed Systems, IEEE Transactions on*, vol. 5, pp. 113-120, 1994.

[11] C. Zhu, "Real-coded Genetic Algorithm Mechanism Analysis and Algorithm Improvement Research," *Ph.D. Dissertation*, Chang Sha: Zhong Nan University, (in Chinese), 2009.

[12] P. Y. Chen, C. H. Chen, H. Wang, J. H. Tsai, and W. X. Ni, "Synthesis design of artificial magnetic metamaterials using a genetic algorithm," *Optics Express*, vol. 16, pp. 12806-12818, 2008.

[13] Y. Zhao, F. Chen, H. Chen, N. Li, Q. Shen, and L. Zhang, "The microstructure design optimization of negative index metamaterials using genetic algorithm," *Progress In Electromagnetics Research Letters*, vol. 22, pp. 95-108, 2011.

[14] W. T. Li, X. W. Shi, Y. Q. Hei, S. F. Liu, and J. Zhu, "A hybrid optimization algorithm and its application for conformal array pattern synthesis," *Antennas and Propagation, IEEE Transactions on*, vol. 58, pp. 3401-3406, 2010.

[15] T. Vidal, T. G. Crainic, M. Gendreau, and C. Prins, "A hybrid genetic algorithm with adaptive diversity management for a large class of vehicle routing problems with time-windows," *Computers & Operations Research*, vol. 40, pp. 475-489, 2013.

[16] H. Dawid, *Adaptive Learning by Genetic Algorithms: Analytical Results and Applications to Economic Models*. Springer Science & Business Media, 2011.

[17] M. Srinivas and L. M. Patnaik, "Adaptive probabilities of crossover and mutation in genetic algorithms," *Systems, Man and Cybernetics, IEEE Transactions on*, vol. 24, pp. 656-667, 1994.

[18] A. H. Wright, "Genetic algorithms for real parameter optimization," *Foundations of Genetic Algorithms*, vol. 1, pp. 205-218, 1991.

[19] C. Gu, S. Qu, Z. Pei, H. Zhou, J. Wang, B. Q. Lin, and W. D. Peng, "A wide-band, polarization-insensitive and wide-angle terahertz metamaterial absorber," *Progress In Electromagnetics Research Letters*, vol. 17, pp. 171-179, 2010.

[20] Y. Z. Cheng, Y. Nie, and R. Z. Gong, "Design of a wide-band metamaterial absorber based on fractal frequency selective surface and resistive films," *Physica Scripta*, vol. 88, p. 045703, 2013.

[21] S. Liu, Y. Dong, and W. Xu, "Design optimization for relative bandwidth of left-handed metamaterials with split-ring resonators," *Journal of Optics*, vol. 13, p. 015102, 2011.

[22] L. K. Sun, H. F. Cheng, Y. J. Zhou, J. Wang, and Y. Q. Pang, "Design and preparation of a radar-absorbing material based on metamaterial," *Acta Phys. Sin.*, vol. 64, pp. 108901-108901, 2011.

[23] H. W. Chang, H. Ma, J. Q. Zhang, Z. Y. Zhang, Z. Xu, J. F. Wang, and S. B. Qu, "Optimization of metamaterial based weighted real-coded genetic algorithm," *Acta Phys. Sin.*, vol. 63, pp. 87804-087804, 2014.

[24] K. N. Rozanov, "Ultimate thickness to bandwidth ratio of radar absorbers," *Antennas and Propagation, IEEE Transactions on*, vol. 48, pp. 1230-1234, 2000.

Sai Sui receiveed his master degrees from Air Force Engineering University of China. His research interests include metamaterial of electromagnetic wave design and optimization design.

Design of Dielectric Resonator Band Stop/Band Pass Filters

Noha A. Al-Shalaby [1*] and Shaymaa M. Gaber [2]

[1] Electronic and Communication Department, Faculty of Engineering, Kafer El-shiekh University, Egypt
noha1511ahm@yahoo.com

[2] Electronic and Communication Department, Faculty of Engineering, Egyptian Russian University, Egypt
shaymaa.gaber@yahoo.com

Abstract ─ A square dielectric resonator element (SDR) with a defected ground structure (DGS) is investigated. The proposed DGS is composed of two rectangular slots connected by two transverse slots and is placed in the ground plane. It is fed by a strip line through the substrate layer. The objective of this structure is to design dielectric resonator band-stop filter (DRF) and enhance the performance in terms of better insertion loss and increased bandwidth. The DRF has been fabricated and some measurements are taken. The cut-off frequency of the band- stop filter is 2.25 GHz, with transmission loss of 2-dB. The 3-dB of the band-stop filter is 1.24 GHz. The effect of the transverse slot width on the filter response curve is studied. The same structure is modulated to be frequency reconfigurable DRF to achieve frequency agility by using ideal metallic switches. The cut-off frequency is moved to 1GHz, and the 3-dB bandwidth in 1.5 GHz, while the transmission loss is decreased by 0.75 dB. Finally, the effect of loading SDR with metal plate is investigated. This structure combines the dielectric resonator antenna (DRA) and the DRF to propose dielectric resonator antenna filter (DRAF), this structure is used to miniaturize the global-positioning-system receivers that contain both the antenna and filter. The DRAF has been fabricated and measured, it has 3-dB pass bandwidth in 1GHz. Factors such as return loss, insertion loss, radiation pattern and mutual coupling of DRAF are calculated using finite element method (FEM). Comparison of calculation and measurement factors of DRAF shows a good agreement.

Index Terms ─ DGS, DRA, DRAF, DRF, FEM.

I. INTRODUCTION

The filter and the antenna are playing an important role in wireless communication, satellite communication, radar systems, telecommunication, and other military and commercial applications. The antenna is a necessary component for transmitting and receiving microwave signals. Filters are used to pass or eliminate specific frequency and are classified to low-pass (LP), high-pass (HP), band-pass (BP), and band-stop (BS) filters. The band-pass filter (BPF) passes a desired range of signal frequencies while blocking others; however, the band-stop filter suppresses a desired range of signal frequencies and allows all other frequencies. Many researches seek to combine both filtering and radiating functions with simplicity and miniaturization through integrating the filter and the antenna into a single component, known as filtering antenna, or "filtenna" [1]. The filtenna improves both the noise performance of the system and the impedance bandwidth. It reduces the requirement of pre-filtering and enhances the overall performance of the system. The filtenna has been implemented in different forms, Yagi antenna [2], monopole antenna [3], slot dipole [4], rectangular patch [5], circular patch [6], patch array [7], r-shaped antenna [8], and dielectric resonator antennas (DRA) [9]. The filtering antenna is composed by a feed line, two hairpin resonators, and rectangular patch. Defected ground structures (DGS) have been attracting researches in recent years because of their use in radar, microwave oscillators, microwave filters, microwave amplifiers, and mobile communication systems. The DGS can provide size reduction, cross polarization reduction and harmonic suppressions for different applications. In addition, DGS can be used to improve the performance of power dividers and couplers, reduce the side lobes in phased arrays and provide beam steering in antennas [10]. The resonant gap or slot in the ground metal is the basic element of DGS. It is aligned directly under a transmission line for efficient coupling to the line [11] and has different shapes for filter applications, such as dumbbell DGS [12], arrowhead dumbbell DGS [13], H-shaped DGS [14], spiral DGS [15], and U-slot DGS [16]. Each of these shapes differs in occupied area, coupling coefficient, equivalent L-C ratio and other electrical parameters. The equivalent circuit for a DGS is parallel-tuned circuits in series with its coupled transmission line. The equivalent values of L, C and R are determined by the

dimensions of the DGS structure and its position relative to the transmission line [10] as shown in Fig. 1. This defect in the ground plane disturbs the shielding current distribution due to its natural resonant characteristics. The shielding current distribution depends on the shape and the dimensions of the defect.
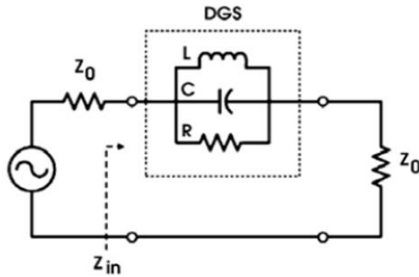
Fig. 1. The equivalent circuit of DGS.

The proposed structure gives some advantages of using the DR element to achieve several purposes. Among these advantages we can cite; high radiation efficiency, high temperature tolerance, low loss, wide bandwidth, small size, low cost, light weight, high power-handling capability and flexible excitation techniques [17-21]. The first purpose of using DR is designing band stop filter with wide rejection bandwidth from 1.25 GHz to 2.82 GHz. This can be implemented by using a single piece of DR element through employing DGS in the ground plane. The second purpose is to achieve frequency agility by modulating the first structure to obtain frequency reconfigurable DRF [22]. This can be satisfied by varying the rectangular slots effective area using ideal metallic switches. These ideal metallic switches vary the rejection bandwidth for the first design "band-stop filter" from 2.3 GHz to 4 GHz. The last purpose is to integrate the dielectric resonator antenna (DRA) and the dielectric resonator filter (DRF) into one element known as filtering antenna (DRAF). A square DR of the first design loaded with a square metallic plat is used as the resonator for the antenna as well as for the band-pass filter. A square metallic plat has been loaded to the top surface of the DRA (known as SDRA) to achieve reduction in the resonant frequency of the antenna [23]. The DRF and DRAF have been fabricated and measured. The return loss, insertion loss, radiation pattern and mutual coupling of the DRAF are investigated. The measured and simulated results show a good agreement.

This paper is arranged as follows. Introduction in the first Section I, the second Section II discusses the methods used for finding the solution of the proposed antenna and is divided into two sub sections: the first finite element methods and the second finite integration

methods. Section III discusses the simulations and numerical results of defected ground structure filters, in three subsections A, B and C. A summary is presented in Section IV.

II. METHODS OF SOLUTION

A. Finite element method

The finite element method (FEM) is used for finding approximate solution of partial differential equations (PDE) and integral equations. The solution approach is based either on eliminating the differential equation completely (steady state problems), or rendering the PDE into an equivalent ordinary differential equation, which is then solved using standard techniques such as finite differences. In solving partial differential equations, the primary challenge is to create an equation which approximates the equation to be studied, but which is numerically stable, meaning that errors in the input data and intermediate calculations do not accumulate and cause the resulting output to be meaningless. There are many ways of doing this, all with advantages and disadvantages. The finite element method is a good choice for solving partial differential equations over complex domains or when desired precision varies over the entire domain. More details about FEM can be found in [24, 25].

B. Finite integration technique

The finite integration technique (FIT) is a spatial discretization scheme to solve electromagnetic field problems in time and frequency domain numerically. FIT was proposed in 1977 by Thomas Weiland [24, 25] and has been enhanced continually over the years. This method covers the full range of electromagnetics, from static up to high frequency and optic applications. The basic idea of this approach is to apply the Maxwell's equations in integral form to a set of staggered grids. This method stands out due to high flexibility in geometric modeling and boundary handling as well as incorporation of arbitrary material distributions and material properties such as anisotropy, non-linearity and dispersion. Furthermore, the use of a consistent dual orthogonal grid (e.g., Cartesian grid) in conjunction with an explicit time integration scheme (e.g., leap-frog-scheme) leads to extremely high efficient algorithms referred to both computation time and memory requirements which are especially adapted for transient field analysis in RF applications. More details about FIT can be found in [25].

III. DEFECTED GROUND STRUCTURE FILTERS

Figure 2 shown the square design of dielectric resonator filter (SDRF). The square dielectric resonator

element (SDR) of FR-4 material has side length l_r=44mm, height h=1.524mm, and dielectric constant εr=4.5, and loss tangent 0.002. It is mounted on the DGS perfect conductor ground plane of $l_g \times l_g$ dimensions equal to 70mm ×70mm. The DGS section is etched on the ground plane. The DGS is composed of two rectangles, Ws×Ls, Ws=8mm, Ls=16mm, connected with two transverse slots of width t=1mm, and length tt=14mm. The distance between the two slots, k, is 7mm. The substrate material is FR-4 of dielectric constant 4.5, loss tangent 0.002 and has thickness of 1.5mm.
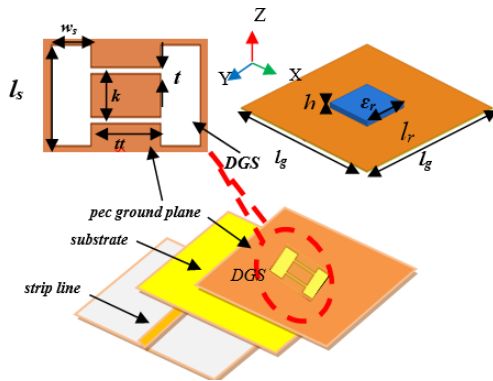
Fig. 2. The structure of the SDR filter antenna.

A. Frequency characteristics of SDRF on DGS unit section

The DGS unit section can provide cut-off frequency and attenuation pole at some specific frequency without any periodicity of DGS. In order to investigate the frequency characteristics of the DGS section, the DGS unit section has been measured and their parameters are calculated using FEM to verify the measured results. Pictures of the fabricated band stop filter system are shown in Fig. 3. The results shown in Fig. 4 indicate a rejection of wide bandwidth of 3dB equal to 1.57 GHz (from1.25 GHz to 2.82 GHz).

(a) Top view   (b) Bottom view
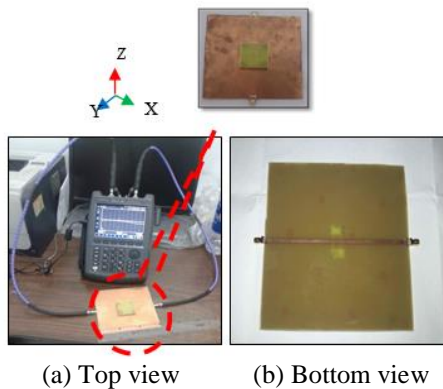
Fig. 3. The photograph of the fabricated BSF.
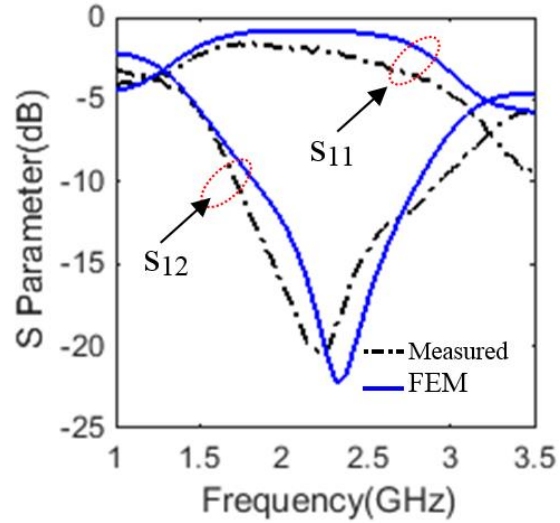
Fig. 4. Measured and calculated return losses, insertion losses.

The cut-off frequency of the slot band-reject response at 3dB is f_c and its pole frequency is f_0. Both are in GHz. Results show that f_c of the unit-slot *is* 1.2 GHz and f_0 *is* 1.98 GHz. The experimental response curves match with the calculated results to a great extent. The characteristics of Fig. 4 shows a band-reject filter response with low transmission loss and wide band-stop features. Tuning the band-stop filter (BSF) is achieved by varying the transverse slot width.

The transverse slot width t of the DGS is varied from 3 mm to 4 mm. Return losses S_{11} and insertion losses S_{21} are calculated and given by Fig. 5. It can be shown from results that the band-stop central frequency f_0 increases, rejection level decrease*s* and transmission loss increases with increasing the transverse slot width.
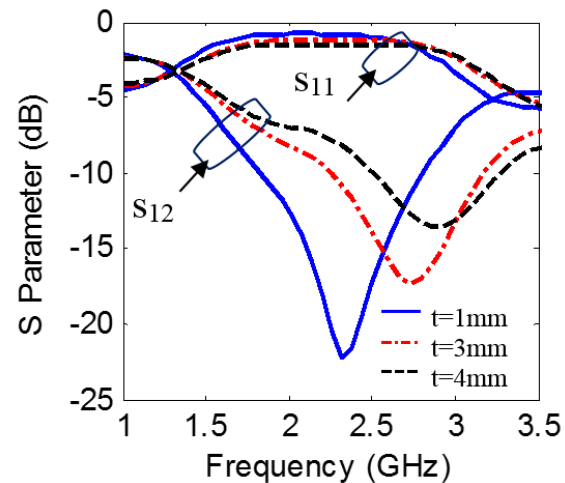
Fig. 5. Calculated return losses, insertion losses for varying the transverse slot width, t.

B. Frequency characteristics of reconfigurable DRF on DGS unit section

In this design, three ideal metal switches are integrated on each rectangular slot of the DGS to split it into four narrow strips to change the resonance frequency due to change in the current distribution. Return losses S11 and insertion losses S21 are calculated and given by Fig. 6. Results show that the band-stop central frequency f_o is moved to 3GHz and f_c is moved to 2.3GHz. A rejection of wide bandwidth of 3dB is equal to 1.7 GHz (from 2.3 GHz to 4 GHz), and the transmission loss is about 1.24dB.
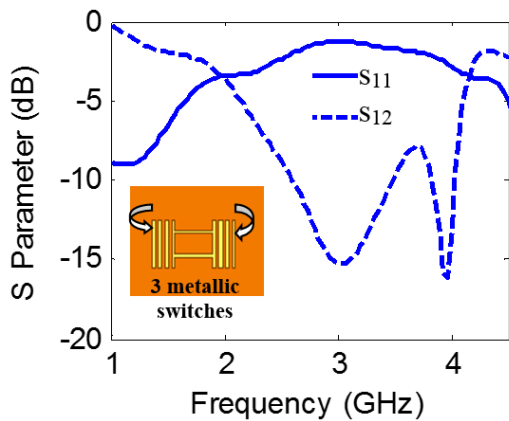
Fig. 6. Calculated return losses, insertion losses for reconfigurable filter.

C. Frequency characteristics of DRAF "filtenna" on DGS unit section

In this section the dielectric resonator antenna filter (DRAF), "filtenna", that combines the DRA and DRF is fabricated as shown in Fig. 7. This structure integrates two types of filters, band-stop filter and band-pass filter. The unit cell in this structure is designed with the same dimensions for the first structure. However, the SDR is loaded with a metallic plate square of length, l_p=22mm, which is then used as the resonator for the antenna as well as for the band-pass filter. The SDRA is characterized by height h, side length l_r, as shown in Fig. 1 and is made of material with dielectric constant ε_r. This geometry is equivalent to a square DRA of the same material placed over a ground plane with the same dimensions, but the height is equal to h/2. The added metallic plate acts as an electric wall, which will reduce the DRA size by half, also it acts as a shorting post for the electric field and the removed part from DRA [23, 26]. The equations for calculating the resonant frequency approximately are given by [26]:

$$k_x^2 + k_y^2 + k_z^2 = \varepsilon_r k_o^2,$$

$$k_o = \frac{2\pi}{\lambda_o}, \tag{1}$$

$$f_o = \frac{c}{2\pi\sqrt{\varepsilon_r}}\sqrt{k_x^2 + k_y^2 + k_z^2}, \tag{2}$$

$$k_y = k_x, \, k_z = \frac{\pi}{h}, \tag{3}$$

$$k_x \tan\left(\frac{k_x l_r}{2}\right) = \sqrt{((\varepsilon_r - 1)k_o^2 - k_x^2)}, \tag{4}$$

where k_x, k_y, and k_z denote the wave numbers along the x, y, and z directions inside the DR, respectively, and k_o is a free space wave number.

This structure can be used as the resonator for the antenna as well as for the band-pass filter. The DRAF has been fabricated and measured. Figure 8 shows the photograph of the fabricated DRAF "filtenna".
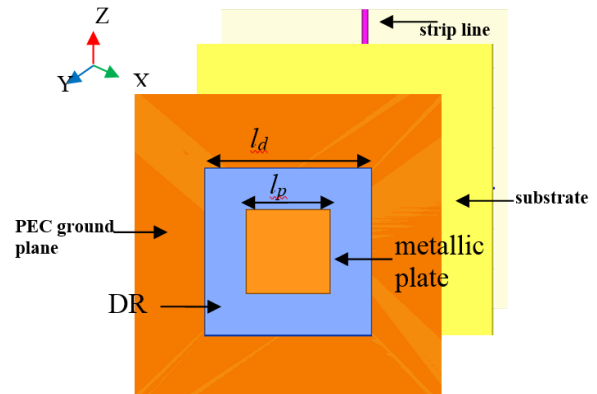
Fig. 7. The structure of the filter antenna with top metallic plate.

(a) Top view   (b) Bottom view
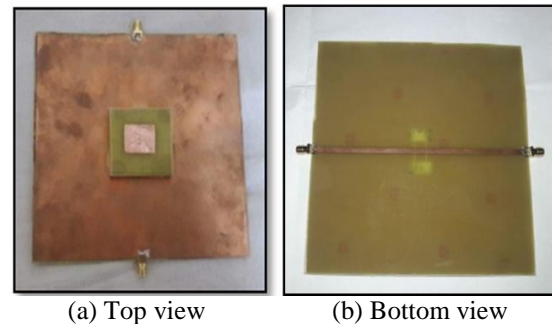
Fig. 8. The photograph of the fabricated DRAF "filtenna".

The measured and simulated results show a good agreement as shown in Fig. 9. Results show that the DRAF has two band-stop filter with bandwidths of 800 MHz and 650 MHz.The return losses of the filters are 0.52 dB for a central frequency f_0 =1.78 GHz and 2 dB for a central frequency f_0 = 3.88 GHz. It can be shown from Fig. 9 that the band-pass filter has central frequency f_0 at 2.78 GHz, the 3-dB cut-off frequency f_c at 2.1 GHz, the 3-dB pass bandwidth is about 1.3GHz, the rejection level 22dB and insertion loss about 0.89

dB. The total loss of the filtering antenna is almost the same as the filter insertion loss. The calculated radiation patterns at 2.78GHz, for the designed filtering antenna system in the x-y, y-z, and x-z planes are shown in Fig. 10.
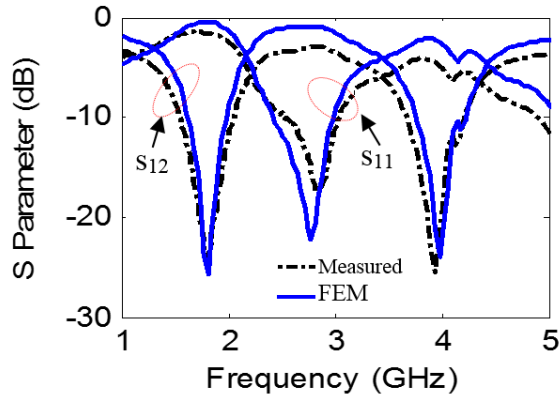
Fig. 9. Measured and calculated return losses, insertion losses for filter antenna with top metallic plate.
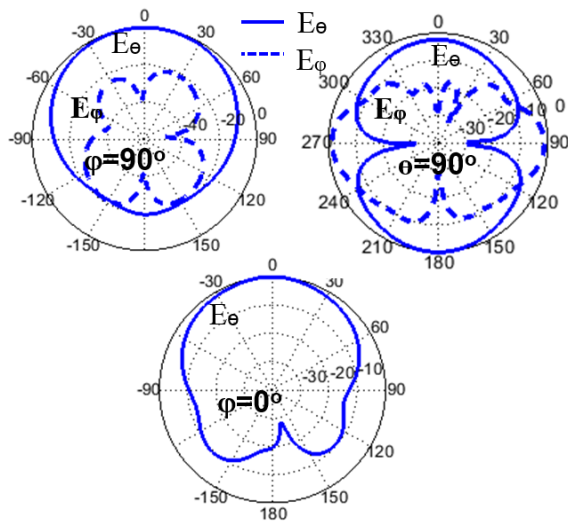
Fig. 10. Calculated radiation patterns for filter antenna with top metallic plate at f = 2.78GHz.

The band-stop and band-pass filters are tuned with varying metallic plate length. The metallic plate length l_p is given for 3 values 11mm, 33 mm and 44 mm and then the return losses S_{11}, insertion losses S_{21} are calculated as shown in Fig. 11. It is noted that the central frequencies f_0, the rejection levels and an insertion loss of the two filters are affected as shown in figure.

IV. CONCLUSION

This article proposes the square dielectric resonator element with a defected ground structure (DGS) and

investigates different geometrical structures. Two structures of filter (band-stop filter, band-pass filter) have been successfully designed and investigated. The first structure is a dielectric resonator band-stop filter (DRF). The filter has bandwidth of 1.57GHz and transmission losses of 0.6dB at 2GHz. The second structure is a dielectric resonator filter antenna (DRFA). Results show that the DRFA has two band-stop filters with bandwidths of 800MHz and 650MHz. The band-pass filter has an insertion loss about 0.89 dB at 2.78 GHz with bandwidth about 1GHz. To verify the performance, the filters are fabricated, calculated and measured. The measurements show a good consistency with the calculations.
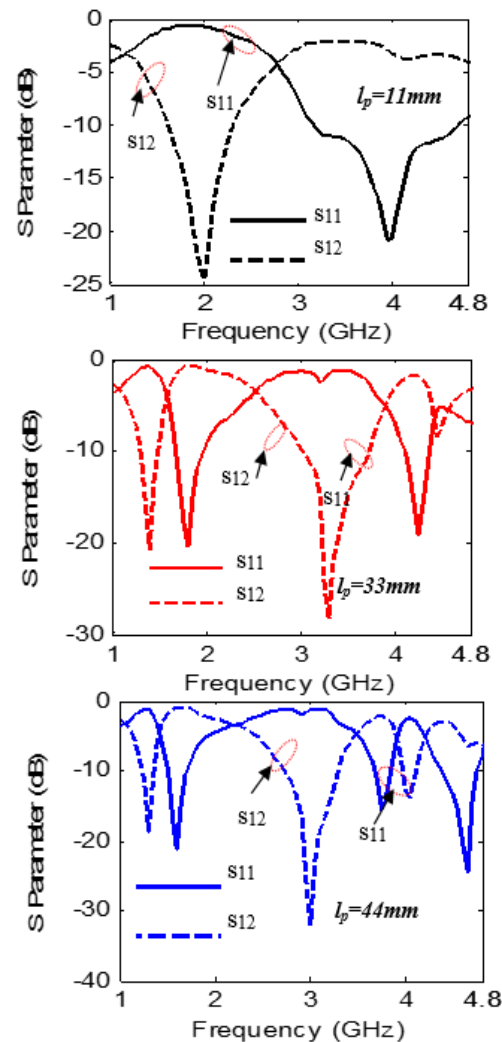
Fig. 11. Calculated return losses, insertion losses for varying l_p.

REFERENCES

[1] X. Chen, F. Zhao, L. Yan, and W. Zhang, "A compact filtering antenna with flat gain response within the passband," *IEEE Antennas Wirel. Propag. Lett.*, vol. 12, pp. 857-860, 2013.

[2] S. P. Wang, P. S. Hall, and P. Gardner, "Yagi antenna with frequency domain filtering performance," *Antennas and Propagation Society International Symposium (APSURSI)*, 2012 IEEE, 2012.

[3] C. T. Chuang and S. J. Chung, "New printed filtering antenna with selectivity enhancement," *Microwave Conference,* 2009, *EuMC, European IEEE*, 2009.

[4] S. Oda, et al., "Electrically small superconducting antennas with bandpass filters," *IEEE Transactions on Applied Superconductivity 17.2*, 878-881, 2007.

[5] F. Queudet, et al., "Integration of pass-band filters in patch antennas," *Microwave Conference*, 2002, *32nd European IEEE*, 2002.

[6] A. I. Abunjaileh, I. C. Hunter, and A. H. Kemp, "A circuit-theoretic approach to the design of quadruple-mode broadband microstrip patch antennas," *IEEE Transactions on Microwave Theory and Techniques 56.4*, 896-900, 2008.

[7] C. K. Lin and S. J. Chung, "A filtering microstrip antenna array," *IEEE Transactions on Microwave Theory and Techniques 59.11*, 2856-2863, 2011.

[8] W. J. Wu, et al., "A new compact filter-antenna for modern wireless communication systems," *IEEE Antennas and Wireless Propagation Letters 10*, 1131-1134, 2011.

[9] E. H. Lim and K. W. Leung, "Use of the dielectric resonator antenna as a filter element," *IEEE Transactions on Antennas and Propagation 56.1*, 5-10, 2008.

[10] G. Breed, "An introduction to defected ground structures in microstrip circuits," *High Frequency Electronics*, 50-54, 2008.

[11] K. Annam, "Design of bandstop filters using defected ground structures," *Diss. University of Dayton*, 2015.

[12] D. Ahn, et al. "A design of the low-pass filter using the novel microstrip defected ground structure," *IEEE Transactions on Microwave Theory and Techniques 49.1*, 86-93, 2001.

[13] A. B. Abdel-Rahman, et al., "Control of bandstop response of Hi-Lo microstrip low-pass filter using slot in ground plane," *IEEE Transactions on Microwave Theory and Techniques 52.3*, 1008-1013, 2004.

[14] M. K. Mandal and S. Sanyal, "A novel defected ground structure for planar circuits," *IEEE Microwave and Wireless Components Letters 16.2*, 93-95, 2006.

[15] J. S. Lim, et al., "A spiral-shaped defected ground structure for coplanar waveguide," *IEEE Microwave and Wireless Components Letters 12.9*, 330-322, 2002.

[16] D. J. Woo, et al., "Novel U-slot and V-slot DGSs for bandstop filter with improved Q factor," *IEEE Transactions on Microwave Theory and Techniques 54.6*, 2840-2847, 2006.

[17] A. Petosa, *Dielectric Resonator Antenna Handbook*, Artech House. Inc., Norwood, USA, (2007).

[18] K. W. Leung, et al., "Bandwidth enhancement of dielectric resonator antenna by loading a low-profile dielectric disk of very high permittivity," *Electronics Letters 33.9*, 725-726, 1997.

[19] A. A. Kishk and K. F. Lee, "Wideband simple cylindrical dielectric resonator antennas," *IEEE Microwave and Wireless Components Letters 15.4*, 241-243, 2005.

[20] Y. Hwang, et al., "Gain-enhanced miniaturised rectangular dielectric resonator antenna," *Electronics Letters 33.5*, 350-352, 1997.

[21] K. P. Esselle, "A low-profile rectangular dielectric-resonator antenna," *IEEE Transactions on Antennas and Propagation 44.9*, 1296-1297, 1996.

[22] R. Mahmood and M. T. Beg, "Dual band dielectric resonator filter (DBDRF) with defected ground structure (DGS)," *World Applied Sciences Journal 32 (4)*, pp. 582-586, 2014.

[23] G. D. Makwana and K. J. Vinoy, "Design of a compact rectangular dielectric resonator antenna at 2.4 GHz," *Progress In Electromagnetics Research C*, vol. 11, 69-79, 2009.

[24] H A. Malhat, S. H. Zainud-Deen, and K. H. Awadalla, *Radio Frequency Identification Antenna: Design and Applications*, LAP Lambert Academic Publishing, 2012.

[25] A. Noha and S. H. Zainud-Deen, *Dielectric Resonator Antennas on Curved Surfaces*, LAP Lambert Academic Publishing, 2013.

[26] P. Rezaei, M. Hakkak, and K. Forooraghi, "Design of wide-band dielectric resonator antenna with a two-segment structure," *Progress In Electromagnetics Research, PIER*, vol. 66.

Noha Abd Al Salam Al-Shalaby as born in Gharbya, Egypt, on November 15, 1975. She received the B.Sc. and M.Sc. degrees from Tanta University in 1998 and 2005 respectively. She received her Ph.D. degree in Antenna Engineering from Menoufia University, Egypt 2013. She is currently a Lecturer in the

Department of Electrical Engineering in the Faculty of Engineering, Kafer El-Shiekh University, Egypt. Her research interest at present include plasma antennas, DRA, transmitarray, reflectarray filters antenna and RFID.

Shaymaa Mostafa Gaber was born in Cairo, Egypt, on August 5, 1980. She received the B.Sc. and M.Sc. degrees from Helwan University in 2002 and 2008 respectively. She received her Ph.D degree in Antenna Engineering from Helwan University, Egypt 2013. She is currently a Lecturer in the Department of Telecomm-unication Engineering in the Faculty of Engineering, Egyptian Russian University, Egypt. Her research interest at present include DRA, Graphene antennas, plasma antennas, transmitarray, reflectarray and RFID.

Design of a Compact Hybrid Branch Line Coupler with 2-D Implementation of Stepped Impedance Transmission Lines of High Impedance Ratio for Wide Range of Harmonic Suppression

Zafar Bedar Khan [1], Ghulam Mehdi [1], and Huiling Zhao [2]

[1] Center of Excellence for Science and Applied Technology, H-11/4 Sector, Islamabad, Pakistan
zafarbedarkhan@hotmail.com, mehdi.engr@gmail.com

[2] Department of Electronics and Information, Northwestern Polytechnical University, Xian, 710072, P. R. China
zhhl@nwpu.edu.cn

Abstract ─ In this paper stepped impedance transmission line (TL) structure is adopted by using proposed unorthodox technique to design a hybrid branch line coupler (HBLC) in micro-strip technology. In addition to achieving good fractional bandwidth of 30% and size reduction of 56%, the proposed technique ensures a high impedance ratio (M) over a wide range of electrical lengths of the high-Z low-Z (stepped impedance) sections. Maintaining high M ensures a good harmonic suppression of the proposed design up to $9f_0$ (f_0 is the design frequency which is 1GHz for this work). Experimental verification of the proposed technique is demonstrated by designing an HBLC at 1GHz. Experimental and simulation results show excellent conformance.

Index Terms ─ Harmonic suppression, high impedance low impedance structure, hybrid branch line coupler, impedance ratio.

I. INTRODUCTION

Branch line coupler, owing to its capability to couple a fraction of signal with controllable power and phase makes it essential for many useful applications at microwave and milli-metric frequency regimes. A quadrature hybrid branch line coupler (HBLC) is one such device which equally splits the signal with a 90° mutual phase difference and may be particularly useful in applications like antenna array network, balanced mixers and amplifiers, phase shifter, crossover design [1] and Butler matrix design [2] etc. In addition, it may also be used in signal sensing and monitoring in measurement equipment (like network analyzers) and radio frequency front-ends (RFFE) of most radar and communication systems. A passive directional branch line coupler (BLC) is usually employed for the task to couple a fraction of the signal and monitor its frequency and phase without disturbing the main transmission. Conventional BLCs, however suffer from bigger size (due to quarter-wave

($\lambda g/4$) transmission lines (TL)) and inherent narrow bandwidth typically around 8-10% [3-4] making it not suitable for ever reducing, bandwidth hungry modern systems. Yet another disadvantage is its poor ability to suppress the higher order harmonics which are produced due to periodic nature of $\lambda g/4$ transformers. These unwanted harmonics may adversely affect the performance of other sub-systems/systems. Thus, good out-of-band response is highly desirable. Different design strategies have been proposed to address the above mentioned shortcomings in the conventional HBLC [5-26]. A careful analysis of the literature reveals that simultaneous achievement of miniaturization, wide operational bandwidth and reasonable out-of-band rejection has not been possible and there has always been a tradeoff between these characteristics. For example a fairly wide bandwidth (BW) of 49% and 50.9% was achieved in [5-6] respectively at the cost of size enlargement to almost three fold with no harmonic suppression. On the contrary, a BLC with size reduction of 67.5% was reported in [7] operational over a very narrow BW of 1.8%, again with no harmonic suppression. A lot of efforts have been done in order to strike a balance between the two extremities of BW and size as mentioned above, without considering harmonic suppression [8-17] and with harmonics suppression as design parameter [18-26]. In [8-9], a fractional bandwidth (FBW) of 10% was achieved with size reduction of 33% and 55% by employing defected ground structure (DGS) and cascaded transmission line (TL) with open stub techniques respectively. Comb-line structure was used in place of $\lambda g/4$ transformers in [10], and asymmetrical T-shaped TLs in [11] to improve the FBW to 23% and 24% with area reduction rate of 22.6% and 55% respectively. Yet another BLC design technique utilizing the polar curves [12] was used to achieve a FBW of 30% with an overall size of 50% of the conventional BLC. Recently, remarkable size reduction of about 62% has been achieved by employing high-low

impedance TL in substrate integrated suspended line technology [13] and cascaded slow-wave cells in [14]. The reported FBWs for the two design approaches were 20% and 32% respectively. Artificial TLs based design approaches were presented in [15-17]. A BLC with area reduction of 47% operational over a FBW of around 40% was achieved in [15] by utilizing a combination of dual TL and π-model technique, while in [16] only dual TL and in [17] only π-model based artificial TL were implemented to achieve a size reduction of 63.9% and 62% and FBW of 43% and 33% respectively. In all the above cited works [5-17], out-of-band performance or harmonic suppression capability of the BLC was not considered which has become another important design consideration in modern systems.

Many researchers have proposed different design techniques to achieve good out-of-band performance of the BLC at the cost of FBW and/or circuit size [18-26]. Reference [18] used slow-wave methodology by using four high-low impedance resonant cells to achieve second harmonic suppression only ($2f_0$, where f_0 is the design frequency). The reported FBW was 10% with an impressive area reduction of 72%. In [19], similar specifications of harmonic suppression (up to $2f_0$ only), FBW (about 13%) and size reduction (73.2%) were achieved by employing interdigitated shunt capacitor with high-impedance TL. Harmonic suppression was improved to $3f_0$ in [20] by incorporating T-shaped micro-strip lines in place of $\lambda g/4$ transformers. Compromise was made on the circuit area which was about 70.5% of the conventional BLC (29.5% area reduction) with an operating FBW of 10%. Another design with harmonic suppression up to $3f_0$ used meandered T-shaped TL technique [21] with an improved area reduction of 63.5% (owing to meandering of TLs). An improved out-of-band response up to $5f_0$ was achieved by using two shunt open stubs separated by a TL (π-shape) in [22] at the cost of more circuit area (37% size reduction) and narrow FBW (8%). The situation was improved in [23] where a unit consisting of a TL and triple stub was proposed to achieve harmonic suppression up to $6f_0$. Reported size reduction rate in [23] was 44% with a narrow operational FBW of 9%. In [24] a very wide out-of-band response up to $10f_0$ was reported by employing a triangular dumbbell shaped DGS scheme. Circuit area was significantly reduced to 65% at the cost of narrow FBW of about 8%. In a recently reported work exploiting modified T-shaped TLs [25], remarkable size reduction of 74% was achieved with harmonic suppression up to $8f_0$. The FBW however was less than 14.4%. Stepped impedance (low-high impedance) TLs were used to replace $\lambda g/4$ transformers in [26]. More specifically, the low-Z high-Z low-Z (where Z stands for impedance) micro-strip structure shown in Fig. 1 (a) with impedance ratio M > 1 (where $M = Z_2/Z_1$), was used in the place of the vertical $\lambda g/4$ transformers of the conventional BLC,

whereas high-Z low-Z high-Z structure shown in Fig. 1 (b) with M < 1, was integrated horizontally. Using this technique, an area reduction of 50% was reported but the harmonic suppression was merely up to $2f_0$. From the above discussion, the fact stands out that for BLC design, there has been a trade-off between parameters like harmonic suppression, FBW and circuit area.
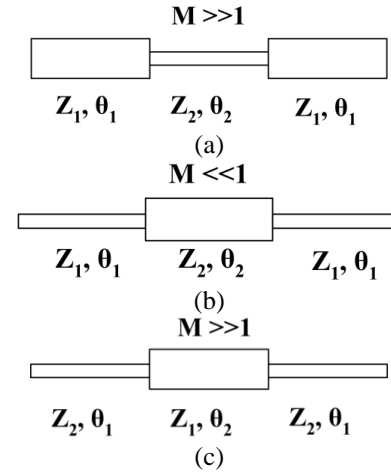
Fig. 1. Stepped impedance structures: (a) Conventional low-Z high-Z low-Z structure with M > 1, (b) conventional high-Z low-Z high-Z structure with M < 1, and (c) proposed high-Z low-Z high-Z structure with interchanged impedances and M >> 1.

In this paper we propose an unorthodox approach of analytically solving the structure in Fig. 1 (a) with a proposed length constraint ($2\theta_1 + \theta_2 = 45°$, for size reduction), to calculate low-Z (Z_1) and high-Z (Z_2) and interchanging them resulting in structure given in Fig. 1 (c), enforcing the condition M (Z_2/Z_1) >> 1 on the high-Z low-Z high-Z (stepped impedance sections of electrical length θ_1, θ_2, θ_1 respectively) structure. Please note here that the electrical length of the respective sections is kept the same as in Fig. 1 (a). The proposed methodology gives a superior out-of-band response as compared to that implemented in [26]. The primary reason behind an excellent harmonic suppression is a high M which ensures a transmission response (S_{21}) of HBLC approaching that of an ideal low pass filter (LPF) response [3]. This argument is based on the rationale given in section 2. The proposed structure shown in Fig. 1 (c) has an additional advantage of easier integration in 2-dimensions (2-D, vertical and horizontal arms) of the BLC primarily due to high-Z section with relatively thin width at the beginning. The proposed analytical solution results in high impedance ratio over a wide range of electrical lengths subsequently resulting in a wide range of high and low impedances (Z_2 and Z_1) to achieve good performance parameters. The designed HBLC based on proposed technique at a center frequency of 1 GHz,

achieved excellent harmonic suppression up to $9f_0$, an area reduction of 56% and a reasonable operational FBW of 30%.

II. ANALYSIS OF PROPOSED TECHNIQUE

Stepped impedance TL comprising of low-Z high-Z low-Z structure with an electrical length of θ_1, θ_2, θ_1 respectively as depicted in Fig. 1 (a) is adopted and analyzed first for evaluation and calculation of the impedances (Z_1 and Z_2) and respective electrical lengths. Subsequently by interchanging the Z_1 and Z_2 segments the structure is transformed to high-Z low-Z high-Z as shown in Fig. 1 (c) (enforcing M >> 1), which ultimately is integrated in place of horizontal 35Ω TL and vertical 50Ω TL (in 2-D) of the conventional HBLC. The effectiveness of this methodology, particularly in harmonics suppression is explained through comparison of the structures of Figs. 1 (a) and (c) later in this section.

Since the low-Z high-Z low-Z structure of Fig. 1 (a) can be considered as cascaded TLs, 2-port network analysis is applicable. In order to effectively replace conventional BLC TL of $\pi/2$ length (quarter wavelength) and impedance of Z_0, the equivalent ABCD parameters of this structure are kept equal to the ABCD parameters of the conventional BLC TL as given in Equation (1):

$$\begin{pmatrix} \cos\theta_1 & jZ_1\sin\theta_1 \\ \dfrac{j\sin\theta_1}{Z_1} & \cos\theta_1 \end{pmatrix}\begin{pmatrix} \cos\theta_2 & jZ_2\sin\theta_2 \\ \dfrac{j\sin\theta_2}{Z_2} & \cos\theta_2 \end{pmatrix}\begin{pmatrix} \cos\theta_1 & jZ_1\sin\theta_1 \\ \dfrac{j\sin\theta_1}{Z_1} & \cos\theta_1 \end{pmatrix}$$
$$= \begin{pmatrix} 0 & jZ_0 \\ \dfrac{j}{Z_0} & 0 \end{pmatrix}_{\text{Conventional BLC}},$$
(1)

Form Equation (1) it can be easily found that A = D and is given in Equation (2):

$$A = \cos\theta_1\cos\theta_2 - (M+M^{-1})\cos\theta_1\sin\theta_1\sin\theta_2,$$ (2)

Where $M = Z_2/Z_1$ is the impedance ratio. Putting A=0 and after some algebraic manipulations, M and M-1 can be given as:

$$M = a + \sqrt{a^2 - 1}$$
$$M^{-1} = a - \sqrt{a^2 - 1},$$
(3)

Where,

$$a = 0.5 \times \sec\theta_1\cot\theta_1\cot\theta_2.$$

Similarly, B parameter derived from (1) can be equated to jZ_0 to get an analytical equation for Z_1 as presented in Equations (4-5):

$$B = jZ_1(2\cos\theta_1\cos\theta_2\sin\theta_1 + M\cos^2\theta_1\sin\theta_2 - M^{-1}\sin^2\theta_1\sin\theta_2)$$
$$= jZ_0,$$
(4)

Therefore,
$$Z_1 =$$
$$Z_0 / [(2\times\cos\theta_1\cos\theta_2\sin\theta_1) + (M\cos^2\theta_1 - M^{-1}\sin^2\theta_1)\sin\theta_2)].$$
(5)

It is worth mentioning here that Z_0 in Equation (5) is 35Ω and 50Ω for horizontal and vertical quarter wavelength TL of the conventional BLC respectively. It may also be noted here that Z_2 can either be calculated from C parameter derived from Equation (1) or directly from M once Z_1 is known, we use the latter calculation of Z_2. In order to solve Equations (3) and (5) to get M (and M^{-1}) and Z_1, a length constraint is introduced in Equation (6), which also serves as a means for miniaturization of the proposed HBLC:

$$2\theta_1 + \theta_2 = 45°.$$ (6)

At this point Equation (3) coupled with Equation (6) is solved and the impedance ratio and its inverse is plotted in Fig. 2 (a) against θ_1 and θ_2. Subsequently, Equation (5) is solved for the calculated values of M (and M^{-1}), θ_1 & θ_2 and the curves for Z_1 and Z_2 (Z_2 obtained from $M = Z_2/Z_1$) for both 35Ω and 50Ω TL are plotted in Fig. 2 (b). It is imperative to note that the shaded area in Figs. 2 (a) & (b) indicates the practically implementable limits of M (M^{-1}), Z_1 and Z_2. Two primary parameters of concern in defining these bounds are Z_1 and M. The lower bound is set by considering Z_1 (for $Z_0 = 35Ω$) such that its value should not be too low which translates into a very wide width of TL which may not be practically implementable. On the other hand upper bound is determined from M such that its value should not be too high which translates into a very high Z_2 (considered for $Z_0 = 50Ω$) indicating a very thin TL which may not be fabricated by the machine (the machining lower limit in most cases is 0.1mm). Fine tuning of the layout circuit with or without meandering/mitering may be required for compact size.

The 'bath tub' like curve of M shown in Fig. 2 (a) depicts clearly that in the workable range (shaded area), M is greater than 10, fairly flat and ensures the condition of M >> 1 in the impedance interchanged structure of Fig. 1 (c) over a wide range of θ_1 & θ_2. It gives the designer a leverage of selecting suitable lengths θ_1 & θ_2 with a high M causing the transmission response (S_{21}) of proposed high-Z low-Z high-Z structure (with interchanged Z_1 and Z_2) shown in Fig. 1 (c) to follow that of an ideal LPF giving a good harmonic suppression. To prove this hypothesis, a comparison of S_{21} response of conventional structure in Fig. 1 (a) and proposed structure in Fig. 1 (c) is drawn in Fig. 3, for $\theta_1 = 14°$, $\theta_2 = 17°$, M = 13.5, $Z_1 = 8.42Ω$, $Z_2 = 113.25Ω$ (Z_1 and Z_2 selected for 35Ω TL from Fig. 2 (b)).
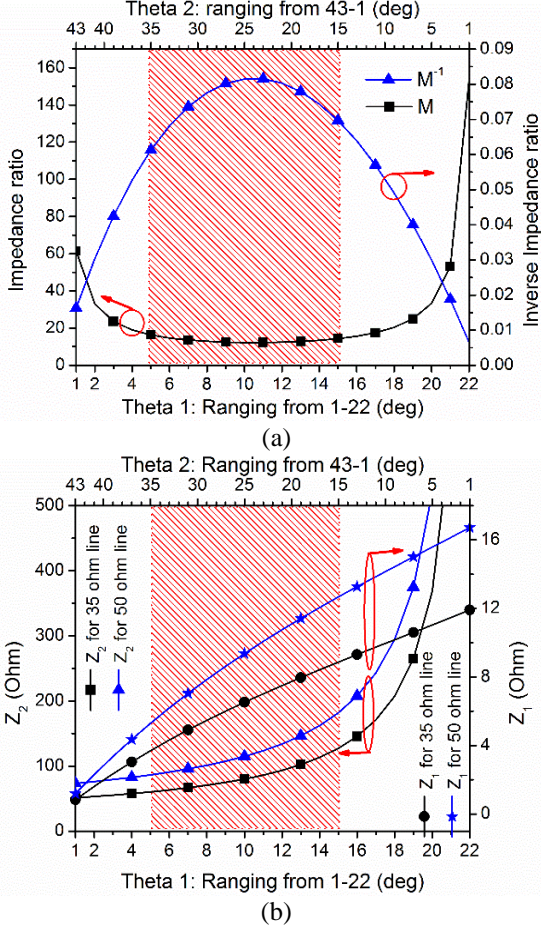
Fig. 2. Design graphs based on analytical solution: (a) Impedance ratio and its inverse, M (& M^{-1}) against wide range of θ_1 & θ_2, and (b) Z_1 and Z_2 for structure in Fig. 1 (a) against θ_1 & θ_2.

The simulation is carried out in Agilent's Advanced Design System (ADS) considering a 0.8mm thick substrate with dielectric constant of 2.2. It is very clearly shown in Fig. 3 that for a tuned response at 1 GHz, the proposed structure promises a good out-of-band performance as compared to the conventional structure. Very similar response can be simulated for structure replacing the 50Ω vertical branch of conventional BLC. It may be noted that Fig. 3 presents simulated response of just horizontal arm to prove the point. Actual response of the complete circuit may be different as shown subsequently.

The proposed high-Z low-Z high-Z structure (with M >> 1) is ultimately integrated in 2-D to get the schematic of the proposed HBLC as shown in Fig. 4. The design steps are stipulated as: 1) select suitable electrical lengths θ_1 & θ_2 (such that the condition $2\theta_1 + \theta_2 = 45°$ is satisfied), 2) from Fig. 2 (a) get M (& M-1), 3) get the value of Z_2 and Z_1 for 35Ω and 50Ω TLs respectively from Fig. 2 (b), 4) calculate the widths corresponding to

Z_1 and Z_2, 5) layout as per Fig. 4 by interchanging Z_1 and Z_2 (low-Z high-Z sections) and optimize.
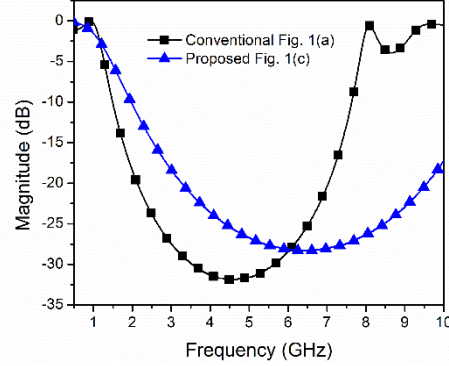
Fig. 3. Comparison of transmission coefficient (S_{21}) of structure in Fig. 1 (a) and proposed structure in Fig. 1 (c).
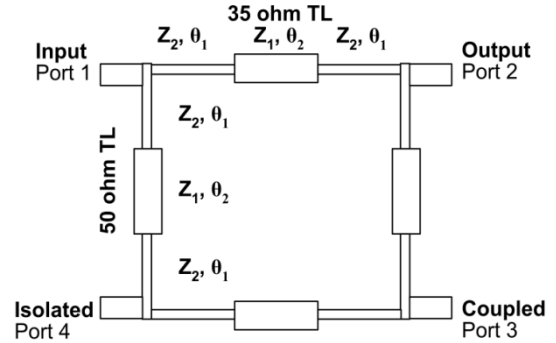
Fig. 4. Schematic of HBLC with proposed structure integrated in 2-D (not drawn to scale).

III. EXPERIMENTAL VERIFICATION

In order to validate the proposed technique, a hybrid branch line coupler was designed at 1 GHz and simulated in ADS. The designed HBLC was subsequently fabricated on a F4BM-2 substrate with dielectric constant of 2.2 and thickness of 0.8mm. For the purpose, the proposed high-Z low-Z high-Z structure was designed by: 1) selecting $\theta_1 = 14°$, $\theta_2 = 17°$, 2) M = 13.5, $M^{-1} = 0.074$, 3) for 35Ω TL, $Z_2 = 113.25\Omega$, $Z_1 = 8.42\Omega$; for 50Ω TL $Z_2 = 162\Omega$, $Z_1 = 12\Omega$, 4) for 35Ω TL, $w_2 = 0.51mm$, $w_1 = 21.9mm$; for 50Ω TL $w_2 = 0.16mm$, $w_1 = 14.8mm$, 5) with all these parameters known, the proposed high-Z low-Z high-Z structure was integrated in 2-D of the conventional BLC as per Fig. 4. The final layout of the designed HBLC was simulated. Some optimization, mainly mitering of low Z (Z_1) TL section of both 35Ω and 50Ω lines at an angle of 30°, and adjustment of width (within 4-6% of the original value) was carried out. Since the discontinuity between the High Z (less width) and Low Z (more width) TL section is bigger due to high M, slight adjustment of the width may optimize the results.

Fabricated HBLC at 1 GHz is depicted in Fig. 5.

Size of the proposed HBLC is reported to be 3.3cm × 3.9cm (or $0.15\lambda g \times 0.18\lambda g$). The achieved area reduction as compared to conventional BLC (with dimensions of 5.39 cm × 5.4 cm) at 1 GHz was 56%.
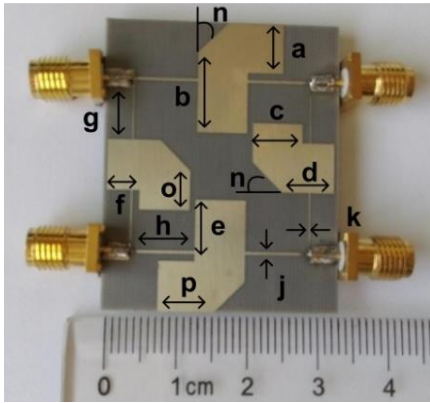
Fig. 5. Fabricated HBLC with proposed methodology. Dimensions (mm): a=7, b=11.3, c=7, d=7.3, e=8.5, f=4.35, g=7.2, h=8.82, j=0.41, k=0.16, o=5.5, p=7.8 and n=30°.

A. Results and discussions

All subsequent measurements were performed on Agilent's Microwave Network Analyzer model no. E8363B. Figure 6 (a) shows excellent conformance between the measured and simulated response of reflection (S_{11}) and transmission (S_{21}) coefficients of the designed HBLC. Measured return loss and insertion loss at port 1 stand at 29 dB and 3.5 dB respectively at 1 GHz. For S_{11} the measured 10 dB and 20 dB FBW is 29.4% (0.916 GHz – 1.21 GHz) and 13% (0.99 GHz – 1.2 GHz) respectively. For S_{21}, 1 dB FBW is reported to be 30% (0.94 GHz – 1.23 GHz). In addition, a very good out-of-band performance can be observed. The harmonic suppression of better that 15.5 dB is achieved up to $9f_0$. Insertion loss at port 3 (S_{31}), isolation between output ports 2 & 3 (S_{23}) and isolation at port 4 (S_{41}) are depicted in Fig. 6(b). Here too, almost overlapping simulated and measured responses can be observed. At 1 GHz, $S_{31} = 3.02$ dB and $S_{23} = S_{41} = 29.7$ dB indicating excellent power division, and isolation (both between the output ports 2 & 3 and isolated port 4). Achieved 1 dB FBW of S_{31} is 40% (0.76 GHz – 1.16 GHz) whereas 10 dB and 20 dB FBW of each of S_{23} and S_{41} are reported to be 33% (0.86 GHz – 1.16 GHz) and 11% (0.98 GHz – 1.09 GHz) respectively. S_{31} (transmission coefficient) exhibits an excellent harmonic suppression of better than 19.8 dB whereas out-of-band response of S_{23} and S_{41} is better than 15.5 dB till $9f_0$. Lastly, Fig. 7 shows the amplitude imbalance/difference ($|S_{21}| - |S_{31}|$) and phase imbalance/difference ($\angle S_{21} - \angle S_{31}$) between the signals at output ports. At 1 GHz, measured value of amplitude difference

is 0.48 dB (less than ± 0.5dB), which can be verified from the inset graph of S_{21} and S_{31} in Fig. 7. The phase difference is 87.9° (which is within 90° ± 5°).

(a)

(b)
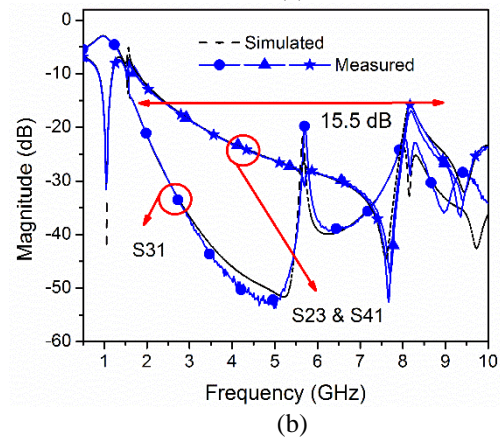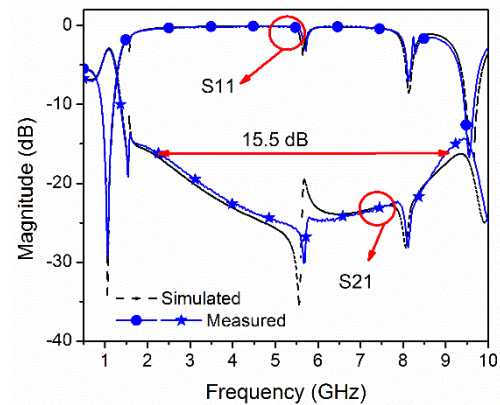
Fig. 6. Simulated and measured S-parameters response: (a) Reflection coefficient (S_{11}) at input port 1 and Transmission coefficient (S_{21}) at port 2, and (b) Transmission coefficient (S_{31}) at port 3, output port isolation (S_{23}) and isolation at port 4 (S_{41}).
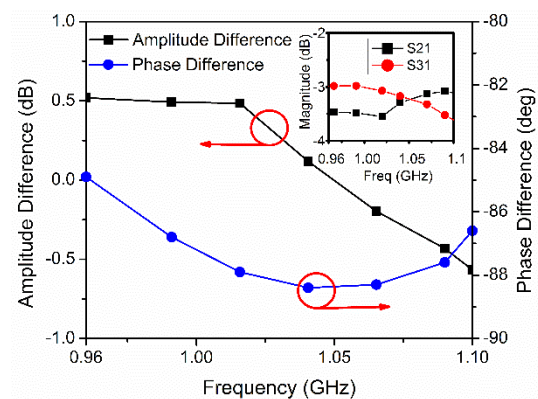
Fig. 7. Amplitude and phase difference of the signal at the output ports of the design HBLC.

B. Comparison with previous works

A candid comparison of the proposed design with already published work is presented in Table 1.The main focus is comparison of three design parameters namely FBW, circuit size reduction (as compared to the conventional BLC) and harmonic suppression. It can be clearly seen in Table 1 that $[8-12]$ offer a size reduction rate of up to 50% and FBW of up to 32% but with no harmonic suppression, while $[13-17]$ give superior area reduction of up to 63% and a wider FBW at the cost of out-of-band performance. From the works reporting good out-of-band performance $[18-25]$, it can be inferred that a relatively narrow FBW was achieved although area reduction in some cases have been phenomenal ($> 60\%$) [18],[19],[24],[25].

Our proposed design, although achieved a size reduction of 56%, promises wider FBW of about 30% with a superior harmonic suppression up to $9f_0$ (except for [24] where harmonic suppression is $10f_0$ but FBW is very narrow). Another important thing to note is that the proposed technique of utilizing the stepped impedance TL gives much better results as compared to similar structure used in [26].

Table 1: Comparison of proposed work with literature

Ref.	Freq. (GHz)	Circuit Configuration	FBW[a] (%)	Size Reduction	Harmonic Suppression
[8]	2.4	DGS	10	33	No
[9]	0.9	Cascaded TL with centrally loaded open stub	10	55	No
[10]	1.94	Comb line structure	23	22.6	No
[11]	2.4	Asymmetrical T-shaped structure	~24	55	No
[12][b]	1.8	Polar Curves	32	50	No
[13]	1.5	Substrate integrated suspended line (SISL) technology	21	62	No
[14]	1	Cascaded slow-wave cells	32	62	No
[15]	2.4	Combination of dual TL & π-model	40	47	No
[16]	2.4	Dual TL	43	63.9	No
[17]	2.4	π-model artificial TL	33	62	No
[18]	2	Slow-wave resonant cells	10	72	Up to $2f_0$
[19]	0.836	High impedance TL with interdigitated capacitance	<13	73.2	Up to $2f_0$
[20]	2	T-shaped structure	10	29.5	Up to $3f_0$
[21][b]	2.1	Meandered T-shaped structure	Not given	63.5	Up to $3f_0$
[22]	0.5	π-shaped structure	8	37	Up to $5f_0$
[23]	1	TL with triple stub	9	44	Up to $6f_0$
[24]	1	DGS	<8	65	Up to $10f_0$
[25]	0.9	Modified T-shaped structure	<15	74	Up to $8f_0$
[26]	1	Stepped impedance TL	Not given	50	Up to $2f_0$
This work	**1**	**Stepped Impedance TL**	**30**	**56**	**Up to $9f_0$**

[a] 10 dB fractional bandwidth.
[b] only BLC results have been quoted.

IV. CONCLUSION

A novel technique of utilizing the stepped impedance TL structure is presented for the design of HBLC in micro-strip technology. First of all conventional low-Z high-Z low-Z structure is analysed by imposing a length constraint. After finding out the impedance of each section, they are interchanged to form a high-Z low-Z high-Z structure of Fig. 1 (c) ensuring impedance ratio, M $(Z_2/Z_1) \gg 1$. Owing to high impedance ratio (M) over a wide range of electrical lengths, the transmission coefficient (S_{21} and S_{31}) response follows that of an ideal LPF promising wide range of harmonic suppression. The proposed theory is practically verified by fabricating an HBLC at 1 GHz. An excellent harmonic suppression of up to $9f_0$ was achieved with an operational FBW of 30% and size reduction of 56%. In short, the proposed HBLC is easy to fabricate, has no lumped elements and is compact enough to fulfill the requirements of bandwidth

hungry micro-wave systems requiring wide harmonic suppression.

REFERENCES

[1] F. Lin, Q. X. Chu, and S. W. Wong, "Dual-band planar crossover with two-section branch-line structure," *IEEE Trans. Microw. Theory Techn.*, vol. 61, no. 6, pp. 2309-2316, 2013.

[2] S. Koziel and P. Kurgan, "Low-cost optimization of compact branch-line couplers and its application to miniaturized Butler matrix design," *In Proc. EuMC.*, Rome, Italy, pp. 227-230, 2014.

[3] D. M. Pozar, *Microwave Engineering.* Second edition, Wiley, New York, 2009.

[4] R. Mongia, I. Bahl, and P. Bhartia, *RF and Microwave Coupled-Line Circuits.* Artech House, 1999.

[5] W. A. Arriola, J. Y. Lee, and I. S. Kim, "Wideband 3 dB branch line coupler based on λ/4 open circuited coupled lines," *IEEE Microw. Wireless Compon. Lett.*, vol. 21, no. 9, pp. 486-488, 2011.

[6] S. Lee and Y. Lee, "Wideband branch-line couplers with single-section quarter-wave transformers for arbitrary coupling levels," *IEEE Microw. Wireless Compon. Lett.*, vol. 22, no. 1, pp. 19-21, 2012.

[7] J. Zhang, J. Tao, B. F. Zong, and C. Zhou, "Compact branch-line coupler using uniplanar spiral based CRLH-TL," *Progress in Electromagnetic Research, PIER Letters*, vol. 52, pp. 113-119, 2015.

[8] M. Ramesh, D. Packiaraj, and A. T. Kalghatgi, "A compact branch line coupler using defected ground structure," *J. Electromagn. Waves Appl.*, vol. 22, no. 2, pp. 267-276, 2008.

[9] T. Su, C. Zhao, and Z. Li, "Compact broad band branch line coupler with centrally loaded open stub and cascaded transmission line," *Microw. Opt. Technol. Lett.*, vol. 54, no. 9, pp. 2101-2103, 2012.

[10] G. H. Pei and H. K. Choi, "A miniaturized 3-db hybrid coupler using the comb line," *Microw. Opt. Technol. Lett.*, vol. 57, no. 11, pp. 2641-2645, 2015.

[11] S. S. Liao, P. T. Sun, N. C. Chin, and J. T. Peng, "A novel compact-size branch-line coupler," *IEEE Microw. Wireless Compon. Lett.*, vol. 15, no. 9, pp. 588-590, 2005.

[12] J. Johan and J. W. Odendaal, "Design of compact planar rat-race and branch-line hybrid couplers using polar curves," *Microw. Opt. Technol. Lett.*, vol. 57, no. 11, pp. 2637-2640, 2015.

[13] Y. Wang, K. Ma, and S. Mou, "A compact branch-line coupler using substrate integrated suspended line technology," *IEEE Microw. Wireless Compon. Lett.*, vol. 26, no. 2, pp. 95-97, 2016

[14] P. Kurgan and S. Koziel, "Design of high-performance hybrid branch-line couplers for wide-band and space-limited applications," *IET Microw. Antennas Propagat.*, vol. 10, no. 12, pp. 1339-1344, 2016.

[15] V. Iran-Nejad, A. A. Lotfi-Neyestanak, and A. Shahzadi, "Compact broadband quadrature hybrid coupler using planar artificial transmission line," *Electron. Lett.*, vol. 48, no. 25, pp. 1602-1603, 2012.

[16] C. W. Tang, M. G. Chen, and C. H. Tsai, "Miniaturization of microstrip branch-line coupler with dual transmission lines," *IEEE Microw. Wireless Compon. Lett.*, vol. 18, no. 3, pp. 185-187, 2008.

[17] V. Iran-Nejad, A. A. Lotfi-Neyestanak, and A. Shahzadi, "Miniaturization of a broadband quadrature hybrid coupler using π-model transformation-based artificial transmission line," *Applied Computational Electromagnetics Society (ACES) Journal*, vol. 31, no. 3, pp. 304-308, 2016.

[18] J. Wang, B. Z. Wang, Y. X. L. Guo, C. Ong, and S. Xiao, "A compact slow wave microstrip branch line coupler with high performance," *IEEE Microw. Wireless Compon. Lett.*, vol. 17, no. 7, pp. 501-503, 2007.

[19] K. Y.Tsai, H. S. Yang, J. H. Chen, and Y. J. E. Chen, "A miniaturized 3 dB branch line hybrid coupler with harmonics suppression," *IEEE Microw. Wireless Compon. Lett.*, vol. 21, no. 10, pp. 537-539, 2011.

[20] L. Y. Wang, K. Hsu and W. H. Tu, "Compact microstrip harmonic-suppressed quadrature hybrids," *Microw. Opt. Technol. Lett.*, vol. 51, no. 4, pp. 981–985, 2009.

[21] K. S. Choi, K. C. Yoon, J. Y. Lee, et al., "Compact branch line coupler with harmonic suppression using meander T-shaped line," *Microw. Opt. Technol. Lett.*, vol. 56, no. 6, pp. 1382-1384, 2014.

[22] P. Mondal and A. Chakrabarty, "Design of miniaturized branch-line and rat-race hybrid couplers with harmonics suppression," *IET Microw. Antennas Propagat.*, vol. 3, no. 1, pp. 109-116, 2009.

[23] B. Li, X. Wu, and W. Wu, "A miniaturized branch-line coupler with wideband harmonics suppression," *Progress in Electromagnetic Research, PIER Letters*, vol. 17, pp. 181-189, 2010.

[24] S. Dwari and S. Sanyal, "Size reduction and harmonic suppression of microstrip branch line coupler using defected ground structure," *Microw. Opt. Technol. Lett.*, vol. 48, no. 10, pp. 1966-1969, 2006.

[25] K. V. P. Kumar and S. S. Karthikeyan, "Miniaturised quadrature hybrid coupler using modified T-shaped transmission line for wide-range harmonic suppression," *IET Microw. Antennas Propagat.*, vol. 10, no. 14, pp. 1522-1527, 2016.

[26] S. H. Sedighy and M. Khalaj-Amirhosseini,

"Compact branch line coupler using step impedance transmission lines (SITLs)," *Applied Computational Electromagnetics Society (ACES) Journal*, vol. 28, no. 9, pp. 866-870, 2013.

Zafar Bedar Khan received his B.E. degree from National University of Sciences and Technology, Pakistan and M.S. degree from Hanyang University, South Korea in 2002 and 2010 respectively. He received his Ph.D degree from Northwestern Polytechnic University, Xian, China in 2017. Currently, Zafar is working as a Research Engineer at Center of Excellence for Science & Applied Technology (CESAT), Islamabad, Pakistan. His research interests include RF passive component design and RF front-end design for application in Radar and communication systems.

Ghulam Mehdi received his bachelor of Engineering degree from NED University Karachi, Pakistan and Master of Engineering from Linkoping University, Linkoping, Sweden in 2000 and 2007 respectively. He completed his Ph.D. degree from Beihang University, Beijing, China in 2013. Presently, Mehdi is working as Senior Research Engineer at Center of Excellence for Science & Applied Technology (CESAT), Islamabad, Pakistan. Mehdi's research interest includes microwave and millimeter-wave circuits & antenna design and radar system engineering.

Huiling Zhao received her Ph.D degree in Circuit and System from Northwestern Polytechnic University, Xian, China in 2002. Zhao is currently a Professor in the Department of Electronics and Information, Northwestern Polytechnic University, China. She has been a visiting Associate Professor in the Duke University, USA from 2006 to 2007. Zhao's main research interests include optimization algorithm development for beam forming, computational electromagnetics, microwave and millimeter wave circuit and antenna design.

Effects of Return Stroke Parameters and Soil Water Content on EMF Characteristics

Mohammed I. Mousa, Zulkurnain Abdul-Malek, and Mona Riza M. Esa

Institute of High Voltage and High Current, School of Electrical Engineering, Faculty of Engineering
Universiti Teknologi Malaysia, 81310, Johor Bahru, Malaysia
Mohammedimran745@yahoo.com, zulkurnain@utm.my, monariza@utm.my

Abstract ─ Electromagnetic pulses produced by lightning return strokes travel long distances both aboveground and underground. This study investigated the effects of return stroke parameters on electromagnetic propagation over lossy ground. The lightning return stroke channel was modeled using the Modified Transmission Line with Exponential Decay (MTLE) model. Electromagnetics was modeled using a frequency domain solver in the form of finite element analysis via COMSOL software. The studied stroke current parameters were peak, rise time, and decay time. In addition, the effects of soil water content was studied. Aboveground and underground electric and magnetic fields followed and were directly affected by the lightning current waveshape. The underground fields were affected by soil water content. In contrast, the aboveground fields are not affected by water content except for the radial electric field.

Index Terms ─ Current parameters, EMF, FEA, lossy ground, water content.

I. INTRODUCTION

Lightning is a vigorous natural phenomenon that has significant effects on human lives and systems such as power supply, communication, etc. Among the three lightning types, namely, cloud-to-ground, cloud-to-cloud, and intra-cloud, cloud-to-ground lightning poses the most significant threat to the above systems [1]. 90% of the cloud-to-ground lightning produces return strokes with negative current. During the last decade, many studies have calculated the electromagnetic fields radiated by these return strokes [2-5]. Ground properties are known to affect not only the lightning discharge flow in soil [6, 7] but also electromagnetic field propagation and computed fields at a given distance from the lightning source [8-12].

The two main ground properties investigated in this study were soil conductivity and permittivity. Most previous studies considered soil conductivity and permittivity as constant or frequency independent. It is noted that a correct computation of lightning electromagnetic fields requires proper soil modeling. Several soil models [7] with frequency dependency were proposed by Scott [13], Smith-Longmire [14], and Visacro-Alipio [15].

An attempt to consider frequency dependent soil conductivity and permittivity in the computation of electromagnetic fields was proposed by Delfino [16]. Delfino uses an improved numerical solver based on Maxwell equations to compute the field [16]. Later, several other researchers studied the effects of frequency dependent soil on electromagnetic fields using frequency domain solvers [17-20]. However, the full effects of lightning current magnitude, lightning current shape, and soil water content on electromagnetic field characteristics are not fully understood.

The accurate evaluation of the electromagnetic fields propagated by nearby lightning strikes is important in determining lightning induced voltage into power systems. The aim of this paper is to study the effects of lossy ground and various lightning current parameters, such as the peak, front times, and decay time, on the EMF characteristics at a given location. Finite element analysis was used for simulation. Four lightning currents with different magnitudes and shapes were considered. The effects of soil water content on EMF characteristics were also studied.

II. METHODOLOGY

The methodology of this study is comprised of four parts, namely, specification of energizing currents, modeling of the return stroke, modeling of the soil, and modeling of electromagnetic field propagation. Each of these are described below.

A. Return stroke current at base of the channel

An analytical expression was adopted to represent the lightning current at the base of the return stroke channel, as originally proposed by Heidler [21] and modified by Diendorfer and Uman. Mathematically, the return stroke current is given as $i\,(z,\,t)$, where z is the

channel height. At the bottom of the channel, the current is described as [22]:

$$i(0,t) = \frac{k_1\left(\frac{t}{\Gamma_{11}}\right)^{n_1}}{1+\left(\frac{t}{\Gamma_{11}}\right)^{n_1}} e^{\left(\frac{-t}{\Gamma_{12}}\right)} + \frac{k_2\left(\frac{t}{\Gamma_{21}}\right)^{n_2}}{1+\left(\frac{t}{\Gamma_{21}}\right)^{n_2}} e^{\left(\frac{-t}{\Gamma_{22}}\right)}, \quad (1)$$

where $k_1 = {i_{01}}/{\eta_1}$, $k_2 = {i_{02}}/{\eta_2}$,

where i_{01} and i_{02} are the amplitudes of the current components, Γ_{11} and Γ_{12} are the front time constants, Γ_{21} and Γ_{22} are the decay-time constants, n_1 and n_2 are constants, and η_1 and η_2 are the amplitude correction factors. The corresponding values used in this study were categorized as cases 1 to 4 as shown in Table 1. Figure 1 shows the generated lightning currents for all 4 cases.

Table 1: Heidler parameters for lightning return stroke adopted from Diendorfer and Uman [22, 23]

Case	i_{01} (kA)	Γ_{11} (µs)	Γ_{12} (µs)	i_{02} kA	Γ_{21} (µs)	Γ_{22} (µs)	n_1 & n_2
1	19.5	1	2	12	8	30	2
2	17	0.4	4	8	4	50	2
3	10.5	2	4.8	9	20	26	2
4	10.7	0.25	2.5	6.5	2	230	2
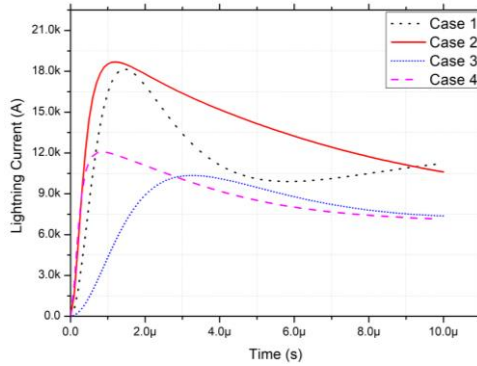
Fig. 1. Lightning current waveforms for four return stroke parameter cases (detailed parameters are given in Table 1).

B. Current distribution along the channel

Currents along the channel were implemented using the modified Transmission Line with Exponential Decay (MTLE) return stroke model. In this model, the channel base current was used to calculate currents at different channel heights. Current distribution along the channels in time domain is specified as:

$$i(z, t) = i(0, t - {z}/{v}) e^{-\left(\frac{z}{a}\right)}, \quad (2)$$

where $i(z, t)$ is the channel current at height z, v denoted the return stroke speed, and α is the height dependent decay constant. Using a Fourier transform of $i(z, t)$ we get:

$$I(z, \omega) = I(0,\omega) e^{-\left(\frac{z}{a}\right)} e^{-i\omega\left(\frac{z}{v}\right)}. \quad (3)$$

Equation (3) was then used in the frequency domain solver.

C. Soil model

Based on the soil equivalent network formula of Smith and Longmire (SL) [14], the relative frequency domains permittivity and conductivity are written as:

$$\varepsilon(\omega) = \varepsilon_o \varepsilon_\infty + \varepsilon_o \sum_{i=1}^{N} \frac{a_i}{1+\left(\frac{\omega}{2\pi f_i}\right)^2}, \quad (4)$$

$$\sigma(\omega) = \sigma_o + 2\pi\varepsilon_o \sum_{i=1}^{N} \frac{a_i f_i \left(\frac{\omega}{2\pi f_i}\right)^2}{1+\left(\frac{\omega}{2\pi f_i}\right)^2}, \quad (5)$$

where,

$$\sigma_o = 8e - 3 \left(\frac{p}{10}\right)^{1.54}, \quad (6)$$

$$f_i = 10^{i-1} \left(\frac{p}{10}\right)^{1.28}, \quad (7)$$

where ε_∞, ε_o, and σ_o are permittivity at high-frequency, permittivity of free space, and initial conductivity, respectively. a_i and f_i are coefficients that have a good fit with the measurement results, and ω is angular frequency (with a frequency range from 100 Hz to 5 MHz). Table 2 shows a_i coefficient values for varying i values, which were used to define the soil relative permittivity and conductivity for different soil water contents.

Table 2: Coefficient a_i of Smith and Longmire expressions adopted from [14]

i	a_i	i	a_i	i	a_i	i	a_i
1	3.4E6	5	5.26E2	9	4.8	13	0.173
2	2.74E5	6	1.33E2	10	2.17		
3	2.58E4	7	2.72E1	11	0.98		
4	3.38E3	8	1.25E1	12	0.392		

Based on Smith and Longmire's soil model, soil properties can be defined for any percentage of soil water content using the initial conductivity value and f_i coefficient.

D. Electromagnetic propagation model

COMSOL software's Radio Frequency (RF-Module) was used for analysis [24] as it allows the 2D and 3D calculation of electromagnetic fields along passive and active devices. All models were based on Maxwell's equations and material laws for propagation in different media. In particular, the electromagnetic wave solver of the RF module, which is based on the finite-element solution of the weak-form representation of the frequency-domain wave equation of the magnetic vector potential [24] was used.

The electromagnetic propagation model was divided into three media channels: air, ground, and lightning. The electric parameters of air are given as $\sigma = 0$, $\varepsilon_r = 1$, while the ground was considered to have frequency dependent conductivity $\sigma(f)$ and relative permittivity $\varepsilon(f)$. In this model, the 2D axisymmetric formulation was utilized to model flat ground with a vertical lightning channel, and each medium was meshed

by triangular prisms based on FEA theory. Maximum element mesh sizes were limited to the skin depth δ and minimum wavelength λ_{min} (associated with maximum working frequency f_{max}). The maximum length of each element was smaller than ($\lambda_{min}/6$). To avoid large computational requirements and inefficient matrix systems in the FEM formulation due to large model dimensions, a thin wire was used to represent the lightning channel. The conductor wire was reasonably modeled as a sequence of mesh edges [17, 20] with a maximum edge length of ($\lambda_{min}/10$).

Electromagnetic wave and frequency domain interfaces were used to solve time-harmonic electromagnetic field distribution. This physics interface solved the second-order vector wave equation for electric fields [21]:

$$\nabla \times (\mu_r^{-1} \nabla \times E) - \frac{\omega^2}{c^2}\left(\varepsilon_r - j\frac{\sigma}{\omega\varepsilon_0}\right)E = 0, \quad (8)$$

while the magnetic field was determined using the first Maxwell equation:

$$\nabla \times E = -j\omega\mu_r\mu_o H, \quad (9)$$

where E, and H are the electric and magnetic fields. The variables μ_r, ε_r, and σ are relative permeability, relative permittivity, and electric conductivity, respectively; ω is angular frequency, c is propagation speed of light, and $\nabla\times$ is the curl of the vector variables.

In COMSOL, the soil–air interface used natural Neumann conditions expressed as:

$$-n \times [(\mu_r^{-1} \nabla \times E)_{Soil} - (\mu_r^{-1} \nabla \times E)_{Air}$$
$$= n \times j\omega\mu_o(H_{Soil} - H_{Air}) - J_s = 0, \quad (10)$$

where E_{Soil} and E_{Air} are the electric fields at the soil–air interface, H_{Soil} and H_{Air} are the magnetic fields at the same interface, J_s denotes surface current density, and n is the unit normal vector directed from soil to air. To prevent the electromagnetic wave from being reflected off of boundaries, a Perfect Match Layer (PML), (available in the frequency domain RF module) was used. PML width is equal to ($2\ \lambda_{min}$) [24].

The electromagnetic field radiated by the lightning channel is defined by three components, the vertical electric field (E_z), the radial electric field (E_r), and the azimuthal magnetic field (H_ϕ). The electromagnetic component was obtained in the time domain using the inverse Fourier transform.

Table 3 lists the parameters used to calculate current along a lightning channel and other simulation details [17]. Figure 2 shows the FEA simulation model consisting of lightning channels for the ground, air, and Perfectly Matched Layers as well as the generated FEA mesh.

Figure 3 illustrates the flow chart of the computational procedure for modeling the electromagnetic propagations over lossy ground.

Table 3: Parameters used for return stroke model and electromagnetic computation

Parameters/Symbols	Values
Return stroke speed v, [m/s]	1.3×10^8
Range of frequency f, [Hz]	$(0 - 5 \times 10^6)$
Number of samples	1024
Lambda λ, [m]	60
Decay constant α, [m]	2000
Max. Mesh size, [m]	$(\lambda/f_{max}) = 30$
Min. Mesh size, [m]	0.07
Height of lightning channel [m]	7000
Width of the model [m]	4500
Depth of ground [m]	1000
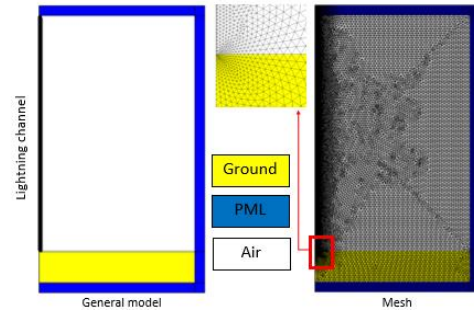
Fig. 2. Lightning channel and electromagnetic model containing ground, air, and Perfectly Matched Layers (PML) as well as the generated FEA mesh.
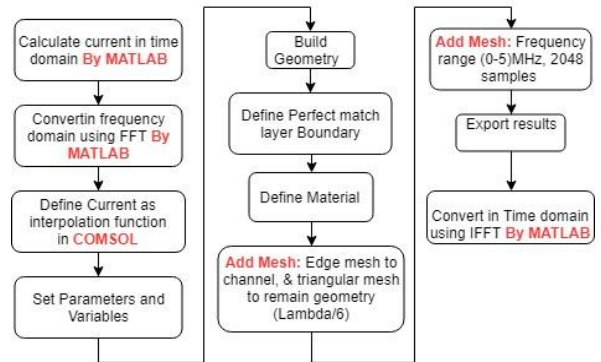
Fig. 3. Flow chart of the numerical solution.

III. RESULTS AND DISCUSSION

This study simulated the effects of lightning current parameters and soil water content on computed electromagnetic fields.

A. Effects of lightning current parameters

Figure 4 shows the resultant radial and vertical components of the electric field and the azimuthal

component of the magnetic field for lossy ground for four lightning return stroke currents. The observation point was located 10 m above ground and 50 m from the lightning channel. It was observed that the measured aboveground electric and magnetic fields followed and were directly affected by the lightning current waveshape. With proper calibration, the measurement of these aboveground fields enables us to determine the magnitude and shape of a lightning current source.

fields followed and were directly affected by the lightning current waveshape. Similar to the aboveground case, the measurement of these two underground fields enables us to determine the magnitude and shape of a lightning current source.

(a)

(b)

(c)
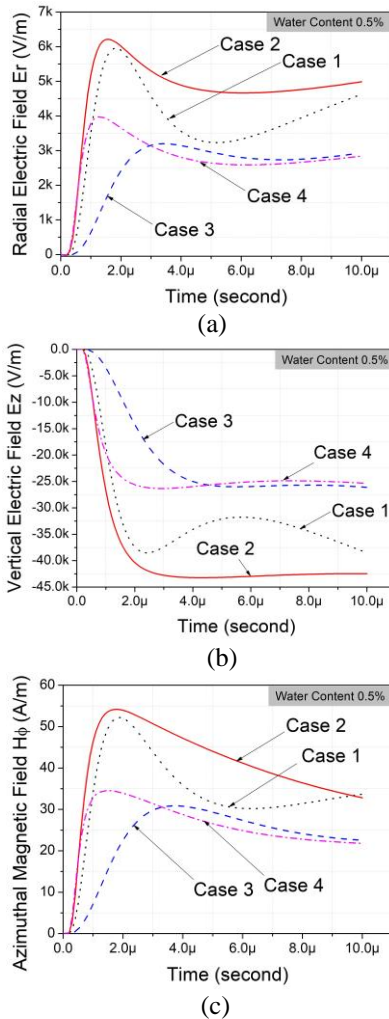
Fig. 4. Variation of electromagnetic components over lossy ground for: (a) Radial component of the electric field (E_r), (b) vertical component of the electric field (E_z), and (c) azimuthal component of the magnetic field (H_ϕ).

Figure 5 shows the effect of lossy ground on the radial and vertical electric fields and the azimuthal magnetic field for all lightning return stroke currents. The observation point was located 10 m belowground and 50 m from the lightning source. It was observed that the measured underground radial electric and magnetic

(a)

(b)

(c)

Fig. 5. Variation of electromagnetic components in lossy ground for: (a) Radial component of the electric field (E_r), (b) vertical component of the electric field (E_z), and (c) azimuthal component of the magnetic field (H_ϕ).

B. Water content effect

Figure 6 shows radial electric fields with water content for return stroke currents at locations 50 m from the lightning channel and 10 m above and below ground. It was observed that the water content impacted the underground currents magnitude and the pattern of the radial electric field until 10% soil water content. For water content above 10%, the field magnitude was approximately zero. Water content (up to 10%) increased the aboveground field. Increment amounts were dependent on current shape.

(a)

(b)
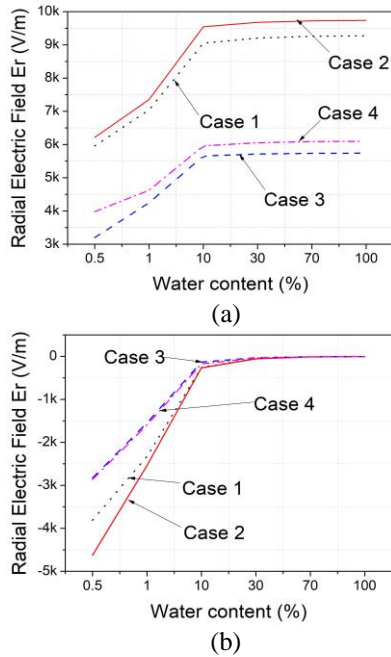
Fig. 6. Peak radial electric fields with water content for four return stroke cases 50 m from the lightning channel at: (a) 10 m aboveground and (b) 10 m below ground.

Figure 7 shows variations in the above and underground vertical electric fields with water content for four return stroke currents 50 m from the lightning channel. It was observed that the water content impacted the underground currents magnitude and the pattern of the vertical electric field until about 10% soil water content. For water content above 10%, the field magnitude was approximately zero. Unlike the radial field, water content did not affect the aboveground vertical field.

Figure 8 shows variations in above and underground azimuthal magnetic fields with water content for four current cases 50 m from the emitting source. It was observed that the underground magnetic field linearly decreased when increased water content from 1 to 100%. The decrement amount depended on current shape. For the vertical electric fields, the aboveground magnetic field remained unaffected by water content.

(a)

(b)
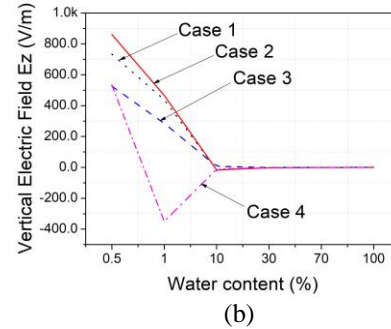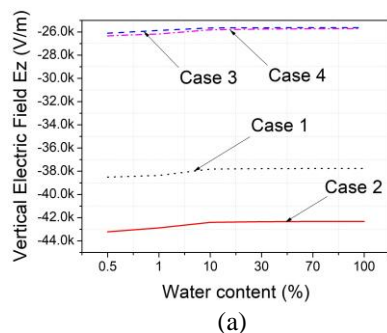
Fig. 7. Vertical electric fields with water content for four return strokes determined 50 m from the lightning channel at: (a) 10 m aboveground and (b) 10 m belowground.

(a)

(b)
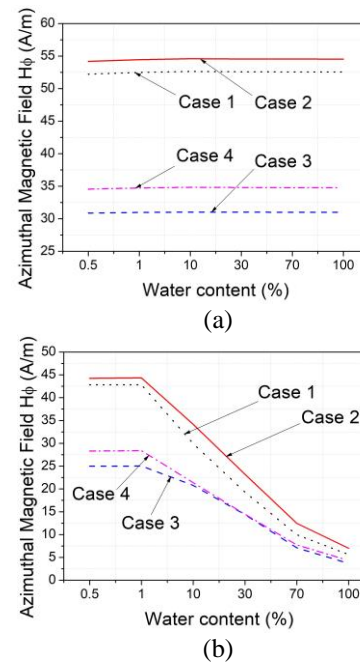
Fig. 8. Azimuthal magnetic fields with water content for four return strokes determined 50 m from the lightning channel at: (a) 10 m aboveground and (b) 10 m belowground.

Results showed that the waveforms of the electric and magnetic fields have similar patterns to the return stroke current waveform above/belowground, with the exclusion of underground vertical electric field. Hence, the waveform shape for the vertical electric field was mainly affected by soil conductivity frequency dependency [17].

For all return stroke cases, the peak value and pattern of the three electromagnetic components behaved differently due to soil electrical parameters. Hence, the peak values of the radial electric field increased with increased soil conductivity and decreased

permittivity (higher water content according to [14]). In contrast, the underground fields were dampened, especially for soil water contents greater than 10%. The peak values for underground vertical electric fields were significantly affected by soil electric parameters. The aboveground fields were unaffected by increased water content. Differences were found in the behavior of peak values between return strokes.

Simulation results were based on the electromagnetic model presented by Akbari [17] and different solver techniques in [16, 19]. The electric and magnetic fields results of case 4 are in good agreement with those presented in [16, 17] for both above/ belowground for various distances from the lightning channel. Using case 4 as reference, other cases were evaluated over different soils.

IV. CONCLUSION

The shape and magnitude of above and belowground electric and magnetic fields were directly affected by the lightning current waveform. The measurement of the lightning electric and magnetic field waveforms enables us to determine the magnitudes and shape of a lightning currents source. Underground fields were found to be affected by 0.5% to 100% soil water content. The effect was more dominant for the azimuthal magnetic field (up to 100% water content) compared to the radial and vertical electric fields, which were only affected by up to 10% soil water content. In contrast, aboveground fields were not affected by soil water content, except for the radial electric field (up to 10% water content).

Soil water content had various effects on electromagnetic component peak values for the four return strokes. There was no significant differences in the effect of water content for the aboveground return strokes. For the underground fields, all three electromagnetic components behaved slightly different at different soil water contents. Electric fields were almost constant after 10% of water content, while the magnetic field continually decreasing with increases in water content up to 100%.

ACKNOWLEDGMENT

REFERENCES

[1] V. Cooray, "Return stroke models for engineering applications," in *Lightning Electromagnetics*, London, United Kingdom: The Institution of Engineering and Technology, 2012.

[2] C. Y. Wang, W. Haojiang, and W. Lipeng, "Characteristics of lightning electromagnetic fields from oblique lightning channel considering vertical stratified ground," *JEIT*, vol. 39, pp. 466-473, 2017.

[3] M. O. Goni, E. Kaneko, and A. Ametani, "Simulation of lightning return stroke currents and its effect to nearby overhead conductor," *Applied Computational Electromagnetics Society Journal*, vol. 24, no. 5, pp. 469-477, 2009.

[4] Y. Baba and M. Ishii, "Characteristics of electromagnetic return-stroke models," *IEEE Transactions on Electromagnetic Compatibility*, vol. 45, pp. 129-134, 2003.

[5] V. Rakov, "Characterization of lightning electromagnetic fields and their modeling," in *14th Int. Zurich Symposium on Electromagnetic Compatibility*, pp. 3-16, 2001.

[6] M. I. Mousa, Z. Abdul-Malek, V. M. Ibrahim, A. I. Elgayar, Z. Nawawi, and M. A. Sidik, "Evaluation and mitigation of underground gas pipeline coating stress due to nearby lightning stroke," in *Electrical Engineering and Computer Science (ICECOS), 2017 International Conference on*, pp. 275-279, 2017.

[7] M. O. Goni, E. Kaneko, and A. Ametani, "Simulation of lightning return stroke currents and its effect to nearby overhead conductor," *Applied Computational Electromagnetics Society Journal*, 24.5: pp. 469-477, 2009.

[8] M. Mokhtari, Z. Abdul-Malek, and C. L. Wooi, "Integration of frequency dependent soil electrical properties in grounding electrode circuit model," *International Journal of Electrical and Computer Engineering*, vol. 6, pp. 792, 2016.

[9] N. Rameli, M. Z. A. Ab-Kadir, M. Izadi, C. Gomes, and N. Azis, "Variations in return stroke velocity and its effect on the return stroke current along lightning channel," in *2016 33rd International Conference on Lightning Protection (ICLP)*, pp. 1-5, 2016.

[10] M. Izadi, M. A. Ab Kadir, and M. Hajikhani, "Evaluation of lightning current and ground reflection factor using measured electromagnetic field," *Applied Computational Electromagnetics Society Journal*, vol. 29.1, 2014.

[11] D. Li, M. Azadifar, F. Rachidi, M. Rubinstein, M. Paolone, D. Pavanello, et al., "On lightning electromagnetic field propagation along an irregular terrain," *IEEE Transactions on Electromagnetic Compatibility*, vol. 58, pp. 161-171, 2016.

[12] K. Arzag, Z. Azzouz, and B. Ghemri, "Lightning electromagnetic pulse simulation using 3D-FDTD method (Comparison between PEC and UPLM Boundary Conditions)," in *Lightning Protection (ICLP)*, 2016 33rd International Conference on, pp. 1-6, 2016.

[13] J. Scott, R. Carroll, and D. Cunningham,

"Dielectric constant and electrical conductivity of moist rock from laboratory measurements," *US Dept. of Interior Geological Survey Technical Letter*, Special projects-12, vol. 17, Aug. 1964.

[14] C. L. Longmire and K. S. Smith, "A universal impedance for soils," *Mission Research Corp*, Santa Barbara, CA, 1975.

[15] S. Visacro and R. Alipio, "Frequency dependence of soil parameters: Experimental results, predicting formula and influence on the lightning response of grounding electrodes," *IEEE Transactions on Power Delivery*, vol. 27, pp. 927-935, 2012.

[16] F. Delfino, R. Procopio, M. Rossi, and F. Rachidi, "Influence of frequency-dependent soil electrical parameters on the evaluation of lightning electromagnetic fields in air and underground," *Journal of Geophysical Research: Atmospheres*, vol. 114, 2009.

[17] M. Akbari, K. Sheshyekani, A. Pirayesh, F. Rachidi, M. Paolone, and A. Borghetti, "Evaluation of lightning electromagnetic fields and their induced voltages on overhead lines considering the frequency dependence of soil electrical parameters," *IEEE Transactions on Electromagnetic Compatibility*, vol. 55, pp. 1210-1219, 2013.

[18] K. Sheshyekani and M. Akbari, "Evaluation of lightning-induced voltages on multiconductor overhead lines located above a lossy dispersive ground," *IEEE Transactions on Power Delivery*, vol. 29, pp. 683-690, 2014.

[19] F. H. Silveira, S. Visacro, R. Alipio, and A. De Conti, "Lightning-induced voltages over lossy ground: The effect of frequency dependence of electrical parameters of soil," *IEEE Transactions on Electromagnetic Compatibility*, vol. 56, pp. 1129-1136, 2014.

[20] S. Visacro and F. H. Silveira, "The impact of the frequency dependence of soil parameters on the lightning performance of transmission lines," *IEEE Transactions on Electromagnetic Compatibility*, vol. 57, pp. 434-441, 2015.

[21] F. Heidler, "Traveling current source model for LEMP calculation," *in Proc. 6th Int. Zurich Symp. Electromagn. Compat.*, pp. 157-162, 1985.

[22] V. A. Rakov and M. A. Uman, "Review and evaluation of lightning return stroke models including some aspects of their application," *IEEE Transactions on Electromagnetic Compatibility*, vol. 40, pp. 403-426, 1998.

[23] M. Izadi, A. Kadir, M. Z. Abidin, C. Gomes, and W. F. Ahmad, "An analytical second-FDTD method for evaluation of electric and magnetic fields at intermediate distances from lightning channel," *Progress in Electromagnetics Research*, vol. 110, pp. 329-352, 2010.

[24] R. Comsol, *Module User's Guide*, Ed: Version: May, 2012.

Mohammed I. Mousa received the B.Sc. degree in Power Electrical Engineering from Al-Furat Al-Awsat Technical University, Babil, Iraq, in 2010, the M.E. degree in Electrical Engineering from the Universiti Teknologi Malaysia, Johor, Malaysia, in 2014, and is currently pursuing the Ph.D. degree in Electrical Engineering at the Institute of High Voltage and High Current (IVAT), Universiti Teknologi Malaysia. His research interest include the high voltage engineering, the power system transient simulation, and lightning phenomena.

Z. Abdul-Malek received the B.E. degree in Electrical and Computer Systems from Monash University, Melbourne, Australia, in 1989, the M.Sc. degree in Electrical and Electromagnetic Engineering with Industrial Applications from the University of Wales Cardiff, Cardiff, U.K., in 1995 and the Ph.D. degree in High Voltage Engineering from Cardiff University, Cardiff, U.K., in 1999. He was a Lecturer with Universiti Teknologi Malaysia (UTM) for 29 years, where he is currently a Professor of High Voltage Engineering with the Faculty of Electrical Engineering. He is currently the Director of the Institute of High Voltage and High Current (IVAT), UTM.

M.R.M. Esa received the B.E. degree in Electrical-Telecommunication in 2003 and the Master degree in Electronic-Telecommunication in 2005 from Universiti Teknologi Malaysia (UTM), in 2005. In 2014, she received the Ph.D. degree with a specialization in atmospheric discharges and lightning physics from Uppsala University, Sweden. Currently, she is a Senior Lecturer at the Faculty of Engineering and the Head of High Voltage Laboratory in UTM.

Predicting Radiation of CISPR 25 Complaint ALSE Environment

Jin Jia [1], Zhida Lai [2], Ruimiao Wang [3], and Xu Li [4]

[1] Chongqing University of Technology, Vehicle Engineering Institute, Chongqing, 401135, China
[2] State Key Laboratory of Vehicle NVH and Safety Technology, Chongqing, 401122, China
[3] State Grid Research Institute of Chongqing Electric Power Company, Chongqing 401123, China
[4] Chang'an Automotive Engineering Institute, Chongqing 401120, China

Abstract – According to the ALSE configuration in CISPR 25, cable bundle is often the dominant radiation structure due to the Common-Mode (CM) current. However this emission test method suffers from a need of a large anechoic chamber. In order to reduce this cost of electronic component development in the EMC test phase, this paper presents a CM current-scan to predict the radiated emissions from 30MHz - 1GHz; moreover, CM-voltage measurement on the cable bundle is also proposed from 150 kHz - 30 MHz. Both methods rely on simple radiating structures and do not take into account the complexity of a real ALSE environment. Therefore a calibration approach based on measured data is proposed to incorporate real influence factors in an anechoic shielded chamber. The proposed approaches are verified by different cable bundles and measurements.

Index Terms – ALSE method, cable bundle, CISPR 25, Common-Mode current, Common-Mode voltage, radiated emission.

I. INTRODUCTION

Due to increasing clock frequencies and electronic modules, automotive cable bundles as primary interconnection medium enhance the complexity of electromagnetic behavior and the potential risk of functional safety. Electromagnetic emission evaluation (EME) for automotive electronic devices connected to cable bundle is necessary. For guaranteeing the reliability and reproducibility of the EME, common commercial electromagnetic compliance (EMC) limits specify test configuration and site. For example the ALSE method from CISPR 25 [1] specifies that radiated emissions measurements from electronic components or modules should be connected to a cable bundle of 1.5 m length. To eliminate extraneous disturbance and avoid wall reflections, it requires an anechoic shielded chamber characterized by high costs and space consumption. In order to reduce electronic-component development cost in EMC test phase, previous works [2]-[3] introduced current scanning method in frequency and time domain to substitute expensive anechoic chamber measurement

of ALSE method according to CISPR 25. One method is the current amplitude scanning method in frequency domain. The phase of CM current is retrieved from a specific optimization algorithm, only based on the measured amplitude of CM current. While the other method is current scanning method in time domain, which can obtain the amplitude and phase information of CM current simultaneously through Fast Fourier Transform (FFT). Both methods are based on a basic assumption that radiated emissions are mainly dominated by the CM current along the cable bundle. Consequently the CM current path can be modeled by a set of elementary dipoles and mirror current to evaluate radiated emissions from cable bundle. For solving the limitation of finite metallic ground in real test configuration, surface current model substituting mirror current is proposed in the final simulation calculation [4]. However, the prediction accuracy of alternative approaches is still confined by the real ALSE test environmental factor. Moreover previous current scan based method cannot solve the low-frequency due to the sensitiveness of phase measurement below 30 MHz [2]. Based on current scan methods in previous works, this paper focus more on measures to further improve radiation prediction accuracy. Besides, the CM voltage measurement is proposed to predict the radiated emissions at low frequencies.

II. RADIATION MODELS OF CISPR 25 CONFIGURATION

According to ALSE method in CISPR 25, the electronic component should be connected to 1.5 m wire or cable bundle to evaluate field emissions. Therefore this configuration mainly consists of a cable bundle and a finite metallic ground based on the assumption that CM current domains field emission, as shown in Fig. 1.
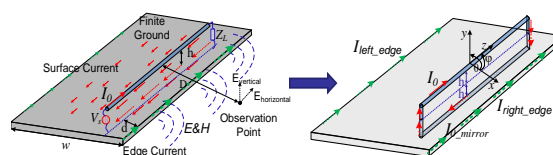
(a) Radiation from a cable bundle on a finite ground

(b) Dipole-model based cable bundle

(c) PO-model based finite ground
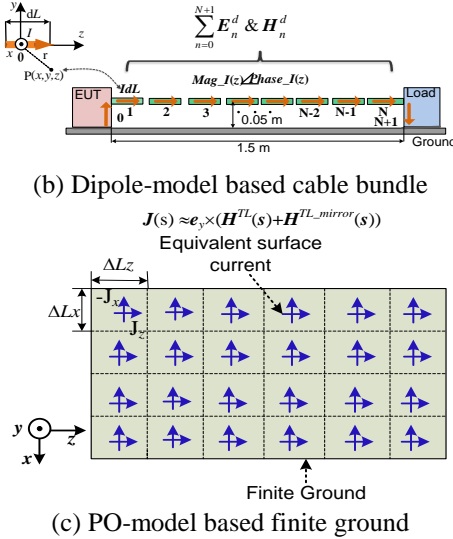
Fig.1. Radiation model from a cable bundle on a finite ground.

In Fig. 1, the radiation from the cable bundle is the sum of radiation from each dipole, according to [4]-[5]:

$$H_x(\omega) = \frac{-IdL \cdot y}{4\pi r}\beta_0^2(j\frac{1}{\beta_0 r} + \frac{1}{\beta_0^2 r^2})e^{-j\beta_0 r}, \quad (1)$$

$$E_y(\omega) = \frac{IdL \cdot zy}{4\pi r^2}\eta_0\beta_0^2(j\frac{1}{\beta_0 r} + \frac{3}{\beta_0^2 r^2} - j\frac{3}{\beta_0^3 r^3})e^{-j\beta_0 r}, \quad (2)$$

where r is the distance from one dipole to the observation point P; ε_0 is dielectric constant of vacuum; dL is Hertzian dipole length; I is the current on a dipole; η_0 is wave impedance in vacuum ($\eta_0 = \sqrt{\mu_0/\varepsilon_0}$), where μ_0 is permeability of vacuum. β_0 is the electromagnetic wave phase constant in vacuum. While the finite metallic ground can be represented by an array of equivalent surface current, which also can be modeled by electric dipoles with physic optics (PO) method [6]. The radiation from this finite ground can be calculated according to (only y-component is shown):

$$E_y^P(\omega) = \sum_{k=1}^{N}\frac{I_{dipx}^k \Delta L_x^k \cdot zy}{4\pi r^2}\eta_0\beta_0^2(j\frac{1}{\beta_0 r} + \frac{3}{\beta_0^2 r^2} - j\frac{3}{\beta_0^3 r^3})e^{-j\beta_0 r}, \quad (3)$$

where N is the mesh number of finite ground, r is the distance from a mesh center to observation point (x, y, z), ΔL_x^k is the kth mesh length along x-direction as shown in Fig. 1. Figure 2 shows the illustration of radiation calculation from typical ALSE method configuration. The total radiated field from the TL-finite ground plate system ($E^{Total}\&H^{Total}$) consists of two components; namely, the field due to TL in the absence of the plate ($E^{TL}\& H^{TL}$), and the field due to induced currents on the finite ground plate in the absence of the TL ($E^P\& H^P$). In the process diagram, $H(s)$ is tangential magnetic on surface of finite ground plate and $J(s)$ is equivalent surface current density on it. While (x, y, z) is Cartesian

coordinate of field observation point.

To verify the multi-dipole model for the cable bundle and surface current model for the finite ground plate [7]-[9], electric fields at the observation point in Fig. 1 are calculated by the proposed model and MoM, as shown in Fig. 3. It can be seen that the simulated electric field from proposed models matches very well with the result from MoM. Besides the field at the observation point with 1 m distance, the far field radiation pattern ($0°\leq \theta \leq 180°$) on the plane $\varphi = 0°$ with 10 m distance are also investigated, which refers to the spherical coordination system in Fig. 4 (up). Figure 4 (down) also shows the good matching of radiation pattern at 300 MHz, which are calculated by MoM and surface current model respectively.
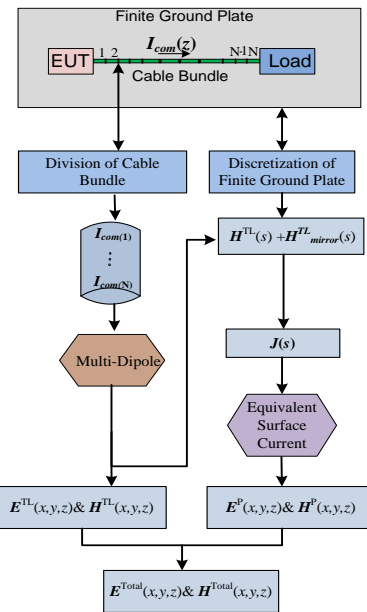
Fig. 2. Illustration of radiation models from cable bundle based on the multi-dipole model and the finite ground based on the surface current model.
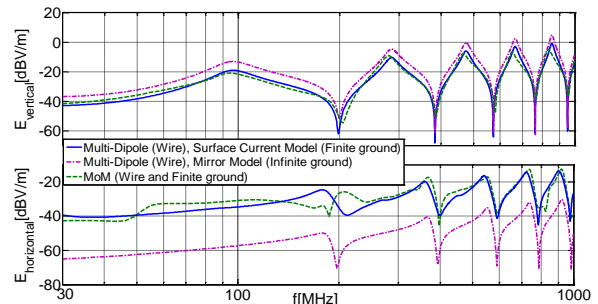
Fig. 3. Comparison of electric field in vertical (upper) and horizontal (lower) polarization at observation point between surface current model and MoM model.
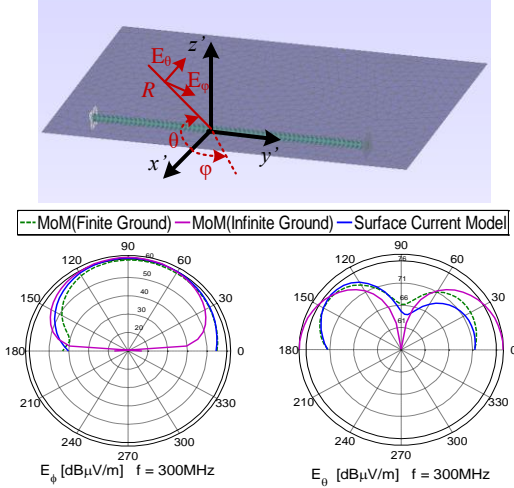
Fig. 4. Radiation pattern from the MoM and the surface current model on the plane $\varphi=0^{\circ}$ at 300.

III. IMPROVING ACCURACY OF RADIATION PREDICTION WITH CORRECTION FUNCTION

According to CISPR 25, the ALSE test method must be implemented in an anechoic shielded chamber with a specific test antenna. From 150 kHz to 30 MHz, an active Rod antenna (SCHWARZBECK VAMP 9243 in this work) can be used to measure the vertical electric coupling field; from 30 MHz up to 1 GHz a Bilog antenna (TESEQ CBL 6141B in this work) can be used to measure both the vertical and horizontal electric field, as shown in Fig. 5. The proposed simplified and ideal radiation models are problematic due to the complex behavior of the anechoic chamber, where peripheral systems and reflections from the chamber walls can influence the antenna voltage. Thereby it is necessary to take these factors into account. For this purpose a measurements based calibration procedure is proposed.

A 1.5 m long single wire, fed by a sinusoidal signal, is used. Then corresponding correction function for the ALSE environment can be obtained:

$$K_C = E_{sim} - E_{antenna} \quad (dB)$$
$$E_{antenna} = V_{antenna} + AF_{antenna}(dB) \tag{4}$$

Here $E_{antenna}$ is the measured electric field, which is the sum of antenna voltage $V_{antenna}$ and the specific antenna factor $AF_{antenna}$. It involves the influencing factors from ALSE environment. E_{sim} is the simulated field at the antenna reference point based on the scanned current data from the measurement configuration model. It involves errors from current data and radiation models. For high accuracy, the measurement equipment and all the coaxial cables in process of current scanning should be maintained similar as in the process of antenna measurement. These correction functions are the fingerprint of a test chamber and will vary from location

to location. Therefore calibration procedure needs to be applied in each test chamber to obtain their respective correction functions. This procedure can also be a very useful method to compare different test chambers.
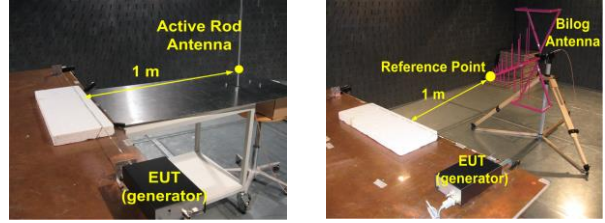
Fig. 5. ALSE test configurations for the active Rod antenna (left) and the Bilog antenna (right).

A. Calibration by an active Rod antenna below 30 MHz

In the active Rod antenna set-up as shown in Fig. 5 (left), the active impedance convertor should give a frequency independent coupling factor, due to the high input impedance. However, taking into account the capacitive coupling between metallic table and chamber floor, as well as the inductive coupling from connected coaxial cable to antenna, this coupling factor is no longer a straight line [10]. For example in Fig. 6, a rise occurs above 2 MHz in the ALSE test configuration, depicted by measurement curve labeled by *ALSE*. When the calibrated wire and active Rod antenna are placed on the chamber floor to remove the capacitive table coupling, this rise cannot be observed anymore as denoted by the measurement curve labeled by *Chamber-Floor*. Some measures could suppress the coupling effects in the ALSE configuration to guarantee the test accuracy, for example adjusting the antenna height or counterpoise grounding. The correction function K_C, which describes the deviation between antenna measurement and simulation from 2 MHz to 30MHz, is about 7 dB. Here the simulation is based on multi-dipole model for the wire and mirror model for the ground plate. K_C can be used as a correction function to compensate the error due to capacitive table coupling.
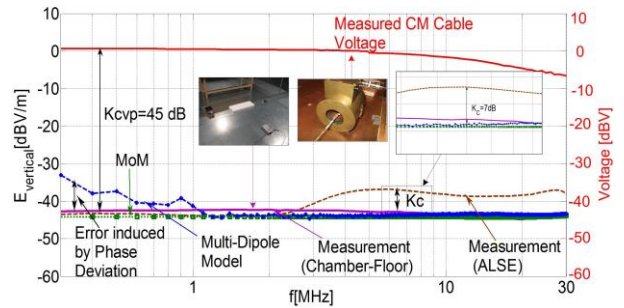
Fig. 6. Normalized measured and simulated data from the calibration of active Rod antenna.

In order to fix low-frequency problem using current scan method, directly measured cable voltage by a Common-mode Voltage Probe (CVP) [11] with known coupling function K_{CVP} can be used as alternative to evaluate radiated field at very low frequencies. The function K_{CVP} between the measured cable voltage and the measured electric field of active Rod antenna is about 45 dB below 5 MHz, and it can be defined by:

$$K_{CVP} = V_{Cable} - E_{Rod-antenna}(dB)$$

$$E_{Rod-antenna} = V_{Rod-antenna} + AF_{Rod-antenna}(dB)$$ (5)

This coupling function should be constant at low frequencies, but it will vary with different CVPs, active Rod antennas or test sit

B. Calibration by a Bilog antenna from 30 MHz to 1 GHz

In the analysis of active Rod antenna below 30 MHz, the mirror currents and multi-dipole radiation model in simulations are accurate enough to model the metallic table in Fig. 5 (left). However for the Bilog antenna used from 30 MHz to 1 GHz, an infinite ground model and mirror theory cannot reflect the influence of the finite metallic plate, especially in horizontal polarization. Therefore, the more accurate surface current model is used. To calculate the correction function with (4), the wire current distribution measurement and antenna measurement are both required. Figure 7 is the configuration to acquire current amplitude distribution on the single wire in the frequency domain. Current acquired in time domain is similar to this configuration, but an extra reference probe is needed.
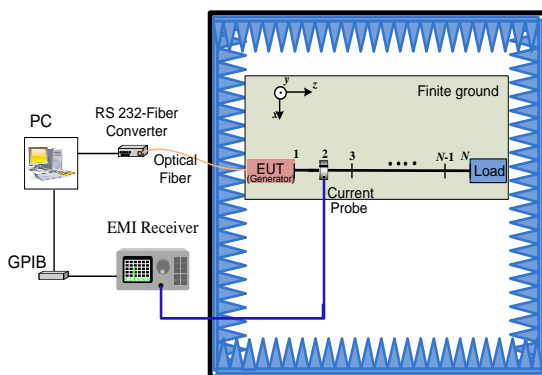
Fig. 7. Calibration configuration for the current scan method in frequency domain.

In the calibration of the Bilog antenna using frequency-domain current scan method, the wire current amplitude distribution is measured by an EMI receiver and the phase distribution is retrieved by proposed retrieval algorithm. Then they are applied to calculate electric fields at reference point depicted in Fig. 5 (right), based on multi-dipole radiation model for the wire and

surface current model for the finite ground plate. Figure 8 shows the vertical electric field from direct antenna measurements, proposed simulation methods, and MoM. K_C denoted in plot is the correction function according to Equation (4), representing the deviation between the simulated field based on scanned current and the measured field directly from Bilog antenna. Also horizontal field at reference point is calculated as shown in Fig. 9. Compared with the vertical component, the horizontal component in measurement is more sensitive to the configuration, especially at high frequencies.
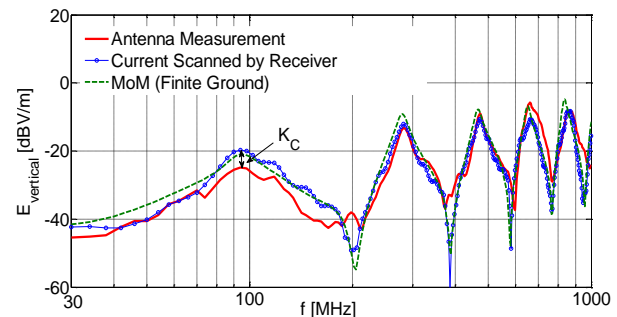
Fig. 8. Measured and simulated vertical field from the calibration configuration based on the scanned current by the EMI receiver.
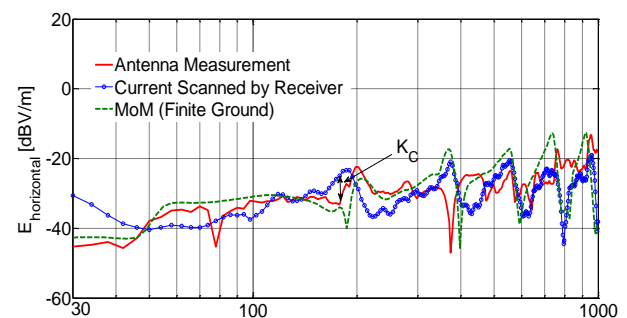
Fig. 9. Measured and simulated horizontal field from the calibration configuration based on the scanned current by the EMI receiver.

Likewise, calibration of the Bilog antenna using time-domain current scan method is implemented with the same procedure. But current amplitude and phase along the calibrated wire are both acquired from an oscilloscope and FFT transformation.

C. Load dependence of correction functions

In the calibration procedure shown above, the single wire is terminated by a 50 Ω load. Correction function is nearly a constant with different loads in the active Rod antenna calibration. However, in the Bilog antenna calibration the correction function varies with different loads over frequency resonance minimums. Therefore,

different loads terminated at the calibrated wire can obtain a set of correction functions. The average of these correction functions is more reasonable, because the common-mode current on a real cable bundle would encounter complex terminal circumstances at different frequencies. Figure 10 present the correction functions with short, open, 1 kΩ loads and their average data in the vertical polarization, respectively. It can be observed that an apparent difference in correction functions due to different loads occurs around 200 MHz, 400 MHz, 600 MHz, 800 MHz and 1000 MHz in vertical polarization, which are also around resonance minimums in vertical electric field curve as shown in Fig. 8. With the same procedure average correction function also can be obtained in the horizontal direction.
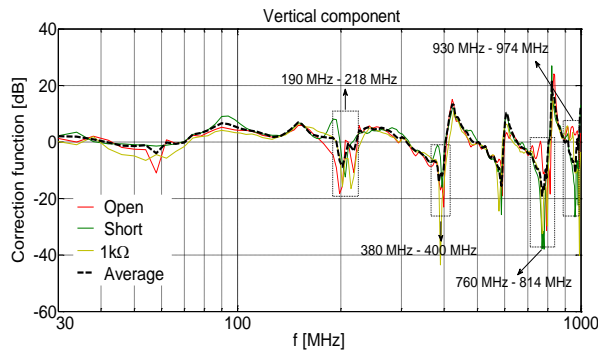
Fig. 10. Correction functions in the vertical polarization.

IV. RESULTS AND EXPERIMENTS

In order to verify the proposed simulation methods considering real ALSE environments, a cable bundle with seven wires is used. Moreover, a real stepper-motor systems is also built to verify proposed methods and improvements.

A. Cable bundle with seven wires

Figure 11 shows the test configuration according to ALSE method. Fed cable is driven by a 3.3 V digital signal with 40 MHz, of which rising time and falling time are about 2.5 ns. Source wire is terminated by a 50 Ω load, and other wires are terminated resistors. In the antenna measurement the reference point of Bilog antenna is 1 m distant to the cable bundle center. The antenna voltage is measured by the EMI receiver (average detector, 120 kHz BW, and 5 ms MT). In the current scan methods, the CM currents on the cable bundle are acquired by the EMI receiver with same setting as the antenna measurement, or acquired by the oscilloscope (single sweep, 550 μs sample time, and 0.5 ns interval time). Multi-dipole radiation model for the cable bundle and surface current model for the finite ground are applied to predict the radiated field at the reference point of Bilog antenna. After correcting these predicted results using the available correction function, the comparisons between the direct

antenna measurement and the simulation are depicted in Fig. 12 (only vertical polarization is shown here).
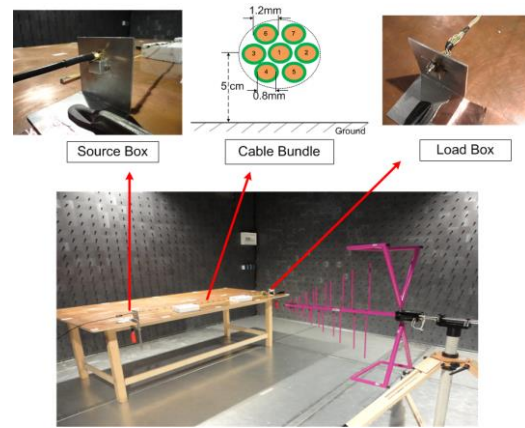
Fig. 11. Configuration with seven-wire cable bundle.

Figure 13 depicts the deviation bar charts compared with the antenna measurement. Twelve main harmonics (integral multiples of the fundamental-frequency 40 MHz) are shown. In vertical polarization, most deviations from the current measured by the EMI receiver are below 4 dB. Deviations from the current measured by the oscilloscope can be less than 5 dB except at 360 MHz. Compared with vertical fields, the calculated horizontal fields show higher deviation. Maximum deviation from simulation nearly amounts to 13 dB at 280MHz and 480 MHz. The proposed averaged correction functions from the calibration procedure can improve the predicted accuracy of current scan methods. For example, the simulation results including correction functions can improve the accuracy by 1.5 dB ~ 11 dB in the vertical field and 3 dB ~ 13 dB in the horizontal field at main radiation peaks, as shown in Fig. 14. However, the accuracy of horizontal field at 280 MHz is reduced after adding an unreliable value of 8.3 dB. This frequency is close to 300 MHz, where the correction function is very sensitive to load impedances.
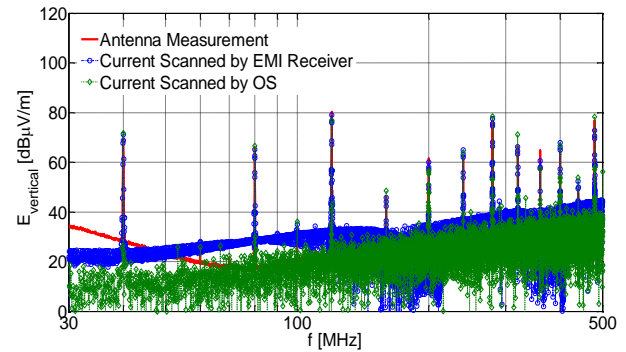
Fig. 12. Vertical electric field from the antenna measurement and the simulation based on the cable current scanned by EMI receiver and oscilloscope (OS).
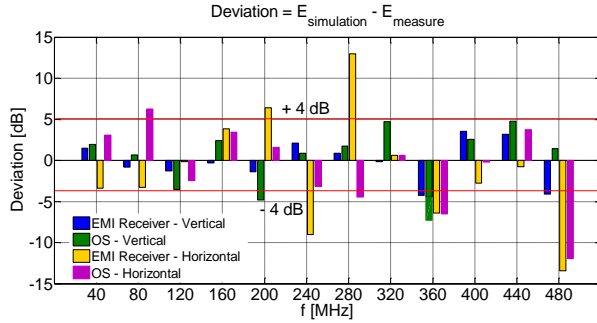
Fig. 13. Deviations of calculated fields based on the cable current scanned by the EMI receiver and the oscilloscope (OS) compared with antenna measurement.
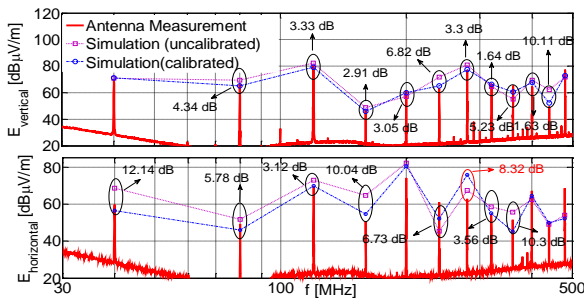
Fig. 14. Electric fields from antenna measurement and simulation based on the cable current scanned by the EMI receiver with and without correction functions.

B. Stepper-motor drive system

Figure 15 shows the radiation test configuration with the Bilog antenna (30 MHz to 1 GHz) and the active Rod antenna below 30 MHz. For flexibility in programming, a microcontroller board (Ardunio with16 MHz-clock frequency) with a motor drive board is applied as EUT, which is similar to typical automotive electronic control units. A 20 dB pre-amplifier (Rohde&Schwarz Hz-16) is used to improve the measurement dynamics.
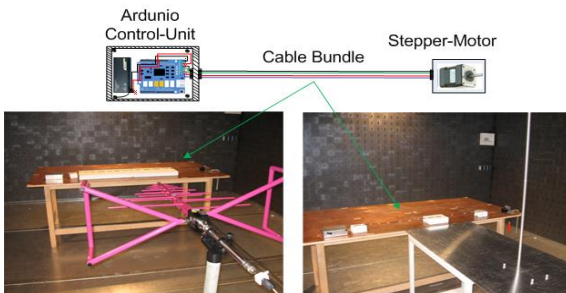
Fig. 15. Analyzed configuration of a stepper-motor drive system.

EMI receiver (average detector, 120 kHz BW, and 5 ms MT) is used to measure the antenna voltage, and the

voltage can be transferred to electric field at the antenna reference point with the antenna factor. Electric fields at the reference point are also calculated based on the acquired cable current by the EMI receiver with same setting as antenna measurement, or by the oscilloscope (single sweep, 550 μs sample time, and 0.5 ns interval time). Figure 16 shows the main radiation peaks of vertical or horizontal fields, which exceed the average limits according to CISPR 25. Some of these peaks might disturb the commercial frequency band, for example the peak at 96 MHz is located in FM band and it exceeds the class-2 limit. In addition, the CM current distributions with respect to these peaks are also depicted. They flow along the cable bundle in the form of current standing wave. From these curves, a current distribution in the order of several decibels in μA also may exceed the radiation limit, for example the maximal value of current distribution at 384 MHz is less than about 10 dBμA.
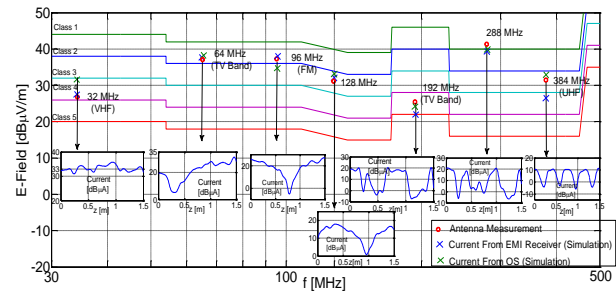
Fig. 16. Average limits for radiated disturbs from CISRP 25 and main radiation peaks from stepper motor drive system associated with the corresponding common-mode current distributions.

As well as the prediction of radiated emissions above 30 MHz, radiated emissions from the stepper-motor drive system at low frequencies are also investigated. Figure 16 (right) shows the active Rod antenna test set-up according to the ALSE method. Due to the difficulty of the proposed frequency-domain scan method to predict the field emission at low frequencies, only time-domain scan method is applied here. Capacitive coupling from the metallic table to the chamber ground can be corrected by K_C denoted in Fig. 17. Calculated results from time-domain scan method and antenna measurement are both depicted in Fig. 6. It can be seen that simulation has high accuracy at the clock frequency of 16 MHz and the first harmonic of 32 MHz, where the error is less than 2 dB. However, the results still have a large deviation below 5 MHz, due to the high sensitivity of the multi-dipole radiation model to phase distribution error. Moreover, the noise from the pre-amplifier during current acquisition at low frequencies is also an important factor in degradation of the prediction accuracy. In order to solve this problem at very low frequencies, the cable

voltage measurement by the CVP with correction function K_{CVP} is another alternative as shown in Fig. 6. Figure 18 depicts the vertical field from direct antenna measurement and the cable voltage minus K_{CVP} in decibel. Compared with cable-current based alternative, the cable-voltage based method can obtain better prediction accuracy with higher reliability especially below 5 MHz.
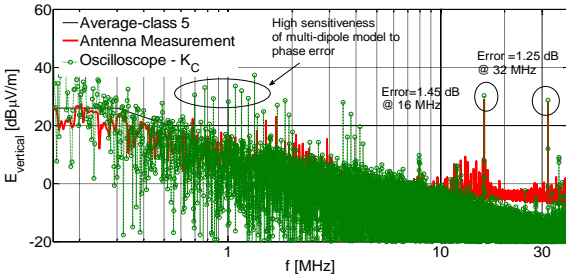
Fig. 17. Vertical electric fields from the stepper-motor drive system by the antenna measurement and the simulation based on the cable current scanned by the oscilloscope.
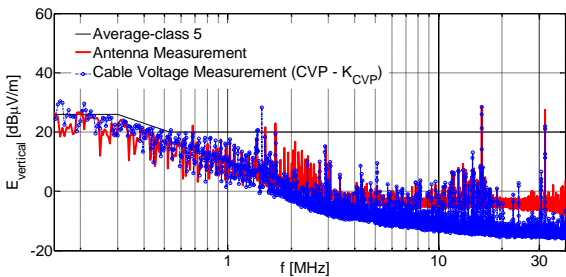
Fig. 18. Vertical electric fields from the stepper-motor drive system by the antenna measurement and the cable voltage measurement.

V. CONCLUSION

This paper proposed some measures to improve the accuracy of radiation prediction, which is based on current scan methods and typical ALSE radiation models in previous works. After acquiring current on the cable bundles, the electromagnetic fields can be calculated quickly by a multi-dipole model and surface current model. Real ALSE measurement environment influences need to be integrated in the simulation models for the comparison to the direct antenna measurements. Therefore, In order to reduce the deviations a calibration procedure was introduced to improve the prediction quality. In the calibration procedure, average correction functions was used considering different load impedance in real test scenarios. Moreover, a CM voltage alternative was proposed to predict radiation, which can overcome the low-frequency problem when using current scan methods. For validation of the methods, different configurations were analyzed. Radiated emissions from

a seven-wire cable was analyzed. Furthermore, a 4-wire bundle terminated with a stepper-motor and a micro-controller based motor driver were investigated. It could be shown that the proposed measures can improve prediction accuracy effectively considering the real ALSE configuration.

ACKNOWLEDGMENT

REFERENCES

[1] CISPR 25 Ed.3, "Vehicles, boats and internal combustion engines-Radio disturbance characteristics – Limits and methods of measurements for the protection of on-board receivers," 2007.
[2] J. Jia, D. Rinas, and S. Frei, "Prediction of radiated fields from cable bundles based on current distribution measurements," *EMC Europe 2012*, Rome, pp. 1-7, Sept. 2012.
[3] J. Jia, D. Rinas, and S. Frei, "Predicting radiated emissions of automotive systems according to CISPR 25 using current scan methods," *IEEE Trans. Electromagn. Compat.*, vol. 58, no. 2, pp. 409-418, 2016.
[4] C. Paul and S. Nasar, *Introduction to Electromagnetic Field*. 2nd ed., McGraw-Hill, New York, 1987.
[5] D. Schneider, M. Beltle, B. Siegel, S. Tenbohlen, and W. Kohler, "Radiated emissions of an electric drive system estimated on a bench using disturbance currents and transfer functions," *IEEE Trans. Electromagn. Compat.*, vol. 57, no. 3, pp. 311-321, Mar. 2015.
[6] V. Volski and G. A. E. Vandenbosch, "Efficient physical optics approximation for the calculation of radiation pattern of planar antennas located on a finite ground plane," *IEEE Trans. Electromagn. Compat.*, vol. 53, no. 1, pp. 460-465, Jan. 2005.
[7] J. Jia, F. Kremer, and S. Frei, "Modellierung von CISPR-25 antennenmessungen mittels schneller approximierender berechnungsverfahren," *EMV-Düsseldorf*, Germany, 2012.
[8] J. Meng, Y. X. Teo, D. W. P. Thomas, and C. Christopoulos, "Fast prediction of transmission line radiated emissions using the Hertzian dipole method and line-end discontinuity models," *IEEE Trans. Electromagn. Compat.*, vol. PP, no. 99, pp. 1-9, May 2014.
[9] Y. Vives-Gilabert, C. Arcambel, A. Louis, F. De Daran, P. Eudeline, and B. Mazari, "Modeling magnetic radiation of electronic circuits using near-

field scanning method," *IEEE Trans. Electromagn. Compat.*, vol. 49, no. 2, pp. 391-400, May 2007.

[10] C. W. Fanning, "Improving monopole radiation emission measurement accuracy; RF chamber influences, antenna height and counterpoise grounding (CISPR 25 &MIL-STD-461E vs MIL-STD-461E)," *IEEE International Symposium on EMC*, Chicago, pp. 103-109, Aug. 2009.

[11] S. Frei, T. Nägel, and R.Jobava, "Bestimmung der störaussendung im KFZ durch die getrennte betrachtung der elektrischen und magnetischen verkopplungen," *EMV-Düsseldorf*, Germany, 2004.

Jin Jia received his Ph.D. degree in Electrical Engineering from the TU Dortmund University, Germany, in 2015. From 2015 to 2018 he worked as EMC engineer in China Automotive Engineering Research Institute (CAERI), Chongqing, China. Now he works in Chongqing University of Technology as a Senior Engineer. His main research interests include radiation modeling of complex cable bundles and EMC modeling of automotive electrical and electronic systems in electric and intelligent vehicles.

Design of Metal Mesh THz Filters Exploiting Adjoint Sensitivity Analysis

Ahmed Y. Elsharabasy, Mohamed H. Bakr, and M. Jamal Deen

Department of Electrical and Computer Engineering
McMaster University, Hamilton, ON L8S 4K1, Canada
elsharay@mcmaster.ca, mbakr@mcmaster.ca, jamal@mcmaster.ca

Abstract — We introduce a novel approach for tuning the bandwidth of metal mesh THz filters. Our approach utilizes the adjoint sensitivity with respect to user-defined shape control parameters. Derivative-based optimization is exploited to evolve the initial template of the filter to a new design which satisfies the design specifications. We suggest a smoothing step for the sharp metallic edges that can be implemented in the final structure. Examples are presented to illustrate the efficiency of the technique in tuning the filter's bandwidth.

Index Terms — Adjoint sensitivity, derivative-based optimization, frequency selective surfaces, metal mesh filters, simulation, terahertz filter.

I. INTRODUCTION

The Terahertz (THz) frequency range has recently attracted the attention of many researchers [1-10] because it can be used for many applications such as space-based astronomy [2], biotechnology [3], THz spectroscopy [4], imaging [5-6], materials' research [7], security for military and civil applications [8], and sensing [9]. In addition, greater bandwidths are expected from wireless communication systems operating in the THz range. Such systems would require new types of filters. This is one of the motivations for the current research on filter designs that operate in frequency bands from hundreds of GHz to few THz [10].

THz bandpass filters (BPFs) [11-12] are used to eliminate out of band radiation reaching the detector or limit the radiation from a broadband source. In addition, a BPF can be used to improve the signal-to-noise ratio for better detection and measurement by blocking out-of-band thermal radiation. Terahertz BPFs may be classified into three main types; absorption filters [13], multilayer dielectric filters [14], and metal mesh filters [11]. The cross absent filter (CAF) is one of the most successful metal mesh bandpass filters because of its simple design and manufacturability. The CAF filter's response is determined by the geometrical dimensions of each cell, i.e. the arm length and width. Previous studies [11,15-16] succeeded in adjusting the filter response by

tuning these geometrical parameters, in addition to the periodicity [17].

The previous approaches in [11,17] had limitations in improving the performance of the filter. Tuning was carried out with the cross arm length and width, and the periodicity. To improve further the performance of CAF bandpass filters, we introduce a derivative-based optimization algorithm that is capable of evolving the filter geometry by exploiting the well-studied adjoint sensitivity technique [18-20]. Our optimization approach exploits more geometrical variables thus enabling more degrees of freedom to improve the performance. The sensitivities are estimated using only one EM simulation regardless of the number of designable parameters. In our approach, the finite element electromagnetic solver ANSYS HFSS [21] is driven by a MATLAB optimization algorithm to change the bandwidth of the filter while maintaining the same centre frequency.

II. OPTIMIZATION PROBLEM

The optical performance, i.e. the transmission of the filter, is a function of the parameters of the filter geometry. Therefore, an efficient optimization algorithm is required to get the optimal parameters that achieve the desired performance.

A. Objective function

The addressed design problem can be put in the following mathematical form:

$$\min_{x} F(\omega, x), \qquad (1)$$

$$\text{subject to: } g(x) \le 0. \qquad (2)$$

where $F(\omega, x)$ is the objective function (e.g., magnitude of the *S*-parameters) to be minimized over the desired frequency range and $x \in \mathbb{R}^n$ is the vector of designable parameters. This objective function includes all the design specifications over different frequency bands. The vector $g(x)$ represents the linear and nonlinear constraints.

B. Adjoint sensitivities

The sensitivities of the *S*-parameters with respect to all design parameters can be obtained at minimal extra

computational cost exploiting adjoint sensitivities. The original simulation supplies the S-parameters and their sensitivities with respect to all parameters. This technique is known as self-adjoint sensitivity analysis (SASA) [18]. Variations of this approach are available in a number of commercial EM solvers (e.g., ANSYS HFSS).

In the frequency domain, the objective function is formulated as a complex function $F(x, E)$ where E is the vector of electric fields in the frequency domain. E is the solution of the linear system of equations representing a frequency domain method with the system matrix Z and the known excitation vector Q [19]:

$$ZE = Q. \tag{3}$$

By computing the original E and the adjoint $\tilde{E}$ fields, the sensitivities of the objective function with respect to the jth parameter are given by [19]:

$$\partial F / \partial x_j = \tilde{E}^T \left(\left(\partial Q / \partial x_j \right) - \left(\partial (Z\bar{E}) / \partial x_j \right) \right), \ \forall j \tag{4}$$

where $\bar{E}$ is the solution of (3) at the current set of parameters. Estimating (4) for all parameters requires only the original and adjoint field information. The derivatives of the system matrix with respect to all parameters are already available through the utilized frequency domain solver.

III. METHODOLOGY

The metal mesh filter design in the THz range consists of a frequency selective surface (FSS) with a repeated pattern of fixed template. In our work, the pattern template shown in Fig. 1, is evolved during each step. This creates new filter templates that is more likely to satisfy the required design specifications. For a metal mesh filter with fixed thickness, the filter is divided into four two-dimensional symmetrical quarters allowing each quarter to evolve according to the optimization algorithm. N control points are selected on each quarter including one point on the horizontal x-axis and another one on the vertical y-axis. The origin is considered the centre of the filter template with constant coordinates. It follows that for N control points, we have ($2N$-2) design parameters in addition to the length of the unit cell of the array G. This results in ($2N$-1) design parameters. The vector of design parameters $x = [x_1, x_2, y_2, x_3, y_3, \ldots, x_{N-2}, y_{N-2}, y_{N-1}, G]^T$ is shown in Fig. 2. The initial values of these points are set and passed to the EM simulator HFSS. HFSS then simulates the structure and returns both the S-parameters at the selected frequencies and their adjoint sensitivities with respect to all the design parameters. These sensitivities represent the gradient to be utilized within the optimization algorithm. A custom script is used to control HFSS and allow the MATLAB optimizer to drive the EM simulator. The built-in constrained optimization algorithm in MATLAB, which is derivative-based optimization, is utilized to reach the optimal set of design variables satisfying the design specifications.
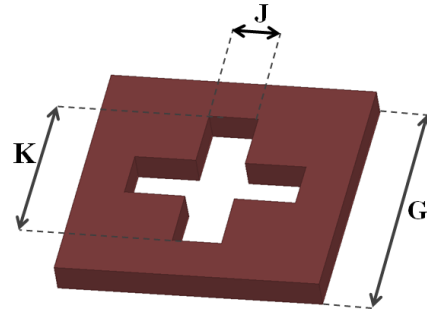
Fig. 1. The main dimensions of a one cell of a cross-absent metal mesh filter.
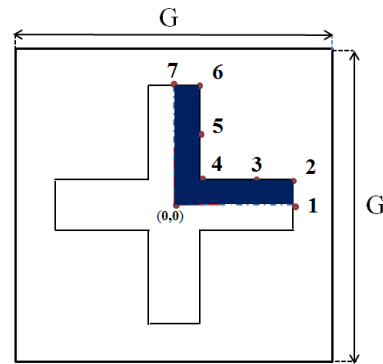
Fig. 2. The control points (1, 2…, 7) with control variables (x_1, x_2, y_2... , y_7, G) that enable the optimizer to evolve the filter template.

Following this procedure, the shape of the filter evolves to a completely different one from the initial template. In some cases, the optimal design may include some sharp edges which could make the filter design too lossy or unrealistic. In our work, we added a smoothing approach as a final step so that design template is smoothed.

IV. EXAMPLES

In our examples, we utilize a cross absent filter (CAF) with initial template parameters from [11,17] and a 12 μm thick copper grid operating at 2.1 THz. We are interested in controlling the bandwidth of this filter. We use one quarter of the filter due to its symmetry. Seven vertices are selected resulting in a total number of parameters of 13 after the length of the unit cell is included ($x \in \mathbb{R}^n$, n=13). COMSOL Multiphysics [22] is used to verify the simulation results obtained using HFSS for the initial filter template. Good matching is achieved confirming the accuracy of our simulations.

First, we consider the case where our target is to widen the bandwidth of the initial bandpass filter while keeping the same resonant frequency. The objective function is the transmittance $|S_{21}|^2$ of the BPF which is to be maximized over the frequency range from 1.4 THz

to 2.6 THz. Assuming that the response is symmetrical around the centre (resonant) frequency of 2.1 THz, the optimization problem is given by:

$$\max_{\boldsymbol{x}} \min_{i} \left\{ \left| S_{21}\left(f_i, \boldsymbol{x}\right) \right|^2 \right\}, \tag{5}$$

$$\text{subject to} \qquad \boldsymbol{x}_l \le \boldsymbol{x} \le \boldsymbol{x}_u,$$

where, $1.4\,\text{THz} \le f_i \le 2.6\,\text{THz}$, $i = 1, 2, \ldots, 26$.

To increase the bandwidth of the filter response, we have to maximize the minimum of the transmittance over the defined frequency range. EM simulations are carried out for 26 linearly distributed frequency points over the bandwidth 1.4 THz to 2.6 THz. $\boldsymbol{x}_l$ and $\boldsymbol{x}_u$ are the lower and upper bound constraints preventing the evolution to an unrealizable design. The minimax optimizer starting from the initial point $\boldsymbol{x}_0$ drives HFSS to calculate the S-parameters and sensitivities. These steps are repeated until the predetermined stopping criteria achieved. Following this procedure, we obtain the optimal parameters values $\boldsymbol{x}_f$ that are listed in Table 1.

Table 1: Initial ($\boldsymbol{x}_0$) and final ($\boldsymbol{x}_f$) values of the control parameters for broader bandwidth filter design template

Parameter	$\boldsymbol{x}_0$ (μm)	$\boldsymbol{x}_f$ (μm)
x_1	36.5	39.4
x_2	10.5	22.5
y_2	36.5	47.0
x_3	10.5	20.2
y_3	24.0	25.6
x_4	10.5	26.8
y_4	10.5	29.2
x_5	24.0	25.6
y_5	10.5	19.7
x_6	36.5	45.7
y_6	10.5	24.8
y_7	36.5	47.0
G	113.0	108.8

Figure 3 (a) shows the final filter template. We then eliminate the sharp edges of the optimal design with two different smoothing approaches according to the position of these sharp edges as illustrated in the Fig. 3 (b). The achieved response in Fig. 4, i.e., the optimal one before smoothing. This results show that the bandwidth has been increased by almost 3 times as compared to the initial design. The smoothed filter templates using the both smoothing approaches (additive and subtractive) are shown in Fig. 5. The smoothing responses are similar to the optimal one as shown in Fig. 6. One advantage arising from the smoothing step is that it maintains the same symmetry of the final template as the original

(initial) one. Hence, the optical properties of the filter remain independent of the polarization of the incident wave. The same steps were carried out to achieve a narrower bandwidth template, and it successfully shows the capability to obtain one third of the original bandwidth around the same resonant frequency 2.1 THz.

(a) (b)
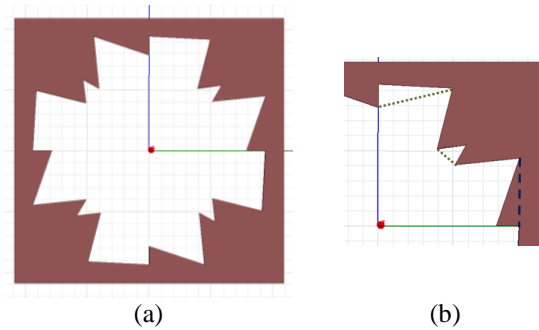
Fig. 3. (a) A top view of the optimal (final) design for the filter with a wider bandwidth. (b) The smoothing process, the dashed line shows the first subtractive smoothing approach while the dotted line shows the other additive smoothing approach.
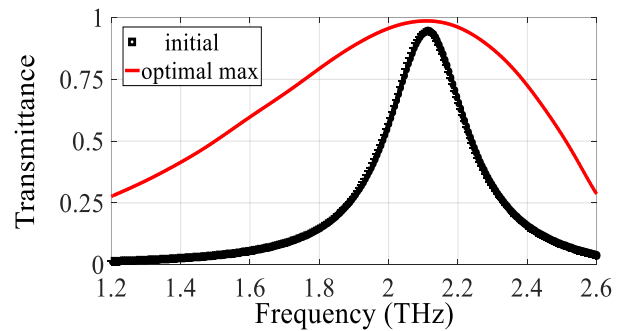
Fig. 4. The transmittance of the initial filter template (…), and of the final (optimal) design (—).

(a) (b)
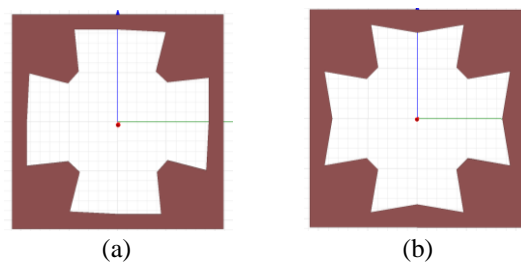
Fig. 5. A top view of the first smoothed (modified) version of the filter with a wider bandwidth: (a) subtractive smoothed 1, and (b) additive smoothed 2.
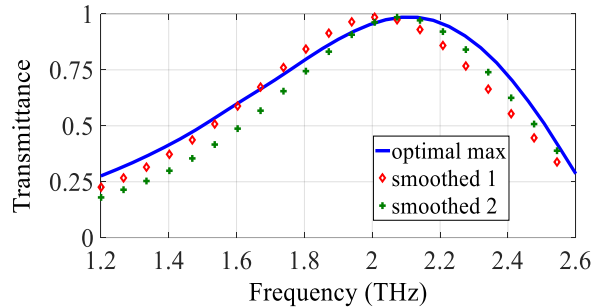
Fig. 6. The transmittance of the optimal filter template (——) and the two smoothed versions for the wide band filter (◊) and (+).

V. CONCLUSION

In this work, we presented an optimization algorithm that exploits efficient adjoint sensitivity analysis to evolve the geometry of the cross-absent metal mesh THz filters. We are able through simulations to increase or decrease the bandwidth by a factor of three. The final (smoothed) design is polarization independent. In addition, it is easy to fabricate and integrate with other THz systems. The presented technique offers a systemic approach for adjusting the bandwidth of the THz filters for different applications.

REFERENCES

[1] P. Siegel, "Terahertz technology," *IEEE Trans. Microwave Theory Tech.*, vol. 50, no. 3, pp. 910-928, 2002

[2] C. Kulesa, "Terahertz spectroscopy for astronomy: From comets to cosmology," *IEEE Trans. Terahertz Science and Technology*, vol. 1, no. 1, pp. 232-240, 2011.

[3] K. Ajito, "Terahertz spectroscopy for pharma-ceutical and biomedical applications," *IEEE Trans. Terahertz Science and Technology*, vol. 5, no. 6, pp. 1140-1145, 2015.

[4] B. Gompf and M. Dressel, "THZ-micro-spectro-scopy," *IEEE J. Sel. Top. Quantum Electron.*, vol. 14, no. 2, pp. 470-475, 2008.

[5] P. Jepsen, D. Cooke, and M. Koch, "Terahertz spectroscopy and imaging - modern techniques and applications," *Laser & Photonics Rev.*, vol. 5, pp. 124-166, 2011.

[6] M. J. Deen, ed., *Silicon-based Millimeter-wave Technology*, Advances in Imaging and Electron Physics, Academic Press, Amsterdam, vol. 174, 2012.

[7] P. D. Cunningham, *et al.*, "Broadband terahertz characterization of the refractive index and absorption of some important polymeric and organic electro-optic materials," *Journal of Applied Physics*, vol. 109, pp. 043505-1-043505-5, 2011.

[8] N. Palka, *et al.*, "THz spectroscopy and imaging in security applications," *19th International Conference on Microwaves, Radar and Wireless Communica-tions*, vol. 1, pp. 265-270, 2012.

[9] B. Ung, *et al.*, "Terahertz detection of substances for security related purposes," *Proc. SPIE Smart Structures, Devices, and Systems III*, vol. 6414, pp. 1-6, 2006.

[10] S. Koenig, *et al.*, "Wireless sub-THz communication system with high data rate," *Nat. Photonics*, vol. 7, pp. 977-981, 2013.

[11] D. W. Porterfield, *et al.*, "Resonant metal-mesh bandpass filters for the far infrared," *Appl. Opt.*, vol. 33, pp. 6046-6052, 1994.

[12] C. Winnewisser, *et al.*, "Characterization and application of dichroic filters in the 0.1-3-THz region," *IEEE Trans. Microwave Theory Tech.*, vol. 48, pp. 744-749, 2000.

[13] A. J. Gallant, *et al.*, "Terahertz frequency bandpass filters," *Journal of Applied Physics*, vol. 102, pp. 023102-1-023102-5, 2007.

[14] R. Wilk, *et al.* "Highly accurate THz time-domain spectroscopy of multilayer structures," *IEEE J. Sel. Top. Quantum Electron.*, vol. 14, no. 2, pp.392-398, 2008.

[15] Y. Wang, *et al.*, "Micromachined thick mesh filters for millimeter-wave and terahertz applications," *IEEE Trans. Terahertz Science and Technology*, vol. 4, no. 2, pp. 247-253, 2014.

[16] S. A. Alaverdyan, *et al.*, "Development and computer-aided design of metal gratings for micro-wave mesh polarizers," *IEEE Trans. Microwave Theory Tech.*, vol. 63, no. 8, pp. 2509-2514, 2015.

[17] A. M. Melo, *et al.*, "Metal mesh resonant filters for terahertz frequencies," *Applied Optics*, vol. 47, no. 32, pp. 6064-6069, 2008.

[18] H. Akel and J. P. Webb, "Design sensitivities for scattering-matrix calculation with tetrahedral edge elements," *IEEE Trans. Magn.*, vol. 36, no. 4, pp. 1043-1046, July 2000.

[19] N. K. Nikolova, *et al.*, "Sensitivity analysis of network parameters with electromagnetic frequency-domain simulators," *IEEE Trans. Microwave Theory Tech.*, vol. 54, no. 2, pp. 670-681, 2006.

[20] M. H. Bakr, *Nonlinear Optimization in Electrical Engineering with Applications in Matlab*, IET, 2013.

[21] 'HFSS' ver. 15.0, ANSYS, Inc., Canonsburg, PA, 2014.

[22] 'COMSOL' ver. 5.1, COMSOL Inc., Burlington, MA, 2015.

Forecasting of Electromagnetic Radiation Time Series: An Empirical Comparative Approach

Zeydin Pala [1], İbrahim Halil Ünlük [1], and Erkan Yaldız [2]

[1] Department of Computer Engineering/Computer Programming
University of Mus Alparslan, Mus, 49250, Turkey
z.pala@alparslan.edu.tr, ih.unluk@alparslan.edu.tr

[2] Municipality Information Processing Office, Mus, Turkey
erkan1yaldiz@gmail.com

Abstract ─ This study compares the performance of time series models for forecasting electromagnetic radiation levels at Yesilce neighborhood in Mus, Turkey.

To make successful predictions using EMF time series, which is obtained in the 36-month measurement process using the calibrated Wavecontrol SMP2 device, nine different models were used. In addition to Mean, Naive, Seasonal Naïve, Drift, STLF and TBATS standard models, more advanced ANN models such as NNETAR, MLP and ELM used in the R software environment for forecasting. In order to determine the accuracy of the models used in the EMF time series used in the study, mean absolute error (MAE), relative mean absolute error (RMAE) metrics were used. The best results obtained with NNETAR, Seasonal Naïve, MLP, STLF, TBATS, and ELM models, respectively.

Index Terms ─ Electromagnetic radiation, ELM, forecasting models, MLP, NNETAR, time series.

I. INTRODUCTION

Based on past and current data, predicting the future and making plans according to it has a very great meaning for practical life. Predicting the future is of great importance in health as well as in many areas. Time series analysis for forecasting of time depending variables, which is the collection of data at specific intervals over a period is not new [1], but is an important area of machine learning. Usually, the measurement of time series is made at regular time intervals that are a list of observation where the ordering matters. Due to dependency, ordering is very important in time series. In other words, changing time series of measurements means changing means of the data. Time series analysis is frequently used to estimate a relationship between adverse health outcomes and short-term exposes to ambient electromagnetic radiation (EMR) [2]. Modeling some forecasting models for low-frequency high voltage EMR characteristics based on these historical data may

be useful. In order to model the time series correctly and efficiently and predict the future, it is possible to find many important models in the literature.

Therefore, time series used extensively in the fields of industry, engineering, and science, especially in the fields of economics, business, physical sciences [3], and finance.

The research question in this paper is that in living environments weather EMR effects on humans and forecasting EMR time series data using popular algorithms.

The main objectives of this study are: To act an empirical study and compare analysis and highly extensible forecasting methods of R, which is a language and environment for statistical computing and graphics. To compare the performance of statistical and ANN based models. To investigate the influence of electromagnetic radiation on humans.

II. MATHEMATICAL BACKGROUND

Time series are sequential measurements data points of the same variable over successive times. Our EMF time series can be mathematical defined as a set of vectors $\{x_1, x_2, x_3, \ldots, x_T\}$, t=0,1,2,3,…, T, where T is the set of times at which the process was, will or can be observed, t is an index denoting the period in time in which x occurs. Here x_t is treated as a random variable. Time series are called univariate or multivariate according to the time-dependent variable they contain. The EMF time series used in this study is called univariate because it is based on one time-dependent variable [4].

For a time series modeling a general approach is to plot the series and examine the main features of the graph, checking in particular whether there is (i) a trend, (ii) a seasonal component, (iii) any apparent sharp changes in behavior and any some observations [5].

In time series, forecasting predictor variables are used usefully. In this study, we wish to forecast the

monthly low-frequency electromagnetic fields (EMF) of a high voltage electric lines. A model with predictor variables might be of the form:

$$EMF = f(\text{device sensitivity, } distance, \ time, \grave{\alpha}). \quad (1)$$

The ϵ_t term on the right allows effects of relevant variables and for random variation that is not included in the model. Since the model helps explain, what causes the variation in EMF it can be calls, explanatory model. In this situation, a convenient time series forecasting equation is of the form:

$$EMF_{t+1} = f(EMF_t, \ EMF_{t-1}, \ EMF_{t-2}, \ldots, \grave{\alpha}), \quad (2)$$

where t is the present month, t+1 is the next month, t−1 is the previous month, t−2 is two months ago, and so on [6].

A. Forecasting methods in R

The statistical functions of the R language are very strong. In this study, all functions such as Mean, Naive, Seasonal Naive, Drift, STLF, and TBATS, which are used for prediction purposes in the R environment, are defined within the forecast class. All of the above-mentioned functions can be used for prediction of the desired time series after importing the forecast class. The following paragraphs give a brief description of these functions:

The Main method in the forecast class, which returns estimates and prediction ranges, for an independent and identically distributed (iid) model that is applied to the time series. If we use the data of EMF time series y_1, y_2, y_3, ..., y_T, then we can write the forecasts as:

$$\hat{y}_{T+\Delta|T} = \frac{y_1 + y_2 + y_3 + \cdots + y_T}{T}. \quad (3)$$

Where, the left side of the equation expresses the short-term forecast, in other words, it means the forecast $y_{T+\Delta}$ taking account of y_1, y_2, y_3, ..., y_T and Δ is the forecast horizon.

We used the Naïve method for forecasts and we simply set all forecasts to be the value of the last observation of the EMF dataset. That is,

$$\hat{y}_{T+\Delta|T} = y_T. \quad (4)$$

The Seasonal Naïve method, which is a similar and useful method for highly seasonal data. Using this method, we foresee that each estimate will be equal to the last observed monthly value starting from the same month of the year.

Estimating the monthly EMF, which is normally much more than $T + \Delta$, can be written as follows:

$$\hat{y}_{T+\Delta|T} = y_{T+\Delta - \alpha(\beta+1)}, \quad (5)$$

where α is the seasonal period and β is the integer part of (∆−1)/α. For example, with monthly data, the forecast for all future January values is equal to the last observed January value.

One of the simplest method to predict using the general trend of the time series is the Drift method, a variation on the naïve method. Thus, the forecast for time

T+∆ is given by [6]:

$$\hat{y}_{T+\Delta|T} = y_T + \frac{\Delta}{T-1}\Sigma_{t=2}^{T}(y_t - y_{t-1}) = y_t + \Delta\left(\frac{y_T - y_1}{T-1}\right). \quad (6)$$

The Drift method is equivalent to drawing a line between the first and last observations and calculating it for the future. TBATS model uses a combination of Fourier terms with an exponential smoothing state space model and a Box-Cox transformation. One drawback of TBATS models, however, is that they can be slow to estimate, especially with long time series. The STLF function, which is expressed as seasonal and trend decomposition using loess, is a fairly simple yet powerful estimation function. The STLF model assumes that time series can be divided into trend, seasonality, and error components.

B. Artificial Neural Networks (ANN) in R

Artificial neural networks (ANNs), which is accepted as one of the applications of artificial intelligence, is the information processing technology that analyzes the existing data by mimicking the working structure of the human brain and creates new information with different learning algorithms. In this study, along with the NNETAR algorithm, which is based on the artificial neural network in the Forecast class, multilayer perceptron (MLP) and Extreme learning machines (ELM) algorithms in the NNFOR class were used.

The neural network autoregression (NNAR) model consists of three layers: input, hidden and output. This model is defined in the R forecast library and the NNAR model becomes available after the forecast library is imported. It generally performs better than conventional algorithms such as Main, Naive, Seasonal Naive, and STLF. The NNAR model is a parametric and non-linear estimation model [7]. The MLP is a fully connected feed-forward networks, supervised learning network with up to one or more hidden layers, and probably the most common network architecture in use. Training of the model is usually performed by error backpropagation or a related procedure [8, 9]. The ELMs are also feed-forward neural networks, primarily used in classification, regression and clustering with a single layer or multiple hidden node layers. They are especially preferred in terms of presenting models for a large class of natural and artificial phenomena, which are difficult to handle using classical parametric techniques [10].

C. Predictive results comparative analysis

The estimation error of a model can be defined as the difference between the actual value of the model and its estimated value. It can be written as [6]:

$$e_{T+\Delta} = y_{T+\Delta} - \hat{y}_{T+\Delta|T}, \quad (7)$$

where the training data is given by $\{y_1, y_2, y_3, \ldots, y_T\}$ and the test data is given by $\{y_{T+1}, y_{T+2}, y_{T+3}, \ldots\}$.

The performance of the models used in this study was evaluated using statistical metrics such as the mean absolute error (MAE) and relative mean absolute error

(RMAE). The MAE, which is measures the average absolute deviation of forecasted values from original ones can be defined as:

$$MAE = \frac{1}{n}\sum_{i=1}^{n}|e_{T+\Delta}|. \qquad (8)$$

Where n is the number of observation. The RMAE is used to evaluate models [11]:

$$RMAE = \frac{1}{|\hat{y}_{T+\Delta|T}|}\sum_{i=1}^{n}|e_{T+\Delta}|. \qquad (9)$$

MAE is the average absolute deviation of forecasted values from original ones.

III. IMPLEMANTATION AND DISCUSSION

The dataset used in this study was obtained as a result of 36 months of regular measurements. Measurements were made at a height of 2.9 m from the high voltage line and 2.5 m from the ground. In the measurements, the highest EMF value was measured as E_{max}=6792 V/m in January 2018 and the lowest value was E_{min} 5388 V/m in July 2017. All measurements made at the points where high voltage lines are located in Yeşilce neighborhood of Muş province have been carried out according to the standards determined by ICNRP. The measurement time was made as the average of 6-minute measurements as determined by these standards. These values measured monthly using the Wavecontrol SMP2 device exceed ICNIRP (1998) and Council of European Union (1999) public exposure limits. Using the R programming language version 3.5.1, all analyzes were performed in RStudio.

In addition, the time series is divided into multiple components using the decomposition method to make predictions more realistic. Equipment used for the periodic measurement of the electric field of high voltage lines in outdoor environment and decomposition graphs of the data obtained in the measurements are shown in Fig. 1 and Fig. 2, respectively. As seen in the time series, it is observed that electricity consumption decreases in summer and increases in winter months. Accordingly, EMF values also varied. By using decomposition method in the Studio environment, EMR time series is divided into four components as data, seasonal, trend and remainder. These components are shown in Fig. 2.

Fig. 1. Periodic measurement image under high voltage line.
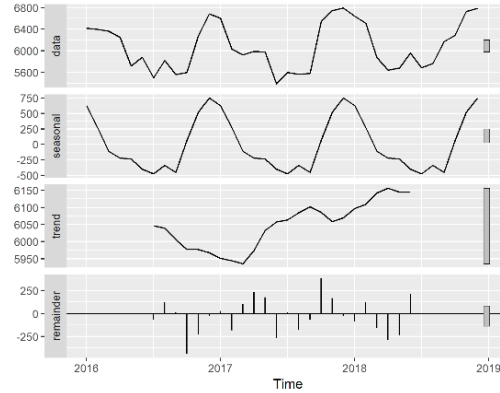
Fig. 2. The EMF data series (top) and its three additive components.

In the first analysis, the first 30-month portion of the EMF time series, which was generated as a result of the 36-month measurement, was used for training (84%) purposes, and the remaining were used for testing (16%) purposes.

In the second analysis, the dataset was divided into 70% and 30% for training and testing, respectively. It is also necessary to consider the forecasting horizon (Δ) when using forecasting methods. For all functions used in the analysis, the value of the Δ parameter was taken as 12 for the prediction of the next 12 months.

In order to have a better understanding on the performance of the selected methods, the performance metrics of the forecasted methods are shown in Table 1. When both MAE and RMAE performance metrics were evaluated together, Seasonal Naive from the standard functions showed the best performance, whereas, for neural network functions, the NNETAR function showed the best performance. In general, the RMAE average value of ANN algorithms such as NNETAR, MLP, and ELM is smaller than the average value of the other classical algorithms. This result shows that ANN algorithms perform better than classical algorithms [7]. As shown in Table 1, the division of the dataset (84%, 16%) for training and testing operations resulted in a better performance than dividing by (70%, 30%).

Table 1: Comparison metrics of forecasting methods

Model Strategy	Training (84%) Test (16%)		Training (70%) Test (30%)	
Method/Metric	MAE	RMAE	MAE	RMAE
Seasonal Naïve	190.66	0.184	262.36	0.475
STLF	205.59	0.198	262.47	0.476
TBATS	209.86	0.202	239.80	0.434
MEAN	402.90	0.389	358.98	0.650
NAIVE	434.00	0.419	585.18	1.060
DRIFT	473.65	0.457	606.68	1.098
MLP	205.55	0.197	504.76	0.880
NNETAR	183.71	0.177	486.75	0.875
ELM	303.04	0.292	612.13	1.108

The visual predictions of the classical algorithms defined in the Forecast class and the ANN algorithms defined in the NNFOR class are shown in Fig. 3 and Fig. 4, respectively.
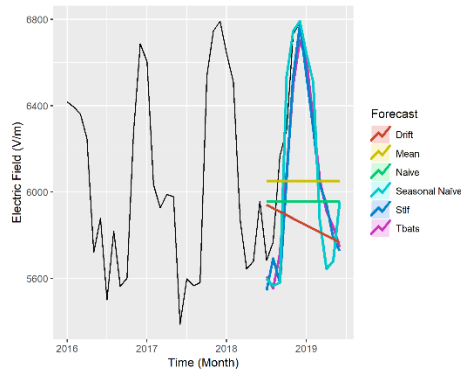
Fig. 3. Comparative forecasts for EMF monthly time series.

As shown in Fig. 3, considering the seasonal changes in the EMF time series, it is possible to say that the 12-month estimates of the Seasonal Naive, STLF and TBATS functions are quite satisfactory.

The MLP and ELM models used in the estimation process consisted of three layers. The numbers of neurons in the inputs, hidden and output layers of each model were respectively (3, 5, 1) and (3, 17, 1). As shown in Table 1, ANN based algorithms are NNETAR, MLP and ELM, respectively, based on metric values.
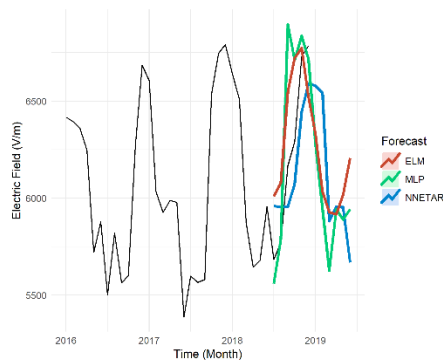
Fig. 4. Future predictions of ANN-based algorithms.

IV. CONCLUSION

In this study, a dataset based on 36-month EMF measurements was used. The monthly values obtained in the measurement environment generally exceed the ICNIRP public exposure limits. In addition, we compared the accuracy of Mean, Drift, Naïve, Seasonal Naïve, STL, and TBATS model as representative methods when forecasts EMF time series data. The comparative study of presented work is also performed with the ANN models for forecasting of the EMF time series. In the next 12-month forecasting of the EMF time series, the best performance values were obtained using NNETAR, Seasonal Naïve, MLP, STLF, TBATS and ELM models, respectively.

REFERENCES

[1] C. Chatfield and A. S. Weigend, "Time series prediction: Forecasting the future and understanding the past," *International Journal of Forecasting*, vol. 10, p. 161-163, 1996.

[2] G. Redlarski, B. Lewczuk, A. Zak, et al., "The influence of electromagnetic pollution on living organisms: Historical trends and forecasting changes," *BioMed Research International*, vol. 2015, pp. 1-18, 2015.

[3] Z. Pala and R. Atici, "Forecasting sunspot time series using deep learning methods," *Solar Physics*, vol. 294, no. 50, pp. 1-14, 2019.

[4] K. W. Hipel and A. I. Mcleod, *Time Series Modelling of Water Resources and Environmental Systems*. Amsterdam, Elsevier 1994.

[5] P. J. Brockwell and R. A. Davis, *Introduction to Time Series and Forecasting*. 3rd ed., Springer, Switzerland, 2016.

[6] R. J. Hyndman and G. Athanasopoulos, *Forecasting: Principles and Practice*. 2nd ed., Monash University, Australia, 2018.

[7] D. Sena and N. K. Nagwani, "A neural network autoregression model to forecast per capita disposable income," vol. 11, pp. 13123-13128, 2016.

[8] K. S. R. Krishna, J. L. Narayana, and L. P. Reddy, "ANN models for microstrip line synthesis and analysis," *World Acad. Sci. Eng. Technol.*, vol. 2, no. 10, pp. 724-8, 2008.

[9] Z. D. Marinković and V. V. Marković, "Temperature-dependent models of low-noise microwave transistors based on neural networks," *Int. J. RF Microw. Comput. Eng.*, vol. 15, no. 6, pp. 567-77, 2005.

[10] G. B. Huang, Q. Y. Zhu, and C. K. Siew, "Extreme learning machine: Theory and applications," *Neurocomputing*, vol. 70, no. 1-3, pp. 489-501, 2006.

[11] F. Güneş, P. Mahouti, S. Demirel, M. A. Belen, and A. Uluslu, "Cost-effective GRNN-based modeling of microwave transistors with a reduced number of measurements," *Int. J. Numer. Model. Electron. Networks, Devices Fields*, vol. 30, no. 3-4, pp. 1-12, 2017.

A High Density 16-bit Polarization-Independent Chipless Passive RFID Tag

**Adeel Nasir Khan [1], Shabbir Majeed Chaudhry [1], Rashid Saleem [2],
Muhammad Farhan Shafique [3], and Sabih ur Rehman [4]**

[1] Department of Electrical Engineering
University of Engineering and Technology, Taxila, 47050, Pakistan
adeelnasir100@gmail.com, shabbir.majeed@uettaxila.edu.pk

[2] Department of Telecommunication Engineering
University of Engineering and Technology, Taxila, 47050, Pakistan
rashid.saleem@uettaxila.edu.pk

[3] Center for Advanced Studies in Telecommunication (CAST)
COMSATS University Islamabad, Park Road, Tarlai Kalan, Islamabad, 45550, Pakistan
farhan.shafique@comsats.edu.pk

[4] School of Computing and Mathematics
Charles Sturt University, Australia
sarehman@csu.edu.au

Abstract ─ A compact, polarization-independent, chipless, passive Radio Frequency Identification (RFID) tag with 16 bits binary encoding is presented in this paper. The design is prepared with the placement of 16 Convoluted Square Loops (CSLs), in a nested loop arrangement. The proposed CSL structure is formed by inwards semi-circular bending of each edge of a square geometry. This configuration not only offers high Quality (Q) factor for each resonance but also polarization independence. The design is fabricated on a 1.6 mm thick FR-4 substrate having an area of 20.8 mm $\times$ 10.8 mm. The presented design occupies small area with the bit density of 7.12 bits/cm^2 and requires no unit cell repetition for enhancing the Q factor. The tag is tested on the frequency range of 2 to 26 GHz with various E-field polarizations, in order to achieve a polarization independent behavior.

Index Terms ─ Chipless RFID, Convoluted Square Loops (CSL), Internet of Things (IoT), multi-bit, passive tag, polarization independence.

I. INTRODUCTION

RFID tags are finding considerable applications in tracking, sensing, wireless communication and Internet of Thing (IoTs) [1]. RFID tags offer excellent read rate, non-line-of-sight communication and longer reader-to-tag range [2]. RFID tags with integrated chips are expensive for bulk deployment. In order to make RFID tag cost effective, chipless RFID tags are gaining considerable attention [3].

Generally, RFID tags are classified into two categories: time domain based and frequency domain based [2]. Surface Acoustic Wave (SAW) based RFID tags can have a high bit density up to 64 bits but their realization is expensive and challenging. On the other hand, frequency domain based tags can be manufactured economically with standard fornication technologies like Printed Circuit Borad (PCB) [4]. For designing frequency domain based tags, a common practice is to use metallic loops of same shape but different lengths and arrange them concentrically on a substrate. A tag, a reader and a host computer constitute a complete RFID system [4]. RFID encodes data into a unique binary pattern with the help of simple radiators/loops that can be read through the Radar Cross-Section (RCS) response. Electromagnetic waves generated by the tag reader induce simultaneous inductive and capacitive effects on the tag, resulting in the desired resonant behavior. This resonance pattern corresponding to the encoded data is detectable through the RCS response [2]. A number of structures have been proposed in literature such as hexagonal, rectangular or square and E-shaped [2, 5, 6]. The tag proposed in this paper occupies a much smaller area than the tags reported previously [2, 5, 6].

The overall shape of a loop dictates the resonances, Quality Factor (Q) and polarization behavior of the passive RFID tag. Rectangular shape loops produce

higher Q factor resonance [5]. A symmetric shape makes a tag polarization independent and a non-symmetric geometry limits the tag operation in random orientations [2]. A perfectly symmetric shape such as a circle is best suited for the polarization independence. However, as articulated in [2], a circle does not produce a high Q factor. A trade-off has to be made between the Q factor of resonances and polarization independence. A customized hybrid structure having attributes of both, circle and square has a potential to produce polarization independent response while also exhibiting considerably high Q factor.

The rest of the paper is arranged as follows: Section II describes the design of the proposed loop/resonator. Section III describes the layout of a full tag in consolidated fashion. Results obtained from simulation and testing of the design are discussed in Section IV. Finally, Section V concludes the paper.

II. DESIGN OF A UNIT RESONATOR LOOP

The proposed design of chipless RFID tag is built-up from a single customized resonant loop that is modified from a square shape by bending all edges inwards from the middle in a semi-circular form. The complete geometry of a unit cell is formed by repeating the loops with decreasing size with the same geometric ratio. Two unit cells are placed side-by-side on a single substrate to form the complete tag.

The proposed geometry combines benefits of square loops by offering high Q resonance and the modification on edges allows its frequency independent operation [7]. The high Q resonance is very helpful in encoding large number of data bits within limited bandwidth thus allowing various unique combinations for a single tag. The proposed tag in this work is capable of offering more than 65,000 combinations which is sufficient to cater for medium to large scale tagging requirement. The proposed CSL structure is shown in the Fig. 1 with its surface current density plot at its resonant frequency.
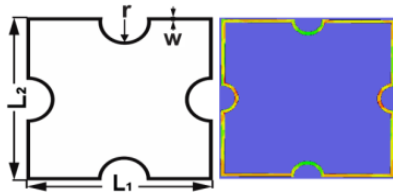
Fig. 1. CSL structure and its surface current density, *dimensions are L1=L2=10.2mm, W=0.2mm, r=0.8mm*.

The area of the CSL is 10.2 mm × 10.2 mm and the edges are bent inside in the form of semi-circle, each with radii of 0.8 mm. When electromagnetic waves illuminate the loop, it responds by resonating at the operating frequency. The presence of resonance at the designated frequency is marked as a bit "1" and the

absence of resonance is perceived as a bit "0". A binary data combination of '1101001110011001' is illustrated in Fig. 2 where the simulated RCS response corresponds to the tag configuration in a particular way.
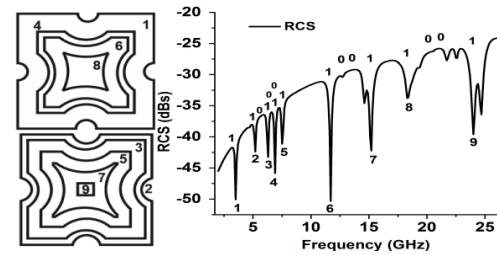
Fig. 2. Simulated RCS results of '1101001110011001' bit combination.

III. OPTIMIZATION OF OVERALL DESIGN

The overall size of CSL is optimized through a full wave electromagnetic simulator HFSS®. The optimized loop is nested 16 times with each loop scaled down in a specific ratio. These CSLs are then arranged in the form of two units of 8 loops each, in a side-by-side configuration. The edge of a loop is scaled down by 1 mm and radius of semi-circle is increased by 0.5 mm in each consecutive inner loop. The outer-most loop of the second unit cell is formed with 9.7 mm edge length and semi-circle of radii 1.05 mm. Inner loops of this unit cell are formed in the same pattern as described for the first unit cell. Separation between loops of both units is kept at 0.3 mm and overall dimensions of the optimized tag are finalized at 20.8 mm × 10.8 mm. All 16 loops are of different electrical lengths thus corresponding to resonant frequencies that represent a 16-bit binary coding scheme.

IV. SIMULATIONS AND MEASUREMENTS

The simulation was setup by placing the RFID tag inside an air box with Perfect Matched Layer (PML) boundary condition on all the edges. In order to compute the RCS of the tag a plane wave excitation was setup which illuminates the tag from the desired direction. A frequency sweep is added to the setup in the bandwidth of interest. The simulation was time consuming since a number of frequency points were included in the sweep. Once the analysis is completed the bi-static RCS was computed in the post processing along the swept frequency. The RFID tag was fabricated through milling on an FR-4 substrate with the thickness of 1.6 mm and copper cladding of 1 oz, as shown in Fig. 3. The measurement setup was established by placing a pair of UWB horn antennas (TDK-HRN-0118) side-by-side and the RFID tag was placed in the front to measure bi-static RCS. Since the tag operates up to 26 GHz, the measurements were taken in parts initially from 1 to 18 GHz and then the wideband double ridge horns were

replaced with WR-42 (18 to 26.5 GHz) standard gain horn antennas. The measurements were taken on Agilent N5242A Performance Network Analyzer. Measurement setup is shown in Fig. 4.
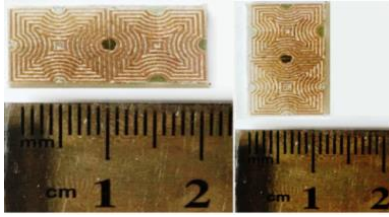
Fig. 3. Fabricated RFID Tag.
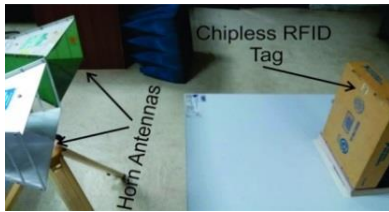
Fig. 4. Measurement setup.

The comparison of the simulated and measured results is presented in Fig. 5. The bits are fairly distinguishable in the measured response. EM analysis of loop resonating at 3.5 GHz is shown in the Fig. 6. Electrical length of this loop is calculated to be 44.4 mm which corresponds to one guided wavelength.
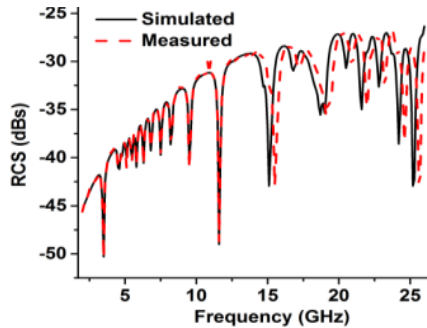
Fig. 5. Measured and simulated RCS plot.
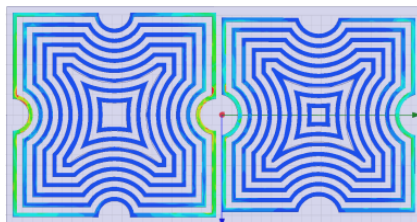
Fig. 6. EM analysis of loop resonating at 3.5GHz.

Contrary to the techniques of replicating unit cells to enhance Q factor, this design does not repeat unit cell.

The loop itself offers better Q factor as compared to designs reported in [2, 5, 6]. High Q factor also allows the enhanced interrogation range. However, that is highly dependent on the environmental conditions and the tag background material. In order to verify its polarization independence characteristics, the tag is read at various polarization angles by rotating the RFID tag. The results of 0°, 30°, 45° and 60° polarization angles are presented in Fig. 7 and the encoded pattern is fairly readable.

The tag has a capacity of 16 bits and occupies an area of 2.25 cm^2 which results in the bit density of 7.12 bits/cm^2. The achieved bit density is higher than the designs reported in [2, 5, 6]. A comparison of this RFID tag with recent relative references is presented in Table 1.
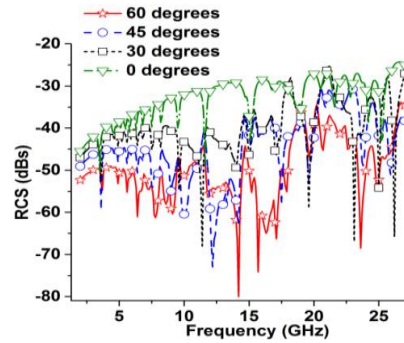
Fig. 7. Measured polarization response.

Table 1: Comparison with other designs

Resonator Shape	No. of Bits	Tag Size (cm^2)	Polarization Independence
CSL (proposed)	16	2.24	Yes
Hexagonal [2]	14	2.30	Yes
Rectangular [5]	03	9.60	Yes
E-shaped [6]	08	17.70	No

V. CONCLUSION

A 16-bit polarization-independent, chipless, passive RFID tag is proposed in this work. CSL structure has been used as a resonating element. The design provides high Q resonance and polarization independence within a compact size of 2.246 cm^2. The tag has high bit-density of 7.12 bits/cm^2 and it offers 16 bits binary encoding option. The tag is fabricated and tested to establish its performance and the results obtained are in agreement with the simulations. The polarization independence has also been tested by rotating the tag at different angles. The large bit capacity of this tag makes it suitable for use in medium to large tagging setup and this proposed tag can offer more than 65,000 unique combinations.

REFERENCES

[1] M. Rehman and J. D. Park, "The smallest form factor UWB antenna with quintuple rejection bands for IoT applications utilizing RSRR and RCSRR," *Sensors*, no. 3, 2018.

[2] M. S. Iqbal, H. Shahid, M. A. Riaz, S. Rauf, Y. Amin, and H. Tenhunen, "FSS inspired polarization insensitive chipless RFID tag," *IEICE Electronics Express*, vol. 14, no. 10, pp. 20170243, May 2017.

[3] F. Parades, C. Herrojo, J. M. Contreras, M. Moras, A. Nunez, E. Ramon, and F. Martin, "Near-field chipless radio-frequency identification (RFID) sensing and identification system with switching reading," *Sensors*, no. 4, pp 1148, 2018.

[4] M. A. Ashraf, Y. A. Alshoudokhi, H. M. Behairy, M. R. Alshareef, S. A. Alshebeili, K. Issa, and H. Fathallah, "Design and analysis of multi-resonators loaded broadband antipodal tapered slot antenna for chipless RFID applications," *IEEE Access*, vol. 5, pp. 25798-25807, 2017.

[5] D. Laila, R. Thomas, C.M. Nijas, and P. Mohanan, "A novel polarization independent chipless RFID tag using multiple resonators," *Progress In Electromagnetic Research*, vol. 55, pp. 61-66, 2015.

[6] M. Sumi, R. Dinesh, C. M. Nijas, S. Mridula, and P. Mohanan, "High bit encoding chipless RFID tag using multiple E-shaped microstrip resonators," *Progress In Electromagnetics Research B*, vol. 61, pp. 185-196, 2014.

[7] M. Nauman, R. Saleem, A.K. Rashid, and M. F. Shafique, "A miniaturized flexible frequency selective surface for X-band applications," *IEEE Trans on Electromagnetic Compatibility*, vol. 58, no. 2, pp. 419-428, 2016.

Adeel Nasir Khan received B.Sc. Electrical Engineering in 2016 from University of Engineering and Technology (UET), Lahore, Pakistan. He is currently working as a Research Assistant at University of Engineering and Technology (UET), Taxila. Recently he is awarded a funded MS studentship by UET Taxila. His main research interests are in RFID Tags, metamaterials and high gain antennas.

Shabbir Majeed Chaudhry received B.Sc. in Electrical Engineering and M.Sc. Electrical Engineering in 2000 and 2003, from University of Engineering and Technology, (UET) Taxila, Pakistan. He joined the Department of Electrical Engineering UET, Taxila, Pakistan, in 2001. He also received his Ph.D. degree in Electrical Engineering from UET Taxila and since 2006 onwards, he is working as an Assistant Professor in the same University. Chaudhry heads the Electronic System Design research group and was appointed as Director of Electronics Laboratory in UET Taxila in 2013.

Rashid Saleem received B.S. in Electronic Engineering from Ghulam Ishaq Khan Institute of Engineering Sciences and Technology, Pakistan, in 1999. He received M.S. from UET Taxila through Center for Advanced Studies in Engineering, Pakistan, in 2006 and Ph.D. from The University of Manchester, United Kingdom in 2011. Currently, he is working as Assistant Professor at University of Engineering and Technology (UET), Taxila, Pakistan where he is supervising several postgraduate students and heading the MAP (Microwaves, Antennas and Propagation) research group.

Muhammad Farhan Shafique received the B.Eng. degree from Hamdard University, Karachi, Pakistan, in 2003, M.S. degree from the University of Paris East Marne-La-Vallée, Paris, France, in 2005 and Ph.D. in Electronic and Communications Engineering from The University of Leeds, UK in 2010. He is working as an Associate Director at Center for Advanced Studies in Telecommunications (CAST) where he has established the MCAD (Microwave Components and Devices) research group. He has also setup a wide range of research facilities in the area of RF engineering which involves 4 state-of-the art laboratories.

Sabih ur Rehman is a Lecturer in Computing with the School of Computing and Mathematics at Charles Sturt University, Australia. Sabih has completed his Ph.D. in the area of vehicular ad-hoc networks. Sabih obtained his Bachelor degree from University of South Australia, Adelaide in Electronics & Telecommunication Engineering. Sabih's research expertise lie in the areas of Quality of Service (QoS), Cross-layer Protocol Architecture Designing, Wireless Propagation and Antenna Modeling. Sabih's current research is focused on the emerging area of Internet of Things (IoT).

Rotated Stacked Yagi Antenna with Circular Polarization for IoT Applications

Ji-Hong Kim [1], Chang-Hyun Jeong [2], and Wang-Sang Lee [2]

[1] Defense Agency for Technology and Quality (DTaQ), Jinju 52851, Republic of Korea

[2] Department of Electronic Engineering/Engineering Research Institute (ERI)
Gyeongsang National University (GNU), 501, Jinju-daero, Jinju, Gyeongnam, 52828, Republic of Korea
wsang@gnu.ac.kr

Abstract ─ This letter proposes a rotated stacked Yagi antenna with high directivity and circular polarization. The proposed antenna consists of three elements with a rotation angle and different lengths: a director, a reflector, and a driven element connected to the coaxial feeder. The coaxial feeding is connected to the driven element of the proposed antenna via a LC-balun, and the others are coupled with the driven element. Each stacked element with different lengths is equally rotated at an angle of 60° with respect to the lower element so that the dipole array antenna forms a high directive circular polarization. The size of the proposed antenna is $0.49\lambda_0 \times 0.49\lambda_0 \times 0.17\lambda_0$ at 2.45 GHz and achieved a 10 dB impedance bandwidth of 6.3%, a 3 dB axial ratio bandwidth of 8%, and a peak gain of 4.3 dBic.

Index Terms ─ Array, circular polarization, dipole antennas, IoT, rotated stacked, Yagi antenna.

I. INTRODUCTION

Recently, the number of wireless communications for automobiles, unmanned aerial vehicles (UAVs), internet of things (IoT), and health-care sensors is increasing. In particular, communication performance of the IoT sensor module with a linear polarized antenna depends on multi-path effect and polarization loss factor. The circular polarization (CP) antenna can receive a signal of a linearly polarized antenna disposed in any direction. To reduce the polarization loss of the multi-path effect of the linear polarization (LP) antennas used on these smart devices, several studies on achieving circular polarization are being conducted [1]-[13].

Generally, in a single-fed microstrip patch antenna, the CP is formed by cutting the patch edge of the antenna [1]-[3] or by disposing the feeding point on the diagonal line of the patch [4]. Additionally, inserting a U or L-shaped slot into a patch [5]-[7] is one of the methods to create the CP. However, the problem with these antennas is that the area is large owing to the space needed to place the patches of the antennas. On the other hand, for multi-fed antennas, the CP can be obtained by a feeding network that generates phase differences [8]-[10]. In [11], each feeding point was provided the signals 0°, 120°, 240° Those phase differences achieved CP. In addition, studies have conducted using meta-material or ring antenna structures [12]-[13]. However, these methods to generate CP need complex feeding networks, including hybrid couplers or splitters. In this paper, we propose a simple structure antenna that can achieve a high directive CP antenna with a single feed. The stacked structure produces not only circular polarization but also a high degree of directivity, which makes it suitable for IoT applications at 2.45 GHz.

II. ANTENNA CONFIGURATION AND ANALYSIS

Figure 1 shows the configuration and design parameters of the proposed rotated stacked Yagi antenna with circular polarization. The proposed antenna consists of three elements with a rotation angle and a spacing distance as shown in Fig. 1 (a). In Fig. 1 (b), the proposed antenna obtains the directivity of the antenna by the length difference of the three elements and the stacked structure as a Yagi antenna. Due to the difference in length of the three elements constituting the proposed antenna, each of the elements serves as a director that forms the directivity of the antenna, a driven element that directly connects to the coaxial feed point, and a reflector that gets rid of the backside radiation. In addition, each element of the proposed antenna is arranged with a rotation angle of 60° with respect to the lower elements to achieve circular polarization. In this case, in order to realize a phase difference of 180 degrees with two elements, they are arranged at a rotation angle of 90 degrees (180/2) between antenna elements. Thus, when CP is typically implemented in three elements, it is designed to have a rotation angle of 60 degrees (180/3) between antenna elements. The operating frequency of the proposed antenna depends mainly on the length of the driven element. Therefore, the performance of the proposed antenna is determined by the spacing distance and the rotation angle. Figure 1 (c) shows an expanded

view of the antenna input with the LC-balun. The input of the antenna is connected to the signal of the coaxial cable through the LC-balun. Figures 1 (d) and 1 (e) represent the top and side views of the prototype of proposed antenna including three antenna supports.
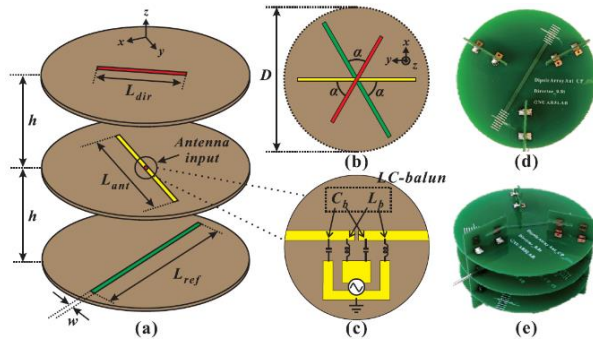
Fig. 1. Geometry of the proposed rotated stacked Yagi antenna configuration and its prototype: (a) perspective view, (b) top view, (c) expanded view of antenna input, (d) top view of fabricated antenna prototype, and (e) side view of fabricated antenna prototype.
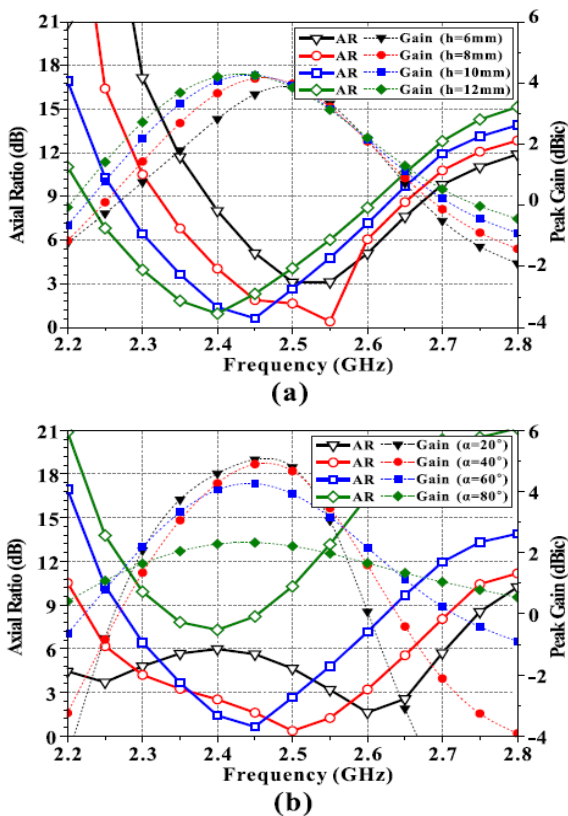
Fig. 2. Simulated axial ratio and peak gains of the proposed antenna with regard to the design parameters: (a) spacing distance, h, and (b) rotation angle, α.

Figure 2 shows the results of parameter studies for variation of the spacing distance and angle. The index on the left represents axial-ratio, and the index on the right represents the peak gain. As the spacing distance increases in Fig. 2 (a), where the rotation angle is 60 degrees, the frequency at which circular polarization of the proposed antenna is formed decreases, while the peak gain of the proposed antenna increases. Figure 2 (b) shows the result of the axial ratio and peak gain according to the angle variation. When the rotation angle of the elements is 60°, the CP of the proposed antenna is most accurately obtained. In Fig. 2 (b) with the same distance of 10 mm, the coupling effect from the radiator decreases as the rotation angle increases. As a result, the larger the rotation angle, the smaller the gain of the antenna. Therefore, to obtain circular polarization, the proposed antenna must have appropriate spacing distance and an appropriate rotation angle. The process of forming the circular polarization by the proposed antenna is shown in Fig. 3, which depicts the E-field at the point 30 mm away from the driven element of the proposed antenna on the z-axis. The figure confirms that the direction of the E-field vector is rotated according to the variation of phase.
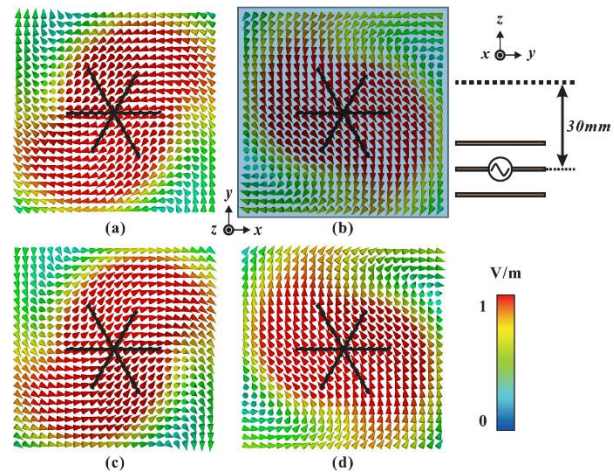
Fig. 3. E-field distributuons at xy plane of 30mm away from the driven element in the proposed antenna with regard to the phase variation: (a) 0°, (b) 90°, (c) 180°, and (d) 270°

III. RESULTS AND DISCUSSIONS

For the experimental verification, the proposed rotated stacked antenna was designed and implemented on a FR-4, the most representative substrate with a thickness of 0.8 mm, a dielectric constant $\varepsilon_r = 4.5$, a loss tangent $\delta = 0.02$, and a copper thickness of 18 um. The parameters of the designed antenna are $L_{dir} = 43.1$ mm, $L_{ant} = 46.0$ mm, $L_{ref} = 50.9$ mm, w = 1.41 mm, h = 9.8mm,

$\alpha = 60°$, D = 58 mm, L_b = 3.3 nH, and C_b = 1.2pF.
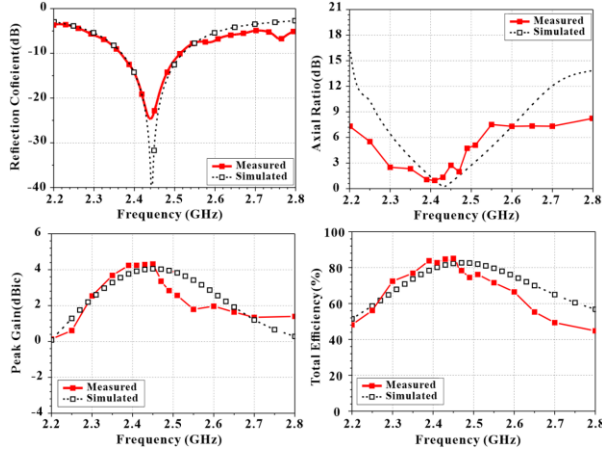
Fig. 4. Simulated and measured results of proposed antenna according to frequency: (a) reflection coefficients, (b) axial ratio, (c) peak gain, and (d) total efficiency

Figure 4 presents the simulated and measured results of a fabricated prototype antenna. The simulation results are using a full-wave electromagnetic tool (CST Microwave Studio 2018). Figure 4 (a) shows the simulated and measured reflection coefficients of the proposed antenna, and the 10 dB impedance bandwidth is approximately 6.3%. The axial ratio of the proposed antenna according to frequency is shown in Fig. 4 (b). The proposed antenna has approximately 8% of the 3 dB axial ratio bandwidth performance around 2.45 GHz. The peak gain and total efficiencies of the proposed antenna at 2.45 GHz are approximately 4.25 dBic and 85% in Figs. 4 (c) and 4 (d), respectively. The simulated and measured results indicated that the proposed antenna has a resonance characteristic at 2.45 GHz where it supported various IoT networks.
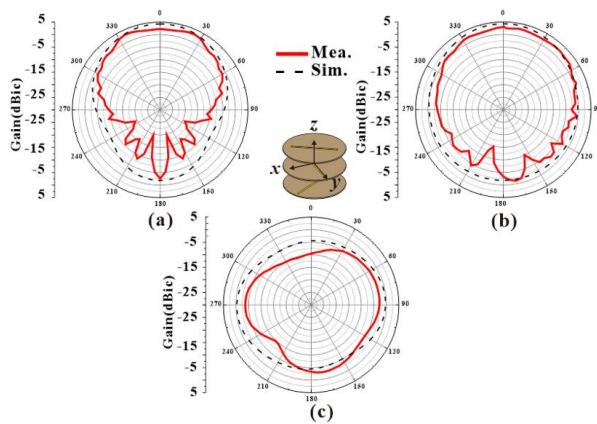
Fig. 5. Simulated and measured radiation patterns of the proposed antenna at 2.45GHz: (a) xy-plane, (b) yz-plane, and (c) xy-plane.

Figure 5 describes the simulated and measured radiation patterns of the proposed antenna at 2.45 GHz in the xz, yz, and xy planes. The radiation pattern represents the high directivity of the proposed antenna for z-direction. Table 1 shows the characteristics between antennas for 2.45GHz. The proposed antenna can form a CP with a miniaturized size.

Table 1: Comparison with circular polarization antennas for 2.4GHz

	FRQ (GHz)	Peak Gain (dBic)	Electrical Size (λ_0)	AR. BW (%)	Imped. BW (%)
[3]	2.45	7.5	0.65 ×0.65 × 0.07	6.94	20.6
[7]	2.4	6.8	0.48 × 0.48 × 0.1	3.3	16
[9]	2.4	13.1	1.6 × 1.6 × 0.1	60	50
[10]	2.4	5.1	0.58 × 0.58 × 0.1	8.33	16.67
[12]	2.5	12	1.67 × 2.17 × 0.15	89	85
[13]	2.54	7	0.76 × 0.76 × 0.33	8.7	13.94
Prop.	2.45	4.3	0.49 × 0.49 × 0.17	7.93	6.27

IV. CONCLUSION

The study proposed a stacked dipole array antenna with a rotation angle for circular polarization. By applying a stacked structure with space distances, the proposed antenna is featured by directivity and circular polarization. The proposed antenna obtains a peak gain of 4.25 dBic and a performance of 8% of a 3 dB axial ratio bandwidth at 2.45 GHz. The proposed antenna covers the 2.45GHz band supporting the IoT network, and also has enough gain to be used in the actual communication environment, making it suitable for various IoT environments.

REFERENCES

[1] Q. W. Lin, H. Wong, X. Y. Zhang, and H. W. Lai, "Printed meandering probe-fed circularly polarized patch antenna with wide bandwidth," *IEEE Antennas Wirel. Propag. Lett.*, vol. 13, pp. 654-657, 2014.

[2] Nasimuddin, Z. N. Chen, and X. Qing, "A compact circularly polarized cross-shaped slotted microstrip antenna," *IEEE Trans. Antennas Propag.*, vol. 60, no. 3, pp. 1584-1588, 2012.

[3] C. Deng, X. Lv, and Z. Feng, "Low-profile circularly polarised patch–ring antenna with compact

feeding network," *IET Microwav. Antenn. Propag.*, vol. 12, no. 3, pp. 410-415, 28 2 2018.

[4] Y. Guo and D. C. H. Tan, "Wideband single-feed circularly polarized patch antenna with conical radiation pattern," *IEEE Antennas Wirel. Propag. Lett.*, vol. 8, pp. 924-926, 2009.

[5] K.-L. Wong, C.-C. Huang, and W.-S. Chen, "Printed ring slot antenna for circular polarization," *IEEE Trans. Antennas Propag.*, vol. 50, no. 1, pp. 75-77, 2002.

[6] K. Tong and T. Wong, "Circularly polarized U-slot antenna," *IEEE Trans. Antennas Propag.*, vol. 55, no. 8, pp. 2382-2385, 2007.

[7] Nasimuddin and Z. N. Chen, "Aperture-coupled asymmetrical C-shaped slot microstrip antenna for circular polarisation," *IET Microwaves, Antennas Propag.*, vol. 3, no. 3, pp. 372-378, 2009.

[8] M. A. Antoniades and G. V. Eleftheriades, "A broadband Wilkinson balun using microstrip metamaterial lines," *IEEE Antennas Wirel. Propag. Lett.*, vol. 4, pp. 209-212, 2005.

[9] J. M. Kovitz, J. H. Choi, and Y. Rahmat-Samii, "Supporting wide-band circular polarization: CRLH networks for high-performance CP antenna arrays," *IEEE Microw. Magaz.*, vol. 18, no. 5, pp. 91-104, 2017.

[10] S. X. Ta and I. Park, "Dual-band low-profile crossed asymmetric dipole antenna on dual-band AMC surface," *IEEE Antennas Wirel. Propag. Lett.*, vol. 13, pp. 587-590, 2014.

[11] C. Lin, F. Zhang, Y. Jiao, F. Zhang, and X. Xue, "A three-fed microstrip antenna for wideband circular polarization," *IEEE Antennas Wirel. Propag. Lett.*, vol. 9, pp. 359-362, 2010.

[12] K. L. Chung, "High-performance circularly polarized antenna array using metamaterial-line based feed network," *IEEE Trans. Antennas Propag.*, vol. 61, no. 12, pp. 6233-6237, 2013.

[13] T. Chang, J. Lin, and Y. G. Chen, "A circularly polarized ring-antenna fed by a serially coupled square slot-ring," *IEEE Trans. Antennas Propag.*, vol. 60, no. 2, pp. 1132-1135, 2012.

Gain Enhancement of Microstrip Patch Antenna Using Metamaterial Superstrate

Vani H. R. [1], Goutham M. A. [1], and Paramesha [2]

[1] Department of Electronics and Communication Engineering
Adichunchanagiri Institute of Technology (AIT), Chikkamagaluru, Karnataka
Vani4ait@gmail.com

[2] Department of Electronics and Communication Engineering
Government Engineering College, Hassan, Karnataka

Abstract ─ In this work, a gain enhancement of conventional microstrip patch antenna has been treated for WLAN applications. About 1.3dB gain enhancement, compared to a conventional patch, has been achieved by loading the microstrip patch with a metamaterial superstrate composed of 2x3 array of Square Split Ring Resonator. Simulations have been carried out using Ansys HFSS. Measured results have been taken to validate the simulation result.

Index Terms ─ Metamaterials, microstrip patch antenna.

I. INTRODUCTION

Modern wireless communication system requires high data rate that depends on the gain of the antenna. Towards this, metamaterial starts playing a very important role in the design of an antenna [1]-[3]. In [4], gain enhancement of microstrip patch antenna (MPA) is achieved by using graded index dielectric superstrate. In [5], a planar two-layer superstrate over a printed patch antenna to enhance the broadside gain is considered. The problem of enhancing the directivity of an aperture coupled microstrip patch antenna using one dimensional electromagnetic bandgap (EBG) structure is treated in [6]. It was found that the directivity level, beamwidth as well as reflection coefficient and gain could be enhanced by using superstrate with two layers. In [7], study of performance parameters of patch antennas with different feeding methods is presented and compared with that of patch antennas without dielectric superstrate. It was found that the directivity level, beam width as well as reflection coefficient and VSWR could be further enhanced by using superstrate with two layers rather than one, regardless of the feeding method. In [8], a meandered line-double split ring resonator (DSRR) superstrate loaded high gain circular patch antenna is presented for X-band and showed that the superstrate loading has minor effect on the return loss characteristics but a major effect on the gain characteristics of

the circular patch. Scope for miniaturization and compactness of an antenna leads to the design of novel antenna structure loaded with metamaterial. Hence, in the proposed work, a metamaterial superstrate loaded microstrip patch antenna is designed on low cost, FR4 epoxy substrate for WLAN application.

II. ANTENNA DESIGN

A. Microstrip patch antenna without superstrate

The microstrip patch antenna with co-axial feeding is designed using ANSYS HFSS on a less expensive, widely available FR4 epoxy substrate with relative permittivity of 4.4 and dielectric loss tangent of 0.02 for 5.5 GHz WLAN application. Figure 1 shows simulated top view of MPA. The dimension of the patch and the substrate is 12mm x 16mm x 0.1mm and 26mm x 30mm x 1.6mm respectively. The equations to calculate the dimension of patch antenna are given in [9].
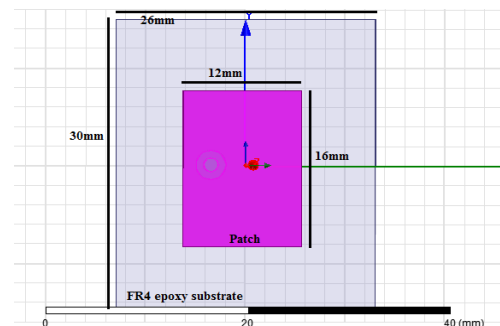
Fig. 1. Simulated top view of rectangular MPA.

B. Proposed MPA with metamaterial superstrate

The proposed design consists of metamaterial superstrate loaded microstrip patch antenna. Figure 2 (a) shows the geometry of square split ring resonator metamaterial. The dimension of the ring is 6mm x 6mm. The gap width is 1.5mm. Figure 2 (b) shows the simulated

metamaterial superstrate loaded microstrip patch antenna. The metamaterial superstrate is composed of 2x3 array of Square Split Ring Resonator on a FR4 epoxy material. The superstrate dimension is 26mm x 30mm x 1.6mm and is placed at a height of 5mm from the substrate. The fabricated metamaterial superstrate loaded MPA prototype is shown in Fig. 2 (c).

III. SIMULATED AND MEASURED RESULTS

The S-parameters for metamaterial unit cell is shown in Fig. 3 (a) S11 and S21 parameters crosses at 4.8 GHz and 6.1 GHz. Hence, the unit cell structure reflects the electromagnetic waves in this band [10]. The measurements are taken on Vector Network Analyzer (Rohde and Schwarz, German make ZVK Model No. 1127.8651). The simulated and measured return loss of microstrip patch antenna with and without superstrate loading is shown in Fig. 3 (b). The summary of simulation and tested results is shown in Table 1.

(c)
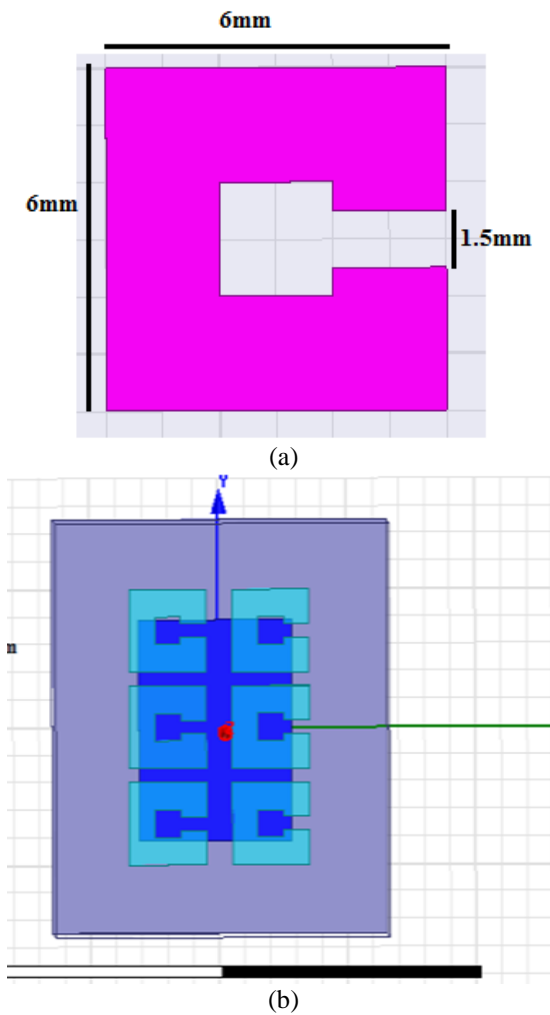
Fig. 2. (a) Metamaterial unit cell, (b) simulated metamaterial superstrate loaded MPA, and (c) fabricated metamaterial superstrate loaded MPA.

(a)

(b)

(a)

(b)
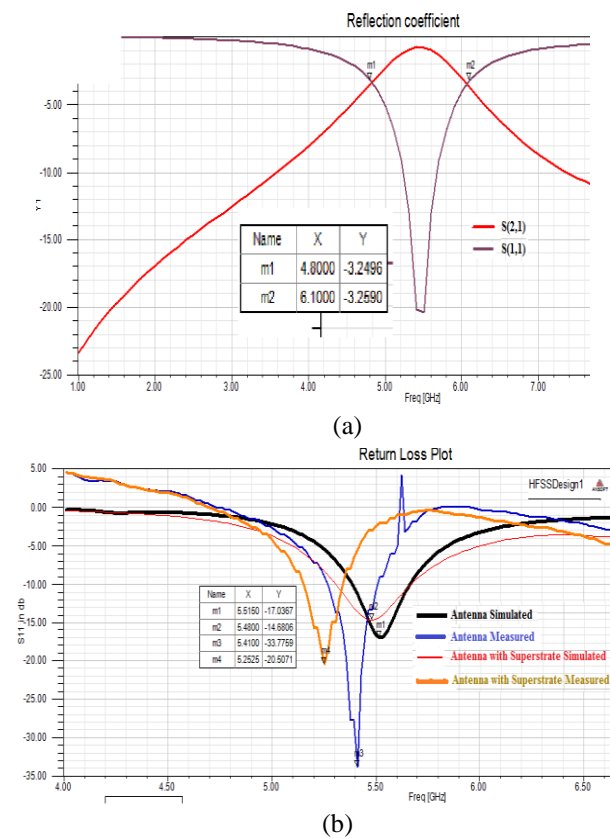
Fig. 3. (a) S-parameters for the metamaterial unit cell, and (b) simulated and measured |S11| responses of the microstrip patch antenna with and without superstrate loading.

Table 1: Summary of simulation and tested results

Parameters	MPA without Superstrate		MPA with Superstrate	
	Simulated	Fabricated	Simulated	Fabricated
Resonant frequency (in GHz)	5.51	5.41	5.48	5.25
Return loss (in dB)	−17.03	−33.77	−14	−20
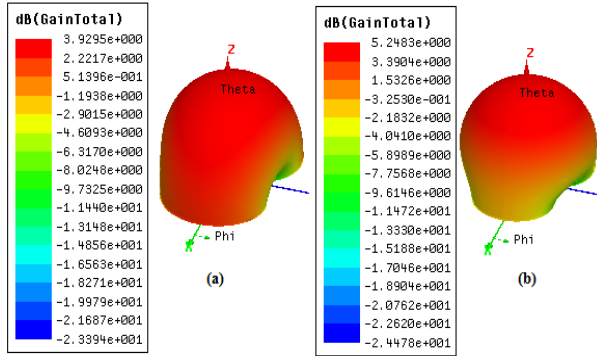
Fig. 4. (a), (b) Simulated 3D gain plot for microstrip patch antenna without and with superstrate loading.

Fig. 5. Experimental setup for the estimation of antenna gain.

From Fig. 4 it is clearly seen from simulation that the antenna gain is increased by 1.2dB when metamaterial superstrate is included in the system.

The experimental setup for the gain measurement is shown in Fig. 5. Two steps were used for the estimation of antenna gain. In the first step estimation of gain without metamaterial superstrate is made followed by estimation of gain with metamaterial superstrate. For gain calculation equation in [7] is used:

$$G(dB) = 10\log\left(\frac{P_r}{P_t}\right) - G_t(dB) - 20\log\left(\frac{\lambda_0}{4\pi R}\right)(dB). \quad (1)$$

Where P_t and P_r are transmitted and received powers respectively. G_t is the gain of the pyramidal horn antenna equal to 17dB. R is the distance between transmitting antenna and antenna under test. The gains obtained from measurements are 3.7dB and 5dB for patch antenna without and with metamaterial superstrate loading respectively. The enhancement in gain is better with less number of rings on the FR4 epoxy superstrate than that obtained in [10].

HFSS simulation of variation of axial ratio with frequency is shown in Fig. 6. At 5.5 GHz, the axial ratio is 26.8dB and 35dB for MPA with and without superstrate respectively. This indicates that the antennas are linearly polarized.
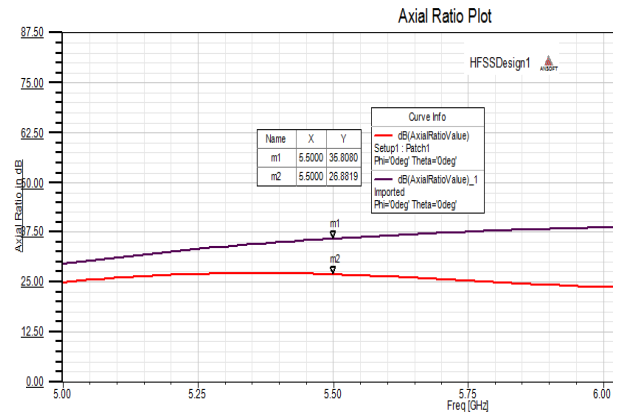
Fig. 6. Variation of axial ratio with frequency.

IV. CONCLUSION

A Square Split Ring Resonator metamaterial superstrate loaded microstrip patch antenna for gain enhancement has been presented in this paper for WLAN applications. A comparison of the characteristics of the proposed antenna with a conventional patch antenna shows that the superstrate loading has minor effect on the return loss characteristics but a major effect on the gain characteristics of the patch. The superstrate loading has enhanced the gain by about 1.3dB as compared to a conventional patch

ACKNOWLEDGMENT

REFERENCES

[1] M. Gil, F. Aznar, A. Velez, et al., "Electrically small resonators for metamaterial and microwave circuit design," in *Passive Microwave Components and Antennas*, V. Zhurbenko, Ed., InTech, 2010.

[2] J. D. Baena, R. Marque's, and F. Medina, "Artificial

magnetic metamaterial design by using spiral resonators," *Physical Review B*, 69, 014402, 2004.

[3] S. A. Tretyakov, C. R. Simovski, and M. Hudlicka, "Bianisotropic route to the realization and matching of backward-wave metamaterial slabs," *Physical Review B*, 75, 153104, 2007.

[4] Y. Li, K. Yoo, R. Mittra, G. Lu, D. Zeng, and Y. Guan, "Directivity enhancement of microstrip antennas using dielectric superstrates," *2010 International Conference on Applications of Electromagnetism and Student Innovation Competition Awards (AEM2C)*, Taipei, pp. 206-209, 2010.

[5] H. Errifi, A. Baghdad, A. Badri, and A. Sahel, "Directivity enhancement of aperture coupled microstrip patch antenna using two layers dielectric superstrate," *Proceedings of 2014 Mediterranean Microwave Symposium (MMS2014)*, Marrakech, pp. 1-4, 2014.

[6] J. C. Iriarte, *et al*., "EBG superstrate for gain enhancement of a circularly polarized patch antenna," *2006 IEEE Antennas and Propagation Society International Symposium*, Albuquerque, NM, pp. 2993-2996, 2006.

[7] H. Errifi, A. Baghdad, A. Badri, and A. Sahel, "Optimization and performance analysis of probe-edge-inset and aperture feed patch antenna covered by dielectric superstrate," *2015 International Conference on Wireless Networks and Mobile Communications (WINCOM)*, Marrakech, pp. 1-8, 2015.

[8] D. Gangwar, S. Das, and R. L. Yadava, "A meander line-DSRR double superstrate loaded high gain circular patch antenna," *2017 IEEE Applied Electromagnetics Conference (AEMC)*, Aurangabad, pp. 1-2, 2017.

[9] C. A. Balanis, *Antenna Theory: Analysis and Design*. Wiley-Interscience, New York, NY, USA, 2005.

[10] M. Saravanan, G. V. Beslin, and S. M. Umarani, "Gain enhancement of patch antenna integrated with metamaterial inspired superstrate," *Journal of Electrical Systems and Information Technology*, 2018.

Vani H. R. did her B.E. in Instrumentation Technology in 1991 from Mysore University, M.Tech. in Industrial Electronics from NITK, Surathkal in 2003. She is working as Associate Professor in ECE at Adichunchanagiri Institute of Technology (AIT), Chikkamagaluru Karnataka. She is a Life Member of ISTE, New Delhi.

Goutham M. A. did his B.E. in Electronics and Communication. Engineering in 2001 from Kuvempu University, M.Tech. in Digital Electronics and Communication Systems from Visveswaraiah Technological University (VTU) Belagavi, in 2005 and Ph.D. from Jadhavpur University, West Bengal, India in 2010. He is Professor in Electronics and Communication. Engineering Dept. with an experience of 15 years at Adichunchanagiri Institute of Technology (AIT), Chikkamagaluru, Karnataka. His current research interest includes MEMS, Wireless and Ad-hoc networks. He is a Life Member of ISTE, New Delhi.

Paramesha did his B.E. in Electronics and Communication. Engineering in 1989, M.Tech. in Microwave Engineering from Banaras Hindu University, Varanasi, India in 1997 and Ph.D. from Indian Institute of Technology (IIT), Kharagpur, West Bengal, India in 2007. He is Professor and Head of Electronics and Communication Engineering Department at GEC, Hassan, Karnataka. His current research interest includes antennas for Satellite Communication, Microwave Antennas, and Millimeter systems. He is a Life Member of ISTE, New Delhi.

Dielectric Resonator Antenna Based Dual Port Multiple Input Multiple Output Antenna

Muhammad Zia Hameed [1], Shabbir Majeed [1], Rashid Saleem [2], Muhammad Farhan Shafique [3], and Sabih ur Rehman [4]

[1,2] Department of Electrical and Telecommunication Engineering
University of Engineering and Technology, Taxila, 47050, Pakistan
ziahameed47@gmail.com, shabbir.majeed@uettaxila.edu.pk, rashid.saleem@uettaxila.edu.pk

[3] Center for Advanced Studies in Telecom (CAST)
COMSATS Institute of Information Technology (CIIT), Park Road, Chak Shahzad, Islamabad, 45550, Pakistan
farhan.shafique@comsats.edu.pk

[4] School of Computing and Mathematics, Charles Sturt University (CSU), Australia

Abstract ─ This paper presents a Dielectric Resonator based dual frequency band Multiple Input and Multiple Output (MIMO) antenna for wireless communication. This antenna is designed for WLAN (5.5–5.8 GHz) and X–band (8–8.1 GHz) applications. A pair of DRAs is placed on a FR-4 substrate and is excited through microstrip feed lines placed on rear side of substrate. A via-less EBG structure is introduced to suppress the mutual coupling among DRAs. The measured isolation among the two antenna ports is 25 dB and 41 dB for 5.6 GHz and 8.05 GHz respectively. The overall dimension of the antenna is $0.72 \lambda_o \times 0.52 \lambda_o$ at lower resonant frequency. Simulated and measured results are in good agreement, which supports the potential application of the proposed antenna for high gain WLAN and X–band applications.

Index Terms ─ Dielectric Resonator Antenna (DRA), decoupling structure, Electromagnetic Band Gap (EBG), Multiple Input Multiple Output (MIMO).

I. INTRODUCTION

MIMO system is the technology of choice in wireless communication to meet the high data rate and high diversity gain requirements [1]. Microstrip patch antennas are extensively reported for MIMO applications. However, these antennas are prone to high metallic losses and lesser radiation efficiency, especially at higher frequencies. Dielectric Resonator Antennas (DRAs) do not have these disadvantages. They have several distinct benefits as compared to microstrip patch antennas, such as high radiation efficiency, higher gain and low losses [2]. MIMO system performance is affected by undesired mutual coupling among the radiating elements which is developed due to miniaturization of the antenna design. Different techniques such as the Defected Ground Structures (DGSs), Electromagnetic Band Gap (EBG) structures and Frequency Selective Surfaces (FSSs) [3, 4] are reported in the literature to enhance isolation between antenna elements for different MIMO systems. A split ground plane is another commonly reported solution to accomplish high isolation in MIM DRAs [5, 6]. Aperture-coupled and probe feedings in hybrid feeding mechanism can also be used to achieve high isolation [7]. However, the techniques presented in [5, 6, 7] make fabrication more complex and compromise the design compactness.

In this work, a compact dual band MIMO DRA is proposed for WLAN and X–band applications. DRAs are placed on a 38.8 mm × 28 mm × 1.6 mm FR-4 substrate. A via-less EBG structure has been used to enhance the isolation among the DRAs.

The rest of this paper is organized as follows: in Section II a discussion of proposed antenna design configuration is given, DRA resonant frequency and modal analysis are given in Section III, simulated and measured results are presented in Section IV, and finally Section V concludes the paper.

II. ANTENNA DESIGN

The proposed design geometry is shown in Figs. 1 (a) and 1 (b) along with the dimensions. The proposed antenna is simulated and optimized in Ansys HFSS®. The realized MIMO design is shown in Figs. 2 (a) and 2 (b). The dimensions of the substrate are $l_1 = 28$ mm × $w_1 = 38.8$ mm × $h_2 = 1.6$ mm, as shown in Fig. 1 (a). The

cylindrical DRAs are mounted on the top side of FR-4 substrate. These DRAs are made of Alumina with: dielectric constant, ε_r, of 9.8; dielectric loss tangent, tan δ of 0.002; radius, r of 6.35 mm and height, h_1 of 9 mm. The spacing between the DRAs is $d_1 = 8.72$ mm. DRAs are proximity/couple-fed through two microstrip feed lines etched at the rear side of substrate, each of length $l_3 = 22$ mm and width $w_3 = 2.05$ mm. Feed lines are separated by a distance $d_2 = 19$ mm.

(a)

(b)
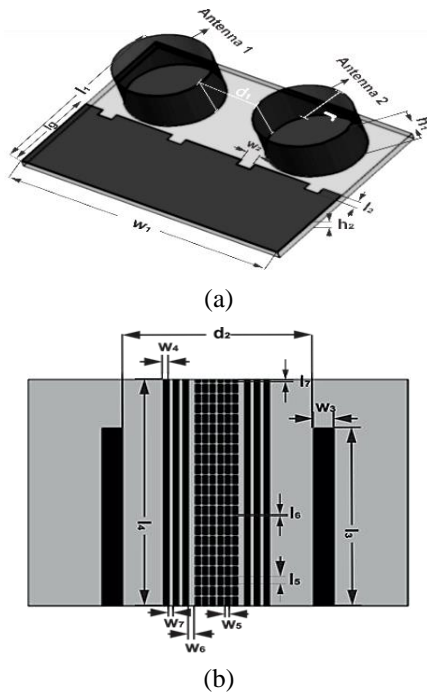
Fig. 1. MIMO DRA design: (a) front side and (b) back side.

A common ground plane arrangement is employed on the front side of substrate in the suggested MIMO design, as shown in Fig. 1 (a). The ground plane dimensions are $l_g = 13.4$ mm $\times$ $w_1 = 38.8$ mm. Rectangular shaped slits are imprinted in the top edge of the ground plane to improve impedance matching for the desired resonant frequencies. These rectangular slits have dimensions of $l_2 = 1.1$ mm $\times$ $w_2 = 2$ mm.

A via-less EBG structure is employed in this design to enhance isolation. This structure is imprinted on the back side of the substrate as shown in Fig. 1 (b).

The dimensions of each single rectangular block in via-less EBG structure are $l_5 = 1$ mm $\times$ $w_5 = 0.5$ mm. The spacing l_6 between adjacent rectangular blocks is 0.25 mm. Furthermore, a pair of three vertical strips is placed on both sides of the via-less EBG structure. The dimensions of each strip are $l_4 = 28$ mm $\times$ $w_4 = 0.5$ mm. The spacing between adjacent strips is $w_7 = 0.5$ mm and first strip is placed at a distance of $w_6 = 0.75$ mm from the EBG structure.

(a)   (b)
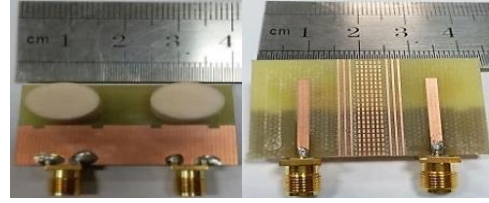
Fig. 2. Fabricated MIMO DRA: (a) front side and (b) back side.

III. RESONANT FREQUENCY AND MODAL ANALYSIS OF DRA

The proposed DRA design has two resonant modes, $HEM_{11\delta}$ and $TM_{01\delta}$. The first resonant mode is $HEM_{11\delta}$ and it produces broadside radiation pattern, as shown in Fig. 3 and it can be theoretically verified with the following relation [9]:

$$f_{o(HEM_{11\delta})} = \frac{c \times 6.324}{2\pi a \sqrt{\varepsilon_r + 2}} \left(0.27 + 0.36 \frac{a}{2h} + 0.02 \left(\frac{a}{2h} \right)^2 \right). \quad (1)$$

Where "a" is the radius of DR and "h" is the height of DR. The above equation is valid for $0 \leq a/h \leq 6$. The theoretical calculation of the resonant frequency from the above equation gives 5.53 GHz.

The second resonant mode is $TM_{01\delta}$ and it offers end-fire radiation pattern, as shown in Fig. 4 and it can be theoretically calculated [9] as:

$$f_{o(TM_{01\delta})} = \frac{c \sqrt{3.83^2 + \left(\frac{\pi a}{2h} \right)^2}}{2\pi a \sqrt{\varepsilon_r + 2}}. \quad (2)$$

The above equation is valid for $0.33 \leq a/h \leq 5$. The theoretical calculation of the resonant frequency from the above equation gives 8.73 GHz.

(a)   (b)
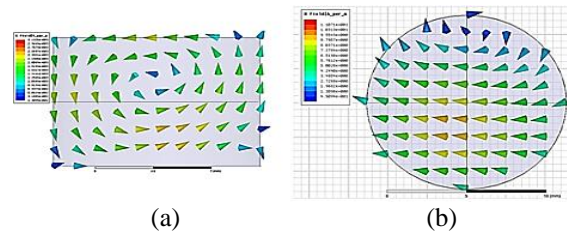
Fig. 3. First resonant mode $HEM_{11\delta}$ of the DRA: (a) E-field pattern and (b) H-field pattern.

(a)   (b)
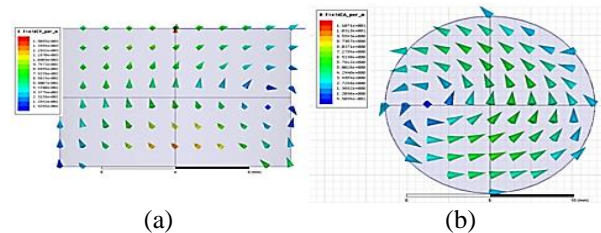
Fig. 4. Second resonant mode $TM_{01\delta}$ of the DRA: (a) E-field pattern and (b) H-field pattern.

IV. SIMULATED AND MEASURED RESULTS

A. S-parameters

Measured and simulated S_{11} and S_{12} results with and without decoupling structure are shown in Fig. 5. The S_{11} result shows that the suggested MIMO antenna design is well matched on 5.6 GHz and 8.05 GHz. The S_{12} result shows that more than 20 dB isolation is achieved between antennas, when the via-less EBG structure is introduced.
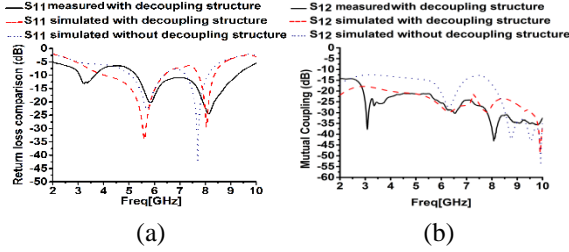
Fig. 5. Simulated and measured S-parameters of MIMO design: (a) S_{11} and (b) S_{12}.

B. Induction current suppression

The surface current density is plotted at 5.6 GHz and 8.05 GHz, as shown in Figs. 6 (a) and 6 (b). The *Jsurf* plots show the undesired induced surface currents on ground plane and the feeding line of antenna, when the MIMO design is simulated without the decoupling structure. However, decoupling structure effectively suppresses the undesired surface currents, resulting in significant isolation between the antenna ports.
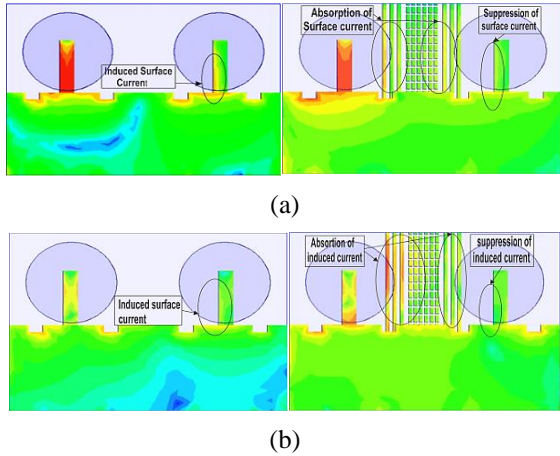
Fig. 6. *Jsurf* current distribution plots at: (a) 5.6 GHz and (b) 8.05 GHz.

C. MIMO performance parameters

The diversity performance of a MIMO system is judged by its performance parameters. In this regard, the envelope correlation coefficient (ECC) and total active

reflection coefficient (TARC) have been measured for the proposed MIMO DRA system. A maximum threshold of ECC < 0.5, TARC < 0 dB is allowed for an acceptable MIMO system [8]. The proposed design has ECC < 0.001 and TARC < -20 dB, in both bands, as shown in Fig. 7 which assures the optimum performance of the suggested MIMO antenna. Simulated and measured radiation patterns for *E*-planes and *H*-planes are shown in Fig. 7 (c). The fabrication and measurements imperfections cause slight distortion in radiation patterns. The comparison of the proposed work with the reviewed literature is given in Table 1.
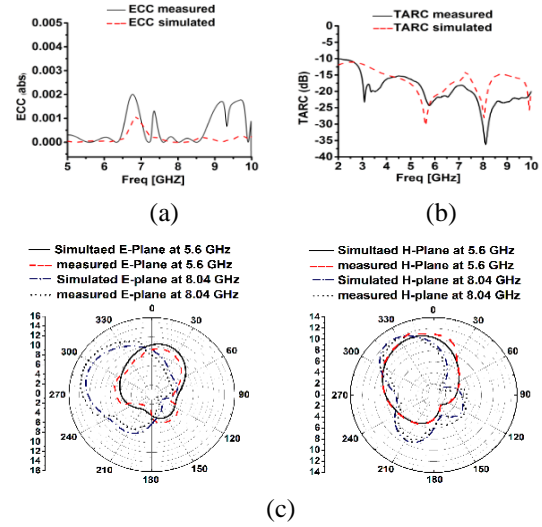
Fig. 7. MIMO performance parameters: (a) ECC, (b) TARC, and (c) radiation patterns.

Table 1: Comparison of the proposed work with the reviewed literature

Ref.	Freq. MHz/GHz	Isolation	Antenna Size [mm³]
[1]	803–823 MHZ 2.44–2.9 GHz	20 dB 14 dB	50×100×1.56
[2]	3.4–3.7 GHz 5.1–5.35 GHz	13 dB 16 dB	50 ×50×1.6
[3]	2.4 GHz 5.2 GHz	20 dB 18 dB	40×80×1
[7]	5.15–5.35 GHz	35 dB	60×60×1
This work	5.5–5.8 GHz 8 –8.1 GHz	28 dB 41 dB	28×38×1.6

V. CONCLUSION

A dual-port dual-band MIMO DRA for high gain WLAN and X–band application is proposed. The design is fabricated on a 1.6 mm thick FR-4 substrate. A via-less EBG structure is employed to achieve effective isolation between antenna elements. The measured results demonstrate the isolation better than 20 dB in both bands. MIMO performance criteria such as ECC,

TARC and radiation patterns also exhibit excellent performance. The proposed design exhibits excellent impedance match and isolation, without compromising the compactness. The total antenna is $0.72 \lambda_o \times 0.52 \lambda_o$ in size at the lower frequency band.

REFERENCES

[1] M. S. Sharawi, A. B. Numan, M. U. Khan, and D. N. Aloi, "A dual-element dual-band MIMO antenna system with enhanced isolation for mobile terminals," *IEEE Antennas and Wireless Propagation Letters*, vol. 11, pp. 1006-1009, 2012.

[2] A. A. Khan, M. H. Jamaluddin, S. Aqeel, J. Nasir, J. U. R. Kazim, and O. Owais, "Dual-band MIMO dielectric resonator antenna for WiMAX/WLAN applications," *IET Microwaves, Antennas & Propagation*, vol. 11, no. 1, pp. 113-120, 2017.

[3] J. Kim, M. Han, C. Lee, and J. Choi, "Dual band MIMO antenna using a decoupling network for WLAN application," *13th International Conference on Advanced Communication Technology (ICACT2011)*, Seoul, pp. 624-627, 2011.

[4] M. T. Islam and M. S. Alam, "Compact EBG structure for alleviating mutual coupling between patch antenna array elements," *Progress In Electromagnetics Research*, vol. 137, pp. 425-438, 2013.

[5] D. Guha, S. Biswas, T. Joseph, and M. T. Sebastian, "Defected ground structure to reduce mutual coupling between cylindrical dielectric resonator antennas," *Electronics Letters*, vol. 44, no. 14, pp. 836-837, 2008

[6] S. H. Zainud-Deen, H. A. Malhat, and K. H. Awadalla, "Reduction of mutual coupling between two dielectric resonator antennas mounted on a circular cylindrical ground plane," *IEEE Antennas and Propagation Society International Symposium (APSURSI)*, pp. 1-4, 2010.

[7] X. M. Wang, Z. B. Weng, Y. C. Jiao, Z. Zhang, and F. S. Zhang, "Dual-polarized dielectric resonator antenna with high isolation using hybrid feeding mechanism for WLAN applications," *Progress In Electromagnetics Research Letters*, vol. 18, 195-203, 2010.

[8] S. H. Chae, S. K. Oh, and S. O. Park, "Analysis of mutual coupling, correlations, and TARC in WiBro MIMO array antenna," *IEEE Antennas Wireless Propag. Lett.*, vol. 6, pp. 122-125, 2007.

[9] R. K. Mongia and P. Bhartia, "Dielectric resonator antennas—A review and general design relations for resonant frequency and bandwidth," *International Journal of Microwave and Millimeter-Wave Computer-Aided Engineering*, vol. 4, no. 3, pp. 230-247.

Muhammad Zia Hameed received B.Sc. Electronics Engineering in 2012 from The Islamia University of Bahawalpur, Punjab Pakistan. He is currently working as a Research Associate at University of Engineering and Technology (UET), Taxila. Recently he is awarded a funded M.S. studentship by UET Taxila. His main research interests are in DRAs, metamaterials and high gain antennas.

Shabbir Majeed Chaudhry received B.Sc. in Electrical Engineering and M.Sc. Electrical Engineering in 2000 and 2003, from University of Engineering and Technology, (UET) Taxila, Pakistan. He also received his Ph.D. degree in Electrical Engineering from UET Taxila and since 2006 onwards, he is working as an Assistant Professor in the same University.

Rashid Saleem received B.S. Electronic Engineering from G.I.K Institute of Engineering Sciences and Technology, Pakistan, in 1999. He received M.S. from UET Taxila through Center for Advanced Studies in Engineering, Pakistan, in 2006 and Ph.D. from the University of Manchester, United Kingdom in 2011. Currently, he is working as Assistant Professor at University of Engineering and Technology (UET), Taxila, Pakistan.

Muhammad Farhan Shafique received the B.Eng. degree from Hamdard University, Karachi, Pakistan, in 2003, M.S. degree from the University of Paris East Marne-La-Vallée, Paris, France, in 2005 and Ph.D. in Electronic and Communications Engineering from The University of Leeds, UK in 2010. He is working as an Associate Director at Center for Advanced Studies in Telecommunications (CAST).

Sabih ur Rehman is working as a Lecturer at Charles Sturt University, Australia. Sabih has completed his Ph.D. in the area of vehicular ad-hoc networks. Sabih's research expertise lie in the areas of Wireless Propagation and Antenna Modeling.

Compact Quad Element UWB-MIMO Antenna with Electronically Reconfigurable WiMAX Band-Stop Capability

Asim Quddus [1*], Rashid Saleem [2], M. Farhan Shafique [3], and Sabihur Rehman [4]

[1] Department of Electrical Engineering
[2] Department of Telecommunication Engineering
University of Engineering and Technology, Taxila, 47050, Pakistan

[3] Center for Advanced Studies in Telecommunication
COMSATS Institute of Information Technology, Islamabad, Pakistan

[4] School of Computing and Mathematics, Charles Sturt University, Australia
[*]asim.quddus@uettaxila.edu.pk

Abstract ─ Miniaturized four port multiple-input multiple-output (MIMO) antenna with electronically reconfigurable WiMAX band-stop capability is proposed for ultra-wideband (UWB) application. The elements of MIMO antenna system exhibit good impedance match (VSWR ≤ 2), while offering high ports isolation ($S_{12} \leq$ -20 dB) over the whole ultra-wideband spectrum. Moreover, reconfigurable band-notch capability at WiMAX (3.2-3.8 GHz) frequency band is achieved by switching the PIN diode to 'ON' state. The antenna is fabricated and measured as well, and the results suggest that the proposed antenna design with switchable WiMAX band-notch characteristics is a suitable candidate for UWB-MIMO applications.

Index Terms ─ Band-stop, multiple-input multiple-output (MIMO), reconfigurable, WiMAX.

I. INTRODUCTION

Wireless communication technologies have gained much attention over last few decades. The prime focus of recent wireless technology is to use minimum resources, achieve high data rate and cause minimum interference to other existing wireless communication standards [1]. To achieve higher data rates and higher channel capacities, MIMO technology is integrated in UWB systems. However, a significant challenge in UWB-MIMO communication is the miniaturization of system. The unwanted mutual coupling is caused by miniaturization and hence the effectiveness of MIMO is compromised. Therefore, in order to provide decoupling between antenna elements, an efficient isolating/decoupling structure is desired in MIMO systems. In existing literature, several MIMO antenna designs with decoupling structures have been reported to attain high isolation between antenna elements [3-4]. To achieve interference

mitigation in UWB communication, several designs with band-notched characteristics have been reported in the existing literature. In [1], inverted stubs added to radiator for interference mitigation at 5.8 GHz is reported. A circularly slotted notching structure is proposed in [2]. However, these proposed antennas have permanent band-notching. For the sake of interference free communication, utilization of whole UWB spectrum may not be possible even if there is no conflicting narrow band system working in the close proximity. Therefore, for the improvement of the UWB system performance, antennas with reconfigurable/switchable band notch performances are desirable [7-8]. PIN diodes are placed on stub at ground plane in [7] to notch WLAN frequency band, while in [8] PIN diodes are placed on the radiating patch in order to achieve reconfigurable band notch characteristics.

A miniaturized four port MIMO antenna exhibiting electronically reconfigurable WiMAX (3.2 - 3.8 GHz) band notch capability is proposed in this research for ultra-wideband MIMO applications. Isolation of more than 20 dB among all radiating elements over entire ultra-wideband band is achieved using a decoupling structure. For design and optimization of the antenna geometry, full wave electromagnetic simulations using Finite Element Method (FEM) have been carried out in Ansys High Frequency Structural Simulator (HFSS)™.

II. DESIGN CONFIGURATION OF ANTENNA

The geometric structure of proposed antenna is presented in Fig. 1. Antenna design is simulated and fabricated on a 0.8 mm thick FR4 substrate. The upper layer contains four radiating elements whereas the defected ground plane and decoupling structure is placed

on the back side of substrate. The decoupling structure as shown in Fig. 1 (b) contains defected rectangular strip line. It is placed between ground planes to isolate the antenna elements placed in diagonal and side-by-side arrangement. The overall decoupling of more than 20 dB between MIMO antenna elements is achieved.
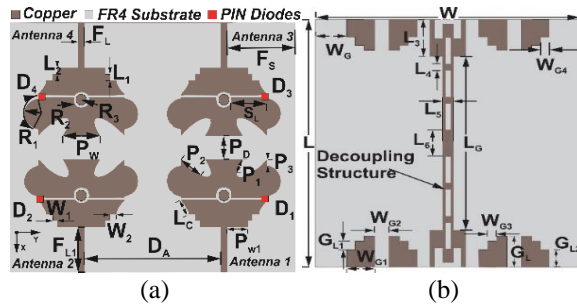
Fig. 1. Antenna structure: (a) front view and (b) back view. L=26, W=30, P_W=3.9, R_3 =0.6, F_{L1}=4.7, L_5=1.2, R_2=0.8, P_D=2.5, W_G=3.5, D_A=14.4, L_6=2.8, G_L=3.2, L_1=0.65, P_1=1.2, W_{G1}=3.2, F_S=7.2, L_C=1.5, G_{L1}=1, L_2=0.7, P_2=2.7, W_{G2}=1.6, S_L=3.75, W_1=0.5, G_{L2}=1.8, L_3=3.8, P_3=0.6, W_{G3}=1, F_L=0.62, W_2=0.7, L_4=0.7, P_{W1}=2.2, W_{G4}=1, L_G=18.5, R_1=1.5 (parameters in mm).

The effective length of notching structure is required to filter out the desired frequency band. Notching at desired frequency bands can be obtained using equation (1):

$$f_r = \frac{C}{4L_{Total}\sqrt{\varepsilon_{eff}}}. \tag{1}$$

Where, $L_{Total} = 2S_L + 2\pi R_2$ and 'C' is the constant of electromagnetic wave velocity. The calculated value of effective dielectric is $\varepsilon_{eff} \sim 3.1$. By putting values in equation, we get $f_r \sim 3.5$ GHz. An Ω-shaped slot is created in main radiator of each antenna element. It provides band notch characteristics at WiMAX 3.5 GHz. The current around the edges of slots reverses its direction causing anti-resonance at the desired notched frequency band. To show this effect, current density (*J-surf*) plots at 3.5 GHz with diodes switching (ON/OFF) is shown in Fig. 4. Moreover, to achieve the reconfigurable band notch functionality in UWB-MIMO antenna, PIN diode is embedded in the slot of each radiator, as shown in Fig. 1 (a). The purpose of PIN diode is to switch the UWB-MIMO antenna between ultra-wideband operation and WiMAX band notch functionality. The PIN diode, D_1, as shown in Fig. 1 (a), controls Antenna 1 band notching. Similarly, D_2, D_3 and D_4 diodes control the band notching functionality of Antennas 2, 3 and 4 respectively. The reconfigurable characteristics of proposed UWB-MIMO antenna have two operations as below:

Case I: When diode is reverse biased or is in its 'OFF State'. Antenna omits the WiMAX band notching behavior and UWB-MIMO antenna provides matching without any band notch.

Case II: When diode is forward biased or PIN diode is in its 'ON State'. Antenna eliminates the WiMAX band from the UWB band and operates as a band notch antenna.

The PIN diode is first modeled in HFSS™ using lumped elements according to the equivalent model for Case I and Case II, as shown in Fig. 2. SMP 1320-079 LF PIN diodes have been used for switching. The diode has low reverse bias (zero volt) capacitance of 0.3 pF at above 10 MHz frequencies and low resistance of 0.9 ohms at 10 mA during forward bias operation. The whole biasing network has been fed through an in-line DC block module to prevent any damage to the network analyzer. The DC block is shown in Fig. 2 (b).
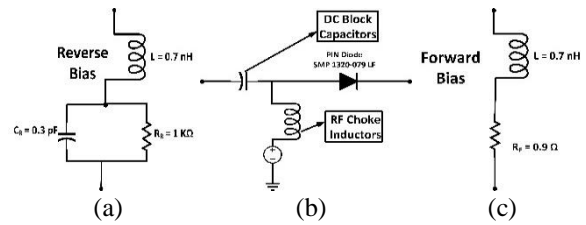
Fig. 2. Equivalent circuit model of PIN diode: (a) Case I, (b) biasing network, and (c) Case II.

III. RESULTS AND DISCUSSIONS

Antenna design is fabricated on FR4 laminate, as shown in Figs. 3 (a) and (b). Agilent N5242A PNA-X network analyzer is used for the measurements. As the antenna elements are identical, impedance matching is similar for each element. The results are presented in Fig. 5. Result shows that four antenna elements are well-matched over entire ultra-wideband spectrum for Case I (diodes switched 'OFF'). However, for Case II (diodes-switched 'ON') proposed UWB-MIMO antenna provides WiMAX (3.2-3.8 GHz) band notching. The RF choke is added to all elements.

To analyze the effect of switching on proposed antenna design, a characteristic mode analysis (CMA) is done in CST Microwave Studio [9]. In Case II, the variation of Mode 1 is clearly observed in Fig. 6. The curve of the characteristic angle associated to this mode presents a sharp slope, which verifies a sharp band notch behavior in this mode. Moreover, it may be noted that the resonant frequency lies at the center of the rejected WiMAX band, as desired.
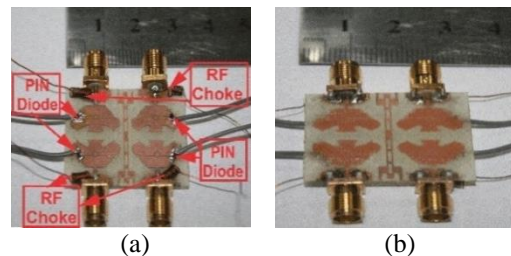
Fig. 3. Fabricated design: (a) front view and (b) back view.
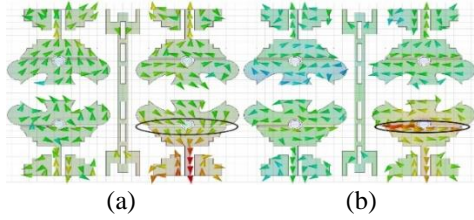
Fig. 4. Surface current density *J-surf* at 3.5 GHz: (a) Case I and (b) Case II.
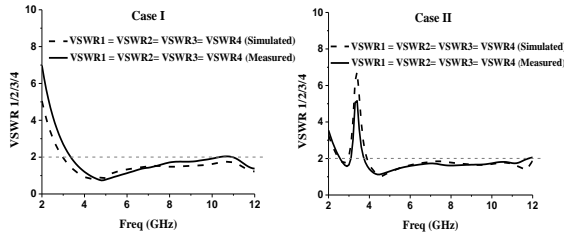
Fig. 5. Impedance matching of proposed prototype.
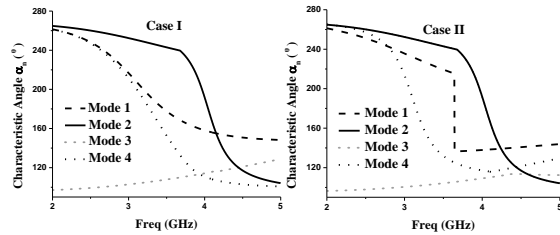
Fig. 6. Characteristic modes analysis.

As in Fig. 1, it can be seen that Antenna 1-2 and 3-4 are placed side-by-side, Antenna 1-4 and 2-3 are diagonal and Antenna 1-3 and 2-4 are placed across each other. The effect of decoupling structure on isolation of antenna elements for both Case I and II, can be observed clearly in Fig. 7. Side-by-side isolation is represented by S_{12} / S_{34} – parameter, diagonal isolation is represented by S_{14} / S_{23} - parameter, while isolation between antenna elements placed across each other is represented by S_{13} / S_{24} – parameter. The overall isolation with isolating structure is better than 20 dB. The radiation patterns in E and H-plane of proposed antenna (Case I and Case II) are observed at 3.5 GHz and 5 GHz and are plotted in Fig. 8. The proposed antenna gives good gain results over whole UWB band except for the notched WiMAX band as depicted in Fig. 9.

(a)
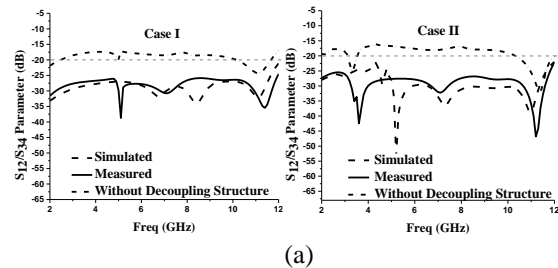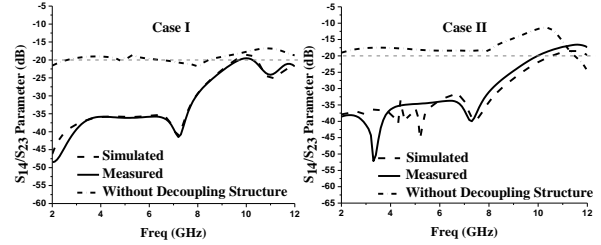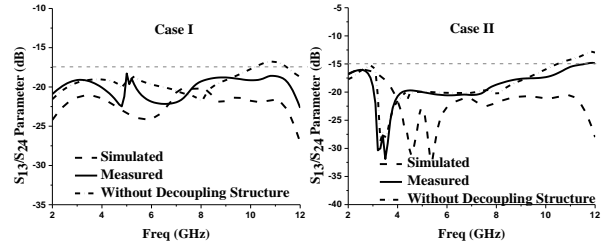
Fig. 7. Mutual Coupling with and without decoupling structure: (a) side-by-side, (b) diagonal, and (c) across.
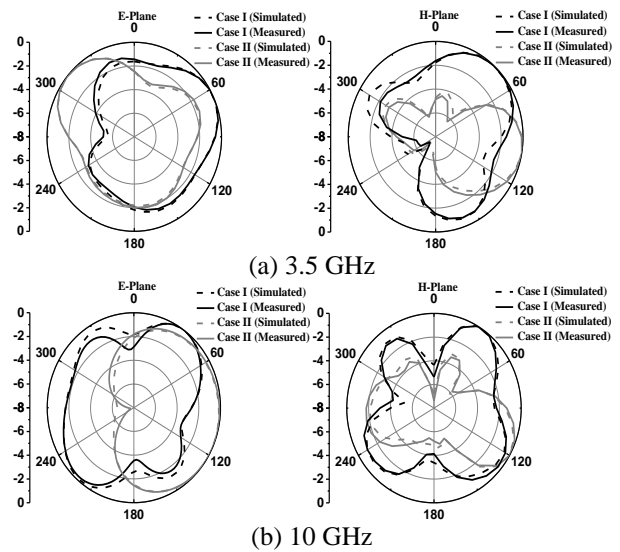
(a) 3.5 GHz

(b) 10 GHz

Fig. 8. Normalized radiation plots: (a) 3.5 GHz and (b) 10 GHz.
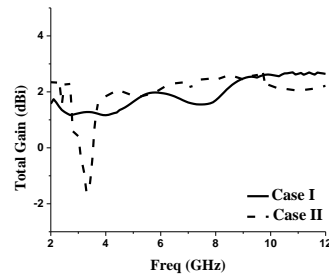
Fig. 9. Gain of proposed antenna.

Channel Capacity Loss (CCL), Total Active Reflection Coefficient (TARC) and Envelope

Correlation Coefficient (ECC) are important diversity parameters to analyze the performance of the proposed MIMO antenna. ECC can be calculated for different antenna topologies (side-by-side, diagonal and across) using equation (2):

$$\rho_e = \frac{\left| S_{ii}^* S_{ij} + S_{ji}^* S_{jj} \right|^2}{\left(1 - |S_{ii}|^2 + |S_{ji}|^2\right)\left(1 - |S_{jj}|^2 + |S_{ij}|^2\right)}. \quad (2)$$

Usually, an ECC value below -3 dB, TARC < 0 dB and CCL< 0.5 bits/sec/Hz in the operating band, is desired. As shown in Figs. 10 (a - f), the results are well within the allowable limits for both Cases (I and II). In Case II the CCL value at WiMAX (3.2-3.8 GHz) band is above 0.5 bits/sec/Hz, because of the anti-resonant effect of band notching structure.
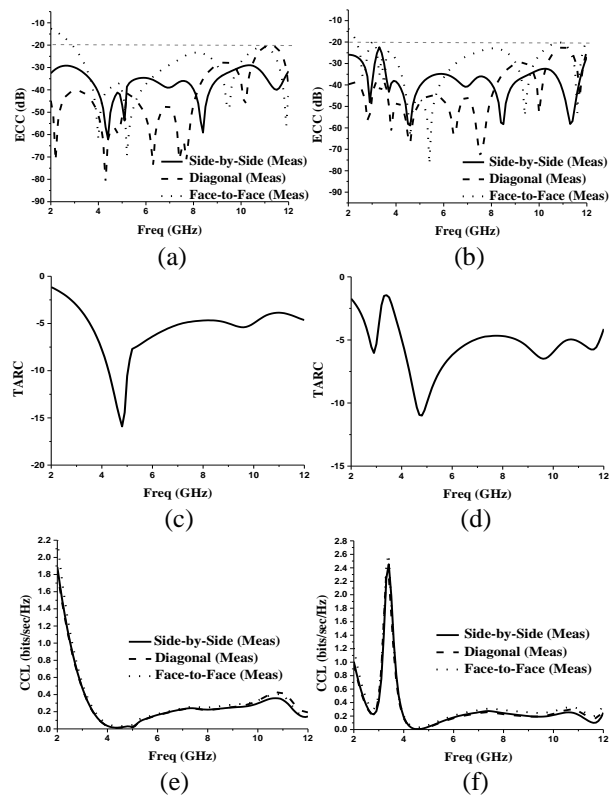
Fig. 10. MIMO/Diversity performance parameters: (a) ECC for Case I, (b) ECC for Case II, (c) TARC for Case I, (d) TARC for Case II, (e) CCL for Case I, and (f) CCL for Case II.

Table 1: Comparison of proposed MIMO antenna with existing literature

Ref.	Isolation (dB)	No. of Ports	Antenna Dimension (mm³)	Reconfigurability
[5]	> 20	2	50ˣ30ˣ1.6	No
[6]	> 20	2	18ˣ34ˣ1.6	No
[7]	> 20	2	23ˣ39.8ˣ1.524	Yes
Proposed antenna	> 20	4	26ˣ30ˣ0.8	Yes

The proposed MIMO antenna elements are compact as compared to various antennas reported in literature previously [5-7]. The comparison of proposed antenna characteristics with these MIMO antenna designs is listed in Table 1.

IV. CONCLUSION

A compact our port multiple-input multiple-output (MIMO) antenna with electronically reconfigurable WiMAX (3.5 GHz) band notch characteristics is proposed for ultra-wideband applications. The design exhibits good impedance match over entire UWB band. Enhanced isolation is achieved by using simple decoupling structure. Diversity parameters are also within the allowed limits. More importantly simulated as well as measured results are in good agreement, suggesting that the proposed MIMO antenna design is suitable candidate for reconfigurable ultra-wideband application.

REFERENCES

[1] J. Zhu, et al., "Compact dual polarized UWB quasi-self-complementary MIMO/diversity antenna with band-rejection capability," *IEEE Trans. Antenna Propag.*, vol. 15, pp. 905-908, 2015.

[2] H. Huang, et al., "Uniplanar differentially driven UWB polarisation diversity antenna with band-notched characteristics," *Electronics Letters*, vol. 51, pp. 206-207, 2015.

[3] S. I. Jafri, et al., "Compact reconfigurable multiple-input-multiple-output antenna for ultra-wideband applications," *IET Microw., Antennas & Propag.*, vol. 10, pp. 413-419, 2016.

[4] M. S. Khan, et al., "Compact 4 × 4 UWB-MIMO antenna with WLAN band rejected operation," *Electronics Letters*, vol. 51, pp. 1048-1050, 2015.

[5] A. Iqbal, et al., "Mutual coupling reduction using F-shaped stubs in UWB-MIMO antenna," *IEEE Access*, vol. 6, pp. 2755-2759, 2018.

[6] R. Chandel, et al., "Tapered fed compact UWB MIMO-diversity antenna with dual band-notched characteristics," *IEEE Trans. Antenna Propag.*, vol. 66, pp. 1677-1684, 2018.

[7] M. S. Khan, et al., "Compact planar UWB MIMO antenna with on-demand WLAN rejection," *Electronics Letters*, vol. 51, pp. 963-964, 2015.

[8] B. Badamchi, et al., "Design of compact reconfigurable ultra-wideband slot antenna with switchable single/dual band notch functions," *IET Microw. Antennas & Propag.*, vol. 8, no. 8, pp. 541-548, 2014.

[9] E. Antonino-Daviu, et al., "Modal analysis and design of band-notched UWB planar monopole antennas," *IEEE Trans. Antenna Propag.*, vol. 58, no. 5, pp. 1457-1467, 2010.

MACA Algorithm to Accelerate Modeling of Eddy Current Position Sensor

Yang Bao [1], Zhiwei Liu [2], and Jiming Song [1]

[1] Department of Electrical and Computer Engineering
Iowa State University, Ames, IA 50011, USA
brianbao@iastate.edu, jisong@iastate.edu

[2] Department of Information Engineering
East China Jiaotong University, Nanchang, Jiangxi 330013, China
zwliu1982@hotmail.com

Abstract ─ In this paper, we proposed a Modified Adaptive Cross Approximation (MACA) algorithm method to model an eddy current probe used as position sensor in Nondestructive Evaluation (NDE). Eddy current based position sensor can be used when optical aids cannot to guide the position of the coil. We use surface integral equation technique with selected Stratton-Chu formulation and apply MACA algorithm to accelerate the calculation of impedance change for the position sensor. Good performance of proposed method is demonstrated with numerical examples.

Index Terms ─ Eddy current nondestructive evaluation, modified adaptive cross approximation, position sensor.

I. INTRODUCTION

Eddy current technique is a high-speed nondestructive method to detect corrosion, cracks or flaws in metallic tubes. Thousands of tubes are used in heat exchangers and steam generators to increase the amount of heat transferred. Eddy current technique is especially important in nuclear power plants where reused, contaminated water must be prevented from mixing with fresh water that will be returned to the environment [1]. To minimize the risk of leakage from the tubes becomes the aim of eddy current technique. For the heat exchangers, in the presence of coolant, the coil position cannot be guided by optical aid, while eddy current technique can be used to sense it [2].

Finite element method has been applied for the modeling of eddy current nondestructive evaluation (NDE) problems for the tubes [3-4], but the drawback is that it needs to discretize the whole solution domain which results in consuming too much computational resource. Adaptive cross approximation (ACA) was proposed by Bebendorf [5], with the help of tree structure, it replaces the well separated far-block interactions by low rank approximation and compute the elements from diagonal and near block interactions with full matrix. Purely algebraic and kernel independent are the key features for ACA algorithm. ACA algorithm uses only part of the elements from the original matrix and makes every skeletons a kind of cross over all the other pivot rows and columns. In this paper, we proposed the modified ACA (MACA) to accelerate boundary element method (BEM) for 3D eddy current modeling of the tubes. MACA is based on the rule that when the diagonal interactions are dominant compared with the far block interactions, these far block interactions can be neglected to decrease the memory requirement and CPU time.

II. MACA BASED BEM

The details of ACA algorithm are shown in [5-7], the details of the selected Stratton-Chu formulation based BEM are shown in [8] and ACA based BEM is shown in [9]. The discretized form of BEM matrix has seven nonzero matrices with four kinds of dimensions (number of edges by number of edges, number of patches by number of edges, number of edges by number of patches and number of patches by number of patches), as:

$$\begin{bmatrix} 0.5\mathbf{T} - \mathbf{K}_1^{\times} & 0 & \mathbf{R}_1^{\times} \\ -i\,\mu_2/\mu_1\,\mathbf{L}_2^{\times} & 0.5\mathbf{T} + \mathbf{K}_2^{\times} & 0 \\ \mu_2/\mu_1\,\mathbf{K}_2^{n} & ik_2^2\mathbf{L}_2^{n} & 0.5\mathbf{D} - \mathbf{R}_2^{n} \end{bmatrix}, \quad (1)$$

where k is the wavenumber, μ is permeability, subscript $i = 1, 2$ stand for medium 1 (air) or medium 2 (metal), the superscript $\times$ and n denote the cross or dot products with normal unit vector $\hat{\mathbf{n}}$, and give the tangential and normal components, respectively. **R, L, K, T, D** are shown in [8], **D** is a diagonal matrix, **T** is a diagonal-dominant sparse matrix, **L** is the electric (magnetic) field due to the electric (magnetic) current directly, **K** is the electric (magnetic) field due to the magnetic (electric) current, and **R** is the electric (magnetic) field due to the electric (magnetic) charge. The dimensions of each matrix are due to number of basis and testing functions.

Octal tree structure is used to divide the object into

blocks which will leads to diagonal, near and far block interactions. For the diagonal and near block interactions, full matrices will be saved, while for the far block interactions, MACA is applied to approximate it which leads to the reduction of the memory requirement.

The basic idea for MACA is that due to the nature of Green's function: localized static field in medium 1 and exponential decay in medium 2, the bigger distance between two far blocks, the smaller interaction between them. In the impedance matrix, when the diagonal block interaction is much larger than the far block interactions, we can neglect these far block interactions which has almost no effects to the accuracy but with a reduction to the total memory requirement. We define the threshold value by:

$$\Delta_1 = |Z_{mn}|/|Z_{11}|, \qquad (2)$$

where Z_{mn} is the interaction between far block pair box m and box n, Z_{11} stands for the first box's self-interaction. By controlling the threshold value, we can decide how to ignore the small far block interactions.

We use a curve strip as an example to show the way MACA works. In Fig. 1, four periods of curve strips are shown. The radius of one period is 1.5 mm, height is 4 mm. We can regard one period as one nonempty box with 32 edges and patches. Expand these four periods vertically to get 60 periods. Totally there are 60 nonempty boxes with 1920 edges and patches.
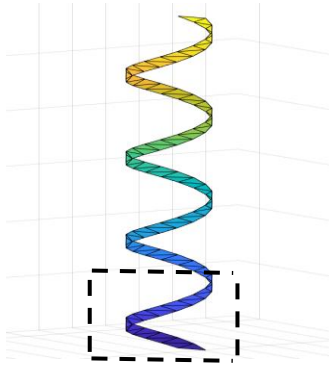
Fig. 1. Four periods of curve strip. One period of curve strip is circled with dash lines.

Then we compare box 1's self-interaction with the interaction between box 1 and other far blocks. Since we have seven nonempty matrices, we need to apply MACA to test all of them. We define other two relative differences as:

$$\Delta_2 = |\Delta Z_{mn}|/|Z_{mn}|, \qquad (3)$$

$$\Delta_3 = |\Delta Z_{mn}|/|Z_{11}| = \Delta_1 \Delta_2, \qquad (4)$$

where $|\Delta Z_{mn}|$ is the difference between original matrix and approximated matrix with ACA algorithm. For all the tests, we set the threshold value $\Delta_1 = 10^{-4}$ which means that we can neglect the far block interactions

when they are 10^4 times smaller than diagonal ones.

Let's take the submatrix $\mu_2/\mu_1 \mathbf{K}_2^n$ which is the normal component of the magnetic field due to the electric current in region 2 with dimension of number of patches by number of edges as an example. Three kinds of relative differences for the interaction between box 1 and its far block interactions are plotted in Fig. 2.
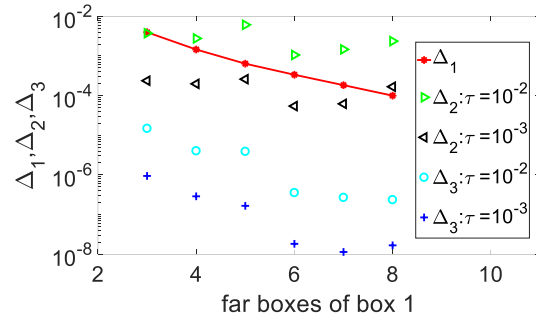
Fig. 2. Relative differences between box 1 and its far block interactions. The relative differences are defined in (2)-(4) for the submatrix $\mu_2/\mu_1 \mathbf{K}_2^n$ which is the normal component of the magnetic field due to the electric current in region 2.

The box 1's far blocks start from box 3. We can see from Fig. 2 that with the increase in accuracy of ACA, more accurate Δ_2, Δ_3 are observed. When ACA tolerance τ is 10^{-2}, from Δ_3, $|\Delta Z_{mn}|$ is 10^5 times smaller than $|Z_{11}|$ which means the difference between original interaction and the approximated one by ACA is very small compared to the diagonal block interaction. As the distance increases, Δ_1 decreases due to the nature of Green's function. After the interaction between box 1 and box 7, Δ_1 will be smaller than 10^{-4} which stands for that the far block interaction is small enough compared to diagonal one. We can neglect the box 1's far block interactions from box 8 to box 60.
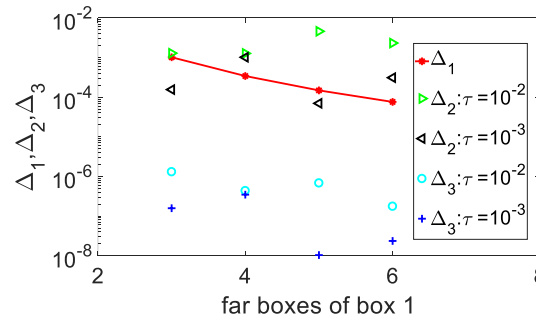
Fig. 3. Relative differences between box 1 and its far block interactions. The relative differences are defined in (2)-(4) for the submatrix $0.5\mathbf{D} - \mathbf{R}_2^n$ which is the normal component of the magnetic field due to the magnetic charge in region 2.

Figure 3 shows the relative differences for the submatrix $0.5\mathbf{D} - \mathbf{R}_2^n$ which is the normal component of the magnetic field due to the magnetic charge in region 2 with the dimension of number of patches to number of patches. From Fig. 3, conclusions can be drew that with the threshold value 10^{-4}, we can neglect the box 1's far block interactions from box 6 to box 60.
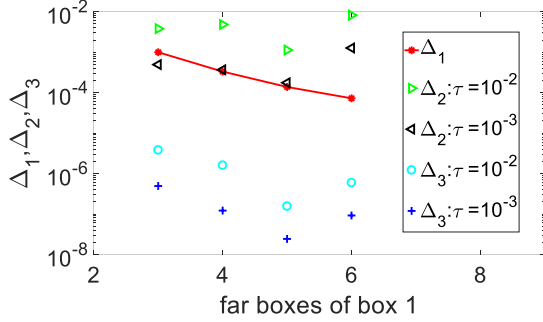
Fig. 4. Relative differences between box 1 and its far block interactions. The relative differences are defined in (2)-(4) for the submatrix $0.5\mathbf{T} + \mathbf{K}_2^{\times}$ which is the tangential component of the electric field due to the magnetic current in region 2.

Figure 4 shows the relative differences for the submatrix $0.5\mathbf{T} + \mathbf{K}_2^{\times}$ which is the tangential component of the electric field due to the magnetic current in region 2 with the dimension of number of edges to number of edges. From Fig. 4, with the threshold value 10^{-4}, we can neglect the box 1's far block interactions from box 6 to box 60.

We do the same test to other submatrices. Figure 5 shows Δ_1 for all the seven submatrices as a summary. It is observed that in the semi-logarithm plot, curves for five submatrices associated with medium 2 are straight lines because the Green function decreases exponentially in the metal. The curves for two submatrices for medium 1 decrease as $1/r^2$ which is due to the static behavior for the Green function in the air region. The three submatrices $0.5\mathbf{T} - \mathbf{K}_1^{\times}$, $0.5\mathbf{T} + \mathbf{K}_2^{\times}$, $0.5\mathbf{D} - \mathbf{R}_2^n$ are diagonal dominant and give much smaller Δ_1 than that of other submatrices for non-diagonal block interactions.

Also, for all the seven submatrices, with the threshold value 10^{-4}, we can neglect a lot of far block interactions which are much smaller than the diagonal ones. For the submatrix $0.5\mathbf{T} - \mathbf{K}_1^{\times}$, $-i\,\mu_2/\mu_1\,\mathbf{L}_2^{\times}$, $\mathbf{R}_1^{\times}$, we can neglect the box 1's far block interactions from box 8, box 14, box 16 to box 60, separately. Above all, we can save a lot of memory while keeping almost same

accuracy because the interactions neglected are trivial.
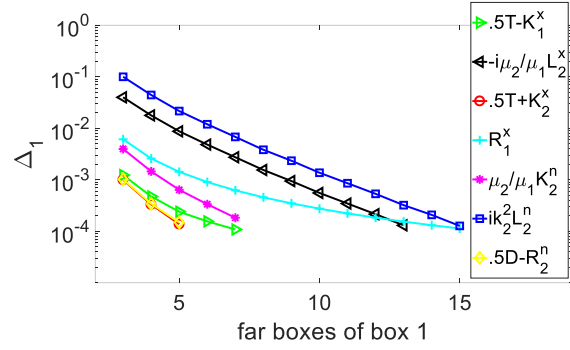
Fig. 5. Relative difference between box 1's self interaction and its far block interactions for seven nonempty submatrices.

III. PERFORMANCE OF MACA

This section shows the performance of MACA when it applies to the steam generator tubes in power plants. The eddy current testing was applied to evaluate the condition of metallic parts in a sodium cooled fast reactor. Coil has the same axis as that of the tube. The coil and tube's parameters are in [10]. All the calculations are done in double precision.

The frequency is 50 kHz, the truncation height is 20 times of skin depth. The impedance change calculated agrees well with that in [10] as shown in Table 1.

Table of impedance change ($\mathbf{m\Omega}$) due to tube

Tao & Bowler [10]	$8.873 + 21.95i$
BEM	$8.862 + 21.96i$
ACA	$8.862 + 21.96i$
MACA	$8.867 + 21.96i$

From Table 1, a good accuracy can be observed in both the real and imaginary parts of impedance changes calculated by semi-analytical method, BEM, ACA and MACA. MACA gets a very good agreement with ACA, semi-analytical method and BEM that the relative differences for real and imaginary parts of impedance changes are smaller than 1%.

For the complexity, the frequency is 30 kHz, with the fixed height of the tube, increase the number of unknowns by decreasing the mesh sizes. The number of unknowns is approximately from 10,000 to 50,000. ACA tolerance is $\tau = 10^{-3}$ and threshold value Δ_1 for MACA is 10^{-4} which results in the relative difference for the impedance changes between BEM and ACA or MACA smaller than 1%. The complexity for memory requirement and CPU time are shown in Figs. 6 (a) and (b).
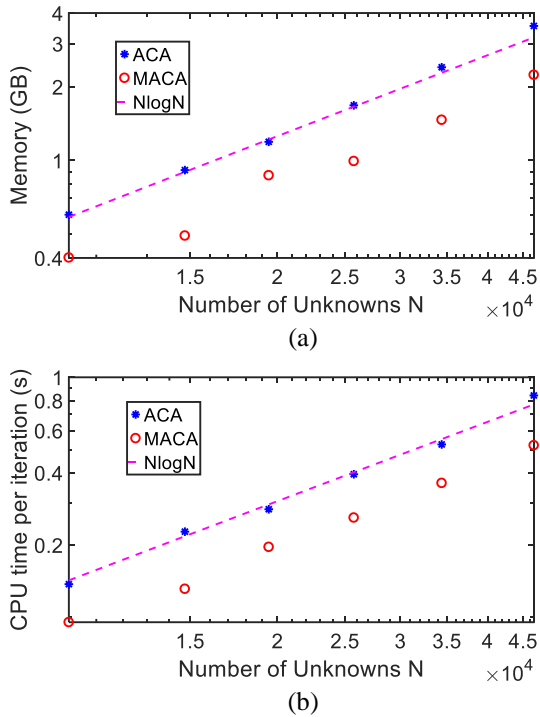
Fig. 6. Performance of ACA and MACA based BEM method for the coil inside the tube. With fixed geometry, different mesh sizes, and number of unknowns from 10,000 to 50,000 at 30 kHz. (a) Memory requirement and (b) CPU time.

From Fig. 6, the complexity of ACA is $O(N \log N)$ for both memory requirement and CPU time per iteration which agrees well with [6]. MACA has more memory and CPU time saving comparing with that of ACA. MACA is very suitable for the tube shape problems because it can neglect the smaller far block interactions which can efficiently deal with the required large truncated area of BEM.

IV. CONCLUSION

The MACA based BEM has proposed to accelerate the modeling of tubes for eddy current NDE problems. With the help of MACA, more memory saving are observed comparing with the ACA algorithm. Performance are shown to validate our proposed method.

ACKNOWLEDGMENT

REFERENCES

[1] NDT resource center, "Tube inspection," [Online]. Available at: https://www.nde-ed.org/Education Resources/CommunityCollege/EddyCurrents/App lications/tubeinspection.htm. [Accessed: 19 Apr., 2018].

[2] T. Wu and J. R. Bowler, "Electromagnetic modeling of an eddy-current position sensor for use in a fast reactor," in *43rd Annual Review of Progress in Quantitative Nondestructive Evaluation*, vol. 1806, Atlanta, GA, USA, July 2016.

[3] N. Ida and W. Lord, "A finite element model for three dimensional eddy current NDT phenomena," *IEEE Trans. on Magnetics*, vol. 21, no. 6, pp. 2635-2643, Nov. 1985.

[4] S. J. Song and Y. K. Shin, "Eddy current flaw characterization in tubes by neural networks and finite element modeling," *NDT & E International*, vol. 33, no. 4, pp. 233-243, June 2000.

[5] M. Bebendorf, "Approximation of boundary element matrices," *Numer. Math.*, vol. 86, no. 4, pp. 565-589, June 2000.

[6] K. Zhao, M. N. Vouvakis, and J. F. Lee, "The adaptive cross approximation algorithm for accelerated method of moments computations of EMC," *IEEE Trans. Electromagn. Compat.*, vol. 47, no. 4, pp. 763-773, Nov. 2005.

[7] S. Börm and L. Grasedyck, "Hybrid cross approximation of integral operators," *Numer. Math.*, vol. 101, no. 2, pp. 221-249, Aug. 2005.

[8] M. Yang, "Efficient Method for Solving Boundary Integral Equation in Diffusive Scalar Problem and Eddy Current Nondestructive Evaluation," *Ph.D. dissertation*, Iowa State Uni., Ames, IA, USA, 2010.

[9] Y. Bao, Z. W. Liu, and J. M. Song, "Adaptive cross approximation algorithm for accelerating BEM in eddy current nondestructive evaluation," *Journal of Nondestructive Evaluation*, under review.

[10] T. Wu and J. R. Bowler, "Eddy-current induction by a coil whose axis is perpendicular to that of a tube," *IEEE Trans. Magnetics*, vol. 53, no. 7, pp. 1-9, July 2017.